DISSERTATION

SPATIAL AND TEMPORAL CHANNEL CHANGES ACROSS THE WATERSHED SCALE FOLLOWING WILDFIRE AND FLOODS

Submitted by

Daniel Joseph Brogan

Department of Civil and Environmental Engineering

In partial fulfillment of the requirements

For the Degree of Doctor of Philosophy

Colorado State University

Fort Collins, Colorado

Fall 2018

Doctoral Committee:

Advisor: Peter A. Nelson

Stephanie K. Kampf
Lee H. MacDonald
Jeffrey D. Niemann

ABSTRACT

SPATIAL AND TEMPORAL CHANNEL CHANGES ACROSS THE WATERSHED SCALE FOLLOWING WILDFIRE AND FLOODS

Fires and floods are important drivers of geomorphic change. The hydrologic and sedimentologic effects of fires have been relatively well studied at the hillslope scale, but we still lack the ability to accurately quantify and predict post-fire flooding and geomorphic changes at larger scales. This lack of understanding stems primarily from two reasons. First, there is generally limited availability of repeat high-resolution topography following fires, and this limits our ability to quantify and explain changes throughout a given channel network. Second and more fundamentally, one cannot simply scale up hillslope processes to the watershed scale, or vice-versa. Since global warming is leading to more wildfires and a higher likelihood of extreme precipitation, understanding downstream flooding and sedimentation is more critical than ever for safeguarding downstream landowners, water users, and aquatic biota.

This dissertation investigates these shortcomings by documenting post-fire channel changes across watershed scales and how extreme floods can alter the more typical post-fire geomorphic response. I focus on two ~15 km^2 watersheds, Skin Gulch (SG) and Hill Gulch (HG), that burned in the 2012 High Park Fire, Fort Collins, Colorado, U.S.A. Over the subsequent four years I used repeat surveys of 10-11 cross sections and longitudinal profiles along the lower channel network of each watershed, and five sequential airborne laser scanning (ALS) surveys, to quantify erosion and deposition. SG was first subjected to a high-intensity convective storm just days after the fire was contained; the resulting flood caused an exceptionally large peak flow, and extensive downstream deposition of cobbles, boulders and woody debris. Fifteen months later SG and HG experienced catastrophic stripping and bed coarsening due to an unusually rare and widespread mesoscale storm, with much greater changes in SG.

These events and the data used to document their effects set up the basis of three separate, yet interdependent comparisons. First, I compare and contrast the peak flows and the effects of the two distinctly different flood disturbances in SG: the short-term peak flow and substantial deposition caused by the convective flood immediately after burning; and the widespread channel and valley bottom erosion caused by the mesoscale flood. Peak flows were estimated using three independent techniques: 1) slope-area method, 2) critical flow, and 3) 2D hydrodynamic modeling. The peak flow estimates for the 2013 flood had a higher relative uncertainty and this stemmed from whether I used pre- or post-flood channel topography. The results document the extent to which a high and moderate severity wildfire can greatly increase peak flows and alter channel morphology, illustrate how indirect peak flow estimates have larger errors than is generally assumed, and indicate that the magnitude of post-fire floods and geomorphic change can be affected by the timing, magnitude, duration, and sequence of rainstorms.

Second, I use the repeat surveys of the cross sections and longitudinal profiles to quantify the channel response to the 2012 wildfire, summer thunderstorms, spring snowmelt, and the mesoscale flood in both SG and HG. The varying response between the two watersheds during the mesoscale flood necessitated further investigation. Discussions with a local landowner indicated that a flood in 1976 caused tremendous channel erosion and widening in the lower portion of HG. Geomorphic changes in HG after the fire and the mesoscale flood were much smaller than in SG, and this can be attributed to: greater post-fire, pre-mesoscale flood deposition in SG; reduced sensitivity in HG as a result of the large erosional flood in 1976; and the spatial distribution of burn severity leading to a lower peak flow in HG from the mesoscale flood. These results suggest that fires can trigger significant and dynamic channel changes over sub-decadal timescales, but unusually long or intense rainstorms can cause larger and more persistent watershed-scale changes regardless of whether a catchment has recently burned. I propose a state-and-transition conceptual model to relate landscape sensitivity to geomorphic changes according to its history of fires and floods.

Third, I use the repeat ALS data to quantify spatial and temporal patterns of erosion and deposition throughout the channel networks of SG and HG. These volumes of change are related to

valley and basin morphology, precipitation amounts and intensities, and burn severity. The results suggest that the amount and location of stored sediment in the valleys is critical for evaluating potential locations of erosion and deposition. Morphometric characteristics, when combined with burn severity and a specified storm, can indicate the relative likelihood and locations of post-fire erosion and deposition risks.

Taken together, this body of work demonstrates: 1) how the timing and sequence of different disturbances affect the relative sensitivity of watersheds to downstream channel changes; 2) that the effects of extreme floods are longer lasting and more dominant than the effects of wildfires; and 3) that the amount and location of stored sediment in the valleys is critical for predicting potential geomorphic change. This information can help resource managers assess downstream risks and prioritize areas for post-fire hillslope rehabilitation treatments.

ACKNOWLEDGEMENTS

Many people have provided support and advice during my graduate studies, but first and foremost I am grateful to my advisor, Peter Nelson. He gave guidance in all aspects of my studies from study design, data collection, analysis, writing, presentations, and beyond. In particular he provided flexibility in my schedule that allowed me to collaborate on several side projects and take personal time to explore the depths of the Grand Canyon, throughout the American and Canadian Rocky Mountain alpine, and beyond the Arctic Circle. Secondly, I would like to acknowledge Lee MacDonald. His willingness to go out of his way to help others, provide insight, and tear apart written work goes far beyond anyone else. He has a huge heart and cares tremendously for those he mentors. The insight and feedback from Stephanie Kampf, Jeff Niemann, and Ellen Wohl helped focus and improve my research.

This work would not have been possible without the help from many friends that aided in the collection of field data. Of these individuals Sam Michels-Boyce always made himself available, even with only several hours notice. I would like to acknowledge Steve Filippelli, who helped in the field and provided guidance on data processing and analysis. Jacob Morgan began as an officemate and has become one of the best friends someone could ask for. He helped innumerably in the field, with data analysis, and data interpretation, but above all he made days in the office much more enjoyable; in particular, his endless knowledge of music trivia amazes me. I am also thankful for the kind and generous H.A. Fonken for sharing access to his family's property and for sharing many enjoyable stories.

This work was supported financially by the National Science Foundation (EF-1250205, EF-1339928, and EAR-1419223), U.S. Department of Agriculture National Institute of Food and Agriculture Hatch project (1003276), the Arapaho-Roosevelt National Forest, and the USDA Forest Service National Stream and Aquatic Ecology Center. Airborne laser scanning was provided by the National Ecological Observatory Network, a project sponsored by the National Science Foun-

dation. This material is based in part upon work supported by the National Science Foundation under Grant No. DBI-0752017.

Above all, I want to thank my wife, Amy. She not only helped survey topography, perform pebble counts, take photos, sieve samples, record data, read drafts of my work, bake cookies, and simply tag along in the field, but she fully supported me through this arduous accomplishment.

DEDICATION

I would like to dedicate my work to the residents that were affected by the High Park Fire and the floods that followed. Their hardships did not go unnoticed.

TABLE OF CONTENTS

LIST OF TABLES

LIST OF FIGURES

Chapter 1

Introduction

"It appears that for a fire to be geomorphically significant, it must be followed by significant precipitation events." - Jeffrey R. Laird and Michael D. Harvey, 1986

1.1 Background

Wildfires and extreme floods can lead to significant impacts on the natural flow and sediment regime of streams (sensu *Poff et al.*, 1997; *Wohl et al.*, 2015). High and moderate severity wildfires act as a catalyst, turning smaller rainfall-runoff floods into more extreme floods that can alter channels and valley bottoms, while floods in unburned areas are themselves a major agent of geomorphic change. Both fires and floods vary in space and time, and their effects range from nil to catastrophic. When fires are followed by floods the effect on water quality, channel morphology, infrastructure, and biology can be devastating (e.g., *Dunham et al.*, 2003; *Ebel and Mirus*, 2014; *Hamilton et al.*, 1954; *Moody et al.*, 2013; *Rhoades et al.*, 2011; *Writer et al.*, 2014). More than ever, understanding hydrologic and sedimentological disturbances are of the utmost concern given that global warming is leading to more wildfires (*Chmura et al.*, 2011; *Rocca et al.*, 2014; *Westerling et al.*, 2006) and a higher likelihood of extreme precipitation (*Berg et al.*, 2013).

After a wildfire a watershed typically responds by progressing from burned and unstable to recovering, and then back to unburned (Figure A.1). The length of time a burned watershed takes to transition through these states depends on many factors, including climate, soil type, and the type of vegetation regrowth (e.g., *Johansen et al.*, 2001; *Moody and Martin*, 2009; *Pausas et al.*, 2009). I use a conceptual figure as the basis for discussing post-fire spatial and temporal channel changes (Figure 1.1). The inspiration for this figure stems from the discussion on basin complex response over varying time periods in *Laird and Harvey* (1986); see Figure 8 in *Laird and Harvey* (1986) specifically. Typically during the first three years after burning wildfires reduce ground and canopy

cover, increase soil water repellency, decrease surface roughness, and decrease infiltration rates at the hillslope scale (< 1,000 m^2; *DeBano et al.*, 1998; *Ebel et al.*, 2012; *Larsen et al.*, 2009; *Moody et al.*, 2013; *Onda et al.*, 2008; *Scott and Van Wyk*, 1990; *Shakesby and Doerr*, 2006). These changes in the hydrologic response cause increased rates of runoff, and rill, inter-rill, and gully erosion (see short-term hillslope scale response in Figure 1.1; *Benavides-Solorio and MacDonald*, 2001; *Moody and Martin*, 2001a; *Pietraszek*, 2006). An increase in the rate of erosion results in the rapid headward expansion of the channel network (*Collins and Ketcham*, 2001; *Wohl*, 2013), which results in greater hillslope-stream connectivity (sensu *Shahverdian*, 2015). As vegetation recovers, infiltration, runoff, erosion, and deposition rates at the hillslope scale return to pre-fire conditions (*Swanson*, 1981), and the transient expanded channel network returns to pre-fire extents (Figure 1.1; *Wohl and Scott*, 2017).

In much of western United States destructive floods after a wildfire are frequently caused by localized, short-duration convective thunderstorms (e.g., *Gary*, 1975; *MacDonald and Stednick*, 2003; *Moody and Martin*, 2009). The increased rates of runoff can then induce severe channel incision and debris flows at the subwatershed-scale (0.1–100 ha, Figure 1.1; e.g., *Cannon*, 2001; *Collins and Ketcham*, 2001; *Hyde et al.*, 2007). Upstream runoff and erosion then leads to down-

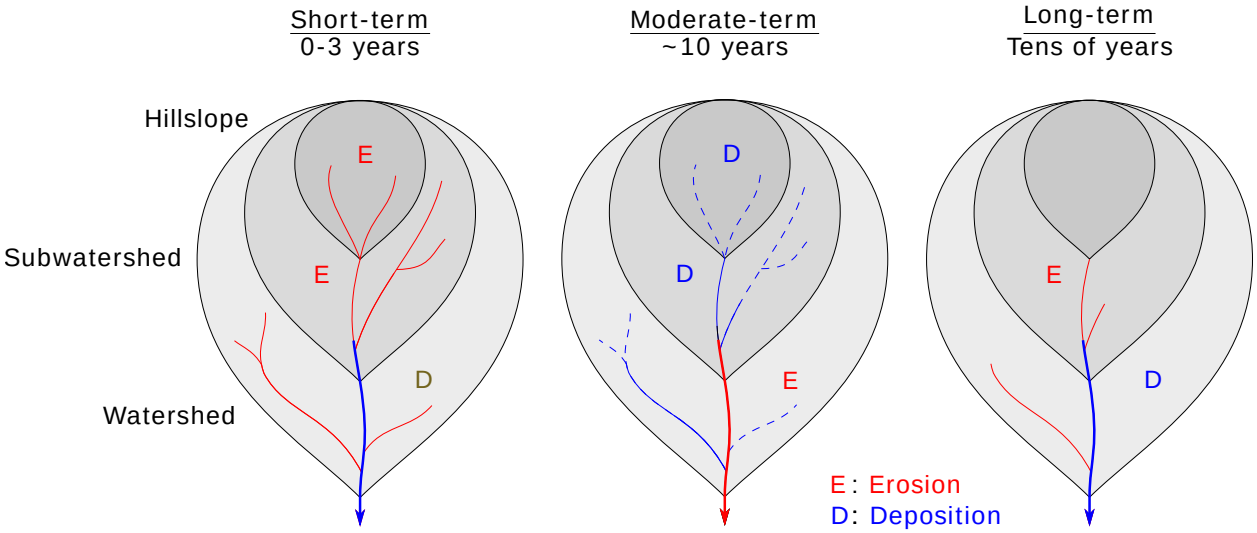

Figure 1.1: Conceptual figure relating spatial and temporal post-fire runoff, erosion, and deposition processes. The amount of runoff changes with time since burning, such that the location of channel heads is transient with time, indicated by the dashed lines. The solid lines indicate channels that persist over time.

stream watershed-scale (> 1 km^2) degraded water quality (e.g., *Rhoades et al.*, 2011; *Writer et al.*, 2014), reservoir filling (e.g., *Moody and Martin*, 2004; *Reneau et al.*, 2007), and a complex response of erosion and deposition (Figure 1.1; e.g., *Laird and Harvey*, 1986; *Moody and Martin*, 2001a). Post-fire downstream erosion is common, however, the literature provides many more examples of post-fire depositional features such as alluvial fans, levees, debris jams, channel infilling, floodplain accretion, braided channels, reservoir filling, and a "sediment superslug" (e.g., *Legleiter et al.*, 2003; *Meyer et al.*, 1992; *Moody*, 2017; *Moody and Martin*, 2001a; *Orem and Pelletier*, 2015; *Reneau et al.*, 2007; *Santi et al.*, 2008; *Wagenbrenner and Robichaud*, 2014). Depending on the sequence of fires and floods (*Germanoski*, 2002; *Moody et al.*, 2008a) downstream sediment deposits can persist for tens to thousands of years (*Cotrufo et al.*, 2016; *Elliott and Parker*, 2001; *Legleiter et al.*, 2003; *Meyer et al.*, 1992, 1995; *Moody and Martin*, 2001a).

In contrast to post-wildfire effects, we have much more information on the geomorphic effects of floods in unburned areas at varying spatial scales (e.g., *de Vente et al.*, 2007; *Fryirs*, 2013; *Walling*, 1983). While some floods do very little geomorphic work (e.g., *Costa and O'Connor*, 1995; *Kochel*, 1988; *Magilligan et al.*, 1998), extreme floods typically generate very large increases in sediment yield (e.g., *Erskine and Saynor*, 1996) and cause significant channel and valley bottom change through erosion and deposition (e.g., *Baker*, 1977; *Friedman and Lee*, 2002; *Krapesch et al.*, 2011; *Magilligan et al.*, 2015; *Miller*, 1990a; *Nanson*, 1986; *Schumm and Lichty*, 1963). The spatial distribution of geomorphic changes in a watershed due to extreme floods vary with local hydraulic and topographic controls (e.g., *Fuller*, 2008; *Surian et al.*, 2016; *Thompson and Croke*, 2013; *Wolman and Eiler*, 1958), although strong correlations between channel changes and local controls are not always apparent (e.g., *Nardi and Rinaldi*, 2015).

Although there has been considerable progress, we still lack the ability to accurately quantify and predict post-fire flooding and geomorphic changes at the watershed scale. This lack of understanding stems primarily from two reasons. First, there is generally limited availability of repeat high-resolution topography following fires (sensu *Passalacqua et al.*, 2015), and this limits our ability to quantify and explain changes throughout a given channel network. Second, and

more fundamentally, is that one cannot simply scale up hillslope processes to the watershed scale, or vice-versa (e.g., *Klemeš*, 1983; *Moody and Kinner*, 2006; *Stoof et al.*, 2012). Understanding downstream flooding and sedimentation is critical for safeguarding downstream landowners, water users, and aquatic and terrestrial resources. This dissertation addresses these shortcomings by documenting post-fire channel changes across watershed scales and how extreme floods can alter the more typical post-fire geomorphic response.

1.2 Study area

The focus of this dissertation is two ~15 km^2 watersheds, Skin Gulch (SG) and Hill Gulch (HG), that burned during the 2012 High Park Fire (HPF), Colorado, U.S.A. (Figure 1.2). Both watersheds drain north into the Cache la Poudre River and are approximately eight kilometers apart. Elevations range from 1890 to 2580 m in SG and 1740 to 2380 m in HG. Average terrain slopes and drainage density in each watershed are very similar at 23% and 24%, and 2.5 and 2.3 km km^{-2} for SG and HG, respectively. The hypsometric and width function curves for each watershed also are very similar (Figures A.2 and A.3). Both watersheds were burned at approximately 65% moderate to high severity, although most of the moderate to high severity burn in SG was in the upper headwaters, while most of the area burned at moderate to high severity in HG was in the middle or lower portion of the watershed (Figure 1.2A). SG is underlain by knotted mica schist, amphibolite, and pegmatite with a large shear zone through the northwestern edge of the watershed (*Abbott*, 1970, 1976), while HG is underlain primarily by knotted mica schist (*Braddock et al.*, 1988). Soils in both watersheds are primarily Redfeather sandy loams (*HPF BAER Report*, 2012). The northern Rocky Mountains in Colorado are characterized as semiarid with mean annual precipitation of 450-550 mm (PRISM Climate Group, Oregon State University, http://prism.oregonstate.edu). Summer precipitation is primarily convective thunderstorms, while frontal storms are more prevalent during the spring and fall. Winter precipitation is predominantly snow, and an intermittent snowpack develops in the upper portions of both watersheds (*Johnson*, 2016).

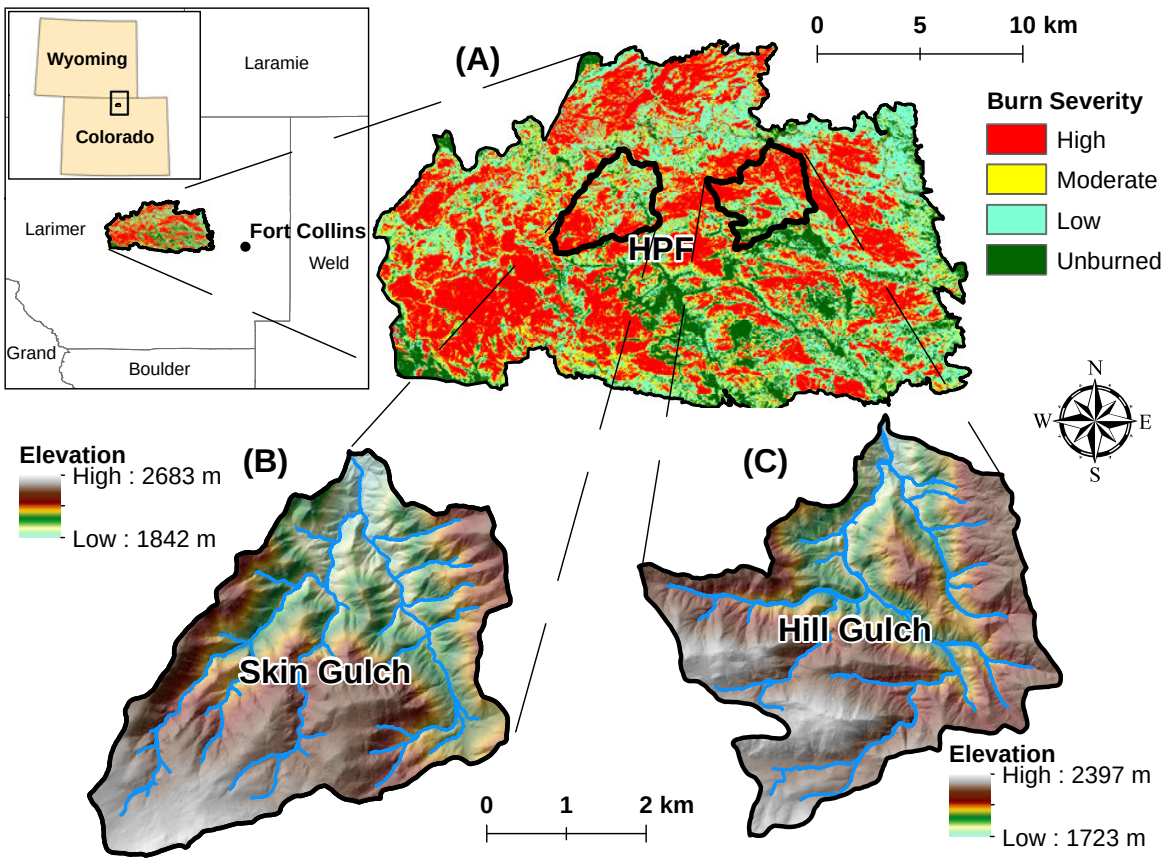

Figure 1.2: Location and burn severity of the (A) High Park Fire (HPF) in the Colorado Front Range of the western U.S., and elevations of (B) Skin Gulch and (C) Hill Gulch.

1.3 Outline of subsequent chapters

My study began with the intention to quantify post-fire geomorphic changes across watershed scales. Within the first week after the wildfire was contained a high-intensity convective storm occurred in the upper portion of SG on an area that had been burned primarily at high severity. The combination of intense rain and high burn severity resulted in an exceptionally large peak flow, and extensive downstream deposition of cobbles, boulders and woody debris. The effects of this initial large storm in SG set up an interesting contrast between SG and HG. During the summer and fall following the fire I established and began intensive monitoring of 10 and 11 cross sections and longitudinal profiles along the lower channel network in SG and HG, respectively.

The expected post-fire response was severely altered by an unusually rare and widespread mesoscale storm 15 months after the fire that caused widespread flooding and channel change (*Gochis et al.*, 2014; *Moody*, 2016; *Yochum*, 2015; *Yochum et al.*, 2017). The geomorphic response in both watersheds was almost exclusively widespread erosion. This extreme flood provided a unique opportunity to compare the effects of two distinctly different flood disturbances in SG—the short-term peak flow and substantial deposition caused by the convective flood immediately after burning, and the widespread channel and valley bottom erosion caused by the mesoscale flood. Surprisingly, the mesoscale flood caused much less channel and valley bottom change in Hill Gulch.

Post-fire, and now post-mesoscale flood, field data collection continued through fall 2016. The differences in mesoscale flood response necessitated further investigation, and whether this difference was primarily due to the deposition caused by the large convective storm in July 2012 in Skin Gulch. Discussions with a local landowner indicated that in 1976, 36 years before the HPF, a thunderstorm caused tremendous channel erosion and widening in the lower portion of HG (H.A. Fonken, pers. comm., 2017). This same rainstorm caused the 1976 Big Thompson Flood, which was notorious in Colorado for killing 144 people and destroying numerous homes and businesses as well as the main state highway up the Big Thompson River (*Jarrett and Costa*, 2006).

In addition to the field surveys, five post-fire airborne laser scanning (ALS) datasets were collected in fall 2012, summer 2013, fall 2013, fall 2014, and spring 2015. These were used to develop rectified high-resolution digital elevation models (DEMs), and the differencing between these led to detailed quantification of channel and valley bottom changes that could be compared to the measured cross section and longitudinal profile changes. Given these data and the sequence of fire and floods, my dissertation consists of three chapters.

In Chapter 2 I quantified the peak flows and channel changes resulting from the convective and mesoscale storms in SG. My specific objectives were to: 1) quantify and compare the peak flows and geomorphic changes from the convective storm and the unusual mesoscale storm; 2) determine the importance of local rainfall intensity, percent bare soil, and sequence of events on

the magnitude of the peak flows from each of these two storms; 3) investigate if the estimated peak flows could be improved by using and comparing different estimation techniques; and 4) determine how the unit-area magnitudes of these peak flows compare to other large rainfall-runoff generated floods in the United States. The results document the extent to which a high and moderate severity forest fire can greatly increase peak flows and alter channel morphology. A comparison between peak flow estimation techniques illustrates how indirect peak flow estimates have larger errors than is generally assumed. The results indicate that the magnitude of post-fire floods and geomorphic change can be affected by the timing, magnitude, duration, and sequence of rainstorms.

In Chapter 3 five years of field data were used to quantify channel response to the fire and the mesoscale flood in SG and HG. Due to legacy effects, I also documented how past disturbances affected the observed sequence of channel changes. The results suggest that fires in the Rocky Mountains can trigger significant and dynamic hillslope and channel changes over sub-decadal timescales, but unusually long or intense rainstorms can cause larger and more persistent changes regardless of whether a catchment has recently burned. Finally I propose a state-and-transition style conceptual model to relate landscape sensitivity to geomorphic changes according to its history of fires and floods.

In Chapter 4 five airborne laser scanning (ALS) datasets collected over four years were used to quantify channel and valley bottom changes in SG and HG after the HPF and long-duration September 2013 mesoscale flood. My objectives were to: 1) quantify spatial and temporal patterns of erosion and deposition throughout the channel network following the wildfire and subsequent mesoscale flood; and 2) investigate the extent these changes can be related to valley and basin morphology, precipitation amounts and intensities, and burn severity. The results suggest that the amount and location of stored sediment in the valleys is critical for evaluating potential locations of erosion and deposition. Morphometric characteristics, when combined with burn severity and a specified storm, can indicate the relative likelihood and locations of post-fire erosion and deposition risks.

Chapter 2

Reconstructing extreme post-wildfire floods: a comparison of convective and mesoscale events

2.1 Introduction

High and moderate severity wildfires consume much of the overlying vegetation and litter, and high severity fires alter surface soils (*Parsons et al.*, 2006). The loss of surface cover and soil organic matter, reduction in surface roughness, and increased soil water repellency cause a dramatic decline in the soil infiltration rate (*Ebel et al.*, 2012; *Larsen et al.*, 2009; *Onda et al.*, 2008; *Shakesby and Doerr*, 2006) with a corresponding potential for large increases in infiltration-excess overland flow and surface erosion (*Moody and Martin*, 2001b). These large increases in hillslope-scale runoff and erosion can lead to extensive rilling and gullying, expansion of the drainage network in the steeper headwater areas (*Moody and Martin*, 2001a; *Wohl*, 2013) and dramatic downstream increases in flooding, erosion, and sedimentation (*Anderson*, 1976; *Doehring*, 1968; *Moody and Martin*, 2009). Burning of the riparian vegetation can further exacerbate these effects by reducing bank stability and exposing the riparian zone to channel scour (*Eaton and Giles*, 2009). The legacy effect of these fire-induced geomorphic changes can persist for tens to thousands of years (*Elliott and Parker*, 2001; *Legleiter et al.*, 2003; *Meyer et al.*, 1992, 1995; *Moody and Martin*, 2001a).

The effects of high and moderate severity wildfires on runoff and erosion are of increasing concern due to the growing population in the wildland-urban interface, and the increasing area and

---

This chapter has been published as: Brogan, D. J., Nelson, P. A., and MacDonald, L. H. (2017) Reconstructing extreme post-wildfire floods: a comparison of convective and mesoscale events. *Earth Surf. Process. Landforms*, 42: 2505–2522. doi: 10.1002/esp.4194.

severity of wildfires due to climate change, earlier snowmelt, and historic wildfire suppression (*Liu et al.*, 2013; *Rocca et al.*, 2014; *Westerling et al.*, 2006). Given the current and projected increases in the number, extent, and severity of forest fires in the western USA and elsewhere (*Flannigan et al.*, 2009; *Littell et al.*, 2009), there is an urgent need to quantify the effects of wildfires on peak flows at the watershed scale.

For much of the western USA, the largest and most destructive floods after wildfires are caused by localized, short-duration convective thunderstorms (*Cannon et al.*, 2001; *Meyer et al.*, 1995; *Moody and Martin*, 2001a; *Morris and Moses*, 1987). The localized and usually remote nature of these storms means that the resulting peak flows are almost never measured on gaged watersheds, with very few exceptions (*Canfield et al.*, 2005; *Kunze and Stednick*, 2006). Rainfallrunoff generated floods from high-intensity, short-duration convective storms have been widely recognized, while postfire floods from low-intensity, long duration mesoscale storms are very uncommon and remain largely unstudied.

Following a wildfire disturbance in Colorado in 2012 I had the opportunity to investigate two post-wildfire floods generated by different types of rainstorms. The first flood on 6 July 2012, just a few days after the fire was fully contained, was the response to a localized convective storm, and is referred to as the 'convective flood' throughout this paper. The second flood was in September 2013, 15 months after the fire, and this was caused by a lower-intensity, but unusually large and longduration storm. This second storm is referred to as the 'mesoscale flood' throughout this paper.

The juxtaposition of these two different rainstorms and resulting large floods allowed us to investigate the relationships between rainfall amount and intensity, flood response, and geomorphic changes after wildfire. Here I seek answers to two key questions: (1) how do the peak flows and geomorphic changes from the unusual mesoscale storm compare with the peak flows and post-flood geomorphology from the convective storm? (2) What is the importance of local rainfall intensity, bare soils, and sequence of events on the magnitude of the peak flows from each of these two storms? In my efforts to answer these two questions, I had to answer a third and more basic set of questions, namely: (3) how precisely can I estimate the peak flows from each storm? And can my

confidence in the estimated peak flows be improved by using and comparing different estimation techniques?

In this study I used the slope-area method, critical flow method, and a 2D hydraulic model to estimate the peak flows from the convective and mesoscale flood. The occurrence of the mesoscale flood meant that I could directly compare the differences in the estimated peak flows using pre- and post-flood topography for each of the three estimation techniques. The intercomparisons of the estimated peak flows among techniques, the different cross-sections, and the pre- and post-flood topography provides insights into the inherent uncertainties and validity of each estimation technique. The exceptionally high magnitude of my estimated peak flows then led us to a fourth question, which was: (4) how do the unit area magnitudes of these peak flows compare with other large rainfall-runoff generated floods in the United States? The answers to these four questions are useful for assessing the potential magnitude and effects of post-fire floods resulting from two very different types of rainstorms, and have much broader implications for the techniques and uncertainties in quantifying peak flows after major floods.

2.1.1 Site description and background

The 2012 High Park Fire wildfire (HPF) was ignited by a lightning strike on 9 June 2012 in the northcentral Colorado Front Range. It burned 353km^2 and nearly 260 homes by the time it was 100% contained on 1 July (*HPF BAER Report*, 2012). My study focused on the main branch in the Skin Gulch (SG) basin (15.5 km^2) that is located nearly in the middle of the HPF burn area (Figure 2.1) with elevations ranging from 1890 to 2580 m, and a main channel width of ~1m at base flow. Geology of the basin is primarily Precambrian metasedimentary and metaigneous schists, gneisses, and plutonic igneous rocks (*Abbott*, 1970), and the soils are typically sandy loams with 10–60% rock content by volume at the surface and 35–80% in the subsurface (*HPF BAER Report*, 2012). Annual precipitation averages about 450–550mm (PRISM Climate Group, Oregon State University, http://prism.oregonstate.edu, map created 19 Feb 2015), with most of the precipitation from November to May falling as snow. Summer precipitation comes mostly

from convective storms. Vegetation in SG prior to the HPF was 81% evergreen forest (primarily ponderosa pine), 15% shrub/scrub, and ~4% deciduous forest, grassland/herbaceous and woody wetland (data derived from the 2011 National Land Cover Database; *Jin et al.*, 2013). RapidEye imagery and a multistage decision tree indicated that approximately 44% of the drainage area burned at high severity, 21% at moderate severity, 35% at low severity, and just 6% unburned (Figure 2.1c). Within Skin Gulch the majority of the area burned at high severity was in the headwaters and west-central part of the watershed.

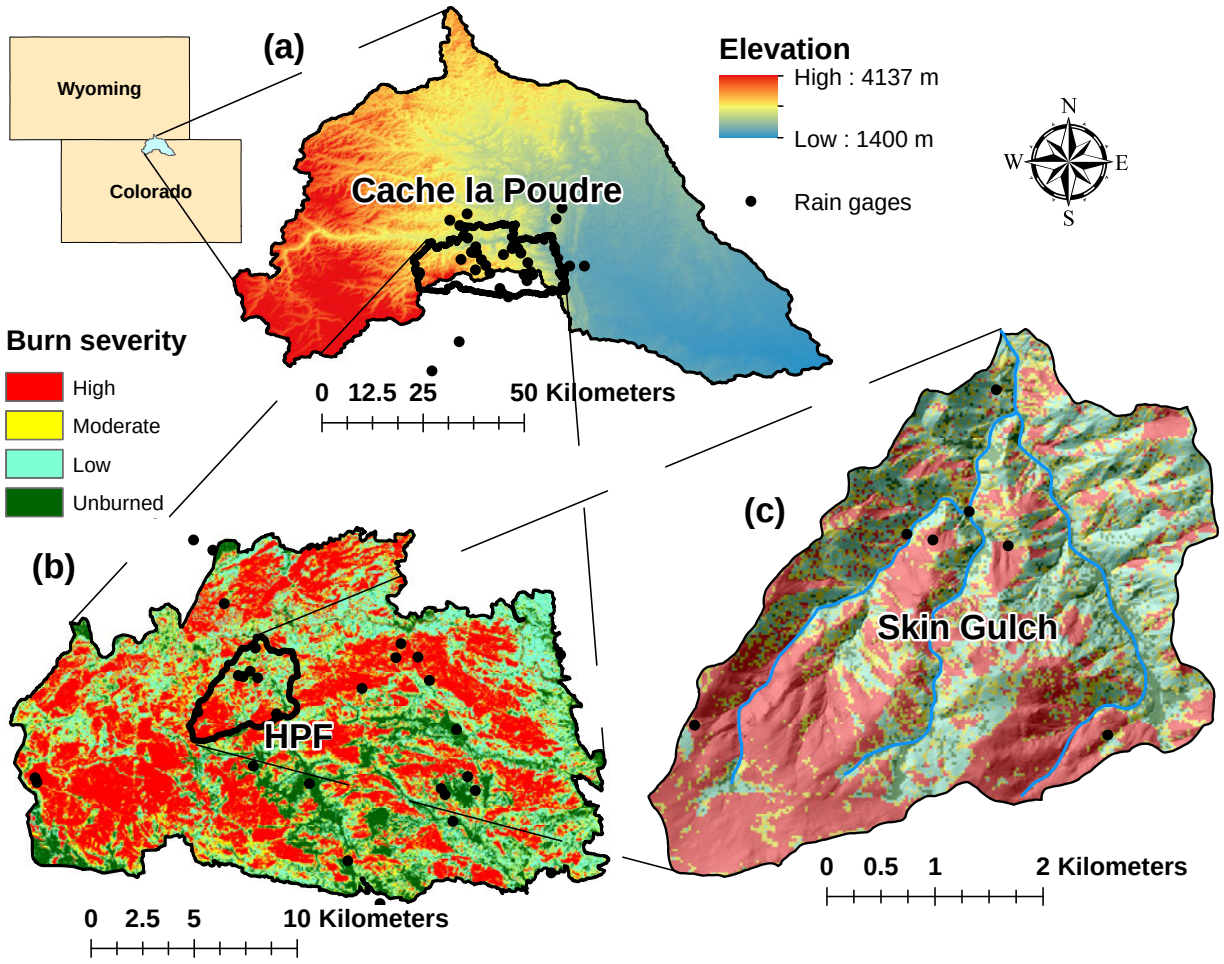

Figure 2.1: Location and elevation of the (a) Cache la Poudre basin in the Colorado Front Range of the western USA, and burn severity in the (b) High Park Fire and (c) Skin Gulch, respectively. Black dots show the location of rain gages used to characterize the September 2013 mesoscale storm.

The convective flood on 6 July 2012 was centered over one main tributary that had burned at high severity. This flood mobilized large amounts of sediment, and deposited cobbles, large boulders, and woody debris in the mainstem channel and valley bottom (Figure 2.2). At that time I had no on-site rainfall data or detailed topographic data, although I had surveyed one cross-section at the base of the watershed prior to the flood. The ash and sediment delivered from this and subsequent floods to the Cache la Poudre (CLP) River affected the primary water supply for several hundred thousand people (*Writer et al.*, 2014).

The mesoscale flood in September 2013 affected the entire central and northern Colorado Front Range, resulting in widespread flooding that washed out numerous major highways (*Gochis et al.*, 2014; *Yochum*, 2015) and triggered over 1100 landslides and debris flows (*Anderson et al.*, 2015). This flood caused extensive geomorphic change in SG (Figure 2.3), and for this flood I had rainfall data from seven tipping bucket rain gages and detailed pre- and post-flood topographic data (*Kampf et al.*, 2016).

2.2 Methods

2.2.1 Field observations

Ten channel cross-sections for repeat surveys were established over the course of several months following the HPF. There were only six days between containment of the HPF and the first rainstorm and associated flood on 6 July, so the only channel data from SG was a single cross-section (XS) that was established near the outlet of SG on 4 July (XS1 in Figure 2.4). The sediment deposits and high water marks (HWM) from the 6 July 2012 flood extended well beyond the original surveyed cross-section. On 22 July 2012 a longer cross-section was reestablished at the same location, and on the same day XS2 was established farther upstream. In early fall 2012 seven additional cross-sections were established on straight reaches along the main branch of SG, and these were selected to represent erosional, depositional, and transport reaches. One additional cross-section was established on Tributary 3 (Figure 2.4), which appeared to be unaffected by the

Figure 2.2: Pictures taken after the convective flood (6 July 2012) indicate the extreme magnitude of this flood. (a) Imbricated boulders above the channel bed looking at the left bank between cross-section (XS) 8 and XS9; (b) extensive deposits of boulders and cobbles on the floodplain looking upstream just downstream from the confluence of Tributary 3; and (c) large pileup of woody debris looking upstream from XS6. See Figure 2.4 for XS and tributary locations.

Figure 2.3: Photos looking downstream between cross-section (XS) 9 and XS10 (a) prior to and (b) after the mesoscale flood (September 2013) showing the large increase in the size of the channel. The same boulder is circled in red in both pictures. See Figure 2.4 for XS and tributary locations.

flood. Above XS1 drainage areas along the main channel ranged from 9.04 km^2 at XS2 to 4.63 km^2 at XS10 (Table 2.1). Longitudinal profiles were established at each cross-section.

I also measured the intermediate axis of 60 of the larger imbricated particles deposited by the convective flood between XS6 and XS9. Frequent pictures and field visits showed that subsequent storms in summer 2012 caused minimal channel change, making us confident that the cross-section surveys accurately captured conditions after the convective flood.

The elevations of HWMs were measured for the convective and mesoscale floods throughout the basin, but not at every cross-section. These were identified after the convective storm by very distinct lines of deposited ash and fine debris, and after the mesoscale storm primarily by matted-down vegetation. All of the HWMs from the mesoscale flood were lower in elevation than the HWMs from the convective flood. For the convective flood two HWMs were noted near XS2 on 22 July 2012; subsequent field visits identified 53 HWMs along the main branch of SG (Figure 2.4). These HWMs were readily identified because no floods within the first year after burning came close to the magnitude of the 6 July 2012 flood. Forty-two HWMs were surveyed shortly after the mesoscale flood (Figure 2.4). In my analyses, I estimate an uncertainty in the elevation of the HWMs of 0.10 m, which reflects potential undulations in the free surface at peak discharge, and uncertainties of this magnitude have been used for indirect discharge analyses of the 2013 flood

Table 2.1: Drainage areas for each cross-section along with the net cross-sectional erosion and deposition due to the mesoscale flood. Net erosion and deposition for the convective flood could not be calculated because pre-flood surveys do not exist.

Cross-section	Drainage area (km^2)	Erosion (m^2)	Deposition (m^2)	Net change (m^2)
XS2	9.04	-2.4	0.6	-1.8
XS3	8.79	-2.8	2.2	-0.6
XS4	8.77	-21.9	2.1	-19.8
XS5	8.33	-14.7	3.4	-11.3
XS7	2.80	-1.6	0.0	-1.6
XS8	5.21	-7.6	0.2	-7.4
XS9	5.12	-4.6	0.1	-4.5
XS10	4.63	-4.7	0.3	-4.4

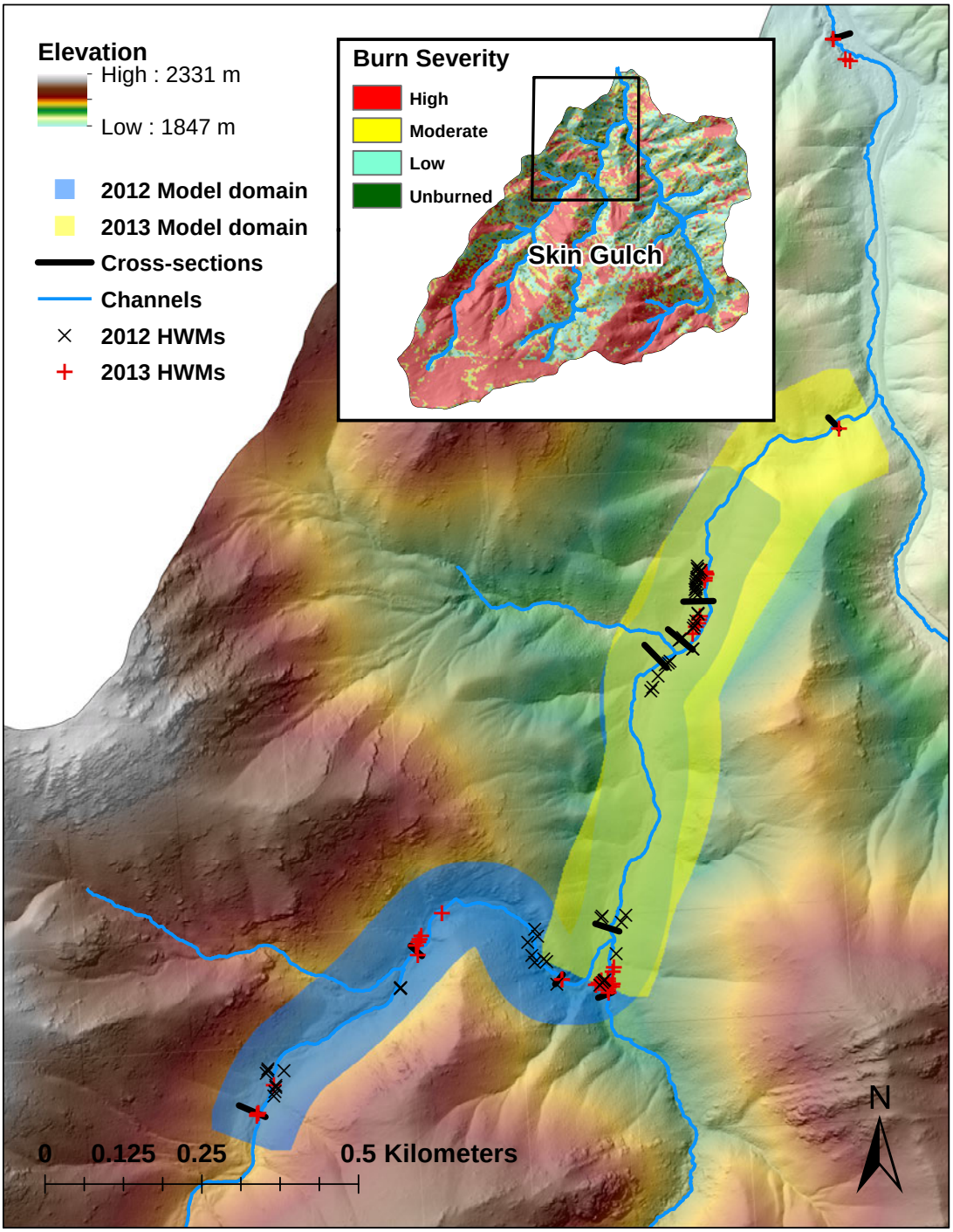

Figure 2.4: Shaded relief map of lower Skin Gulch showing major tributaries, cross-sections (XS), high water marks (HWMs), and hydraulic model boundaries. Inset shows burn severity for the entire SG watershed.

at other locations along the Colorado Front Range (*Moody*, 2016). Stage data were collected near XS1 during the mesoscale flood by an ultrasonic water level sensor, but these could not be used to calculate discharge because the bed aggraded by more than 2m during this flood (*Kampf et al.*, 2016). Maximum inundated area and mean flow depth were calculated for each cross-section that had a nearby HWM by projecting a horizontal water surface elevation across the channel from the measured HWM. Absolute changes in crosssectional area due to the mesoscale flood were summarized in *Kampf et al.* (2016).

The 2012 surveys were conducted using either an autolevel and stadia rod, or a Leica TCR407 total station. The 2013 surveys were conducted with a Topcon GR-5 Real-Time Kinematic Global Navigation Satellite Systems (RTK-GNSS). The total station data were rotated and adjusted for elevation using benchmarks to match the real-world RTK-GNSS coordinates. Average estimated horizontal and vertical root mean square error (HRMS and VRMS) among the methods was 6mm and 10 mm, respectively.

2.2.2 Lidar data and model domains

Three airborne lidar datasets covering the SG watershed were used as topographic input for the 2D modeling of each flood. The first two sets of data were collected in October 2012 and July 2013 by the National Ecological Observatory Network (NEON) Airborne Observation Platform. The third airborne lidar dataset was collected by the USGS 1 month after the mesoscale flood. The primary product from each dataset was a 1m bare-earth digital elevation model (DEM). The DEMs developed from the two NEON datasets required a mean bias correction (i.e. elevation adjustment) to fit my surveyed cross-sections as there was a lack of vertical ground control and possible transformation errors between the NAD83 and WGS84 ellipsoids. After correction the mean absolute error (MAE) between my RTK-GNSS survey data and the lidar surfaces was reduced to 0.13m for the 2012 NEON DEM (n = 2575) and 0.19m for the 2013 NEON DEM (n = 2437). The MAE for the 2013 USGS lidar was 0.24m (n = 3060).

Field observations after the convective storm indicated that the high peak flows and associated channel geomorphic changes were confined to the main stem of SG given the general lack of channel change, HWMs or deposition in the tributaries (Figure 2.4). It was therefore surmised that the tributaries contributed negligible flow during this flood. To take advantage of as many HWMs as possible, the areal domain for the 2D modeling of the convective flood began upstream of XS2 and extended to just upstream of XS10 (Figure 2.4). The contributing area at the upstream end of this model domain was 4.6 km^2, and the HWMs throughout this reach were longitudinally widespread.

In contrast, field observations for the mesoscale flood indicated substantial flows and geomorphic changes throughout the watershed, so it was not possible to use the same domain as for the convective flood. The model domain for the mesoscale flood was therefore focused on the lower portion of the main channel from just below XS2 upstream to the confluence of the main channel with Tributary 3 (Figure 2.4). Although this domain covers a different spatial area than the model domain for the convective flood, they do overlap, and because my models were run under steady-state conditions (discussed below) the different spatial domains should not affect peak flow comparisons. For the mesoscale flood I used the 11 HWMs between XS2 and XS4, which were primarily on the inside of a bend or along one side of straight reaches. The contributing area upstream of XS4 is 8.7 km^2.

2.2.3 Precipitation

The convective storm on 6 July 2012 occurred prior to the installation of any tipping-bucket rain gages, so radar data were used to estimate precipitation from that storm. Amount and intensity of rainfall were determined from 15 min radar data (Hydro-NEXRAD, *Krajewski et al.*, 2011) collected by the National Weather Service (NWS) Doppler radar in Cheyenne, Wyoming, which is approximately 70 km northeast of the study basin. The storm had two main rainfall bursts that were 7 h apart with each burst lasting less than 1.5 h. The radar data were gridded in ~1 km^2 bins and bias-corrected with daily rainfall data from 16 nearby Community Collaborative Rain, Hail

and Snow Network (CoCoRaHS) rain gages (*Cifelli et al.*, 2005). Because the CoCoRaHS data are daily totals collected at 0700 local time, the radar data were summed to obtain daily totals for the 24 h period ending at 0700. A daily mean field bias (MFB) correction was calculated as:

$$B_i = \frac{\sum G_{ij}}{\sum R_{ij}} \tag{2.1}$$

where B_i is the multiplicative bias for a particular day i, G_{ij} is the daily rainfall for day i and gage j, and R_{ij} is the summed 24 h rainfall for day i and the radar pixel containing gage j (*Wright et al.*, 2014). The calculated bias was 0.95, and this value was used to correct all of the 15 min radar rainfall estimates.

Seven tipping-bucket rain gages installed after July 2012 in SG recorded the mesoscale storm. The radar data accurately estimated the total precipitation for this storm but did not accurately reproduce the 15 min rainfall intensities, possibly due to terrain beam blockage (*Zrnić and Ryzhkov*, 1996). Thus the rainfall over SG was estimated by natural neighbor interpolation of the rain gage data. To match other studies (i.e., *Lukas et al.*, 2013) I defined the duration of the mesoscale storm from 0700 mountain daylight time (MDT) on 9 September to 0700 MDT on 16 September 2013. Recurrence intervals for the convective and mesoscale storms were determined from NOAA atlas precipitation-frequency data (*Perica et al.*, 2013).

2.2.4 Peak flow estimation techniques

Three different techniques were used to estimate peak flows from each flood: (1) the slope-area method; (2) the critical flow method; and (3) two-dimensional hydraulic modeling with Nays2D. Peak flow estimates for the convective flood were necessarily based on the topographic data collected after the flood, while peak flows for the mesoscale flood were estimated using both the pre- and post-flood topography. Uncertainty in each method was computed using a Gaussian error propagation approach.

For the slope-area method I used Manning's equation:

$$Q = \frac{AR^{2/3}S^{1/2}}{n} \tag{2.2}$$

where Q is the discharge (m^3 s^{-1}), V is the mean cross-section velocity (m s^{-1}), A is the cross-sectional area of the flow (m^2), R is the hydraulic radius (m), S is the mean water surface slope (m/m), and n is Manning's roughness coefficient ($s/m^{1/3}$). Slope was approximated from the local bed slopes over a 50 m reach since the HWMs were spaced too intermittently to be used to calculate water surface slope. Equation (2) was only used at cross-sections with nearby measured HWMs, so peak flows were estimated at five cross-sections for the convective flood (2, 3, 4, 5 and 8) and four cross-sections for the mesoscale flood (2, 7, 9 and 10). Note that XS7 is on a tributary to the main stem (Figure 2.4), and my cross-sections were established to document channel change rather than estimate peak flows. Hence my cross-sections were not replicated as suggested by *Dalrymple and Benson* (1967).

For each cross-section I made eight estimates of Manning's n using standard empirical equations (*Dingman and Sharma*, 1997; *Ferguson*, 2007; *Hey*, 1979; *Jarrett*, 1984; *Limerinos*, 1970), reference tables (*Arcement and Schneider*, 1989; *Chow*, 1959), and photographic guides (*Barnes*, 1967). Peak flow using the slope-area method was then calculated using the mean of these n values. Uncertainties in the peak flow estimates were computed using Gaussian error propagation, in which the uncertainty in the horizontal and vertical measurement of each survey point was taken to be the horizontal and vertical root mean square error (HRMS and VRMS) from the RTK-GNSS; vertical uncertainty in the HWMs was assumed to be 0.10m as noted above; uncertainty in the slope was taken to be the standard error from the linear regression used to compute the slope; and uncertainty in Manning's n was the standard deviation from the suite of empirical estimates at each location.

The second method to estimate peak flows was the critical flow method, and this calculates discharge by assuming the Froude number is equal to one. Based on this assumption and conservation of mass, discharge is calculated by:

$$Q = A\sqrt{g\overline{h}} \tag{2.3}$$

where g is gravitational acceleration (9.81 m/s^2) and h is the average flow depth (m). The same cross-sections and HWMs were used for the critical flow method as the slope-area method. Uncertainty in the peak flow estimates was again computed using Gaussian error propagation where uncertainty in the horizontal and vertical position of each survey point and the estimated uncertainty in the HWM elevations were used. Previous literature has shown that the Froude number varies considerably during floods (*Costa*, 1987; *Lumbroso and Gaume*, 2012) so I also assign and propagate a 20% uncertainty to the assumed Froude value of one.

The third method used to estimate peak flows was the Nays2D model (*Asahi et al.*, 2013), where a series of steadystate constant discharges were simulated in order to find the peak discharge that best matched the surveyed HWMs. Nays2D is an open-source model distributed with the iRIC interface (International River Interface Cooperative, http://i-ric. org; *Nelson et al.*, 2016). It solves the 2D depth-averaged equations of fluid continuity and momentum to determine water surface elevations and depth-averaged velocities. These equations are solved in a general curvilinear coordinate system, enabling computational meshes of any shape. For the convective and mesoscale simulations I constructed a computational mesh of curvilinear quadrilateral cells with a spacing of approximately 2 m in the downstream direction and 1m in the lateral direction.

To estimate the convective flood the grid cells were assigned elevations by interpolating the 2012 NEON lidar data. Similarly for the mesoscale flood I used the 2013 NEON lidar data and the 2013 USGS lidar data to develop meshes for pre- and post-flood topography, respectively. Upstream and downstream boundary conditions were set to uniform flow. Each simulation was run with a time step of 0.01 s for a total of 1000 s, at which point the flows were at steady-state. The cubic-interpolated pseudoparticle method was used for finite differential calculation of the advection terms. The zero-equation model was used for eddy viscosity parameterization:

$$v_t = C\frac{k}{6}u_* h \tag{2.4}$$

where v_t is the eddy viscosity coefficient, k is the von Karman coefficient (0.4), u_* is the shear velocity (m s^{-1}), and h is depth (m), and C is a user-defined parameter for which I used the default setting (C = 1).

The primary outputs from each 2D simulation were the local depth (h) and the 2D depth-averaged velocity vectors (u, v). Boundary shear stress (τ_x, τ_y) in Nays2D is calculated with a drag coefficient closure:

$$(\tau_x, \tau_y) = \rho C_d \sqrt{u^2 + v^2}(u, v) \tag{2.5}$$

where ρ is the density of the fluid (kg/m^3), and C_d is the drag coefficient as calculated by:

$$C_d = \frac{gn^2}{h^{1/3}} \tag{2.6}$$

This parameterization, which is also used in the momentum equation, allows roughness to decrease with increasing flow depth despite using a spatially uniform n.

I used Nays2D to estimate the peak discharge for each flood by applying the mean estimate of all empirical Manning's n estimates, and imposing a constant discharge. I ran numerous simulations where discharge was varied from 5 to 250 m^3 s^{-1} in 5 to 10 m^3 s^{-1} increments. For each simulation the mean absolute error (MAE) was calculated from the differences between the water surface elevation of the inundated grid cell closest to the surveyed elevation of each measured HWM (53 for the convective flood and 11 for the mesoscale flood). best estimate of the peak flow was the discharge with the minimum MAE.

I characterized the uncertainty of the 2D-modelestimated peak discharges by separately accounting for uncertainty in roughness and uncertainty in HWM elevations. To account for uncertainty in Manning's n, I repeated the series of simulations twice with roughness values equal to the mean value minus and plus the standard deviation of the distribution of empirical estimates, respectively. The range of discharges that minimized the MAE for these two n values were considered to represent the uncertainty in peak flow due to roughness parameterization.

To account for uncertainty in HWM elevation in the 2D modeling, I used the series of simulations where the roughness was the mean Manning's n estimate, and I shifted the HWM elevations vertically up or down by the uncertainty in the relative HWM elevation (0.10 m) plus the uncertainty in the lidar (0.13 to 0.24 m, as discussed above). The MAEs between these adjusted HWM elevations and model outputs were computed, and the discharges that minimized the MAE were taken to represent the uncertainty in peak flow due to HWM elevation uncertainty.

In order to test for the effects of hyperconcentrated flows I varied the fluid density from 1000 to 2000 kg/m^3 and C in the eddy viscosity term from 0.1 to 10. Since these variations did not change the discharge associated with the minimum MAE and had a negligible effect on the absolute MAE, they are not further reported.

Using the best estimates of peak flows from Nays2D I estimate reach average peak unit stream power (ω) as:

$$\omega = \frac{\gamma Q S}{w} \tag{2.7}$$

where γ is the specific weight of the fluid (N/m^3), Q is the peak discharge, and w is the mean channel width (m). Mean channel width and water surface slopes were estimated from the Nays2D model outputs. I also make a rough estimate of the total energy expenditure during each flood by integrating the time series of stream power, assuming it has a triangular shape with a duration estimated from the rainfall data and the peak estimated from Equation (7).

2.3 Results

2.3.1 Precipitation – convective storm

Rainfall for the convective storm on 6 July 2012 was highly variable in space and lasted about 19.5 h. Total rainfall varied from 47mm in the western portion of the watershed to only about 20mm in the eastern portion of the watershed (Figure 2.5a). Peak 15-min rainfall intensities (I_{15}) ranged from about 10 to 50mm h^{-1}, with the highest intensity in the southern portion of the watershed over an area that burned at high severity (Figure 2.5b). The rainfall came primarily in two short bursts,

with the first burst being spatially more widespread with most 15 min intensities exceeding 27mm h^{-1} and peak 15 min intensities approaching 50mm h^{-1} (Figure 2.6a). Rainfall intensities dropped to only 10–15mm h^{-1} at the eastern boundary of the watershed (Figure 2.5b). The second burst was less widespread and less intense (Figure 2.6a), indicating that the flood was almost certainly due to the initial burst at around 1415 MDT. Recurrence intervals for these depths and maximum 15 min intensities are roughly 1–10 and less than 2 years, respectively (*Perica et al.*, 2013).

2.3.2 Precipitation – mesoscale storm

In contrast to the convective thunderstorm, the mesoscale storm lasted roughly 7 days. This extreme storm was due to monsoonal moisture being directed to the central and northern Colorado Front Range (*Gochis et al.*, 2014; *Lukas et al.*, 2013). Rainfall amounts and intensities were quite uniform over the SG catchment, and total rainfall was about 220–235mm or about five times the maximum total rainfall from the July storm (Figure 2.5b). Approximately 150–160mm or 70% of the total rainfall fell in 24 h (Figure 2.6b), but the maximum 15 min intensities were only 25–31mm h^{-1} (Figures 2.5b) and 2.6b). The extreme nature of this storm is indicated by the estimated recurrence intervals of 200–500 years for the 1 day precipitation and roughly 500–1000 years for the 7 day precipitation (*Perica et al.*, 2013).

2.3.3 Field observations of the convective and mesoscale floods

The convective flood led mainly to depositional geomorphic changes in the SG channel. The large magnitude of the peak flows coming from the upper mainstem of SG are shown by the boulder-sized clasts that were imbricated between XS8 and XS9, deep cobble and boulder deposits just below the confluence with Tributary 3 where the steep, bedrock-confined upper mainstem entered a roughly 40m wide alluvial valley, and the 2m high deposits of woody debris against standing trees near XS6 (Figure 2.2). The mean diameter of the 60 imbricated boulders that I measured was just over 300 mm, and the largest had an intermediate axis of just over 1m. My observations of imbrication, a lack of levees, and fan and sheet deposits indicate that the convective flood was not a debris flow (*Costa*, 1988; *Pierson*, 2005; *Pierson and Costa*, 1987). The lack of

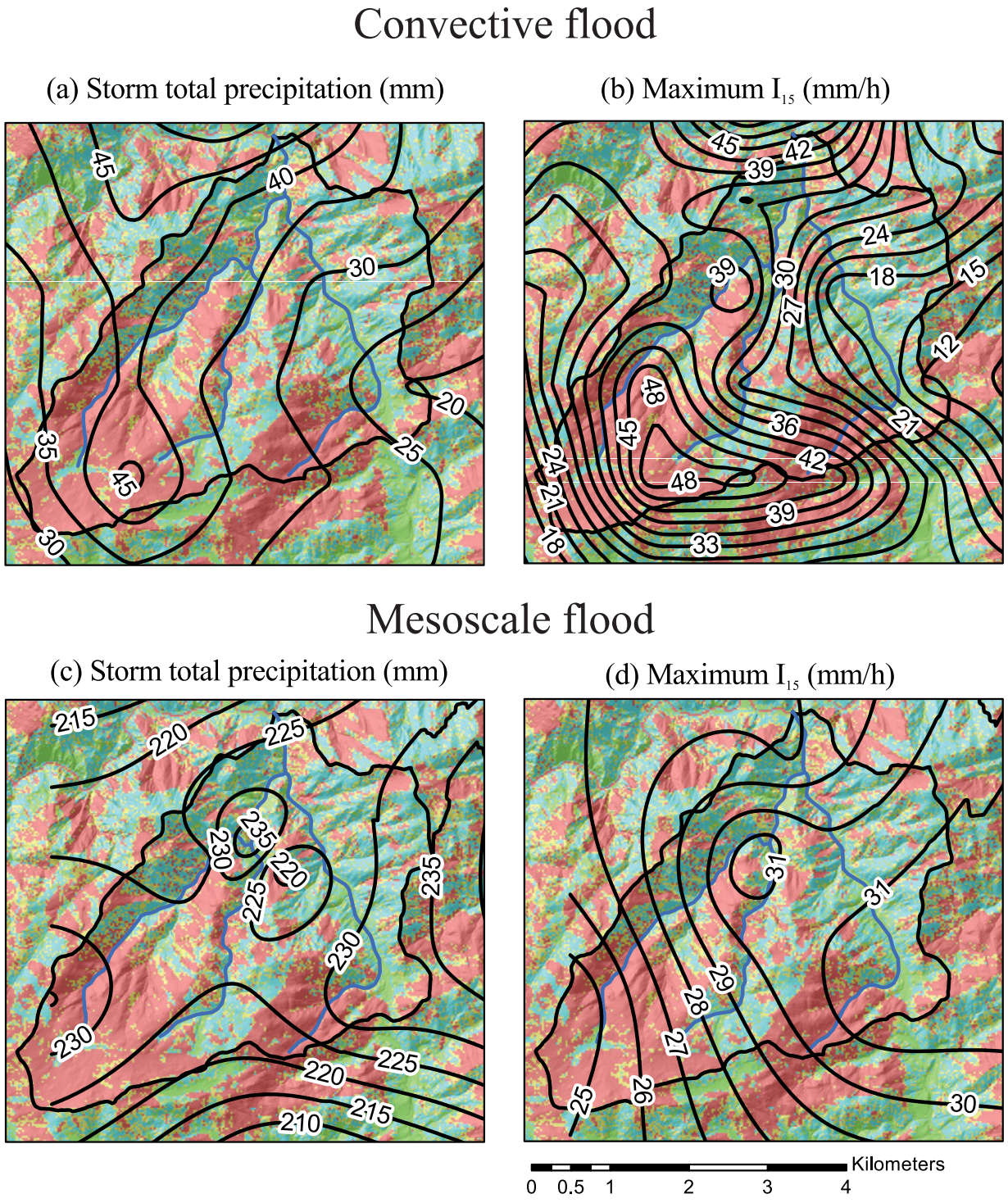

Figure 2.5: Isohyets of storm total precipitation (mm) and maximum 15-minute rainfall intensities (mm/h) over Skin Gulch for the convective storm on 6 July 2012 (a), (c) and mesoscale storm on 9–15 September 2013 (b), (d), respectively. The background of each figure is the burn severity map for the 2012 High Park Fire, where red is high severity, yellow is moderate severity, aquamarine is low severity, and green is unburned.

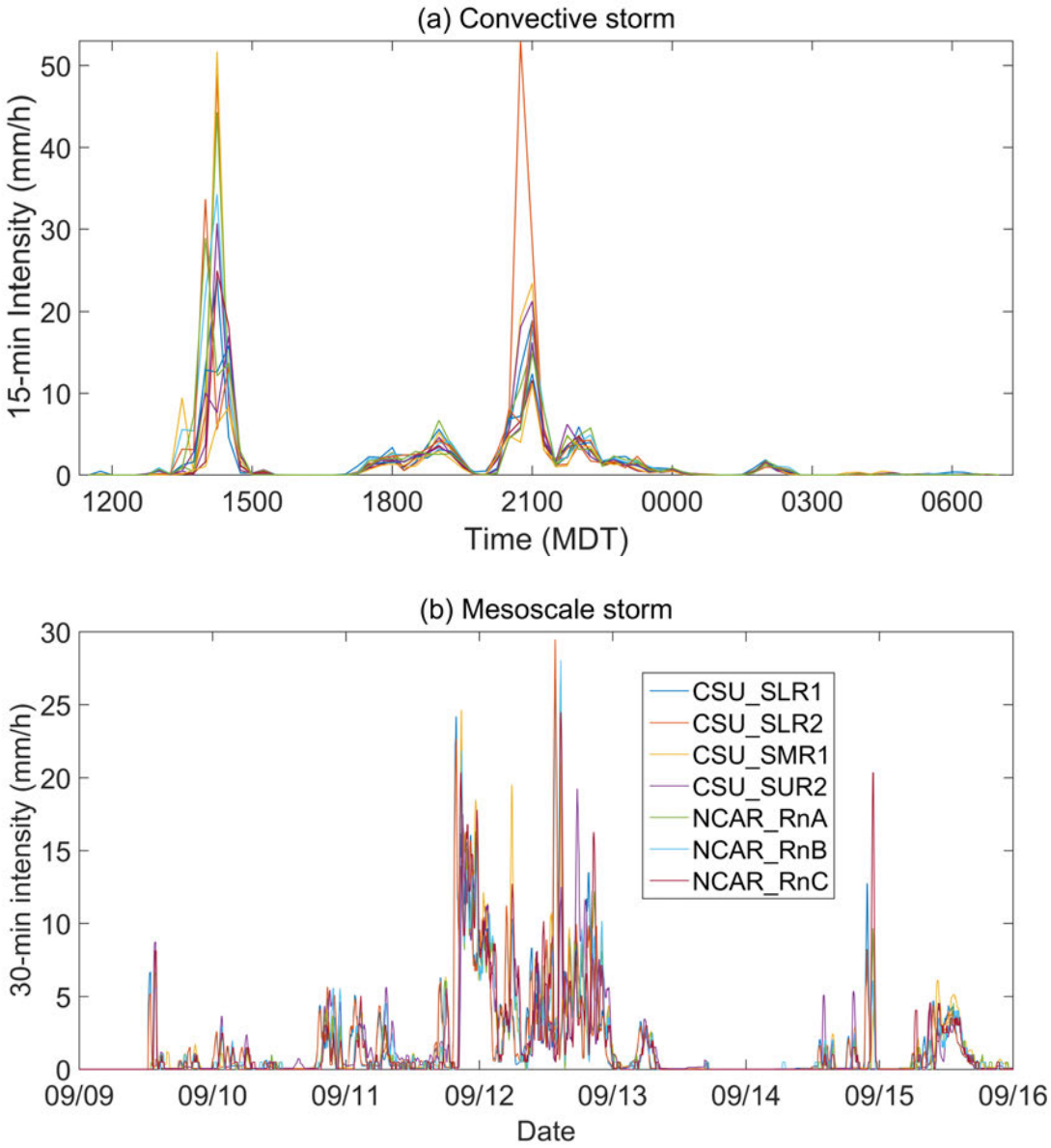

Figure 2.6: (a) 15-min rainfall intensities for the convective storm on 6 July 2012 computed from biascorrected Hydro-NEXRAD radar data; each line is the time series of a 1 km^2 radar bin within Skin Gulch. (b) 15-minute rainfall intensities from the mesoscale storm on 9–15 September 2013 for each recording rain gage in Skin Gulch with dates centered at 0000 MDT. Names in legend refer to rain gages installed and maintained by researchers from Colorado State University (CSU) and the National Center for Atmospheric Research (NCAR), respectively.

HWMs in Tributary 3 or evidence of high flows in the numbered tributaries suggests that nearly all the water and sediment during the convective flood came from the western branch. The spatially varying geomorphic changes show how a highly localized, high-intensity rainfall can combine with high burn severity (Figure 2.5a) to produce a major flood in one portion of SG compared with the other portions that either had less rainfall or were not as severely burned.

The depositional nature of this flood was shown by the extensive deposits from XS8 all the way downstream to XS1. At XS1 there was a maximum vertical aggradation of 0.14 m and a 1.4 m^2 decrease in cross-sectional area, but there was much more deposition on the floodplain and terrace beyond the right-hand side of the cross-section.

In contrast to the depositional nature of the convective flood, the primary geomorphic changes from the long duration mesoscale flood were incision and widening (Table 2.1; Figure 2.7; supplementary Figures B.1–B.10). Only XS1 experienced deposition, and the 2.3 m of aggradation was due to the backing up of a downstream culvert (*Kampf et al.*, 2016). The ultrasonic sensor at XS1 showed that high flows lasted for ~60 h beginning about 1845 MDT on 11 September 2013. At XS8 there was 1.7 m of incision and a corresponding decrease in the flood impacted channel width from 6 m to 4 m, while farther downstream at XS4 the flood expanded the active channel width from about 3 to 23 m with only 0.3 m of incision (Figure 2.7). Bank undercuts and bank failures were common along the lower mainstem, and the bank erosion helped trigger a shallow landslide at XS4.

2.3.4 Estimated peak flows – Slope-area method

Cross-sectional flow areas and depths during the convective flood were greater than for the mesoscale flood (Table 2.2), which accurately corresponds to the observed higher HWMs from the convective flood and erosional nature of the mesoscale flood. The mean Manning's n values among cross-sections increased from the convective flood to pre-mesoscale flood by ~0.005 and again by the same amount from the pre-mesoscale flood to post-mesoscale flood (Table 2.2).

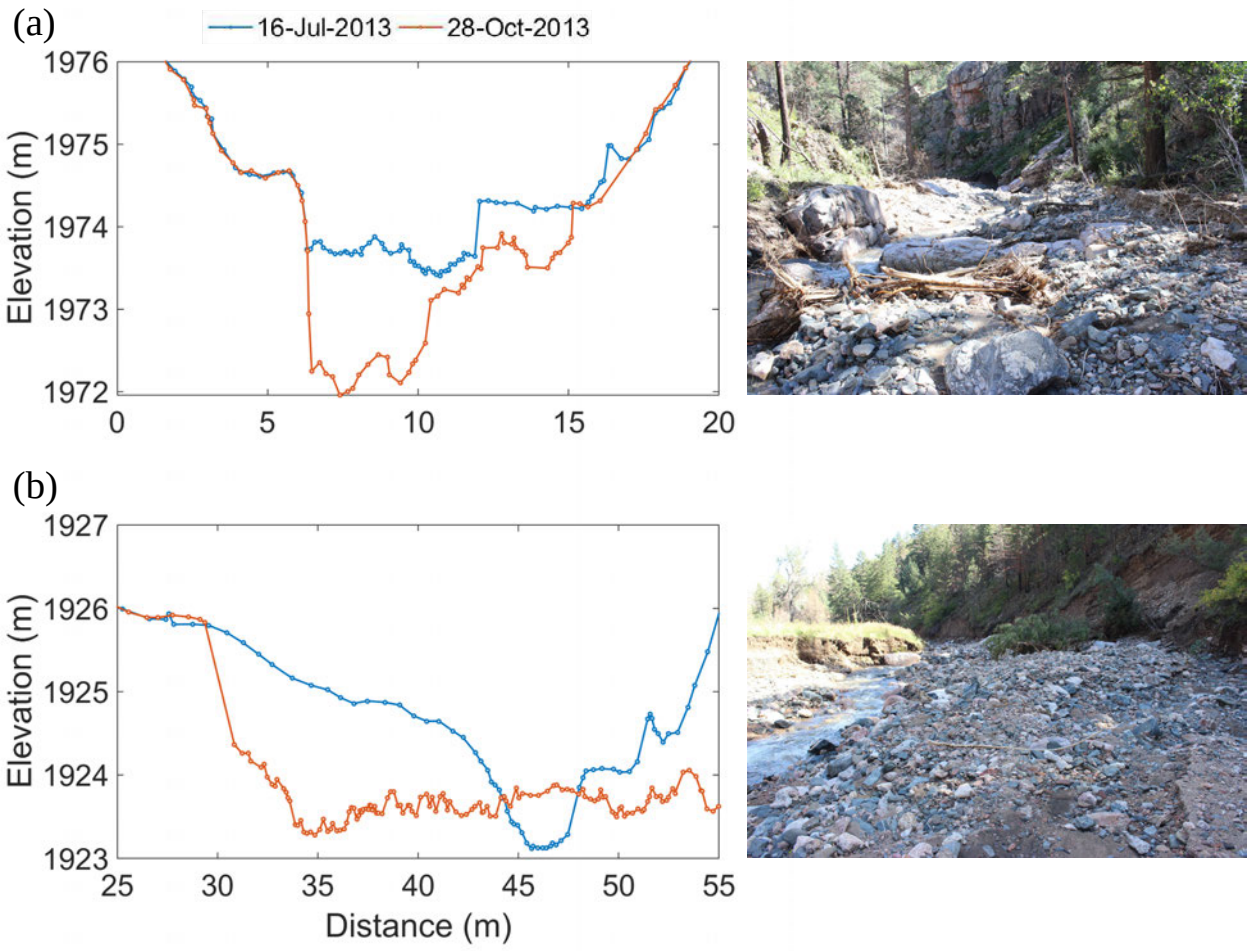

Figure 2.7: Plot of (a) XS8 and (b) XS4 prior to and after the mesoscale flood. The photos at each cross-section were taken on 24 September 2013 looking downstream.

Table 2.2: Inundated cross-sectional areas, mean flow depth, maximum flow depth and hydraulic radius as determined by the HWMs, local slopes, and statistics for Manning's n used for each cross-section and the Nays2D model. The rightmost Manning's n column presents the mean and standard deviation of all of the independent roughness estimates for the flood/topography, and were used in the Nays2D modeling of that flood. XS1 and XS6 are excluded because there were no nearby HWMs for either flood.

Flood	Topography	Cross-section	Area (m^2)	Mean flow depth (m)	Max flow depth (m)	Hydraulic radius (m)	Slope	Manning's n (s/$m^{1/3}$)			Manning's n (s/$m^{1/3}$)	
								Mean	S.D.	Range	Mean	S.D.
Convective	Post-flood	XS2	17.7	0.8	1.3	0.9	0.034	0.05	0.03	0.03–0.09		
Convective	Post-flood	XS3	31.5	1.0	1.9	1.0	0.065	0.06	0.03	0.03–0.11		
Convective	Post-flood	XS4	29.1	1.2	2.9	1.1	0.061	0.06	0.03	0.03–0.11	0.06	0.03
Convective	Post-flood	XS5	12.9	0.6	1.6	0.6	0.061	0.07	0.02	0.04–0.12		
Convective	Post-flood	XS8	23.2	1.4	2.2	1.3	0.093	0.06	0.03	0.03–0.13		
Mesoscale	Pre-flood	XS2	7.8	0.4	0.8	0.4	0.044	0.05	0.03	0.03–0.11		
Mesoscale	Pre-flood	XS7	1.3	0.4	0.8	0.3	0.097	0.08	0.04	0.04–0.16	0.06	0.03
Mesoscale	Pre-flood	XS9	7.2	0.5	1.0	0.5	0.070	0.06	0.03	0.03–0.13		
Mesoscale	Pre-flood	XS10	10.4	0.8	1.4	0.8	0.090	0.07	0.03	0.03–0.13		
Mesoscale	Post-flood	XS2	9.7	0.5	0.9	0.5	0.059	0.06	0.03	0.04–0.12		
Mesoscale	Post-flood	XS7	2.7	0.7	1.3	0.5	0.078	0.08	0.03	0.04–0.14	0.07	0.03
Mesoscale	Post-flood	XS9	11.7	0.8	1.4	0.7	0.064	0.07	0.03	0.04–0.12		
Mesoscale	Post-flood	XS10	14.9	1.2	2.6	0.9	0.086	0.07	0.03	0.03–0.13		

Table 2.3: Inundated cross-sectional areas, mean flow depth, maximum flow depth and hydraulic radius as determined by the HWMs, local slopes, and statistics for Manning's n used for each cross-section and the Nays2D model. The rightmost Manning's n column presents the mean and standard deviation of all of the independent roughness estimates for the flood/topography, and were used in the Nays2D modeling of that flood. XS1 and XS6 are excluded because there were no nearby HWMs for either flood.

Flood	Topography	Cross-section	Slope-area in m^3/s ($m^3/s\ km^2$)		Critical flow in m^3/s ($m^3/s\ km^2$)		Nays2D in m^3/s ($m^3/s\ km^2$)	
			Peak flow	Uncertainty	Peak flow	Uncertainty	Peak flow	Uncertainty Range
Convective	Post-flood	XS2	62 (6.9)	35 (3.9)	51 (5.6)	22 (2.5)		
Convective	Post-flood	XS3	140 (16)	76 (8.6)	100 (11)	43 (4.8)		
Convective	Post-flood	XS4	140 (16)	78 (8.9)	99 (11)	41 (4.7)	130 (28)	90–210 (20–46)
Convective	Post-flood	XS5	32 (3.8)	13 (1.6)	31 (3.7)	15 (1.8)		
Convective	Post-flood	XS8	130 (25)	66 (13)	85 (16)	35 (6.8)		
Mesoscale	Pre-flood	XS2	16 (1.8)	9.7 (1.1)	16 (1.8)	8.5 (0.9)		
Mesoscale	Pre-flood	XS7	2.5 (0.9)	1.4 (0.5)	2.6 (0.9)	1.4 (0.5)	20 (2.3)	10–40 (1.1–4.6)
Mesoscale	Pre-flood	XS9	19 (3.7)	11 (2.2)	16 (3.1)	8 (1.6)		
Mesoscale	Pre-flood	XS10	40 (8.7)	21 (4.6)	30 (6.5)	13 (2.8)		
Mesoscale	Post-flood	XS2	23 (2.5)	11 (1.2)	22 (2.5)	11 (1.2)		
Mesoscale	Post-flood	XS7	6.3 (2.2)	2.8 (1.0)	7.3 (2.6)	3.3 (1.2)	50 (5.7)	20–70 (2.3–8.0)
Mesoscale	Post-flood	XS9	34 (6.7)	14 (2.8)	33 (6.5)	15 (2.9)		
Mesoscale	Post-flood	XS10	60 (13)	28 (6)	51 (11)	21 (4.6)		

Peak flow estimates for the convective flood varied from 32 to 140 $m^3 s^{-1}$ (3.8 to 25 $m^3 s^{-1} km^{-2}$), but I believe that the low value of 32 $m^3 s^{-1}$ is not representative as the HWM for this XS was on the inside of a bend within a stand of unburned trees (Table 2.3; Figure 2.8). If this value is excluded the range is from 62 to 140 $m^3 s^{-1}$, with three of the four remaining cross-sections having values of 130–140 $m^3 s^{-1}$. There was a strong decrease in peak flows per unit area from 25 $m^3 s^{-1} km^{-2}$ at XS8 to only 6.9 $m^3 s^{-1} km^{-2}$ at XS2, and this is consistent with the locations of peak rainfall intensities and the expected decline in unit area peak flows with increasing drainage area (*Smith et al.*, 2005a,b). The uncertainties in the estimated peak flow ranged from 13 to 78 $m^3 s^{-1}$ (1.6 to 13 $m^3 s^{-1} km^{-2}$) depending on the crosssection, and these were proportional to the estimated peak flows in both absolute and unit area terms (Table 2.3).

Using the slope-area method, estimated mesoscale flood peak flows were all smaller than the estimated peak flows for the convective flood (Table 2.3). Excluding XS7 on Tributary 3, the estimated peak flows using pre-flood topography varied from 16 to 40 $m^3 s^{-1}$, while the peak flows per unit area varied from 1.8 to 8.7 $m^3 s^{-1} km^{-2}$. Uncertainties were 9.7 to 21 $m^3 s^{-1}$ (1.1 to 4.6 $m^3 s^{-1} km^{-2}$). Using the postflood topography increased the estimated peak flows from 1.4 to 2.5 times, and this was due primarily to the greater channel cross-sectional area (Table 2.2). Excluding XS7 on Tributary 3, the estimated peak flows using post-flood topography varied from 23 to 60 $m^3 s^{-1}$, while the peak flows per unit area varied from 2.5 to 13 $m^3 s^{-1} km^{-2}$. Uncertainties were 11 to 28 $m^3 s^{-1}$ (1.2 to 6.0 $m^3 s^{-1} km^{-2}$). Direct at-a-station comparisons between floods are difficult because only XS2 had HWMs and peak flow estimates for both floods. For this cross-section, the estimated peak flows for the mesoscale flood using pre- and post-flood topography were, respectively, 26% and 37% of the estimated values for the convective flood.

2.3.5 Estimated peak flows – Critical flow method

The critical flow method yielded estimated peak flows for the convective flood of 31 to 100 $m^3 s^{-1}$ (3.7 to 16 $m^3 s^{-1} km^{-2}$) (Table 2.3; Figure 2.8). Excluding XS5 range is from 51 to 100 $m^3 s^{-1}$ (5.6 to 16 $m^3 s^{-1} km^{-2}$). These values are 18–35% lower than the corresponding peak flows

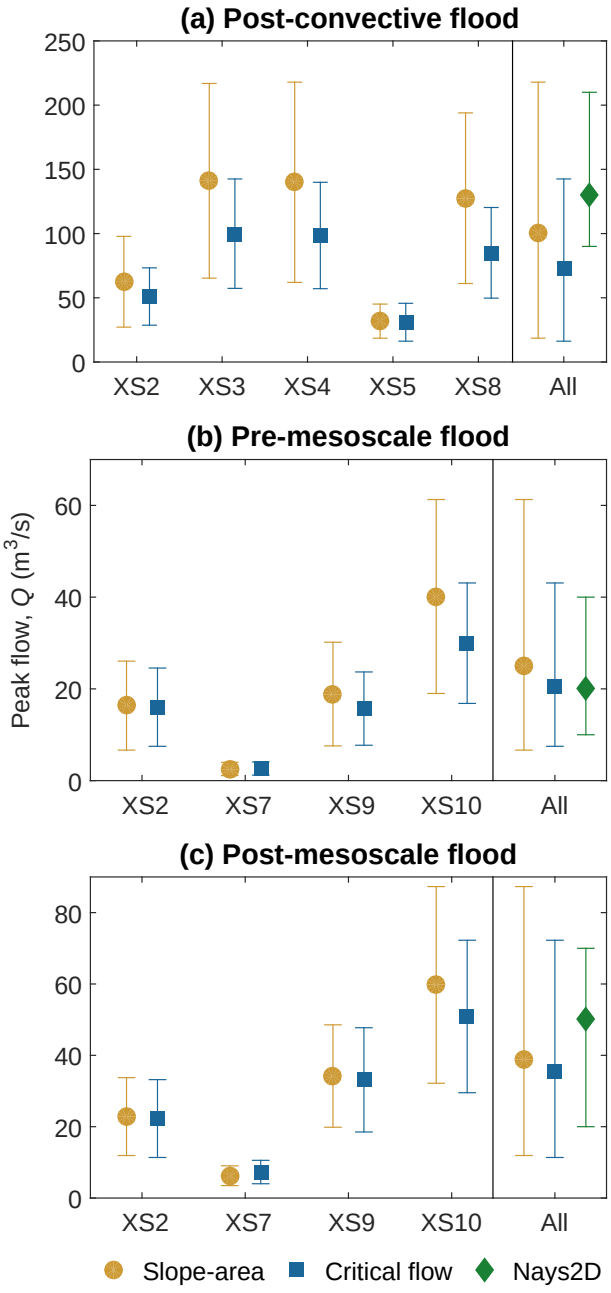

Figure 2.8: Predicted peak flows for each of the three methods for the: (a) convective flood using post-convective flood topography; (b) mesoscale flood using pre-mesoscale flood topography; and (c) mesoscale flood using post-mesoscale flood topography. For the cross-sections the center mark represents the predicted peak flow using the central estimate of Manning's n; the vertical bars represent uncertainty. For the 'All' portion of each figure the at-a-station methods represent the average and range from the crosssections. The Nays2D results represent the best estimate using the average Manning's n and measured HWM elevations, and the range accounting for uncertainty in Manning's n, HWM elevations, and lidar topography (see text for details). Note that XS7 is on Tributary 3 and was not included in the 'All' summary (Figure 2.4).

estimated using the slope-area method, and the pattern of estimated peak flows among the different cross-sections using the critical flow assumption matched the pattern from the slope-area method. Uncertainties were 38 to 140 m^3 s^{-1} (4.5 to 16 m^3 s^{-1} km^{-2}), depending on the cross-section (Table 2.3).

Using the critical flow method, estimated mesoscale flood peak flows were all smaller than the estimated peak flows for the convective flood; this is consistent with the results of the slope-area method (Table 2.3). Excluding XS7 on Tributary 3, the estimated peak flows using pre-flood topography varied from 16 to 30 m^3 s^{-1}, while the peak flows per unit area varied from 1.8 to 6.5 m^3 s^{-1} km^{-2}. Uncertainties were 25 to 87 m^3 s^{-1} (2.7 to 17 m^3 s^{-1} km^{-2}). Using the post-flood topography increased the estimated peak flows from 1.4 to 2.8 times, and this was due primarily again to the greater channel crosssectional area (Table 2.2). Excluding XS7 on Tributary 3, the estimated peak flows using post-flood topography varied from 22 to 51 m^3 s^{-1}, while the peak flows per unit area varied from 2.5 to 11 m^3 s^{-1} km^{-2}. Uncertainties were 51 to 74 m^3 s^{-1} (5.7 to 15 m^3 s^{-1} km^{-2}).

Using the assumed Froude number of 1.0 allowed us to independently estimate Manning's n using Equation (2). Resulting n values range from 0.058 to 0.097, 0.056 to 0.090, and 0.065 to 0.083 for the convective flood topography, pre-mesoscale flood topography, and post-mesoscale flood topography, respectively.

2.3.6 Estimated peak flows - Nays2D modeling

Predicted peak flow for the convective flood using Nays2D and the reach-averaged Manning's n was 130 m^3 s^{-1} (Table 2.3). Peak flow per unit area using the contributing area at the top of the modeled domain, 4.6 km^2, was 28 m^3 s^{-1} km^{-2}. This discharge is very similar to the values of 130–140 m^3 s^{-1} calculated from the majority of the cross-sections using the slope-area method. Uncertainty in peak flow ranged from 90 to 210 m^3 s^{-1}, or 20–46 m^3 s^{-1} km^{-2}, as a result of incorporating the uncertainty in roughness, and lidar and HWM elevations. Differences in elevations

between surveyed HWMs and modeled water surface did not show any longitudinal trend, further supporting the assumption that the tributaries provided negligible additional flow.

The estimated peak flow for the mesoscale flood was 20 m^3 s^{-1} (2.3 m^3 s^{-1} km^{-2}) using pre-flood topography and 50 m^3 s^{-1} (5.7 m^3 s^{-1} km^{-2}) using post-flood topography (Table 2.3). This large difference is consistent with peak flow estimates using the other two methods, and estimated peak flows for the pre-flood topography are consistent with the values calculated from the other two methods (Figure 2.8). In contrast, estimated peak flows for the post-flood topography are slightly higher than the best estimates from the other two methods. The uncertainty range of peak flows was 10 to 40 m^3 s^{-1} (1.1 to 4.6 m^3 s^{-1} km^{-2}) using pre-flood topography, and from 20 to 70 m^3 s^{-1} (2.3 to 8.0 m^3 s^{-1} km^{-2}) using post-flood topography (Table 2.3).

Reach average peak stream power for the convective flood was 3500 W/m^2, which is three to five times the peak stream power estimates for the mesoscale flood (Table 2.4). Durations of the convective and mesoscale floods were estimated as 2 and 24 h, respectively. Using these durations total energy expenditure was estimated as 13 000 kilojoules for the convective flood, which was only 25–46% of the total energy expenditure for the mesoscale flood.

Table 2.4: Estimates of stream power (W/m^2) and order-of-magnitude estimates of energy expenditure (kJ), calculated from the Nays2D peak flow estimates (Table 2.3), average wetted width and water surface (WS) slope from the Nays2D models, and estimated flood durations.

Flood	Topography	Peak flow (m^3/s)	Width (m)	WS slope (m/m)	Stream power (W/m^2)	Duration (hours)	Energy expenditure (kJ)
Convective	Post-flood	130	26	0.072	3500	2	13 000
Mesoscale	Pre-flood	20	19	0.062	650	24	28 000
Mesoscale	Post-flood	50	24	0.058	1200	24	51 000

2.4 Discussion

2.4.1 How do peak flows and geomorphic changes compare between the short-duration, convective flood and the long-duration, mesoscale flood?

Both the convective and mesoscale floods in a burned basin caused extensive geomorphic changes, but the pattern, intensity, and duration of the precipitation and resulting peak flows were very different for the two floods. Studies from nearby fires have shown that nearly all of the hillslope erosion and downstream deposition after wildfire is in response to summer thunderstorms (*Benavides-Solorio and MacDonald*, 2005; *Kunze and Stednick*, 2006; *Moody and Martin*, 2001a). Although I do not have a hydrograph for the convective flood, the radar rainfall data strongly indicates that this would have been a large but short-duration peak flow generated by infiltration-excess overland flow. This runoff mechanism and flashy hydrographs have been widely observed from other thunderstorms on the High Park Fire. In contrast, the mesoscale flood generated a smaller peak flow, but the flows were sustained for a much longer period of time, and my pictures and measured data clearly show that this flood caused substantially greater geomorphic changes across a much larger proportion of the valley bottom (Figures 2.2, 2.3, and 2.7; Table 2.1). As one example, an abandoned dirt road that ran from near the bottom of the watershed up to the confluence with Tributary 3 was cut multiple times by the convective flood, while the mesoscale flood almost completely obliterated the road by reworking the valley bottom.

Costa and O'Connor (1995) posited that the energy available for geomorphic change is the time integral of the unit stream power above an alluvial erosion threshold, where others have shown the alluvial erosion threshold to be ~300 W/m^2 (*Magilligan*, 1992; *Miller*, 1990a). My observations and calculations indicate that both floods clearly exceeded alluvial erosion thresholds (Figures 2.2, 2.3, and 2.7; Tables 2.1 and 2.4). My order-of-magnitude estimates of total energy expenditure (Table 2.4) show that the convective flood produced very high peak unit stream power but relatively low total energy expenditure, while the mesoscale flood had lower peak unit stream

power but a much larger total energy expenditure due to its long duration. The peak stream power and total energy expenditure of both floods fall within the range of 'extreme' geomorphic impact floods presented in *Magilligan et al.* (2015), and they illustrate how both flood magnitude and duration play important roles in determining valley geomorphic changes.

2.4.2 What is the importance of precipitation intensity, bare soils, and sequence of events on peak flows?

Rainfall intensities for the convective storm are very likely too low as there would have been beam blockage from mountainous terrain (*Zrnić and Ryzhkov*, 1996). My best estimate of the peak flow for the convective flood on 6 July 2012 using Nays2D is 28 m^3 s^{-1} km^2. A simple mass balance assuming no storage shows that an equivalent rainfall intensity of ~100mm h^{-1} would be needed to generate this flow. Other studies have shown that infiltration immediately after high severity fires in the Colorado Front Range can be less than 10mm h^{-1} (*Kunze and Stednick*, 2006; *Larsen et al.*, 2009; *Moody and Martin*, 2001a; *Pietraszek*, 2006; *Schmeer*, 2014), so the required peak rainfall intensity is approximately 110 mm h^{-1} or about twice the maximum intensities estimated from the radar data (Figure 2.5b). A maximum intensity of 110 mm h^{-1} for 15 min has an estimated recurrence interval of 25 to 50 years (*Perica et al.*, 2013), which suggests that the July 2012 storm was more extreme than initially conjectured.

From my own observations and those of other researchers, the high flood flow in early July 2012 in SG induced the largest geomorphic changes from any convective storm in a catchment of at least 3 km^2 within the HPF. Other thunderstorms did generate more localized peak flows that flooded roads, overtopped culverts, and delivered sediment into the Cache la Poudre River (*Writer et al.*, 2014), but nowhere did anyone note the imbricated boulders and debris deposits shown in Figure 2.2. The SG convective flood and these other high flows emphasize the dramatic increase in surface runoff, erosion, and peak flows that are common after high and moderate severity fires, particularly in areas subjected to high-intensity convective storms (*Kunze and Stednick*, 2006; *Moody and Martin*, 2001a,b, 2009; *Neary et al.*, 2003; *Shakesby and Doerr*, 2006). The effect of the con-

vective storm was exacerbated by the fact that the most intense rainfall occurred within a month after burning and was concentrated over an area that burned at high severity (*Moody and Ebel*, 2012).

In contrast, the estimated peak flows from the mesoscale storm were 2–9 $m^3\ s^{-1}\ km^{-2}$ or only 10–30% of the unit area peak flows for the convective flood. The lower estimated peak flows for the mesoscale storm can be explained primarily by the much lower 15 min peak rainfall intensities (Figures 2.5 and 2.6). To a lesser extent the lower peak flows from the mesoscale storm also can be attributed to the intervening 15 months of post-fire recovery. In the case of SG, the mean percentage bare soil as measured in 13 or more unmulched swales dropped from 53% in fall 2012 to 42% in fall 2013, and this helped increase the minimum rainfall intensity needed to initiate hillslope-scale erosion from 4 to 9mm h^{-1} (*Schmeer*, 2014). By spring 2014 the mean percentage bare soil had dropped to just under 30%, and this means that a storm in summer 2014 similar to the one observed on 6 July 2012 would generate much less runoff and geomorphic changes. Indeed, my field observations confirm that very little channel change has occurred in SG since the September 2013 mesoscale flood, and this is consistent with other studies that have measured the decline in post-fire erosion over time in similar environments (*Benavides-Solorio and MacDonald*, 2005; *Larsen et al.*, 2009; *Morris and Moses*, 1987; *Wagenbrenner et al.*, 2006).

The sequence of these two floods in SG also may contribute to the geomorphic changes observed as a result of the mesoscale flood. The convective flood was the first flood after the fire, and this generated large amounts of hillslope and upstream channel erosion, with much of this sediment being deposited on the floodplain below the confluence with Tributary 3 (Figure 2.2b). This unconsolidated sediment effectively 'loaded the gun' for the subsequent erosion (sensu *Nanson*, 1986) during the long-duration mesoscale flood, which removed and transported nearly all of the sediment that had been deposited up to that point (Figures 2.3 and 2.7). The short duration of the high-intensity rainfall and large amounts of deposition suggests that the convective flood was more sediment transport capacity limited, while the September flood was eventually more sediment supply-limited because the sustained rainfall and high flows were able to transport all

but the coarsest portion of the previously deposited sediment and increase the size of the channel (Figure 2.3). The sequence of floods can therefore play an important role on the subsequent valley geomorphic changes (*Germanoski*, 2002).

2.4.3 How precisely can I estimate peak flows for each storm? And can my confidence in the estimated peak flows be improved by using and comparing different estimation techniques?

In this study I compared the peak flows from two storms using the slope-area method, critical flow method, and a 2D hydraulic model (Figure 2.8). Each peak flow estimation method comes with inherent limitations; for example, uncertainties in estimating roughness plus expansion and contraction losses can lead to errors of 100% or more in the slope-area method (*Jarrett*, 1987a). The critical flow method (*Grant*, 1997; *Moody et al.*, 2008a,b; *Webb and Jarrett*, 2002) does not require an estimate of roughness but it sets the Froude number equal to 1.0 while larger values can occur during large floods in steep channels (*Costa*, 1987; *Jarrett*, 1987a, and references therein). A larger Froude number will result in an underestimate of velocity and discharge, and in my results the estimated peak flows from the critical flow method were consistently lower than the peak flows estimated from the slope-area method and generally lower than Nays2D.

Two-dimensional (2D) hydraulic models are preferred for paleohydrology because these can better quantify downstream and cross-stream patterns of flow depth, velocity and shear stress (*Morvan et al.*, 2008; *Nelson et al.*, 2003) with a resulting increase in accuracy (*Hicks et al.*, 2005; *Smith et al.*, 2005a,b; *Tonina and Jorde*, 2013). The primary drawback to 2D models is they require detailed topography that can be difficult to acquire; however, this is quickly becoming less of an issue as high resolution topography becomes available (*Passalacqua et al.*, 2015). The peak flow estimates using Nays2D were very consistent with the median values from the slope-area method for the convective storm and the mesoscale flood using pre-flood topography. The uncertainty range in Nays2D was generally larger than the uncertainty for the other two methods when compared with the uncertainty at a single cross-section. However, the uncertainty of the peak flow estimates

using Nays2D is less than the uncertainty that results from the large differences in the estimated peak flows among the different cross-sections (Figure 2.8, 'All'). This suggests that the ability to integrate estimates from different cross-sections and HWMs in a 2D model can reduce the overall uncertainty for estimating peak flows after a large flood.

Common but often unrecognized problems for estimating peak flows after floods are that they implicitly assume: (1) high-water marks (HWMs) accurately represent the water surface profile during the peak flow; and (2) the post-flood bed topography and other parameters such as surface roughness are representative of the conditions when the HWMs were established. It is clear that accurate a posteriori estimates of peak flows are directly related to the accuracy of the HWMs (*House and Pearthree*, 1995; *Jarrett and England*, 2002), but I believe that the elevations of my HWMs are quite accurate given the fineness of the debris lines and the accuracy of my surveys. A potentially much greater source of error is that floods often cause extensive deposition or incision (*Costa and O'Connor*, 1995; *Elliott and Parker*, 2001; *Hicks et al.*, 2005), and the timing of topographic channel change relative to the establishment of the HWMs is nearly impossible to determine. The resulting uncertainties in peak flows due to channel change are typically ignored in indirect peak flow calculations (*Lumbroso and Gaume*, 2012), but the magnitude of erosion and deposition—particularly after moderate to severe wildfires—indicates that intra-event channel change can be a major source of uncertainty for indirect peak flow estimates. Large uncertainties in estimating peak flows also are introduced when cross-sections and HWMs are widely spaced, differences between cross-sections exist (inundated area and local slopes), and there is much uncertainty in roughness (Tables 2.1 and 2.2). Additional sources of uncertainty among cross-sections could be due to possible inflows, transmission losses, and hydrodynamic dispersion, but my results indicate that the two largest sources of uncertainty are the uncertainty in roughness and the intraevent changes in bed topography, which I discuss below.

The uncertainty in roughness generally receives the most attention in studies attempting to make indirect estimates of large flood peaks (*Costa*, 1987; *Wohl*, 1998). My results show that the effect of this uncertainty in roughness varies greatly according to the technique being used.

Peak flows estimated by the slope-area method are most affected by the uncertainty in roughness because the calculated discharge is inversely proportional to Manning's n (Equation (1)). The coefficient of variation of my Manning's n estimates ranges from 36% to 55% depending on the specific cross-section and the topography, which exceeds the 25% uncertainty suggested by *Wohl* (1998). The uncertainty in Manning's n stems primarily from lumping all forms of resistance (e.g. grain roughness, form drag due to bedforms and channel geometry, vegetation resistance, as well as added fluid resistance due to sediment transport) into a single roughness parameter (*Jarrett*, 1987b; *Lumbroso and Gaume*, 2012). Field guides and empirical equations have been developed to facilitate more accurate estimates of Manning's n, but these often perform poorly in small mountain streams (*Ferguson*, 2010; *Marcus et al.*, 1992; *Mrokowska et al.*, 2014; *Smith et al.*, 2007) as evidenced by the wide range of Manning's n values estimated by these different methods for my reach (0.03 to 0.13, excluding XS7).

Manning's n values can be back-calculated from direct discharge measurements, but baseflows in SG are only a couple of decimeters deep, making the extrapolation of a Manning's n to large floods very difficult given that it varies with stream stage (*Ferguson*, 2010; *Lee and Ferguson*, 2002; *Reid and Hickin*, 2008; *Yochum et al.*, 2014). Direct discharge measurements during larger flows are often extremely difficult because the largest post-fire floods in my region are generated by short-duration localized thunderstorms. Uncertainty in the location of and timing of these storms, the lack of ready access, and the flashiness of the flood response makes it highly unlikely that such peak flows can be directly measured.

Momentum extraction due to resistance from the large-scale roughness of bedforms and nonuniform channel geometry are more accurately represented in a 2D model than in 1D or at-a-station calculations (*Morvan et al.*, 2008). Thus, 2D model predictions are less sensitive to the specific choice of n for small-scale roughness (i.e. grain resistance). The reduced sensitivity to n is a major rationale for using a more sophisticated and physically-based technique than the slope-area method.

Most estimates of peak flows do not have the data, or do not attempt to determine, the effects of changes in channel topography on the estimated peak flows. In my study the mesoscale flood increased the cross-sectional areas by a minimum of 24% at XS2 to more than 60% at XS9. Local slopes changed from -20% at XS7 to +34% at XS2 (Table 2.2), with the changes in slope being primarily due to the establishment and movement of local knickpoints (sensu *Gardner*, 1983). All of the tributaries also incised due to the sustained high flows and lower base level in the mainstem of SG during the mesoscale flood. My results show that these changes in cross-sectional area and local slope can cause a similar or larger percentage change in the estimated peak flows than the uncertainties in roughness and HWM elevation (Table 2.3; Figure 2.8). More specifically, there was approximately a two-fold difference in the estimated peak flow for the mesoscale flood when using the slope-area and critical flow method, depending on whether I used the pre- or the post-flood topography. Similarly, the calculated peak flow using Nays2D increased from 20 m^3 s^{-1} using the pre-flood topography to 50 m^3 s^{-1} using the post-flood topography, and this difference of 30 m^3 s^{-1} is larger than the uncertainty for either the pre- or post-flood estimates.

The true peak flow for the mesoscale flood is probably between the values calculated using pre- and post-flood topography, but there is no way to determine the precise bed topography at the time of highest discharge. For the convective flood we are in the more common position of only having post-flood topography. Field observations in my reaches indicate that the convective flood was primarily depositional, so the cross-sectional area during the highest flow would have been at least equal to or greater than the measured post-flood cross-section. This would suggest that the true peak flow was probably larger than my estimated values in Table 2.3. I posit that post-flood topography would more accurately estimate the peak flow from an incising flood than a depositional flood, as stream power and erosion are likely greatest at the peak flow. This would mean that the peak flows for the mesoscale flood are more accurately represented by the post-flood topography.

For a depositional flood the post-flood topography is more likely to underestimate the peak flow due to sediment deposition during the falling limb of the hydrograph. While a depositional flood

could have initial scour, this is unlikely given the usual tendency for peak sediment concentrations and higher sediment transport rates to be on the rising limb of a hydrograph (*Hsu et al.*, 2011; *Walling*, 1977). An incising flood is very unlikely to have an initial depositional phase, and this again would suggest that post-flood topography provides a more accurate estimate of peak flows for incising than depositional floods. Many floods also have multiple peaks and this, plus the complexities of varying sediment sources and supplies, means that all estimates of peak flows based on post-flood topography have a relatively high degree of uncertainty that is typically ignored.

The discussion above indicates that the slope-area method will have the greatest uncertainty because it is sensitive to the assumed Manning's n value as well as the assumption that the cross-sectional areas and slopes measured after a flood reflect the conditions at the time of the highest instantaneous flow. My results for the mesoscale flood did show an unexpected decrease in some of the central estimates for the slope-area peak flows with increasing drainage area (Table 2.3); however, with the exception of XS5 for the convective flood (where the HWM elevation was likely underestimated) and XS7 for the mesoscale flood (which was on a tributary), the uncertainty envelopes among the different cross-sections overlap (Figure 2.8). This illustrates the importance of quantifying uncertainty, which can be quite large, in these types of calculations.

The critical flow method does not require an estimate of roughness, but it necessarily assumes that the Froude number is 1.0 and any deviation from this assumption has a corresponding effect on the calculated peak flows. *Costa* (1987) noted that the Froude number can greatly exceed 1.0 for large floods in steep channels, and this will lead to a severe underestimate of peak flows. *Grant* (1997) suggested that peak flows tend to asymptotically approach critical flow as slope increases in threshold channels, but the 2m piles of debris against standing trees, the elevations of the HWMs, and the estimated peak flows clearly suggest the convective flood was a very exceptional flood and the Froude numbers likely exceeded 1.0 at least around the time of the peak flow.

An important benefit of using the Nays2D model is that it can be used to check on the validity of the critical flow method because it provides location-specific Froude values. My simulation for the convective flood using n = 0.06 and the associated best-fit discharge of 130 m^3 s^{-1} shows that

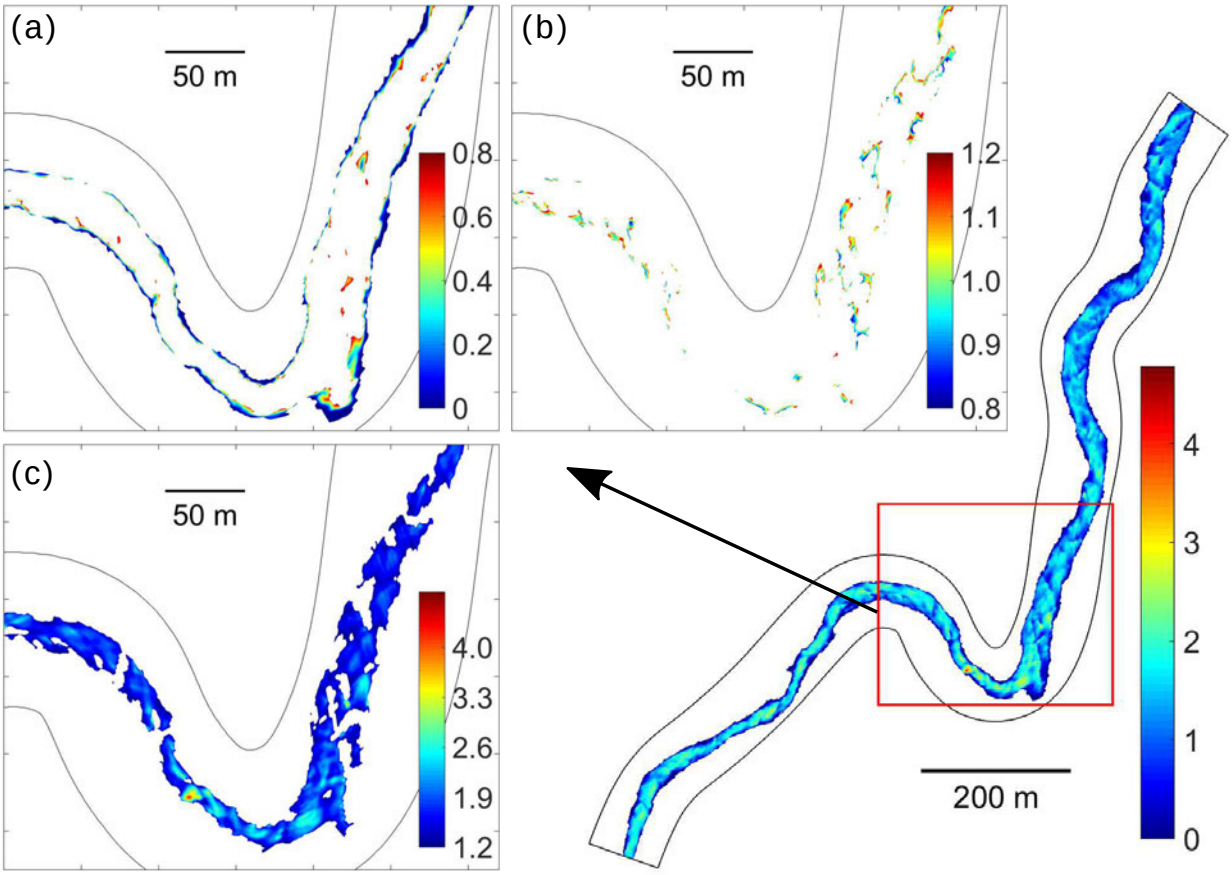

Figure 2.9: Predicted Froude numbers from Nays2D for the convective flood using n = 0.06 and Q= 130m^3 s^{-1}. The entire model reach is shown in the lower right, and the highlighted reach in a-c is centered around XS6 and XS8. (a) Areas with Froude numbers below 0.80, (b) areas with Froude numbers from 0.8 to 1.2, and (c) areas with Froude numbers greater than 1.2.

much of the channel had Froude numbers greater than 1.2 (Figure 2.9). The potential for higher Froude numbers at peak discharge during the convective flood is also supported by the results in Table 2.3, as the estimated peak flows from the critical flow method were generally lower than the peak flows calculated with the slope-area method and Nays2D.

The uncertainties in roughness, topography and Froude number suggest that 2D modeling should be used for indirect estimates of peak flows when possible, and a combination of methods is the best approach as they can be compared and help support or reject certain values and assumptions. As noted above, my results from Nays2D led us to question the basic assumption in the critical flow method (Figure 2.9). On the other hand, the critical flow method provided 11 independent estimates of main channel roughness (excluding XS7) for the three peak flows, which can

help inform the potential validity of different roughness values for the slope-area method. Hence a full assessment of the range and likely uncertainty in peak flow estimates requires the use of multiple estimation techniques, a range of input parameters, multiple cross-sections, and measured or estimated changes in channel topography. A comparison of the results from different locations and methods using different assumptions can help identify and cross-check the most likely range of values rather than estimating a single specific value (*Legleiter et al.*, 2011).

2.4.4 How do these floods compare to other large rainfall-runoff generated floods in the United States?

The convective flood was an exceptionally large flood. Estimated peak flows of 90–210 m^3 s^{-1} from Nays2D for the convective flood fall along the 99th percentile curve for the largest rainfall-runoff floods for similar-sized watersheds in the United States and Puerto Rico (Figure 2.10; O'Connor and Costa, 2004). Few floods of this magnitude have been observed in the central Rocky Mountains United States (Figure 2.10, inset), and most of the floods from drainage basins smaller than 100 km^2 are from the interior west and were caused by isolated convective storms (O'Connor and Costa, 2004). The estimated peak flow of 50 m^3 s^{-1} for the post-mesoscale flood topography falls just below the 90th percentile compared with other rainfall-runoff floods in the US and Puerto Rico (Figure 2.10). My estimated peak flow per unit drainage area (5.7 m^3 s^{-1} km^{-2}) for the mesoscale flood is generally consistent with many other estimates from the Colorado Front Range during the mesoscale storm (Yochum and Moore, 2013; Moody, 2016), although Yochum and Moore's (2013) estimate from SG of 7.9 m^3 s^{-1} km^{-2} is 1.4 times greater than my best estimate of peak flows from Nays2D. The use of a 2D model in conjunction with multiple HWMs at different locations provides a more robust method of estimating peak flows, suggesting that Yochum and Moore's (2013) peak flow assessment for the mesoscale flood is likely an overestimate.

Geomorphic changes from the two floods studied in this paper are still very evident years later. The imbricated boulders, piled woody debris, and some of the higher elevation and particularly coarse sediment deposits from the convective flood are still present. The mesoscale flood re-

worked both the postfire and historic valley fill deposits, and there have been minimal geomorphic changes to the channel or valley bottom since that flood. Given the continuing vegetative recovery

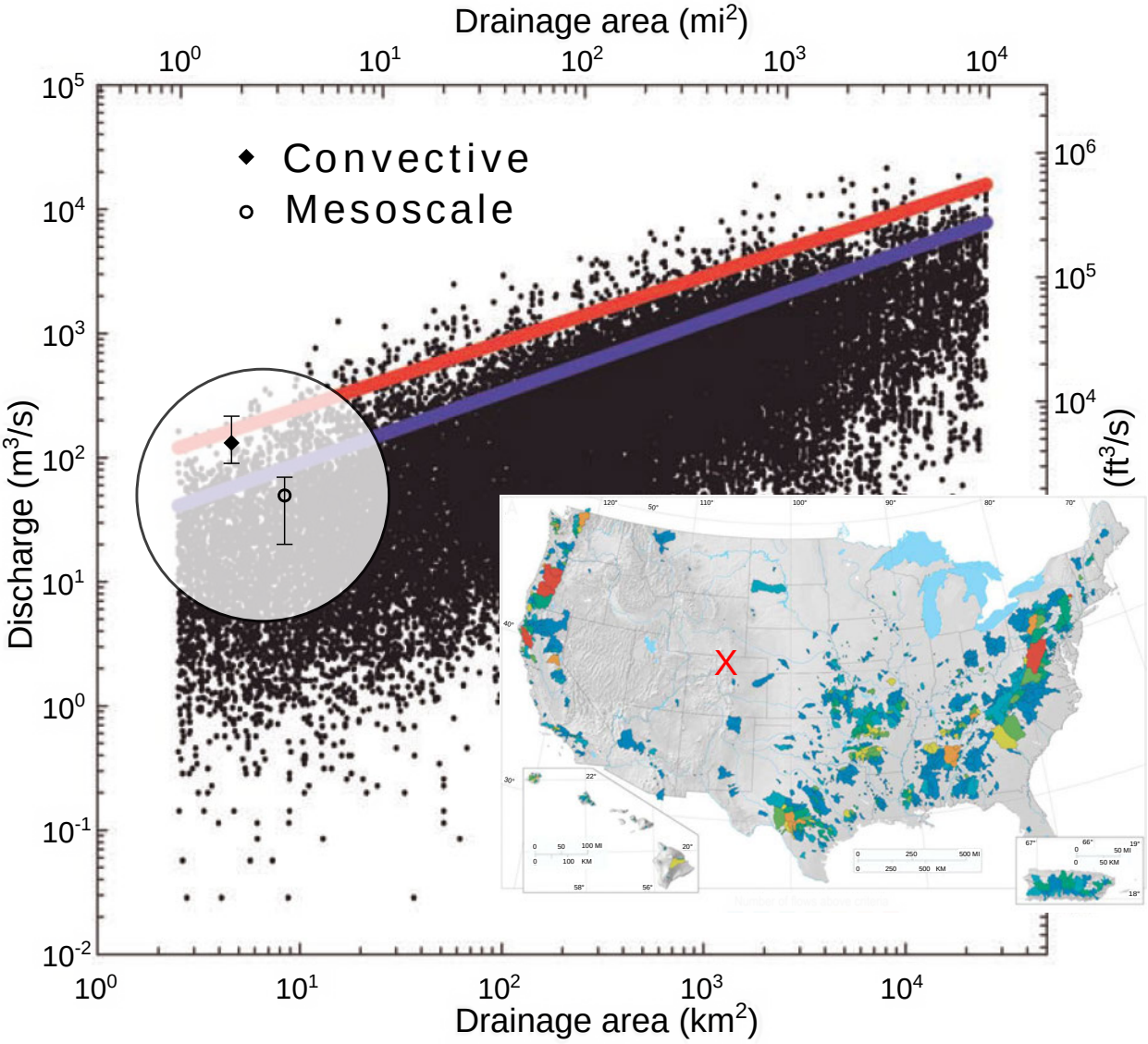

Figure 2.10: Plot of the largest rainfall-runoff floods experienced in the United States and Puerto Rico (modified from *O'Connor and Costa*, 2004) with the diamond and open circle showing the predicted peak flows from Nays2D model for the convective flood (130 m^3 s^{-1}) and the mesoscale flood (50 m^3 s^{-1}) using post-flood topography, respectively. Vertical bars represent the range of estimated peak flow for the convective flood (90-210 m^3 s^{-1}) and the mesoscale flood (20-70 m^3 s^{-1}). The watershed areas for the convective flood (4.6 km^2) and the mesoscale flood (8.7 km^2) are different due to the different model domains used to predict each flow with Nays2D. The diagonal blue and red lines correspond to the 90th and 99th percentiles, respectively. Inset map shows the locations of watersheds contributing to the 90th percentile, and the red X indicates the location of Skin Gulch.

and associated reductions in hillslope runoff and erosion, further channel geomorphic changes are unlikely and these two floods have largely reset the system compared with pre-fire conditions.

There are few data on the frequency of large-magnitude floods following fires in the Colorado Front Range, but charcoal deposits from incised channels indicate a 900–1000 year recurrence interval for fires and floods (Elliott and Parker, 2001) with the potential for even greater timespans (*Cotrufo et al.*, 2016). Since I am unaware of other watersheds in the High Park fire that experienced comparable flooding and geomorphic changes as observed from the convective flood in Skin Gulch, I posit that the post-fire flood deposits and channel change in Skin Gulch constitute a near millennium-scale event. In a stationary world this sequence of severe, basin-scale forest fire and subsequent extreme runoff can cause an aggradational signature that persists for centuries (*Hamilton et al.*, 1954; *Legleiter et al.*, 2003; *Meyer et al.*, 1992, 1995; *Moody and Martin*, 2001a). But in my non-stationary world with increased temperatures, earlier snowmelt, and a shift from snow to rain (*Clow*, 2010; *Liu et al.*, 2013; *Rocca et al.*, 2014), resource managers and the public must be prepared for more of these severe fire-flood events.

2.5 Conclusions

My investigation of two extreme floods that occurred after the Skin Gulch watershed burned in the 2012 High Park Fire shows how precipitation characteristics, burn severity, and time since burning are important controls on peak flows and geomorphic changes in a burned landscape. The convective flood on 6 July 2012 was just one week after burning, when a brief (~2 h) but intense convective summer thunderstorm focused over an area of high burn severity, produced a very large flood (~130 m^3 s^{-1}) with high peak unit stream power (3500 W/m^2) and extensive downstream deposition. The mesoscale flood in September 2013 was from an exceptionally long duration mesoscale storm, which produced a smaller flood peak (~20–50 m^3 s^{-1}), but the long duration (~24 h), and subsequently more total energy expenditure, caused channel incision and widening through extensive reworking of both recent and pre-existing valley bottom alluvial deposits.

Uncertainty in estimates of channel roughness, measured high-water mark elevations, and remotely sensed topographic data led to considerable uncertainties in the estimated peak flows for both floods. Slope-area estimates had the greatest uncertainty due in large part to the uncertainty in Manning's roughness. Estimated peak flows from the critical flow method were generally lower because the assumed Froude number of 1.0 set an upper limit on the estimated peak flows. The 2D model was less sensitive to the assumed roughness, although uncertainty in high-water mark elevations and airborne lidar topography still led to a wide range of peak flow estimates. My peak flow estimates for the mesoscale flood varied by roughly a factor of two depending on whether I used pre- or post-flood topography, and this indicates that the inherent uncertainty in the amount and timing of intra-event channel change can have an even larger effect on estimated peak flows than the uncertainty in roughness.

The estimated peak flow of 130 m^3 s-1 (28 m^3 s^{-1} km^{-2}) for the convective flood is among the largest floods per unit area observed in the United States, and this illustrates the profound effect of brief but intense precipitation over areas recently burned at high severity. The lower peak discharge of 50 m^3 s^{-1} (5.7 m^3 s^{-1} km^{-2}) for the mesoscale flood is attributed primarily to the lower peak rainfall intensities and secondarily to post-fire recovery. However, this flood was geomorphically much more effective due to the long duration of high flows and the large amount of sediment deposited after the fire from previous storms. Climate change indicates that fire-induced floods will become more common in the future; both the magnitudes of peak flows and the methodological implications from this study can help guide resource managers and future post-flood analyses.

2.6 Supporting information

Additional supporting information is in Appendix B.

Chapter 3

Geomorphic complexity and sensitivity of fire and floods in mountain catchments

3.1 Introduction

Fires and floods are of increasing concern given that global warming is leading to more wildfires (e.g., *Rocca et al.*, 2014; *Westerling et al.*, 2006) and a higher likelihood of extreme precipitation (*Berg et al.*, 2013). Wildfires reduce ground and canopy cover, increase soil water repellency, decrease infiltration rates, and decrease surface roughness (*DeBano et al.*, 1998; *Ebel et al.*, 2012; *Larsen et al.*, 2009; *Moody et al.*, 2013; *Onda et al.*, 2008; *Scott and Van Wyk*, 1990; *Shakesby and Doerr*, 2006). These changes not only cause increased rates of runoff and erosion (*Benavides-Solorio and MacDonald*, 2001, 2005; *Johansen et al.*, 2001; *Morris and Moses*, 1987; *Robichaud et al.*, 2000; *Swanson*, 1981; *Wondzell and King*, 2003), but also rapid headward expansion of the channel network (*Collins and Ketcham*, 2001; *Wohl*, 2013) and greater hillslope-stream connectivity due to the burning of vegetation (sensu *Shahverdian*, 2015).

Post-fire sediment produced from hillslopes can be substantial, but rilling and channel erosion can account for over 80% of the total eroded sediment from a watershed (e.g., *Moody and Martin*, 2001a). In certain environments sediment can be evacuated from small tributaries by debris flows, but only if sufficient sediment is available (e.g., *Florsheim et al.*, 1991; *Wohl and Pearthree*, 1991), and if the combination of burn extent, soil properties, morphology, and rainfall conditions are conducive to debris flows (*Cannon et al.*, 2010). Eroded sediment from upstream sources can be transported downstream as suspended sediment, causing degraded water quality (e.g., *Rhoades et al.*, 2011; *Smith et al.*, 2011; *Writer et al.*, 2014), and as bedload (*Wagenbrenner and Robichaud*,

Coauthors for this planned journal submission include L. H. MacDonald, P. A. Nelson, and J. A. Morgan.

2014). Much of the sediment transported as bedload is deposited at alluvial fans, and overbank on floodplains and terraces where slopes decrease and valleys widen (e.g., *Meyer et al.*, 1992; *Moody and Martin*, 2004, 2009; *Reneau et al.*, 2007). A complex response of erosion and deposition ensues depending on the spatial distribution of rainfall amount and intensity (e.g., *Laird and Harvey*, 1986; *Moody and Martin*, 2001a).

As vegetation returns during the post-fire recovery period, infiltration and erosion rates trend back to pre-fire conditions (e.g., *Benavides-Solorio and MacDonald*, 2005; *Larsen et al.*, 2009; *Moody and Martin*, 2001a; *Morris and Moses*, 1987) and the expanded channel network rapidly contracts back to its pre-fire extent (*Wohl and Scott*, 2017). In contrast, downstream sediment deposits can persist for tens to possibly thousands of years (e.g., *Cotrufo et al.*, 2016; *Elliott and Parker*, 2001; *Legleiter et al.*, 2003; *Meyer et al.*, 1992, 1995; *Moody and Martin*, 2001a). The contribution of sediment due to fires compared to long-term sediment yields has been shown to be around 30-50% (*Meyer et al.*, 1995; *Roering and Gerber*, 2005), although this varies drastically depending on the environment (*Swanson*, 1981). Much of our understanding of wildfire effects on hydrologic and geomorphic processes is based on studies conducted at the plot to hillslope scales, so there remains a need to quantify and better understand fire effects at larger scales (*Moody et al.*, 2013). This limitation inhibits my ability to accurately predict watershed-scale sediment yields and geomorphic changes, which are critical for protecting downstream landowners, water users, and aquatic resources.

In burned and unburned watersheds downstream changes are dictated by inputs of water and sediment (*Poff et al.*, 1997; *Wohl et al.*, 2015), and we have much more information on the geomorphic effects of floods at increasing spatial scales (e.g., *de Vente et al.*, 2007; *Fryirs*, 2013; *Walling*, 1983) than wildfire effects at increasing spatial scales (e.g., *Moody et al.*, 2013). While some floods may do very little geomorphic work (e.g., *Costa and O'Connor*, 1995; *Kochel*, 1988; *Magilligan et al.*, 1998), extreme floods typically generate very large increases in sediment yield (e.g., *Erskine and Saynor*, 1996) and cause significant geomorphic changes through erosion and deposition (e.g., *Baker*, 1977; *Friedman and Lee*, 2002; *Krapesch et al.*, 2011; *Magilligan et al.*,

2015; *Miller*, 1990b; *Nanson*, 1986; *Schumm and Lichty*, 1963). Currently, there are much fewer studies of extreme watershed-scale floods following wildfire (e.g., *Doehring*, 1968; *Hamilton et al.*, 1954), and I only know of two studies that document the geomorphic effects of long-duration extreme floods after wildfire (Chapter 2; *Kampf et al.*, 2016). While both long-duration floods and wildfire-induced runoff can cause significant geomorphic changes at the watershed scale, we rarely have had the opportunity to directly compare these two types of floods to determine which has a greater impact on downstream channels and valley bottoms.

In this study I quantify the geomorphic response of the channel networks in two watersheds that experienced a severe wildfire in June 2012 followed fifteen months later by an extreme long-duration flood. The two watersheds pose an interesting contrast, as shortly after burning, part of one watershed was subjected to a particularly intense summer thunderstorm, and this caused much more extensive deposition than in my other study watershed (Chapter 2). In September 2013 both watersheds were subjected to an extreme, long-duration storm that caused sustained high flows (referred to in this paper as the 'mesoscale flood'; *Gochis et al.*, 2014), and there was a marked difference in the geomorphic response of the two watersheds to this flood. Intriguingly, the watershed with a lesser response had been subjected to an extreme flood almost 40 years earlier.

The varying magnitudes and sequence of floods in my two study watersheds allowed us to assess the relative sensitivity of each watershed to post-fire effects and a subsequent extreme rainstorm. Sensitivity, which has been defined as "the propensity of a system to respond to a minor external change" (*Schumm*, 1998, , p.78), varies across the landscape and over time depending on previous and present perturbations of the system (*Fryirs*, 2017; *Thomas*, 2001). High and moderate severity wildfires can greatly increase the sensitivity of a watershed to perturbations (*Swanson*, 1981), while floods can have a wide range of effects depending on their magnitude and duration, intrinsic and extrinsic thresholds of the channel, availability of sediment, and the magnitude and timing and of previous floods (e.g., *Baker and Costa*, 1987; *Brierley*, 2010; *Costa and O'Connor*, 1995; *Newson*, 1980; *Schumm*, 1973; *Wolman and Miller*, 1960).

My initial objective was to evaluate post-fire changes in erosion and deposition over time in the lower portions of the two study watersheds, and use this to help predict post-fire sediment storage and delivery. The large mesoscale flood altered the expected trajectory of post-fire channel changes, so my study objectives expanded from monitoring post-fire channel changes to: 1) quantifying over time the channel response to the fire and the mesoscale flood in two watersheds across scales ranging from ~1 to 15 km^2; 2) documenting how watershed history and the varying post-fire responses in the two watersheds affected the observed sequence of channel changes; and 3) developing a conceptual model to describe potential channel and valley bottom response to both fires and large floods. The results should help resource managers better predict the likely geomorphic changes from fires and floods at scales up to 10-20 km^2, and use this to help assess post-fire risks and management strategies.

3.2 Background and study area

Following the 2012 High Park Fire (HPF) I initiated channel monitoring in two ~15 km^2 watersheds, Skin Gulch (SG) and Hill Gulch (HG) (Figure 3.1). A control watershed was not chosen due to limitations of personnel and funding. Both watersheds drain north into the Cache la Poudre River, which is the primary water supply for Fort Collins and other communities. Prior to burning, the main channels in SG and HG were ~1 m wide with ephemeral to intermittent flow. Elevations in SG range from 1840 to 2680 m, while elevations in HG are slightly lower at 1720 to 2400 m. Mean slopes, drainage densities, and elongation ratios are very similar between SG and HG, which are 23% and 24%, 2.5 km km^{-2} and 2.3 km km^{-2}, and 0.53 and 0.44, respectively. SG is underlain by knotted mica schist, amphibolite, and pegmatite with a large shear zone through the northwestern edge of the watershed (*Abbott*, 1970, 1976), while HG is underlain primarily by knotted mica schist (*Braddock et al.*, 1988). Soils are primarily Redfeather sandy loams with more frequent rock outcrops in HG than SG (*Soil Survey Staff*, 2018).

Mean annual precipitation is 450-550 mm (PRISM Climate Group, Oregon State University, http://prism.oregonstate.edu), with thunderstorms predominating during the spring and summer

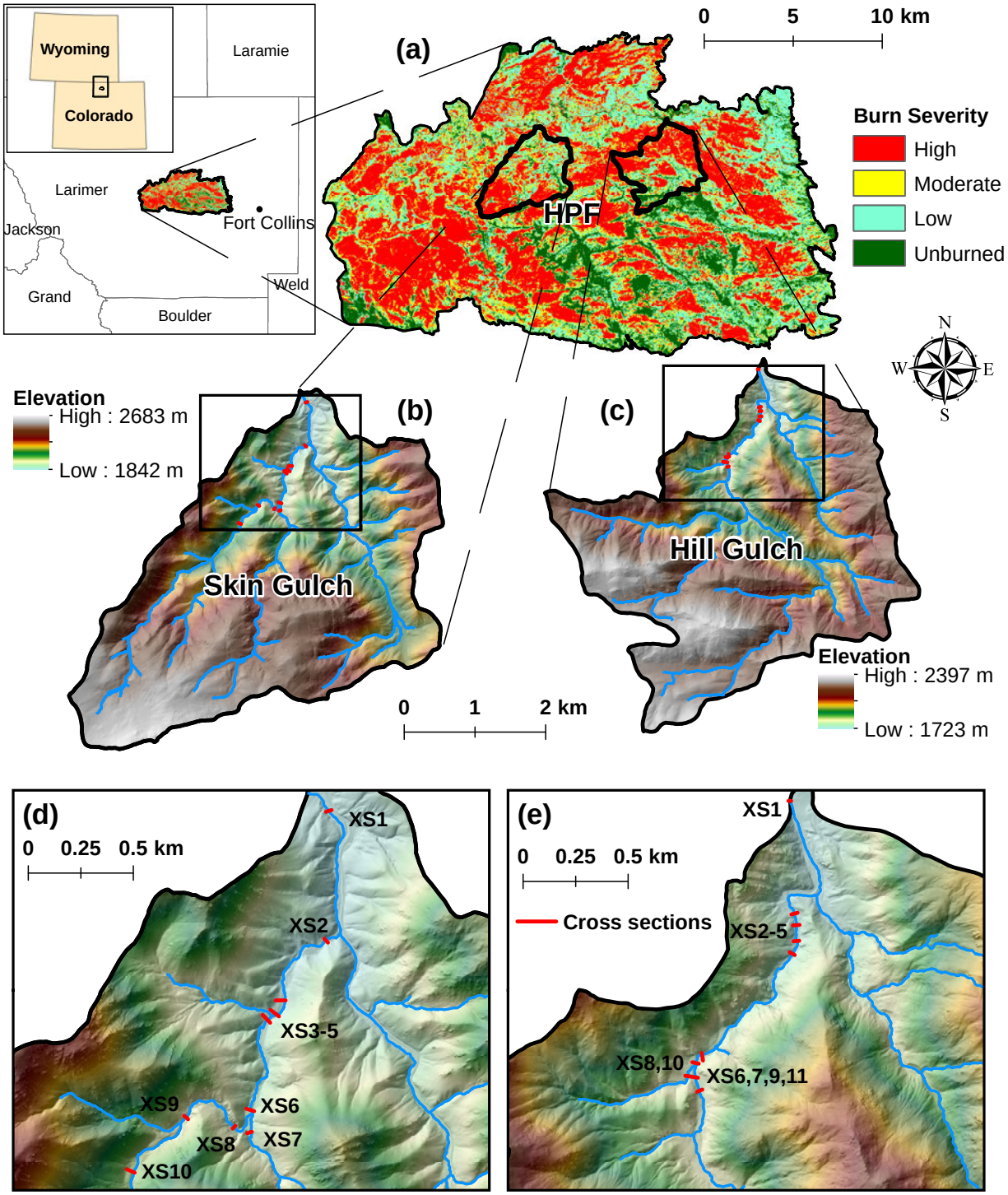

Figure 3.1: (a) Location and burn severity of the High Park Fire (HPF) in the Colorado Front Range of the western U.S.A. Elevation maps of (b) Skin Gulch and (c) Hill Gulch. Black boxes in (b) and (c) indicate the areas that include the ten and eleven cross sections shown in (d) Skin Gulch and (e) Hill Gulch, respectively.

and frontal storms during the fall. Winter precipitation falls primarily as snow. Prior to burning the vegetation in both watersheds was dominated by ponderosa pine with some lodgepole pine at higher elevations and some relatively narrow bands of deciduous riparian trees and shrubs. About 65% of each watershed was burned at moderate to high severity. In SG the areas burned at moderate and high severity were located primarily in the upper watershed, while in HG most of the more severely burned areas were in the lower portions of the watershed (Figure 3.1a). Following the fire both streams became perennial.

3.3 Methods

3.3.1 Data collection

My primary data are repeated field surveys of channel cross sections (XS) and corresponding longitudinal profiles (LP) in the lower portions of the two study watersheds. XSs and LPs were established between July 2012 and fall 2013, and monitoring continued until November 2016. Ten XSs were established in SG and eleven in HG (Figure 3.1). The XSs were established in reaches that I anticipated—based on local geomorphic characteristics such as slope, width, and confinement—would represent a range of geomorphic responses from primarily erosional to primarily depositional. Because sites were selected to focus on specific processes rather than as a random or systematic sample, the site-specific results cannot be extrapolated to long reaches or the entire watershed. Because the first large thunderstorm in SG occurred only one week after the fire, the only pre-storm data are one spatially limited survey of XS1 in SG.

Each XS was resurveyed from 15 to 25 times over the five-year study period, while the LPs were surveyed from 10 to 21 times. I refer to surveys by their collection date following the convention yyyymmdd (e.g., 20120912 and 20130506). Upstream, downstream, and cross-stream photos were also taken during site visits. Some of the initial surveys in summer 2012 used an autolevel and stadia rod, while a Leica TCR407 total station was used in fall 2012. Starting in spring 2013 a TOPCON GR-5 real-time kinematic Global Navigation Satellite System (RTK-GNSS) was typically used to survey topography from monumented benchmarks in each watershed, but an autolevel

and stadia rod were occasionally used in summer 2013. Autolevel and total station surveys were rotated and translated to match RTK-GNSS coordinates using local monumented benchmarks. Average horizontal and vertical root mean square error among the methods was estimated to be 6 mm and 10 mm, respectively.

After the September 2013 mesoscale flood the elevations of 42 high water marks (HWMs) were surveyed in SG and 51 HG. The HWMs were identified primarily by matted down vegetation and deposits of fine debris. Uncertainty in the HWM elevations was estimated to be no more than 0.10 m, and this is similar to the uncertainties used in other indirect discharge analyses (e.g., *Brogan et al.*, 2017; *Moody*, 2016). Ultimately, 11 HWMs in SG and 32 in HG were used to calibrate a two-dimensional model for estimating peak flows as described below.

Pebble count data (*Wolman*, 1954) were collected in June/July 2013 and in February/March 2014 at each XS, and these bracketed the mesoscale flood (the second sample was not possible at XS1 in SG due to post-flood excavation). The pebble counts were conducted across the channel as designated by the edge of vegetation or across flood deposits. From 97-280 particles were measured in each case (mean = 139). At XS8 in HG the deposited sediment was too fine to measure with a standard pebble count, so a 4-L grab sample was collected, air dried, sieved in 1/2-phi increments, and weighed.

Airborne laser scanning (ALS) surveys were collected by the National Ecological Observatory network (NEON) Airborne Observation Platform in July 2013, and jointly by the U.S. Geological Survey (USGS) and the Federal Emergency Management Agency in October 2013. I used 1-m resolution bare-earth digital elevation models (DEM) from these two surveys to develop the two-dimensional model for estimating peak flows from the 2013 mesoscale flood in each watershed.

Conditions in HG prior to and after the 1976 flood from the outlet to about 1 km upstream were determined from historic aerial imagery, along with photographs and an interview with a long-time homeowner. I created precipitation isohyets for this storm from data provided to us by MetStat Inc. The landowner's observations and photos, when combined with my measurements,

are the basis for comparing the channel and floodplain changes from the 1976 flood in HG to the observed changes after the 2012 HPF and 2013 mesoscale flood, respectively.

3.3.2 Data analysis

Contributing area for each cross section was computed in GIS using the October 2013 1-m DEM. Valley widths at each cross section were estimated based on 2-m contours created from the 1-m DEM, aerial imagery, and field knowledge.

Each XS and LP in the two watersheds were surveyed 16-25 and 10-17 times during the course of the study, respectively. These data varied in plan view (XY space) due to geomorphic changes and the exact placement of the survey rod; therefore, the accuracy of the calculated changes for each XS was maximized by normalizing all of the XY data onto a single line. This was done by plotting all the X and Y points from all surveys for a given XS, developing a linear regression to define the best estimate location of the XS, and orthogonally projecting each survey point onto the linearly regressed XS. This approach eliminates any deviations of channel changes that can result from summing the point-to-point cross stream distancesor surveys that deviated from the monumented cross section.

An active channel width was defined for each XS based on the maximum extent of channel changes over the period of surveys and field observations. Elevation differences between different cross section surveys were computed by interpolating elevations every centimeter across the active channel for each XS and then computing the elevation differences at these one-centimeter intervals. Trapezoids were calculated for the profiles of elevation differences between each successive survey and summed to compute positive area (total deposition), negative area (total erosion), net change, and total absolute change. Mean change in elevation of the active channel due to the mesoscale flood was computed by the mean elevation difference between the last pre-flood and first post-flood surveys. The change in thalweg elevation for each XS due to the mesoscale flood was calculated as the difference in the minimum elevation between the last pre-flood and first post-flood surveys.

The mean absolute elevation difference (MAED; i.e., the mean of the absolute values of the elevation differences every centimeter across the active channel width) was computed for each successive XS survey, and this is defined as the variability in surveys. The median MAED for all consecutive XSs and LPs for pre- and post-mesoscale flood were used to summarize the variability. Because the channel bed was primarily composed of gravels and cobbles, there was some inherent variability in the surveys based on the placement of the survey rod relative to these grains. Hence I compared the MAED to one half of the local D_{84} grain size (i.e., the diameter coarser than 84% of the sediment distribution), and this helped us evaluate whether the computed geomorphic changes were larger than the inherent grain-scale variability in the topographic survey data.

The mean length of the longitudinal profiles was 120 m with a range of 74 to 244 m. Similar to the cross sections, the longitudinal profiles were projected onto a hand-delineated polyline that best represented the average centerline over time. At some of my sites two to four XSs were close enough to be included in a single LP. For these LPs the origin for the centerline started downstream of the lowest XS (e.g., XS3 of XS3-5 in SG, and XS2 of XS2-5 in HG). Projecting the LP data onto a common channel centerline ensured that elevations from successive LP surveys could be plotted against each other to compute LP elevation changes similarly to the XSs. Local slopes for each XS were estimated using a linear regression (*Scott et al.*, 2016) for roughly 50-m long segments of the LPs clipped around each XS. Most of the LP segments were centered on the XSs, but if tributary confluences were nearby the LP was asymmetrical to avoid any slope breaks due to the confluence. Mean change in elevation due to the mesoscale flood was computed by taking the mean elevation difference between the last pre-flood and first post-flood LP surveys. MAED was also computed for each LP for each successive survey.

The NEON DEM from July 2013 required translation in order to register with the USGS DEM and my field data. Using my own Python script I calculated differences in slopes and aspects between the NEON DEM and the USGS DEM (following the methodology from *Nuth and Kääb*, 2011), and these were used to estimate the required XYZ translation to best match the NEON DEM to the USGS DEM. This process was performed iteratively until translation changes in X, Y, and Z

were less than 1 cm, or the required shift for that iteration was less than 2% of the overall required shift. Vertical comparison of the DEMs with RTK-GNSS measurements indicated a mean absolute elevation difference of 16 cm and 9 cm for the NEON ALS and USGS ALS, respectively.

Peak flows during the mesoscale flood were estimated using Nays2D, following the procedure described in Chapter 2. Nays2D is a two-dimensional hydrodynamic model distributed with the International River Interface Cooperative (iRIC; http:// http://i-ric.org; *Nelson et al.*, 2016), which computes water surface elevations and depth-averaged velocities by solving the 2D depth-averaged equations of fluid continuity and momentum. Peak flows were estimated for both the pre-flood and post-flood topography by minimizing the mean absolute error (MAE) between the elevation of the surveyed HWMs and the modeled water surface elevations (see Chapter 2 for further details on this approach).

3.4 Results

Contributing drainage areas for the different cross sections ranged from 2.8 to 15.4 km^2 in SG and 0.4 to 14.4 km^2 in HG (Table 3.1). Valley widths varied from 13 to 55 m in SG and 16 to 110 m in HG. XS1 in HG lies within a 15 m armored channel of a wide alluvial fan, which explains its much wider width. In HG two pairs of XSs (XS7 and XS8, and XS9 and XS10) were surveyed as one long transect as these were just upstream from a confluence; hence these pairs each have the same valley width (Table 3.1). Channel slopes indicate the majority of my sites are classified primarily as step-pool or cascade (*Montgomery and Buffington*, 1997), with a range of 0.04 to 0.10 m/m in SG (Table 3.2) and 0.01 to 0.07 m/m in HG (Table 3.3). Plots of valley width, channel width and channel slope versus drainage area generally show considerable scatter around a linear regression (Figures C.1–C.3), indicating that I was successful in selecting sites with a range of topographic characteristics.

Changes in XSs and LPs show three distinct periods and differing magnitudes of post-fire geomorphic changes: 1) initial post-fire response; 2) changes due to the mesoscale flood; and 3) post-mesoscale flood changes due to both limited post-fire effects and post-flood adjustments

(Tables 3.2 and 3.3). Cross section and longitudinal profile changes from two locations in SG (Figures 3.2 and 3.3) and HG (Figures 3.4 and 3.5) are representative (plots for the other XSs and LPs are in Figures C.4–C.24) in showing the varying responses to spring snowmelt and summer thunderstorms during the pre-mesoscale time period, major channel and valley bottom erosion stemming from the 2013 mesoscale flood, and the varied but much smaller changes over the three years following the mesoscale flood. The following sections provide a more detailed explanation of these changes over storms, seasons, years, and locations within the watersheds.

Table 3.1: Cross section (XS) contributing areas and valley widths for Skin Gulch and Hill Gulch. *cross section 1 in HG lies in a wide aluvial fan, although the channel is relatively confined by vegetation and riprap. † and ‡ each denote a pair of cross sections that were surveyed along the same transect and share the same valley width.

XS	Skin Gulch		Hill Gulch	
	Area (km^2)	Valley width (m)	Area (km^2)	Valley width (m)
1	15.4	40	14.4	110*
2	9.0	22	11.2	16
3	8.8	44	11.1	25
4	8.8	55	11.1	23
5	8.3	38	11.1	21
6	8.1	40	10.7	36
7	2.8	21	10.2	49†
8	5.2	13	0.4	49†
9	5.1	26	10.2	68‡
10	4.6	38	0.4	68‡
11	n/a	n/a	10.2	33

Table 3.2: Geomorphic changes pre- and post-mesoscale flood for the cross sections (XS) and longitudinal profiles (LP) in Skin Gulch, including: mean change in elevation, change in thalweg elevation, approximate width of flood impact, median Mean Absolute Elevation Difference (MAED) for pre- and post-mesoscale flood XSs, mean slope pre- and post-mesoscale flood, mean change in LP elevations, and median MAED for LPs. Units are meters (m) except the mean slopes are in m m^{-1}.

XS	Cross sections					Longitudinal profiles					Key observations	
	Mean change in elevation pre- to post-mesoscale flood	Change in thalweg elevation from flood	Approximate width of flood impact	Median MAED		Pre-flood mean slope (s.d.)	Post-flood mean slope (s.d.)	Mean change in elevation pre- to post-mesoscale flood	Median MAED		Cross sections	Longitudinal profiles
				Pre-mesoscale flood	Post-mesoscale flood				Pre-mesoscale flood	Post-mesoscale flood		
1	0.79	0.72	31	0.05	0.06	4.1 (0.1)	4.2 (0.1)	0.95	0.18	0.06	Substantial deposition due to the mesoscale flood, but then altered with heavy machinery	Substantial deposition due to the mesoscale flood, but then altered with heavy machinery
2	-0.11	-0.10	17	0.08	0.04	3.9 (0.5)	6.3 (0.1)	-0.04	0.20	0.04	Frequent but minor changes	Headward knickpoint migration led to an increase in slope
3	-0.04	-1.16	14	0.17	0.06	6.6 (0.3)	7.3 (0.1)	-0.91	0.13	0.05	Channel shifted and incised down to bedrock	Uniform drop in bed elevation
4	-0.43	0.32	30	0.07	0.06	6.4 (0.3)	7.2 (0.1)	-0.02	0.13	0.05	Substantial channel widening with floodplain erosion and a slight increase in thalweg elevation	Slight increase in slope
5	-0.42	-0.37	20	0.06	0.05	6.4 (0.4)	4.8 (0.0)	-0.25	0.10	0.04	Channel shifted and incised with slight widening	Drop in bed elevation with slight decrease in slope
6	-0.38	-1.23	19	0.10	0.04	7.6 (0.5)	6.6 (0.1)	-0.62	0.28	0.05	Channel narrowed and incised	Drop in bed elevation with slight decrease in slope
7	-0.23	-0.48	4	0.05	0.04	10.4 (0.1)	8.2 (0.4)	-0.63	0.05	0.05	Channel widened and incised	Downstream end of profile remained fixed while the rest of the bed elevation decreased, leading to a decrease in slope
8	-0.85	-1.56	9	0.12	0.05	9.3 (0.7)	8.8 (0.4)	-0.81	0.22	0.05	Channel incised down to bedrock	Downstream and upstream end of profile remained fixed while the rest of the bed incised to bedrock
9	-0.33	-0.33	11	0.08	0.06	7.1 (0.4)	7.0 (0.2)	-0.53	0.17	0.05	Decrease in bed elevation	Uniform drop in bed elevation
10	-0.55	-1.14	8	0.07	0.07	8.1 (0.8)	9.2 (0.3)	-0.98	0.20	0.07	Slight channel shift and substantial incision	Uniform drop in bed elevation with a lot of exposed bedrock

Table 3.3: Geomorphic changes pre- and post-mesoscale flood for the cross sections (XS) and longitudinal profiles (LP) in Hill Gulch, including: mean change in elevation, change in thalweg elevation, approximate width of flood impact, median Mean Absolute Elevation Difference (MAED) for pre- and post-mesoscale flood XSs, mean slope pre- and post-mesoscale flood, mean change in LP elevations, and median MAED for LPs. Units are meters (m) except the mean slopes are in m m^{-1}.

XS	Cross sections					Longitudinal profiles					Key observations	
	Mean change in elevation pre- to post-mesoscale flood	Change in thalweg elevation from flood	Approximate width of flood impact	Median MAED		Pre-flood mean slope (s.d.)	Post-flood mean slope (s.d.)	Mean change in elevation pre- to post-mesoscale flood	Median MAED		Cross sections	Longitudinal profiles
				Pre-mesoscale flood	Post-mesoscale flood				Pre-mesoscale flood	Post-mesoscale flood		
1	0.32	0.38	5	0.04	0.04	1.1 (0.2)	1.9 (0.4)	0.62	0.05	0.05	Deposition led to an increase in thalweg elevation	Rise in bed elevation with slight increase in slope
2	0.03	0.04	5	0.07	0.04	5.1 (0.1)	4.2 (0.1)	0.11	0.12	0.04	No real change	Slight decrease in slope
3	0.02	0.12	7	0.06	0.05	3.7 (0.1)	4.2 (0.1)	0.00	0.08	0.04	No real change	No real change
4	-0.16	-0.06	8	0.07	0.05	3.3 (0.2)	3.3 (0.1)	-0.06	0.08	0.04	Slight widening of channel	No real change
5	-0.10	0.01	13	0.09	0.06	2.7 (0.2)	3.7 (0.1)	-0.21	0.11	0.04	Erosion on right bank offset by deposition on left bank	Increase in slope due to downstream incision
6	-0.04	-0.01	5	0.07	0.04	5.4 (0.2)	5.6 (0.1)	-0.15	0.07	0.04	No real change	No real change
7	-0.05	-0.13	4	0.07	0.06	5.2 (0.1)	4.2 (0.0)	-0.22	0.12	0.03	Minor channel incision	Decrease in slope due to upstream incision
8	-0.01	-0.10	6	0.08	0.03	7.1 (0.5)	7.4 (0.2)	-0.33	0.11	0.04	Ephemeral channel incised	Uniform drop in bed elevation
9	-0.06	-0.05	4	0.08	0.05	2.9 (0.1)	3.7 (0.1)	-0.09	0.07	0.03	No real change	Almost 1 m of incision at downstream end, otherwise no real change
10	-0.08	0.04	3	0.10	0.05	6.9 (0.2)	7.2 (0.1)	-0.15	0.07	0.03	No real change	No real change
11	-0.04	-0.15	6	0.06	0.03	3.4 (0.0)	3.1 (0.1)	-0.08	0.06	0.03	No real change	No real change

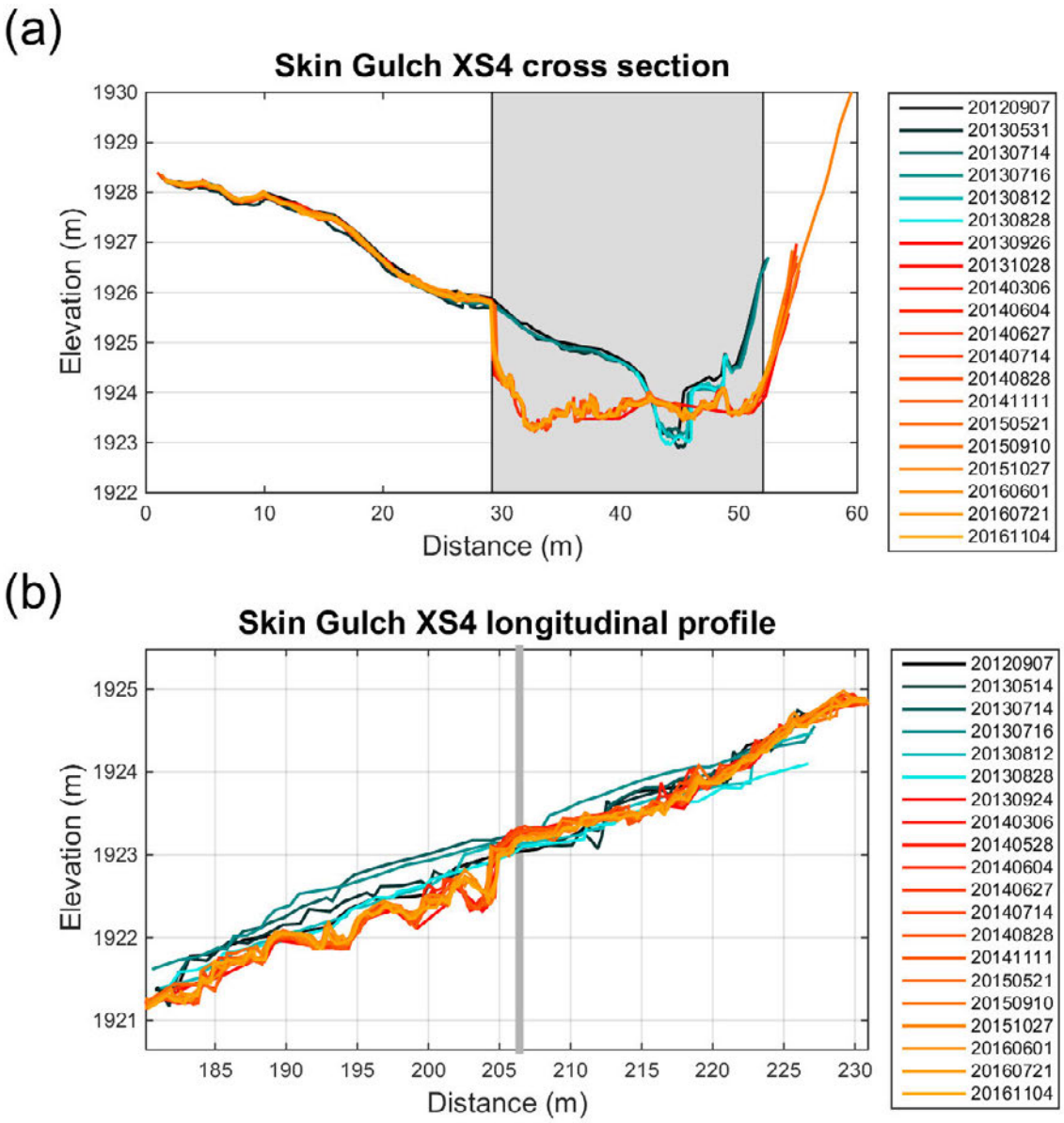

Figure 3.2: Plots over the entire monitoring period of (a) cross section (XS) four in Skin Gulch and (b) the corresponding longitudinal profile. Gray shaded box in (a) delineates the active channel and the vertical line in (b) shows the location of the cross section.

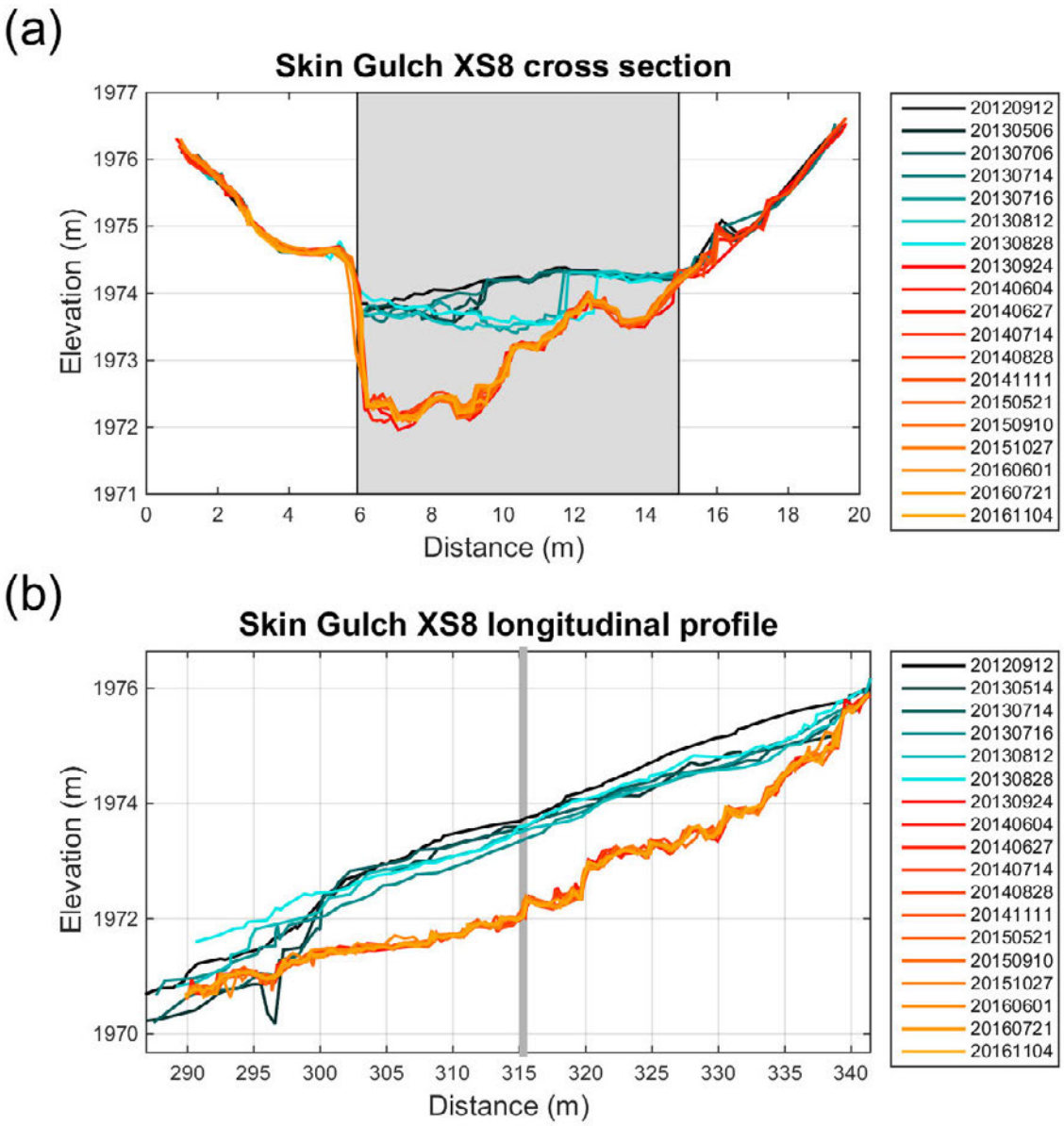

Figure 3.3: Plots over the entire monitoring period of (a) cross section (XS) eight in Skin Gulch and (b) the corresponding longitudinal profile. Gray shaded box in (a) delineates the active channel and the vertical line in (b) shows the location of the cross section.

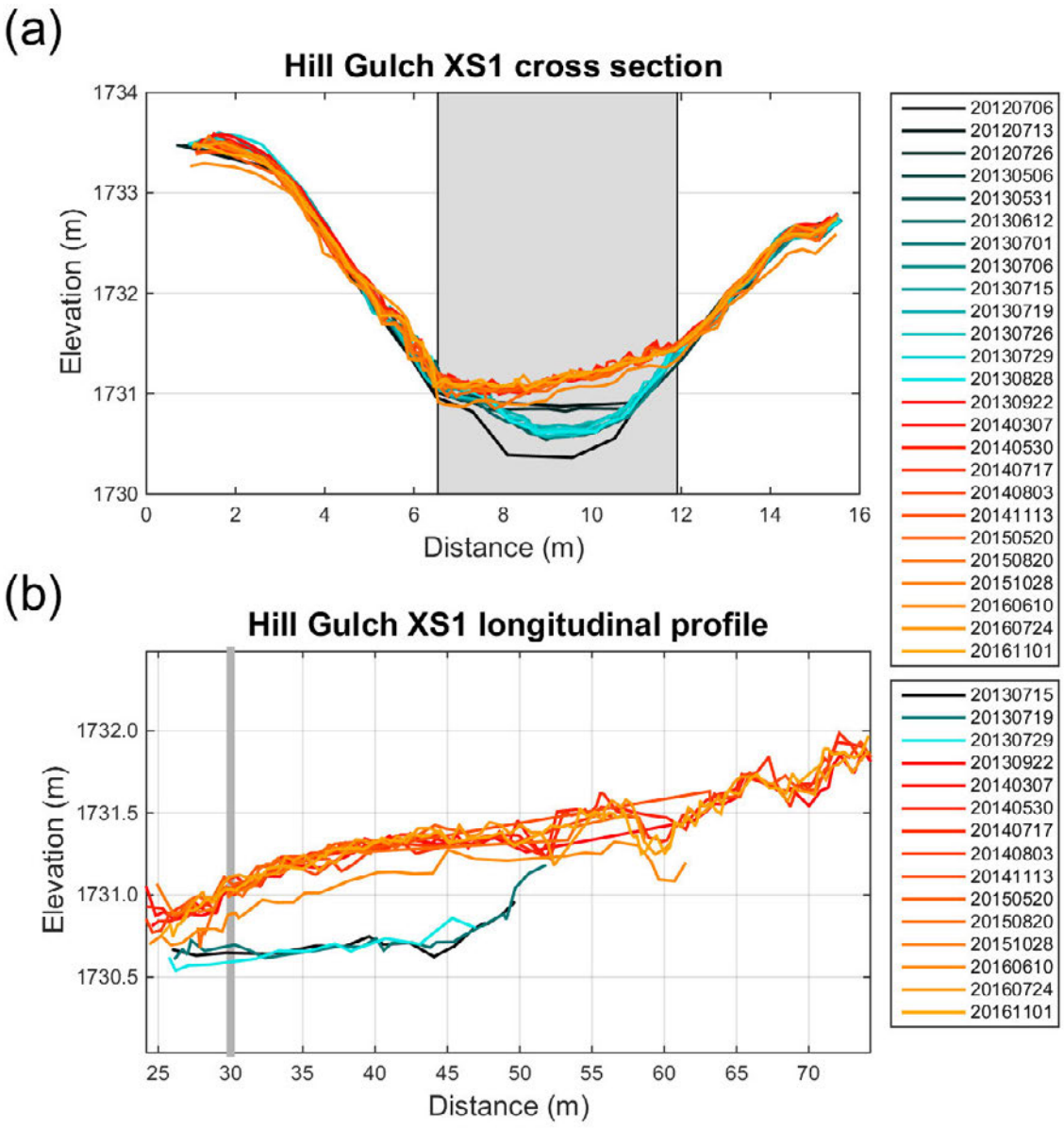

Figure 3.4: Plots over the entire monitoring period of (a) cross section (XS) one in Hill Gulch and (b) the corresponding longitudinal profile. Gray shaded box in (a) delineates the active channel and the vertical line in (b) shows the location of the cross section.

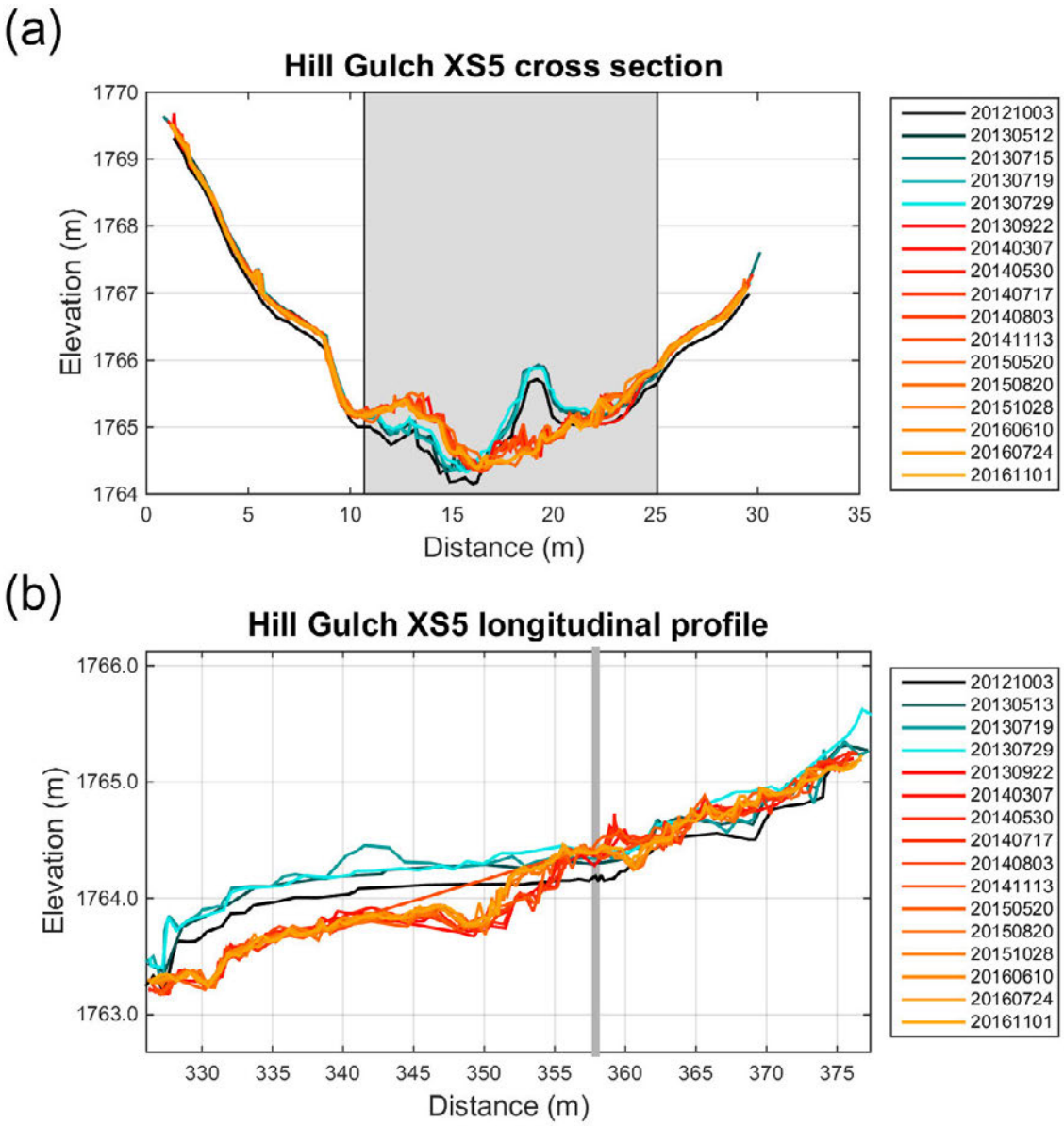

Figure 3.5: Plots over the entire monitoring period of (a) cross section (XS) 11 in Hill Gulch and (b) the corresponding longitudinal profile. Gray shaded box in (a) delineates the active channel and the vertical line in (b) represents the location of the cross section.

3.4.1 Pre-mesoscale flood

Summer 2012

Convective thunderstorms caused extensive hillslope erosion and downstream deposition in the first summer after the fire. Quantitative data are largely lacking other than at XS1 in each watershed, but these showed 0.5 m of aggradation at XS1 in HG and extensive aggradation well beyond the original survey of XS1 in SG (Figures 3.4, 3.6, and C.4). Much of the aggradation in HG was eroded by the next spring, as this was facilitated by local residents cutting and clearing streamside vegetation (Figure C.25).

More extensive visual observations at the hillslope and watershed scales provide a clearer picture of the geomorphic changes in each watershed. The greatest changes occurred just one week after the fire in SG as a result of an intense rainstorm in the upper watershed over an area of high burn severity. This caused an estimated peak flow of 20-46 $m^3\ s^{-1}\ km^{-2}$ and widespread downstream deposition, including 1-m imbricated boulders (Chapter 2). Subsequent thunderstorms caused smaller peak flows in both watersheds with additional sediment deposits and some reworking of previously deposited material. In most cases deposits were dominated by gravel, creating relatively flat cross sections (e.g., Figure 3.7). In SG these flat deposits were particularly evident at XSs 1, 2, 3, 6, 8, 9 and 10, and in some reaches the flow was entirely subsurface due to the large amounts of relatively coarse post-fire deposition. Deposition was also evident in HG, particularly at XSs 1, 7, 8 and 10, but photos and qualitative observations indicate that HG did not experience any storms, hillslope erosion, or downstream deposition comparable to the first storm in SG. The sediment deposits in HG were generally no coarser than gravel, indicating a lack of extreme runoff, while the large flood in SG just one week after the HPF caused extensive boulder- and cobble-sized deposits in some reaches (Figure 3.7a; see also Figure 2.2 in Chapter 2).

Winter 2012-2013

The summer deposits remained largely intact through the winter as the upper portions of both watersheds accumulated snow. Higher flows during spring snowmelt generated little or no hills-

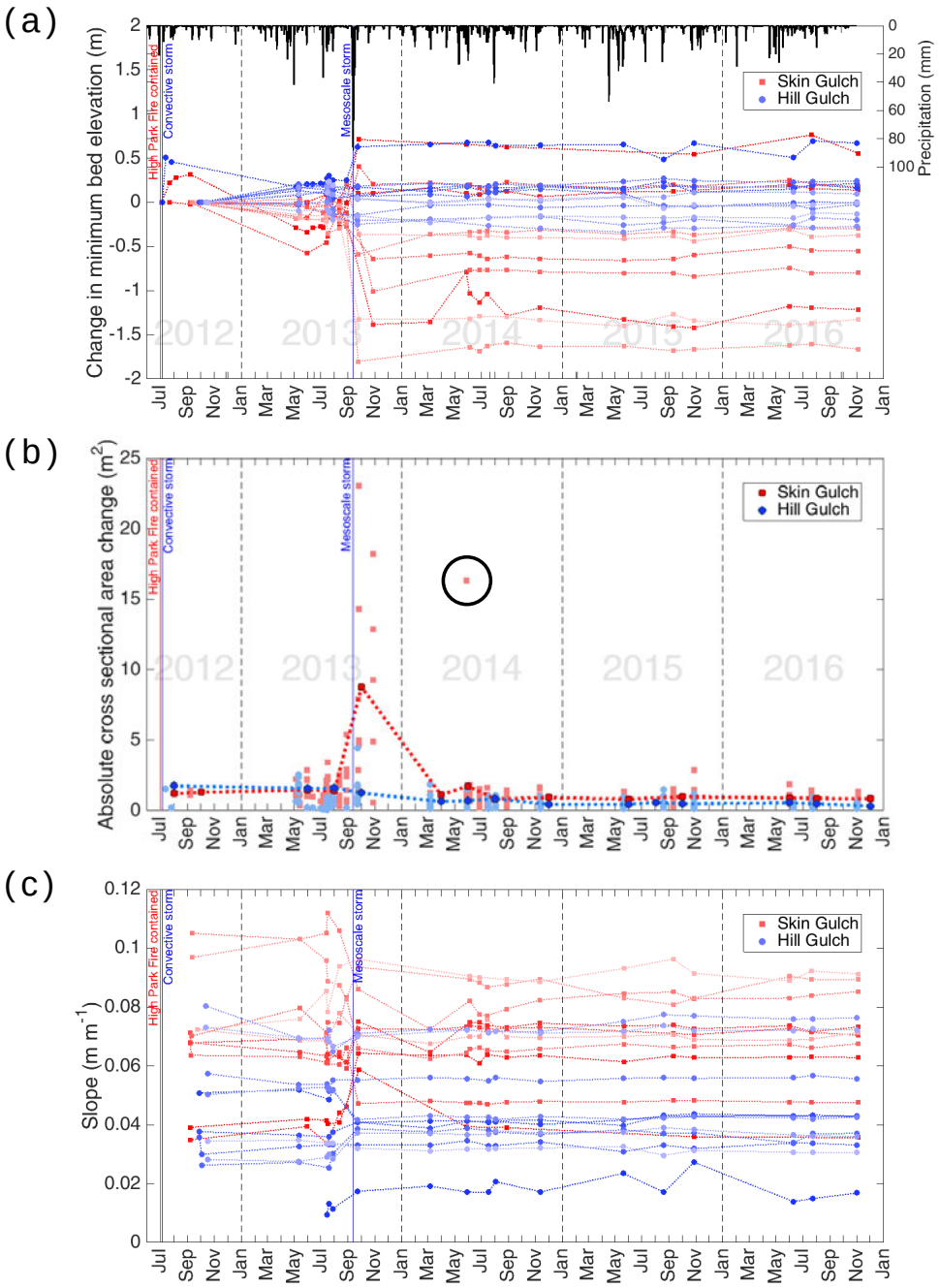

Figure 3.6: Time series for all 21 cross sections from July 2012 through November 2016 for SG (red) and HG (blue). Plots show (a) net change in minimum bed (thalweg) elevations and daily precipitation from a nearby weather station; (b) absolute cross sectional area change with heavy dotted lines showing the two-month moving average for each watershed; and (c) longitudinal slopes. The circled point in (b) represents a large-temporary pile of sediment that was left by excavation crews after the 2013 mesoscale flood [see Figure 10c in *Kampf et al.* (2016)] and subsequently removed.

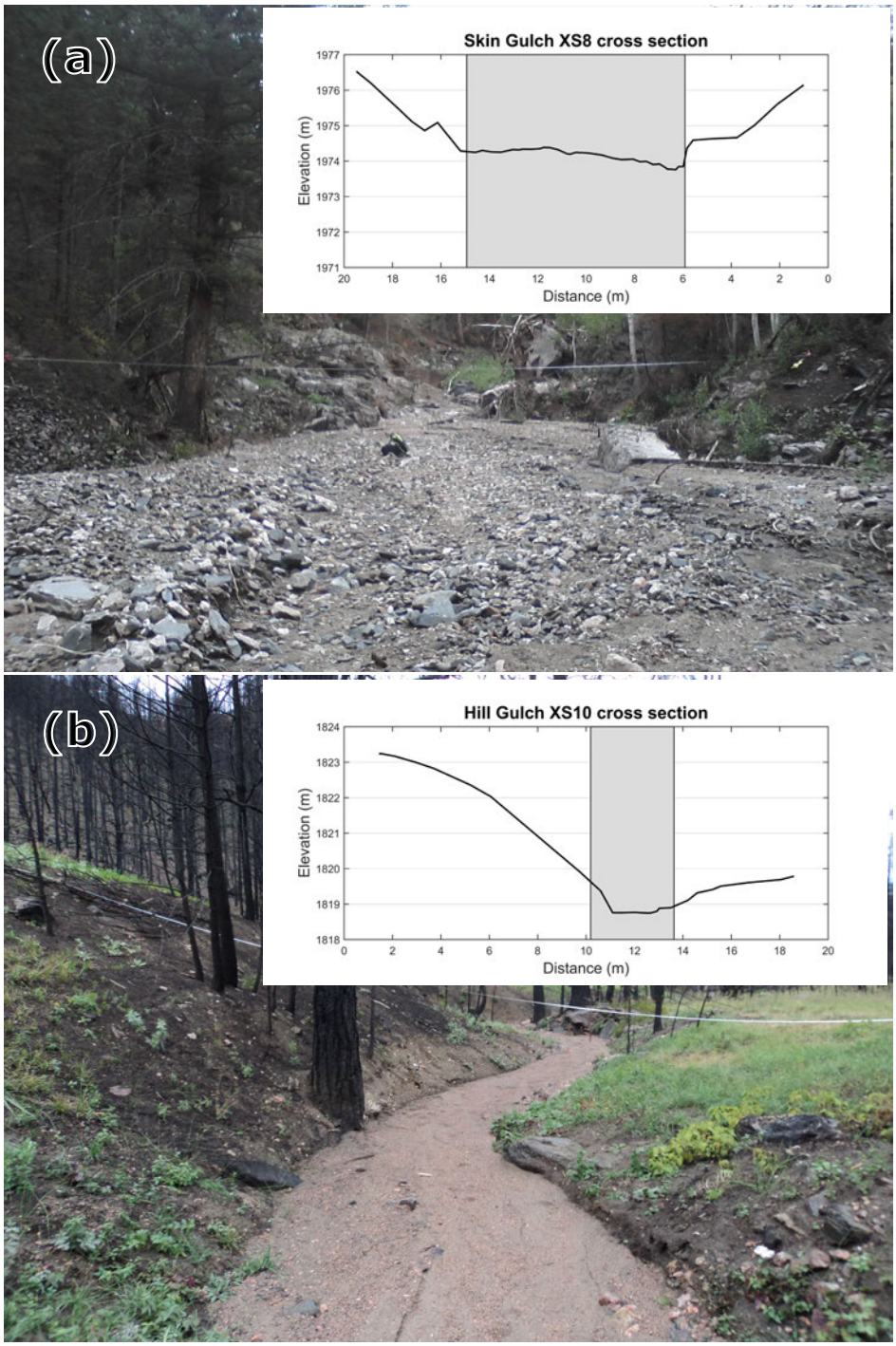

Figure 3.7: Summer thunderstorms caused sediment deposition in most of the downstream channels, resulting in flatter cross sections and smooth longitudinal profiles. (a) Photo of valley bottom filled with gravels and cobbles looking upstream at cross section eight in Skin Gulch on 12 September 2012; inset is a plot of the cross section. (b) Photo looking downstream at cross section ten in Hill Gulch on 12 October 2012 showing sand and gravel completely filling the channel; inset is a plot of the cross section.

lope erosion (*Schmeer*, 2014), while the downstream accumulation of flow was sufficient to cause varying amounts of channel incision through the post-fire deposits in SG (Figure 3.8) and HG (Figure 3.9). This incision was typically in a relatively narrow channel compared to the much wider sediment deposits. In some cases exposed roots indicated incision through the pre-fire streambed, as well as the post-fire deposits. Mean thalweg elevation change in SG between September 2012 and May 2013 was -19 cm (s.d. = 22 cm, Figure 3.6), with maximum measured incision of 60 cm at XS1 and maximum aggradation of only 3 cm at XS7. Mean thalweg elevation change in HG between fall 2012 and May 2013 was +5 cm (s.d. = 15 cm) (July 2012 to May 2013 for XS1), but my field observations indicate that this apparent increase was due to registration errors in the total station surveys in fall 2012. Maximum incision in HG was 29 cm at XS1 and maximum aggradation was 21 cm at XS5.

Summer 2013

In summer 2013 convective thunderstorms again caused extensive hillslope erosion (*Schmeer et al.*, 2018) and downstream deposition in both watersheds (Figures 3.2-3.6). These deposits filled pools and longitudinally smoothed the channel bed. In a few places the channel was dry as all the flow was subsurface through the post-fire sediment deposits. Baseflows between storms incised through the finer sediments, while subsequent stormflows reworked and sometimes added to the sediment deposits in the channels. Overall the trend of geomorphic changes in summer 2013 were similar to those of summer 2012, although changes in bed topography were qualitatively observed to be more frequent given the more frequent stormflows compared to the drier summer of 2012 (Figure 3.6a). Mean thalweg elevation change in SG was only +2 cm (s.d. = 14 cm), but maximum incision was 30 cm at XS1 and maximum aggradation was 41 cm at XS6. Mean thalweg elevation change in HG also was very small at -2 cm (s.d. = 9 cm), but the maximum incision was 37 cm at XS8 and the maximum aggradation was 22 cm at XS8.

Data from the entire pre-mesoscale flood period indicates the magnitude and variability of geomorphic changes were greater in SG than HG (Figure 3.6; Table 3.2). For example, the average change in cross-sectional area in SG prior to the pre-mesoscale flood was 1.38 m^2, which is nearly

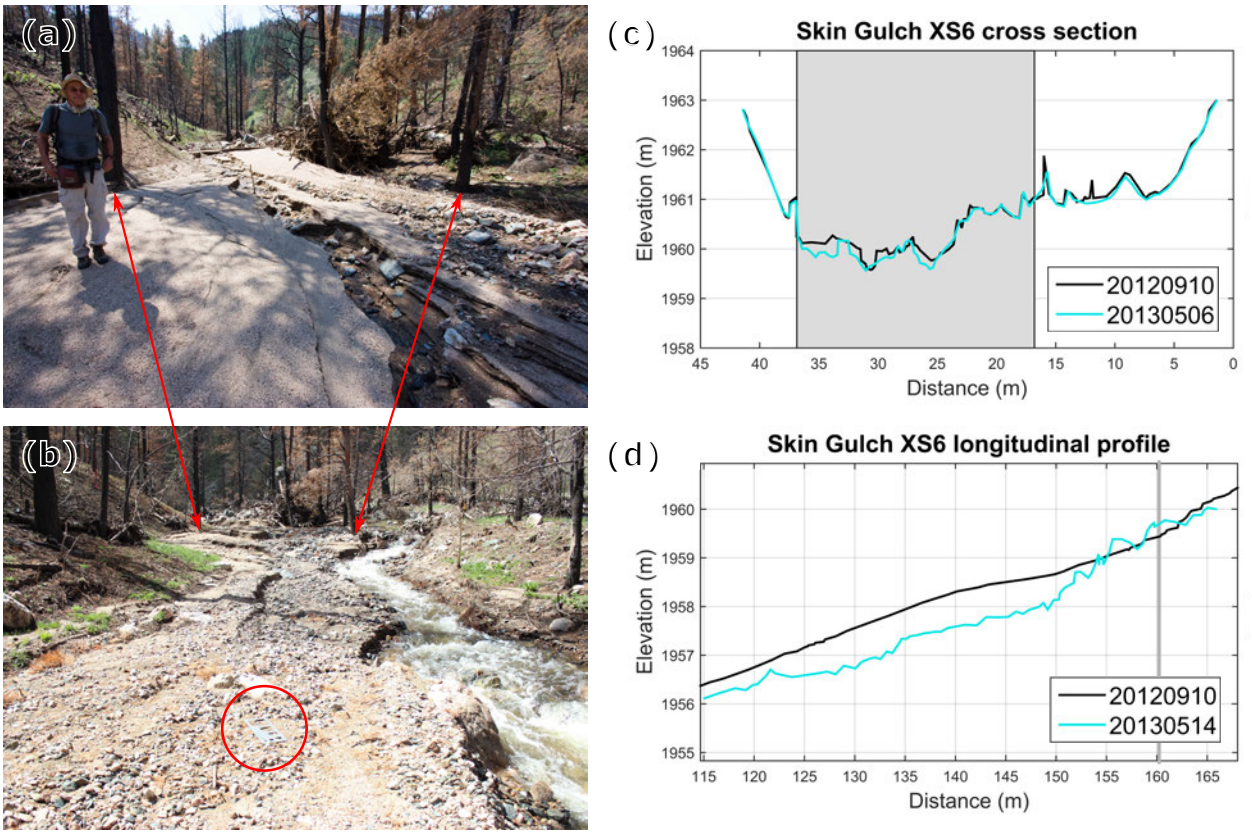

Figure 3.8: (a) Photo looking upstream from below cross section six in Skin Gulch on 8 March 2013 showing the extensive deposition from the summer thunderstorms. (b) Photo taken at the same location on 10 May 2013 showing the subsequent incision and floodplain coarsening during spring snowmelt; red circle indicates a gravelometer for scale. (c) are the cross sections and (d) are the longitudinal profiles in fall 2012 (black line) and spring 2013 (blue line). Gray shaded box in (a) delineates the active channel and the vertical line in (b) represents the location of the cross section. XS6 is in the foreground of the photo in (a) and in the far background of the photo in (b), and in (c) XS6 is plotted looking upstream to match the perspective of the two photos.

double the mean change of 0.71 m^2 in HG (Figure 3.6b). However, the pre-mesoscale flood Mean Absolute Elevation Differences (MAED) for the XSs were similar for both watersheds with a mean of 8 cm and a range of 4 to 17 cm (Tables 3.2 and 3.3; Figures 3.10a and 3.10c). The MAED results for the LPS were generally greater than the XSs, with values for LPs around 5-10 cm greater in SG than HG (Figures 3.10b and 3.10d). Most elevation changes were larger than the pre-mesoscale flood mean D_{84} of 6.8 cm in SG and 6.0 cm in HG (Figure 3.10).

Figure 3.9: (a) Looking upstream at cross section seven (left) and cross section eight (upper right; tributary channel filled with gravel) in Hill Gulch on 22 October 2012 showing deposition following the fire. (b) Looking upstream from near cross section 8 on 12 May 2013 showing the incision during spring snowmelt. The straw mulch in (b) blew into the channel from the adjacent hillside where it had been applied to reduce erosion.

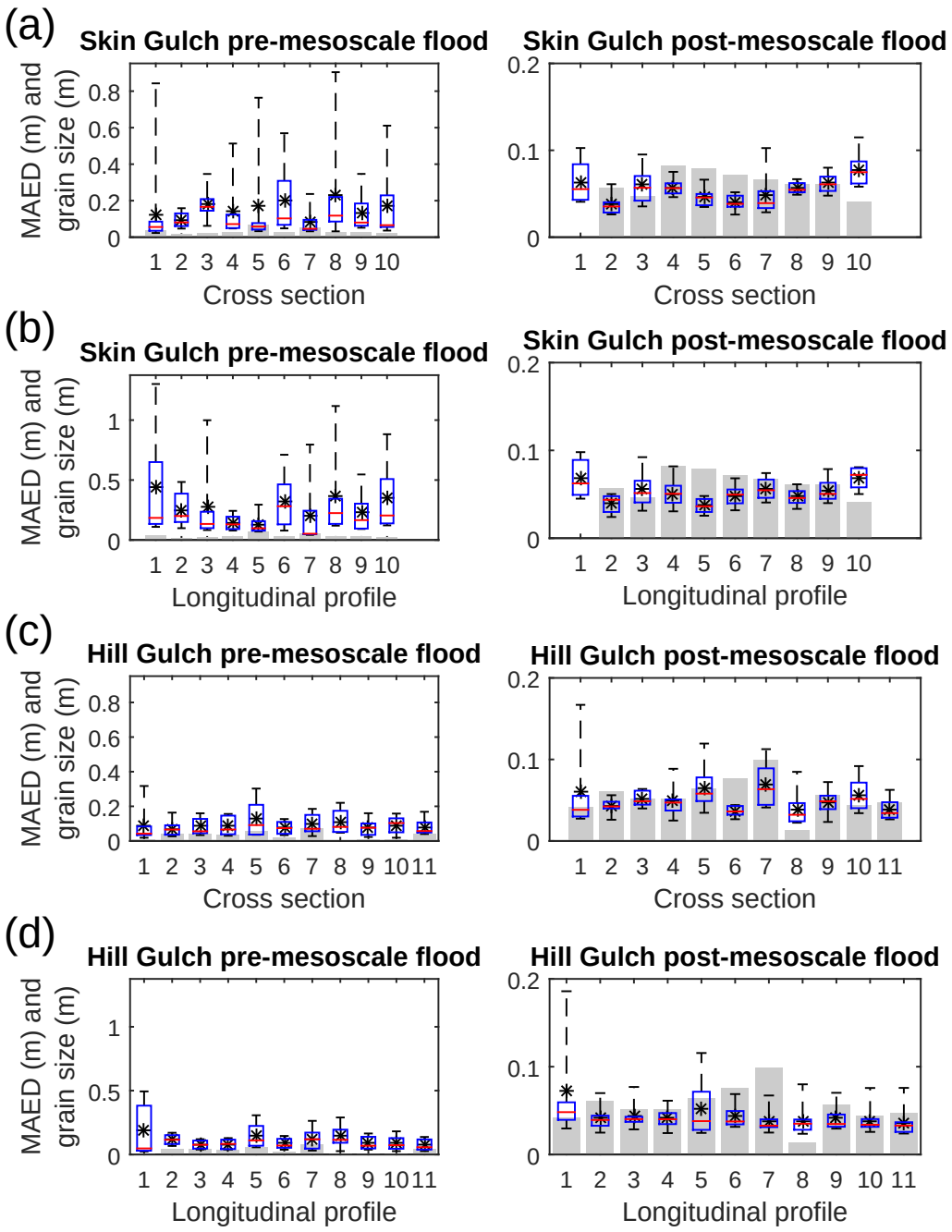

Figure 3.10: Paired boxplots of the maximum mean absolute elevation differences (MAED) for pre- and post-flood conditions for the cross sections (a, c) and longitudinal profiles (b, d) in Skin Gulch and Hill Gulch, respectively. Boxes represent the 25th and 75th percentiles, red line is the median, mean is indicated by an *, and the whiskers show the minimum and maximum values. The gray bars in each pair of plots show the local D_{84} grain size divided by two (i.e., the diameter coarser than 84% of the sediment distribution); no D_{84} could be collected at XS1 in SG after the mesoscale flood because of the extensive sediment removal and channel reconstruction. Median MAED results are provided in Table 3.2 and Table 3.3.

3.4.2 Mesoscale flood of September 2013

In September 2013, fifteen months after the HPF, a long-duration mesoscale storm hit the Colorado Front Range causing widespread flooding, erosion, and sedimentation (e.g., *Gochis et al.*, 2014; *Moody*, 2016; *Yochum*, 2015; *Yochum et al.*, 2017). Mean rainfall for this storm was 257 mm in SG and 283 mm in HG, with maximum 15-minute intensities of 33 mm h^{-1} in both watersheds (*Kampf et al.*, 2016). Sustained high flows from the mesoscale flood caused the largest channel and valley changes that I measured over the monitoring period in both watersheds (Figure 3.6; Table 3.2). Nearly all of the sediment that had been deposited after the HPF was eroded along with substantial amounts of the pre-existing floodplain deposits. The stripping of deposited sediment throughout the channel networks generally decreased the thalweg elevations and increased channel cross sectional areas (e.g., Figures 3.2-3.6, and 3.11-3.13; Tables 3.2 and Table 3.3).

The extensive channel erosion resulted in a considerable difference in the estimated peak flows from the 2D model depending on whether I used the pre- or post-flood topography. In SG my best estimate of the calculated peak flow using pre-flood topography was 2.3 m^3 s^{-1} km^{-2}, while the estimated peak flow using post-flood topography was more than twice this value at 5.7 m^3 s^{-1} km^{-2} (Chapter 2). In HG my best estimate of the peak flow using pre-flood topography was 0.9 m^3 s^{-1} km^{-2} and about 50% larger using post-flood topography or 1.4 m^3 s^{-1} km^{-2}. The estimated peak flows in HG were only 25-39% of the estimated peak flows in SG.

Channel and valley bottom changes were far greater in SG than in HG, which is consistent with the large difference in the estimated peak flows between the two watersheds. In SG there was a general trend of incision at XSs farther upstream where the valley widths were narrower (e.g., Figure 3.3), while channel widening was more common in the downstream XSs where the valleys were wider (e.g., Figure 3.2; Tables 3.1 and 3.2). An undersized culvert at Colorado Highway 14 near the outlet of SG caused substantial yet localized deposition upstream, including XS1 (Figure 10 in *Kampf et al.*, 2016). Much of this sediment was excavated before I was able to resurvey, so these data are excluded from the SG results. For the other nine XSs in SG the mean absolute change in cross-sectional area was 7.7 m^2 (Figure 3.6b), and in all cases there was net erosion.

The greatest absolute cross-sectional change was 18.2 m^2 at XS5 (Figure 3.11). This XS had experienced substantial overbank deposition from the 2012 convective flood and that sediment was removed by the 2013 flood (Figures 3.11a and 3.11b; Chapter 2). XS4, just downstream from XS5, had the next most pronounced channel change of 14.3 m^2 (Figure 3.2), and this was due in part to a shallow landslide that was presumably induced by lateral bank erosion (Figure 2.7b in Chapter 2). The mean change in elevation for the XSs in SG due to the mesoscale flood was 0.37 m, and the mean thalweg incision was 0.67 m (Figure 3.6a; Table 3.2). The greatest incision of nearly 1.6 m occurred at XS8 (Figure 3.3), and this cross section had the narrowest valley width of all my XSs of just 13 m (Table 3.1).

In HG there was not a general trend of incision at XSs farther upstream and channel widening in the downstream XSs that was apparent in SG (Table 3.3). This lack of a downstream trend in channel changes could partly be due to the selected locations for cross sections in HG do not have valley widths that increase in the downstream direction (Table 3.1). The mean absolute change in cross-sectional area due to the mesoscale flood in HG was 1.3 m^2, which is only 17% of the corresponding mean value for SG (Figure 3.6b). The largest change of 4.4 m^2 was at XS5 (Figure 3.12), and this can be attributed to the erosion of the tail end of a medial floodplain deposit. The upper eight XSs all incised, but the mean elevation change for these eight XSs was only -0.07 m or 18% of the mean elevation change for XS2-XS10 in SG (Table 3.2). The three lowest XSs in HG all had net deposition instead of net erosion, with XS1 having by far the greatest mean aggradation of 0.32 m and the greatest thalweg increase of 0.38 m (Table 3.2). This amount of deposition is consistent with its much lower slope of 1.1% compared to the 4-5% slope of the other two depositional XSs (Figure 3.13; Table 3.2).

Channel incision and widening during the mesoscale flood also led to knickpoint migration, which resulted in changes in the local bed slope around my XSs, especially in SG. For XS2-10 in SG the mean absolute change in slope was 1.2%, with a maximum increase of 2.4% at XS2 (Figure 3.6c; Table 3.2). Incision was limited by bedrock along portions of LP3, LP6, LP7, LP8, LP9, and LP10. Similar to the XSs, there was much less change in LP slopes in HG than in SG,

as the mean absolute change in LP slope in HG was only 0.5%, with a maximum increase of 1.0% at XS5 (Figures 3.6c and 3.12). Scour to bedrock was observed only along portions of LP7, LP9, and LP11 along with two pools in LP6. For both watersheds there was greater incision in the LPs with greater slopes, and the mean slope—using either pre- or post-flood values—explained just over 50% of the mean change in LP elevations (Table 3.2).

Sustained high flows and channel incision during the mesoscale flood caused substantial increases in the D_{84} at nearly all of the XSs (Figure 3.14). Prior to the mesoscale flood the mean D_{84} for the XSs in SG was 68 mm with a standard deviation of 31 mm. After the mesoscale flood the mean D_{84} in SG nearly doubled to 126 mm and the standard deviation dropped to 26 mm (Figure 3.14). This large increase in D_{84} and decrease in variability can be attributed to the removal of finer particles by the sustained high flows. In HG the mean D_{84} also nearly doubled from 60 mm to 110 mm (Figure 3.14), with a nearly eightfold increase at XS10 due to the loss of the relatively fine material deposited in summer 2012 (Figure 3.7b). In contrast to SG the standard deviation of the D^{84} values in HG only decreased from 45 mm to 41 mm. The large increase in D_{84} in HG can again be attributed to the removal of finer particles by the sustained high flows.

3.4.3 Post-mesoscale flood

In the three years after the mesoscale flood there were much smaller and less frequent changes to the channel XSs and LPs than in the first 15 months after burning (Figures 3.2-3.6, C.4 and C.24; Table 3.2). For the entire post-flood period from fall 2013 to summer 2016 the median MAED values for all XS and LP changes were typically only about 5 cm (Tables 3.2 and 3.3). In both watersheds the median post-flood MAED values were about 50% lower than the pre-flood values, and the range of decreases was from 10% to 82%. In only two XSs (SG XS1 and 10) and two LPs (SG LP7 and HG LP1) were the post-flood changes larger than the measured pre-flood changes, and the maximum increase in MAED was only 14% (Table 3.2). In only two cases were the median MAED values for the post-mesoscale flood period greater than the D_{84} (XS8 and LP8

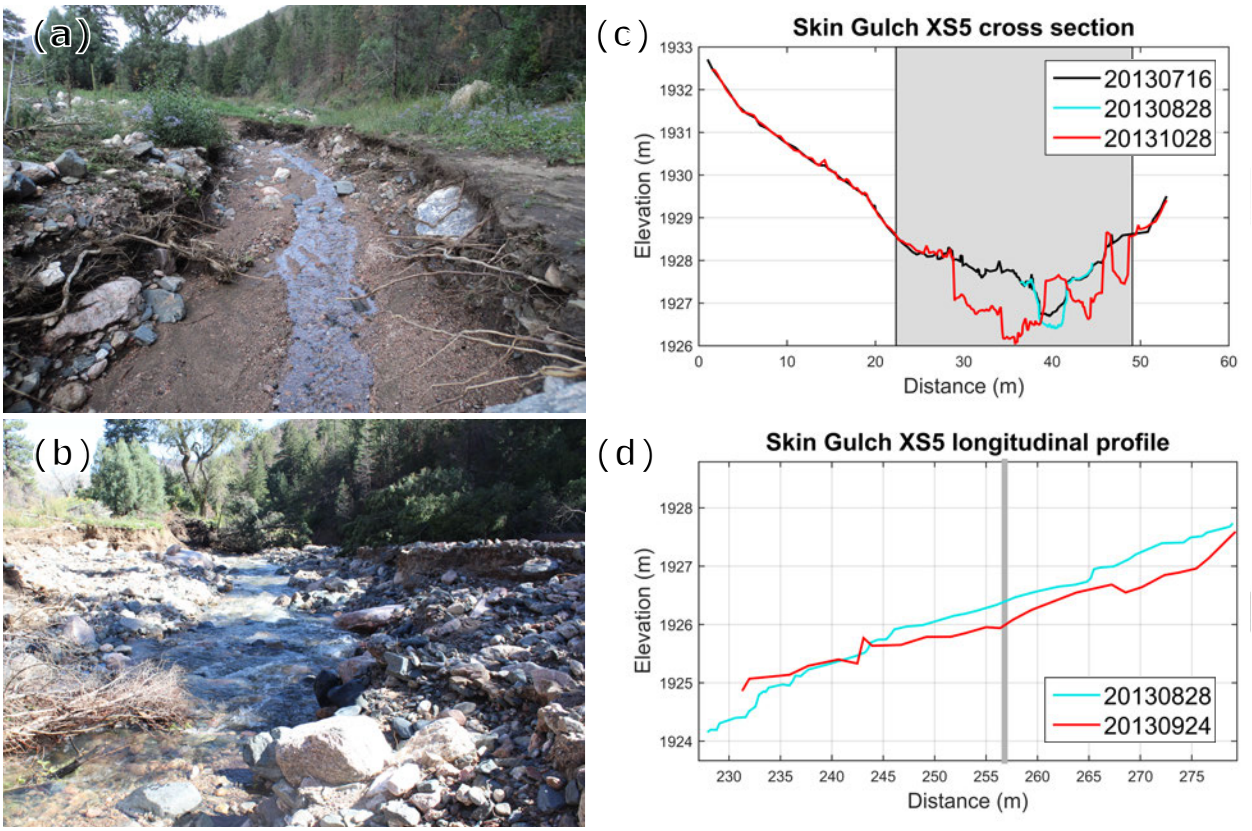

Figure 3.11: Photos looking downstream at cross section five in Skin Gulch on (a) 28 August 2013, and (b) 24 September 2013 showing the channel erosion caused by the mesoscale flood. Plots of the (c) cross section and (d) longitudinal profile prior to (blue line) and just after the mesoscale flood (red line). The 16 July 2013 XS (black line) in (c) is also shown because the XS surveyed on 28 August 2013 was limited to the main channel. Gray shaded box in (a) delineates the active channel and the vertical line in (b) represents the location of the cross section.

in HG; Figure 3.10), but the data and field observations did document some localized channel changes.

Qualitatively, field observations indicated that the first spring after the mesoscale flood had the highest spring runoff due to the combination of snowmelt and higher groundwater inputs. Despite these higher spring flows the only channel changes I observed were at XS7 in SG, where a scour hole filled in, and a slight widening on the left side of the channel at XS3 in SG (Figure C.6). In summer 2014 I observed virtually no deposition or erosion at any of my XSs or LPs (e.g., Figures 3.2-3.6), and this is almost certainly due to the increased vegetation cover and fewer high-intensity summer thunderstorms (*Schmeer et al.*, 2018).

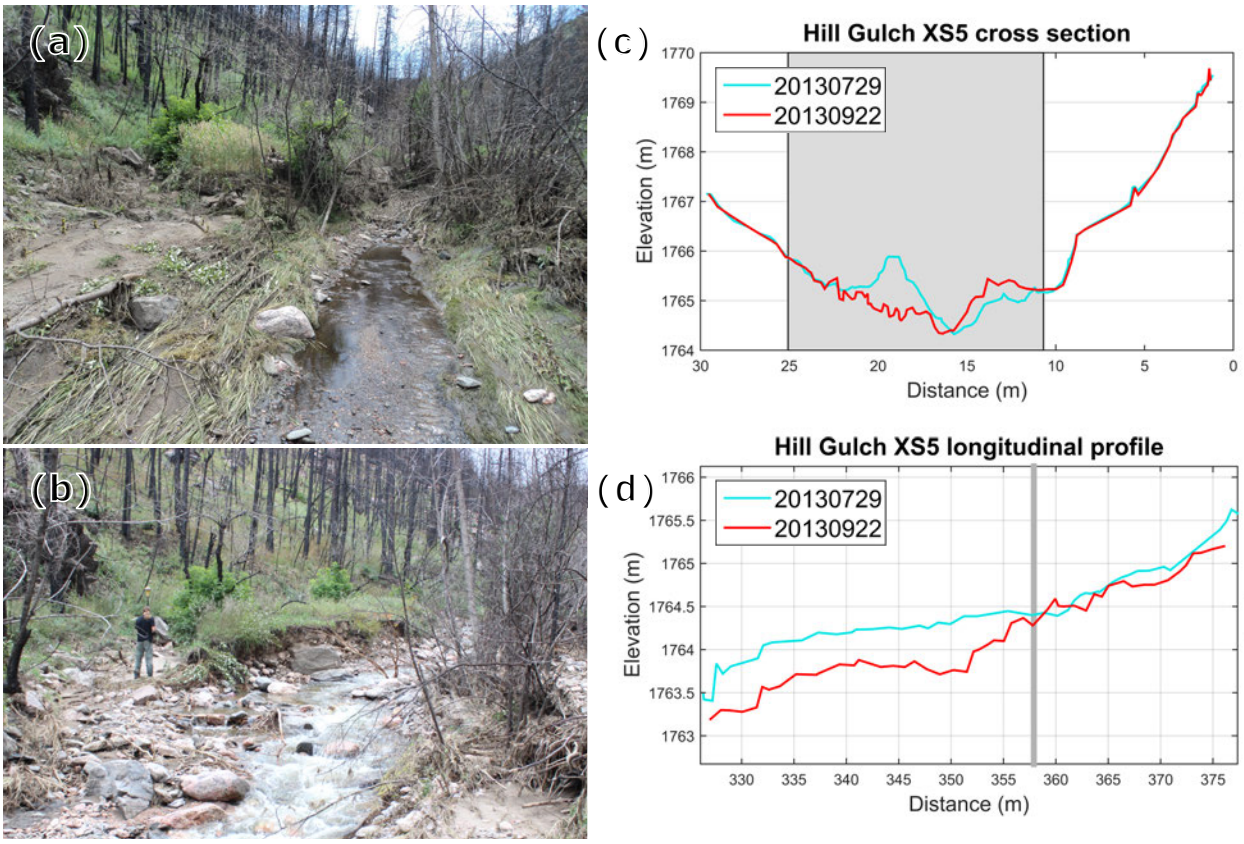

Figure 3.12: Photos looking upstream at cross section five in Hill Gulch on (a) 1 August 2013, and (b) 22 September 2013 showing the more moderate erosion due to the mesoscale flood. Plot of the (c) cross section and (d) longitudinal profile prior to (blue line) and just after the mesoscale flood (red line). A person in (b) provides scale. The cross section is plotted looking upstream to match the perspective in the photos. The cross section in (c) is approximately where the person is standing in (b).

In 2015 there were more channel changes than in 2014, but these were relatively minor. In late spring to summer 2015 small pools formed in HG at the downstream end of LP8 (Figure C.21) and along LP10 (Figure C.23), while a pool filled in along LP11 in HG (Figure 3.5). In fall 2015 a boulder in the center right portion of XS3 in SG tipped over and partly slid downstream across the steep exposed bedrock (Figure C.6). There also were some fluctuations in LP1 in HG, although some of these changes may have been due to RTK-GNSS error because of the thick tree cover. In 2016 the spring snowmelt and summer thunderstorms caused virtually no detectable channel changes, indicating a cessation of significant post-fire and post-flood geomorphic channel response.

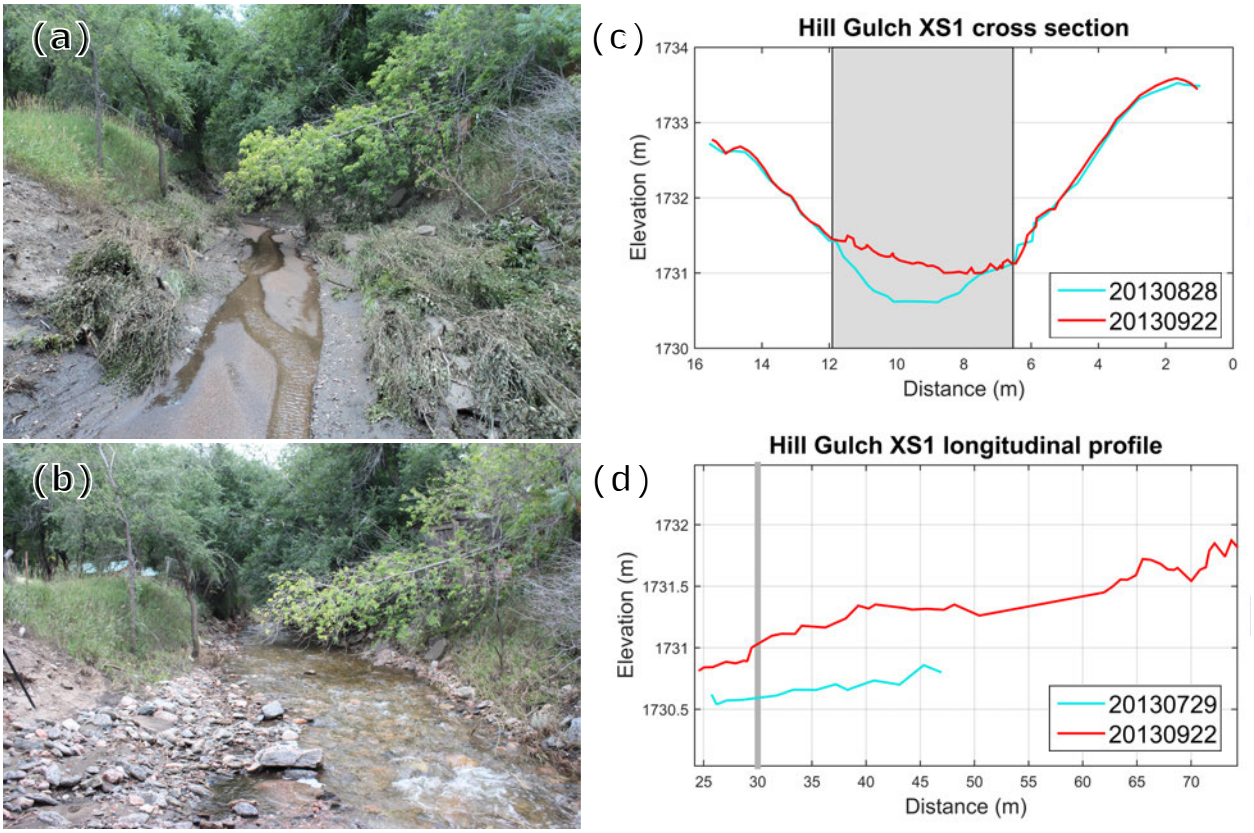

Figure 3.13: Photos looking upstream at cross section one in Hill Gulch on (a) August 2013, and (b) 22 September 2013 showing the aggradation caused by the mesoscale flood. Plots of the (c) cross section and (d) longitudinal profile prior to (blue line) and after the mesoscale flood (red line). The cross-section is plotted looking upstream to match the perspective in the photos.

3.4.4 Historic 1976 Flood

The July 1976 flood in the Big Thompson River just to the south of my study watersheds was notorious for killing 146 people and destroying Colorado Highway 36. This storm spilled over into parts of the Cache la Poudre watershed, and the total rainfall was estimated at 240 to nearly 300 mm in HG but only 200-240 mm in SG (Figure 3.15). Aerial imagery taken two months after the flood shows that a historic dirt road and the valley bottom in the lower portion of SG (XS2 to XS6) experienced no dramatic flood-induced changes (Figure 3.16). This same road was cut numerous times as a result of the first thunderstorm-driven flood in July 2012, and largely obliterated during the September 2013 mesoscale flood.

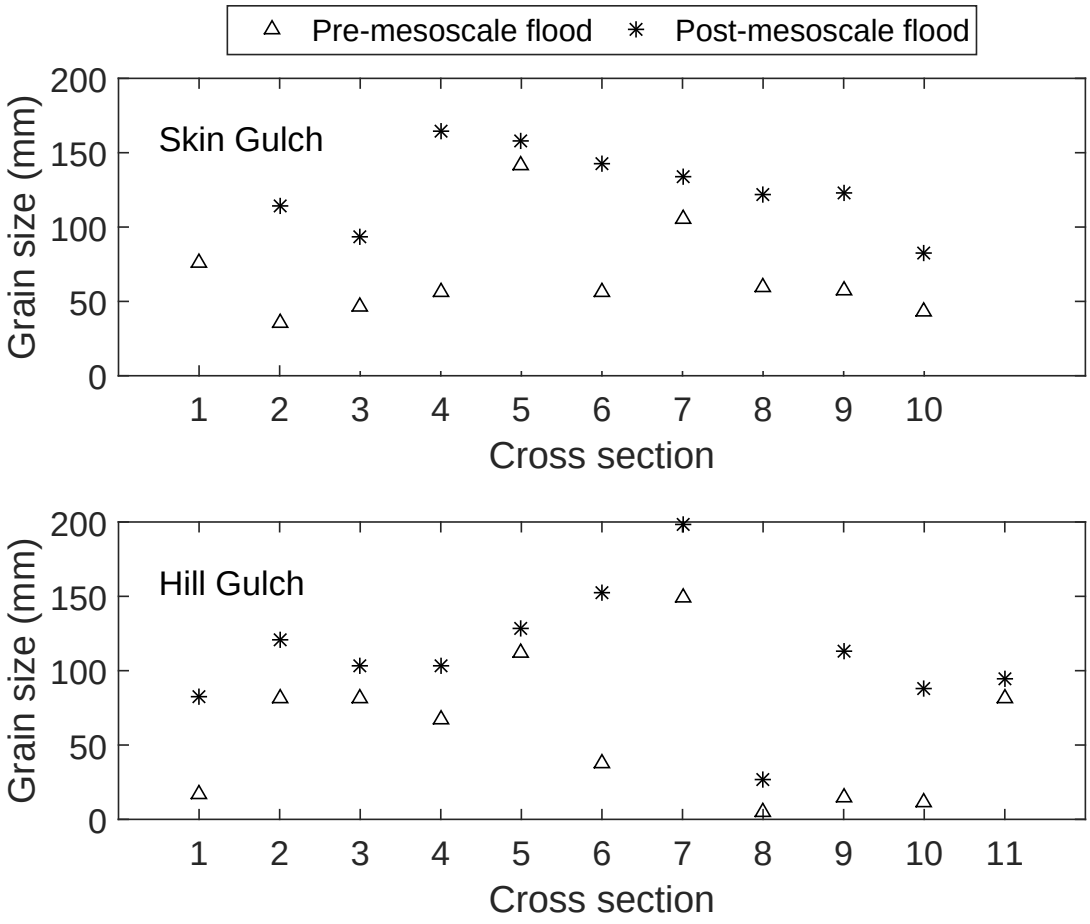

Figure 3.14: D_{84} (i.e., the percent by which 84% is finer) values for each cross section prior to and after the mesoscale flood for Skin Gulch (top) and Hill Gulch (bottom).

In contrast to SG, the 1976 flood eroded substantial portions of the valley bottom and mobilized large boulders in the lower portion of HG (Figure 3.16). The landowner recalls that the flood eroded into the floodplain, causing a 1.8-m raw vertical bank near his house (Figure 3.17a and 3.17b). The dirt road from his house down to the highway was completely destroyed and "there were a lot more cobbles and boulders exposed. . . boulders five and six feet [1.5-1.7 m] high in diameter" (H.A. Fonken, pers. comm., 2017; Figure 3.17c). He also reported that the tributary just below XS2 deepened 2 or 3 feet [0.6–0.9 m] due to the 1976 flood; this same channel scoured to a similar level after the mesoscale flood. These observations indicate that the mesoscale flood removed much of the sediment that had accumulated in some of the lower tributaries of HG over the 37 years after

the 1976 flood. It also is clear that the 2013 mesoscale flood had a much smaller effect in HG than the 1976 flood, even though the two storms had similar total precipitation (Figures 3.17, and C.28-C.28). The landowner noted that Hill Gulch and Falls Gulch, the smaller watershed just to the west of HG, were the only watersheds to sustain damage, which corroborates that the SG valley bottoms were not impacted by the 1976 rainstorms.

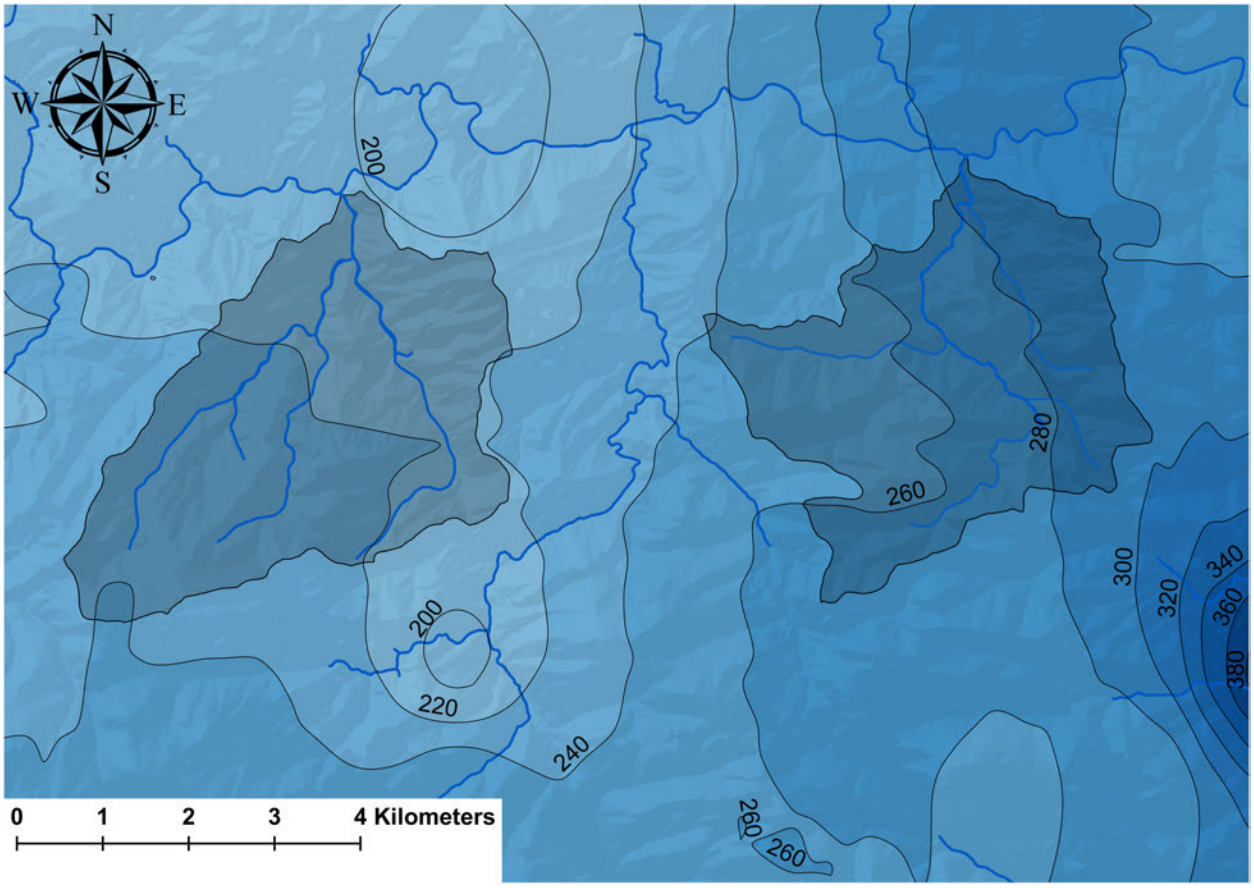

Figure 3.15: Isohyetal map of total precipitation over the greater study area for 31 July to 1 August 1976. Skin Gulch is outlined on the left and Hill Gulch is to the right. Source of precipitation data: MetStat Inc.

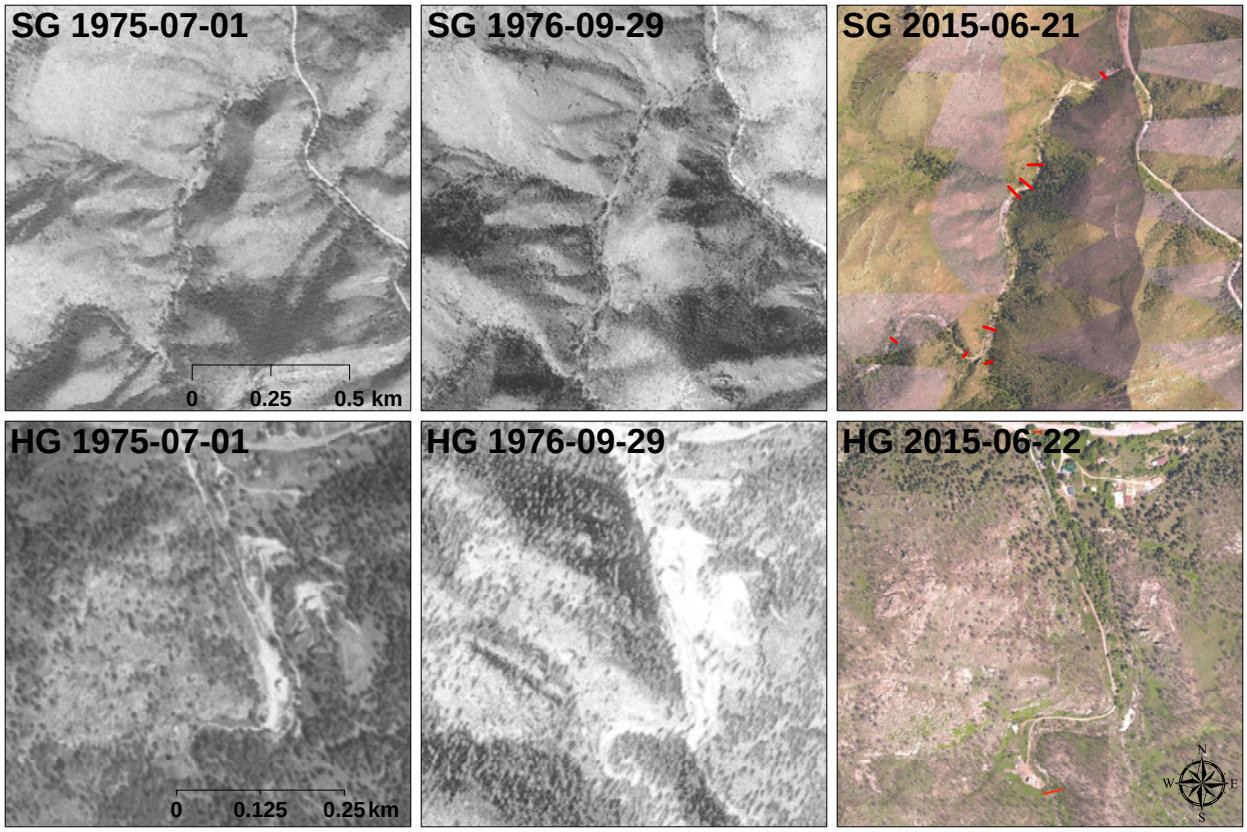

Figure 3.16: Aerial photos from 1975, 1976, and 2015 for the lower portions of Skin Gulch (top series) and Hill Gulch (bottom series) showing the much greater impact of the 1976 flood in Hill Gulch than Skin Gulch. Cross sections 2-9 in SG and 1-2 in HG are shown as red lines in the right most photos.

3.5 Discussion

3.5.1 Complex response after wildfire

Prior to the mesoscale flood the channels in Skin Gulch and Hill Gulch exhibited a complex post-fire response (cf. *Laird and Harvey*, 1986; *Moody and Martin*, 2001a). Convective thunderstorms brought spatially varying and temporally short-term amounts of runoff and sediment from the hillslopes and upstream tributaries to the main channels and valley bottoms. Field data and my observations indicate that the ash, silt, and clay were largely delivered into the Cache la Poudre River, as evidenced by the very high turbidities in the storm runoff (*Hohner et al.*, 2016; *Writer et al.*, 2014). In contrast, there was a relative lack of silts and clays in the post-fire sediment deposits in SG and HG. Some of the lower-lying deposits in the valley bottoms (i.e., deposits closer to

Figure 3.17: (a, b) Photos looking upstream from below cross section two in Hill Gulch contrasting the effect of the (a) 1976 flood in and the (b) 2013 mesoscale flood. The house in (a) burned in the 2012 High Park fire and the access road in (a) and (b) had been eroded by the 1976 flood. (c, d) Photos looking downstream towards the outlet of Hill Gulch showing that the 1976 flood substantially reworked the channel and valley floor (c) while the 2013 flood had little effect on this portion of the channel (d). A reconstructed house at nearly the same location as the house in (c) was unaffected by the 2013 flood.

the channel margin), particularly the finer gravel and sand, were eroded and reworked by the runoff from subsequent thunderstorms, while the higher deposits remained largely undisturbed. Similar to other studies, spring snowmelt incised through the recently deposited sediment (e.g., *Reneau et al.*, 2007). Thunderstorms during the second summer again generated overland flow and hillslope erosion, with much of this sediment being deposited in the valley bottoms. Between storms the higher baseflows induced by the vegetation loss would cause some incision and downstream sand transport. A similar pattern, where higher intensity storms resulted in net aggradation while

low intensity storms resulted in net erosion, was noted in two ephemeral watersheds about 10 km west of SG (*Rathburn et al.*, 2017).

While the trends of erosion and deposition were similar in time and to a lesser extent in space for the two study watersheds, the magnitude and complexity of channel changes were greater in SG than HG. I attribute the greater magnitude and complexity of channel changes in the lower portion of SG to the exceptionally large amount of sediment deposited after the high-intensity, short-duration convective thunderstorm that occurred in the western part of SG just after the HPF was contained (Chapter 2). The largest and coarsest deposits from this storm were near XS6, which is just below a confluence in a rapidly expanding and lower gradient valley bottom. This, and the overall patterns of erosion and deposition, indicate the importance of topographic controls on localized sedimentation, and that a geomorphic characterization could help characterize and predict the spatial and temporal patterns of sediment storage and erosion (see Chapter 3 for more detail; e.g., *Fuller*, 2008; *Surian et al.*, 2016; *Wolman and Eiler*, 1958; *Yochum et al.*, 2017).

The spatial scale of reference in the channel network (i.e., hillslope, subwatershed, watershed) and the time since burning, in addition to the precipitation characteristics, control the changes in the complex response between aggrading or eroding (e.g., Figure 3.1) *Laird and Harvey*, 1986). The expected trajectory of these changes between aggradation and erosion was completely altered only fifteen months after the fire by the September 2013 mesoscale flood, as the sustained high flows not only stripped away nearly all of the post-fire deposited sediment but also reworked much of the valley floodplains and older terraces (e.g., *Schick*, 1974). In the absence of the mesoscale flood a relatively rapid decrease in the amount of deposition and scour in the channels and valley bottoms would have been expected as the hillslopes revegetated. As documented in nearby fires, hillslope vegetative recovery greatly reduces surface runoff and hillslope erosion by about the third summer after burning (*Benavides-Solorio and MacDonald*, 2005; *Larsen et al.*, 2009; *Wagenbrenner et al.*, 2006). This timescale of recovery is consistent with the measured erosion rates for 29 convergent hillslopes in SG and HG, with the exception of one large localized storm in HG in August 2015 (*Schmeer et al.*, 2018). This decline in hillslope runoff and erosion causes a corresponding reduc-

tion in downstream flooding, deposition, and sediment transport (e.g., *Moody and Martin*, 2001a; *Morris and Moses*, 1987), and subsequently—along with riparian vegetation regrowth—leads to a stabilization of the downstream channels. In some cases, such as the granitic deposits after the Buffalo Creek and Hayman fires in Colorado, the coarse-textured substrate and associated poor growing conditions would result in slower channel recovery and the continued mobilization of the sediment deposited in or adjacent to the channels (*Moody*, 2017). But in this study the mesoscale flood effectively reset the system by evacuating nearly all of the post-fire sediment.

The evacuation of the post-fire sediment and coarsening of the channel bed by the mesoscale flood also has greatly reduced the sensitivity, or increased the threshold, of the channels to future geomorphic change (*Schumm*, 1979). More specifically, the removal of so much sediment has made the downstream channels much less sensitive to subsequent floods (*Hooke*, 2015). This reduced sensitivity is evidenced by the very limited geomorphic changes in the cross sections and longitudinal profiles after the mesoscale flood, despite the exceptionally high spring flows in 2014 and again in May 2015 when there were two large, rapidly-melting snowstorms. The implication is that if the mesoscale flood had not occurred, the threshold for channel changes would have been lower as more of the finer deposits would have remained and been susceptible to channel and floodplain erosion. Hence my study provides a unique example of how a mesoscale flood not only altered the expected post-fire trajectory of channel changes, but also allowed a direct comparison of post-fire flood, erosion, and deposition with the effects of an exceptionally large sustained flood.

3.5.2 Differences in mesoscale flood response

The geomorphic changes from the 2013 mesoscale flood were much greater in SG than in HG, despite the similarity of my two study watersheds in size, hypsometry, drainage density, slope, pre-fire vegetation, and burn severity. Additionally, the rainfall depth and intensity during the mesoscale storm were very similar for each watershed. I suggest three main reasons for the different responses between the two watersheds as a result of fire and floods.

First, the estimated peak flow in SG was 2.5–4 times larger than in HG. Stage measurements indicated that the duration of unusually high flows was about 24 hours for both watersheds (cf. *Kampf et al.*, 2016), but the actual amounts of flow cannot be realistically calculated because of the extensive deposition that occurred during the flood where stage was being measured. The difference in estimated peak flows means that the total energy available for geomorphic work, which is estimated by integrating the time series of stream power, was estimated at 28,000–51,000 kJ in SG (Chapter 2) as compared to only 11,000-16,000 kJ in HG. This difference converts to a much lower sediment transport capacity (e.g., *Julien*, 2010) and less energy available for geomorphic work in HG (*Costa and O'Connor*, 1995).

Given the relatively similar rainfall in the two watersheds (*Kampf et al.*, 2016) I posit that much of the difference in peak flows and total energy expended between SG and HG may be due to the spatial differences in burn severity. In burned areas reduced rainfall interception and infiltration, reduced roughness, and greater hillslope-to-channel connectivity leads to more rapid runoff. In SG the areas burned at high and moderate severity were mostly in the upper part of the watershed, while in HG the majority of the moderate and high burn severity was in the lower part of the watershed. The rainfall data shows that there were two distinct higher-intensity bursts of rainfall that caused the largest peak flows, and in the upper portion of SG the higher burn severity would have resulted in more rapid runoff and a shorter time to concentration than in HG (e.g., *Moody et al.*, 2008a). This more rapid hydrograph peak would synchronize better with the timing of the peak flows from the lower portion of the watershed, increasing the absolute magnitude of the peak flow for a given rainfall (sensu *Mejía and Moglen*, 2010). In HG there would be less and slower runoff from the upper portion of the watershed given the lower burn severity, while the runoff from the more severely burned lower portion of the watershed would have a shorter time of concentration, resulting in a desynchronization of the runoff peaks from the upper and lower portions of the watershed.

Previous research has shown that the magnitude of peak flows can also be influenced by the shape of the channel network geometry (e.g., *Costa*, 1987; *Strahler*, 1964). In particular, water-

sheds with a rounder shape (i.e., elongation ratio closer to one) are more conducive to higher peak flows. Given the similar elongation ratios in SG and HG, and the very similar shape of the width function (Figure A.3), the relative shape of the channel network geometry between the two study watersheds was likely not that influential in the difference in peak flows.

A second important reason for the larger geomorphic response to the mesoscale flood in SG than HG is the differing legacy of the 1976 flood. Anecdotal evidence suggests the 1976 flood removed much of the valley fill and coarsened the channel in HG, and the legacy of the 1976 flood is still clearly evident in HG from hillslope and floodplain escarpments, and large cobble-boulder depositional bars (e.g., Figure 3.18). These changes are remarkably similar to the changes observed in SG as a result of the 2013 mesoscale flood (e.g., Figure 3.19). Since erosion rates in the Colorado Front Range are only about 20–60 mm/k.a. (e.g., *Dethier et al.*, 2014; *Foster et al.*,

Figure 3.18: Photo taken on 11 August 2012 between XS2 and XS3 in Hill Gulch highlighting 1976 flood effects, including a steep cutbank (blue box) and medial cobble/boulder bar (blue box).

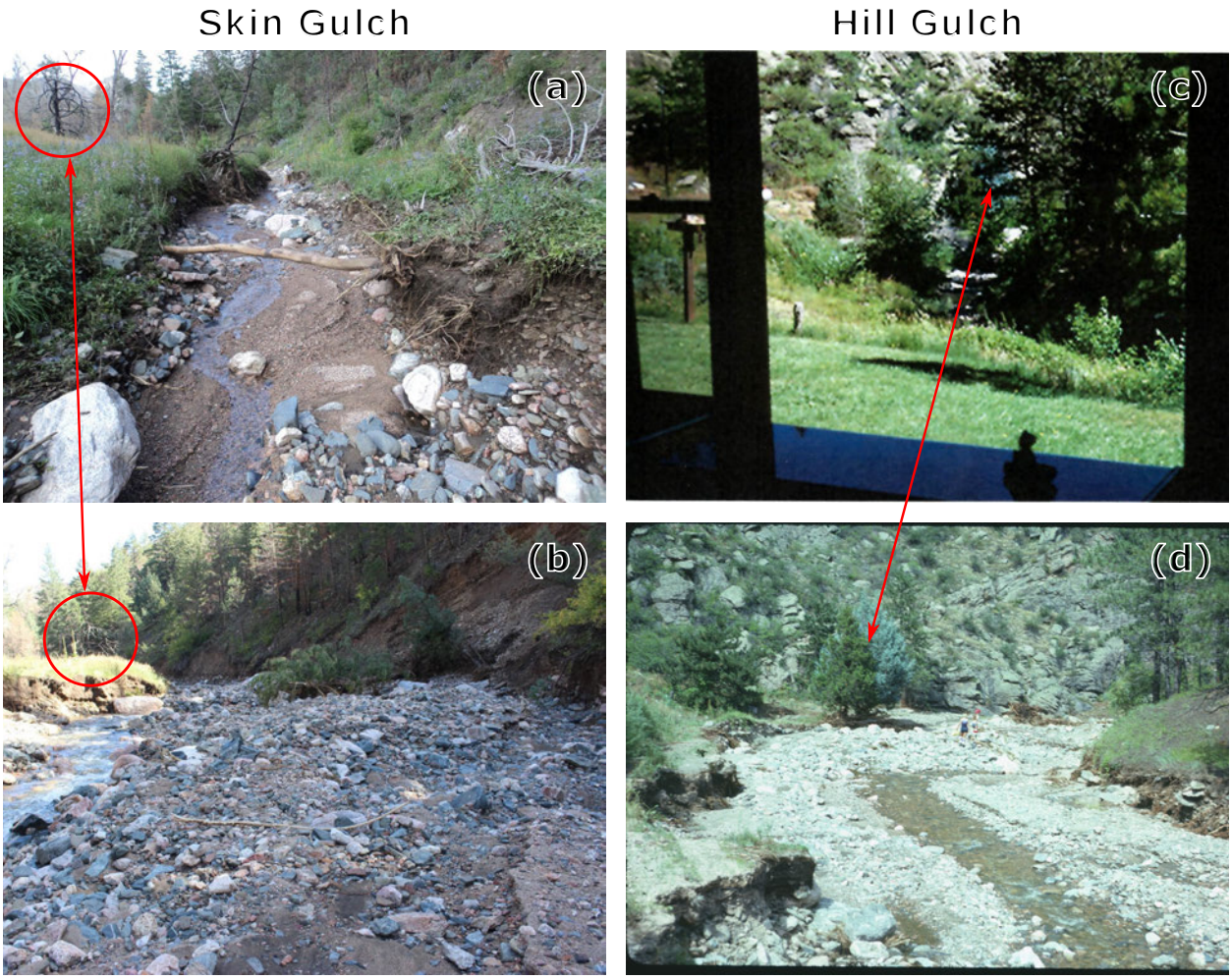

Figure 3.19: Photos looking downstream at XS4 in Skin Gulch (a) prior to and (b) after the 2013 mesoscale flood. Photos looking downstream below XS2 in Hill Gulch (c) prior to and (d) after the 1976 flood. Note the similarity of the mesoscale flood effects in SG (b) and the 1976 flood effects in HG (d). Additional pre- and post-flood photos are in Appendix C (Figures C.28–C.31).

2015), the 36 years of hillslope erosion and downstream deposition since the 1976 flood represents only a relatively small amount of sediment. Hence the scoured and coarsened channel and valley bottoms in lower HG made them much less sensitive to subsequent geomorphic changes than the channels and valley bottoms in SG, especially given the large deposits of post-fire sediment in SG (e.g., *Costa and O'Connor*, 1995; *Hooke*, 2015; *Schumm*, 1979). The implication is that predicting the geomorphic effects of large floods requires an assessment and understanding of the legacy effects from past fires and other disturbances, as this can greatly alter the relative sensitivity to a given future external forcing. Our understanding of post-fire erosion and deposition at the water-

shed scale will greatly benefit from additional research on watersheds with different disturbance histories and physiographic conditions.

A third reason for the larger response from the 2013 mesoscale flood in SG than in HG could be due to SG having much larger sediment deposits in the valley bottoms as a result of the high-intensity convective storm in July 2012 (Chapter 2). The large volumes of sediment in and adjacent to the stream channels in the lower portion of the watershed effectively 'loaded the gun' (sensu *Nanson*, 1986) by increasing the sediment supply for subsequent high flows to erode and transport the very large amounts of deposited sediment. My data and field observations show that most of this post-fire sediment, along with some of the older floodplain and valley bottom deposits, were removed during the 2013 mesoscale flood. In contrast, there was much less post-fire sediment deposited in HG after the HPF, resulting in less net channel change. It follows that if the 2012 flood in SG had not happened, the 2013 flood effects in SG and HG would not have been as dramatic. This shows that the effect of a given disturbance can vary greatly depending on the pre-existing sequence of events (e.g., *Germanoski*, 2002; *Hooke*, 2015; *Wolman and Gerson*, 1978).

3.5.3 Comparing fire and flood effects

Direct comparisons of the geomorphic impacts of fires and floods are complicated by differing spatial and temporal scales, their variability with rainfall amounts and intensities, they each involve multiple interacting processes, and the persistence of their effects are not consistent over time, space, and among events (*Brunsden and Thornes*, 1979; *Moody et al.*, 2013). Anecdotal evidence suggests that prior to 1976 the downstream valleys in both SG and HG had a similar sensitivity and were on a similar trajectory of slowly increasing sensitivity as sediment accumulated in the downstream valley bottoms from hillslope processes such as diffusion (rainsplash, sheetwash, and soil creep), fluvial processes (upstream channel erosion), and mass movements (slides, debris flows, and falls) (Figure 3.20). Pictures and personal accounts document the catastrophic stripping and bed coarsening in HG by the 1976 flood (Figures 3.16-3.19), and this reduced the sensitivity of

the downstream channels to subsequent disturbances and hence the potential for future geomorphic changes.

Thirty-six years after the 1976 flood the High Park Fire induced extensive hillslope erosion and downstream deposition, and the greater sediment deposition due to the convective flood in SG caused a larger increase in downstream sensitivity due to the greater abundance of readily available sediment (Figure 3.20). In both watersheds the September 2013 mesoscale flood stripped much of the sediment from the channels and adjacent valley bottoms, and created a similarly insensitive condition in lower SG and lower HG. The insensitive condition of lower SG following the 2013 mesoscale flood was similar to the condition of lower HG following the 1976 flood (e.g., Figure 3.19). If SG had not first burned and the convective flood had not brought substantial deposition to the valley, the magnitude of erosion would almost certainly been much less, although still substantial. Thus, the two study watersheds took two very different pathways to a very similar state of relative insensitivity, and this difference affected the relative magnitude of geomorphic changes post-fire and from the mesoscale flood.

Resilience is conceptually similar to sensitivity, as this has been defined as the ability of a system to absorb a perturbation without changing to a new state (*Tabacchi et al.*, 2009), and it can be quantified by how fast a system returns to its initial state (*Holling*, 1996). *Relative sediment resilience* has been defined as the timescale for sediment recovery divided by the recurrence interval of the disturbance (cf. *Brunsden and Thornes*, 1979; *Rathburn et al.*, 2017). Ratios less than one indicate that the average time scale for recovery from a disturbance is shorter than the average recurrence interval, yielding a *high* relative sediment resilience. In contrast, ratios greater than one indicate the average time scale for recovery from a disturbance is longer than the average recurrence interval, yielding a *low* relative sediment resilience. The relative sediment resilience of the 1976 flood in HG should be considered moderate as the disturbance and the recurrence interval of the disturbance were very high, and the valley bottom had still not recovered 36 years later (Table 3.4). In contrast to HG, the 1976 flood in the Big Thompson River, which is about 30 km south of

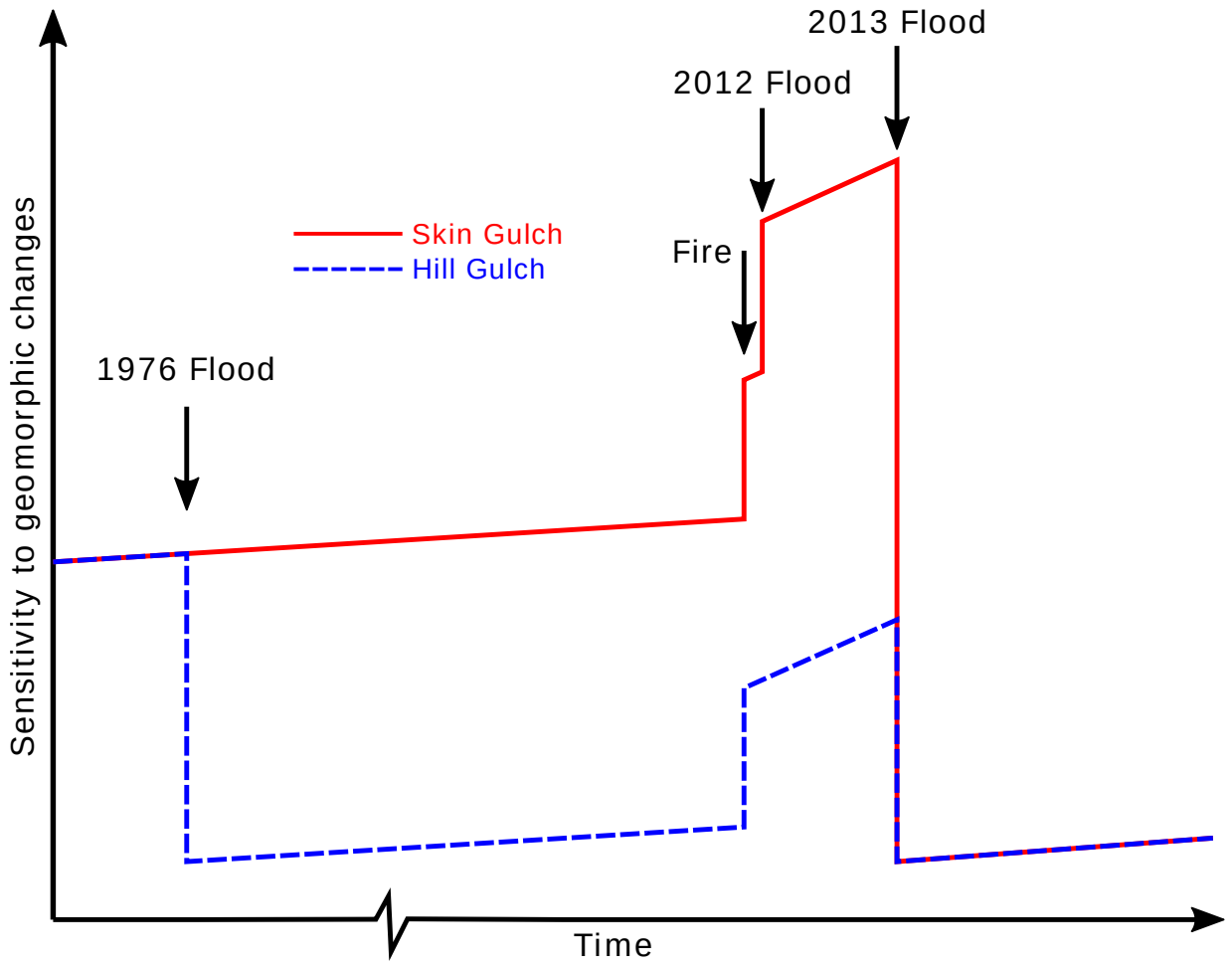

Figure 3.20: Relative sensitivity over time of the channels and valley bottoms to geomorphic change in Skin Gulch (red line) and Hill Gulch (dashed blue line). The step changes in sensitivity are respectively attributed to the 1976 flood in Hill Gulch, the 2012 High Park Fire, the 2012 convective flood in Skin Gulch, and the 2013 mesoscale flood.

HG, caused major channel and valley changes but had an estimated recurrence interval of 10,000 years (Jarrett and Costa, 1988), resulting in a high relative sediment resilience.

In contrast, forest fires would be expected to have a varying relative sediment resilience according to the spatial scale of concern. In the ponderosa pine forests of the Colorado Front Range the mean fire interval is about 10-50 years (*Kaufmann et al.*, 2000; *Veblen et al.*, 2000), and at the hillslope scale the resulting effects on runoff and erosion may only last a few years (e.g., *Benavides-Solorio and MacDonald*, 2005; *Larsen et al.*, 2009; *Moody and Martin*, 2001a; *Morris*

and Moses, 1987; *Wohl and Scott*, 2017). This results in a high relative sediment resilience. When high intensity rains fall over areas burned at high and moderate severity, as was the case for the 2012 convective storm in SG, the large amounts of downstream deposition can result in a longer recovery time, but the recurrence intervals for fire-flood sequences at larger scales are hundreds to thousands of years in the Colorado Front Range (e.g., *Cotrufo et al.*, 2016; *Elliott and Parker*, 2001). This means that downstream areas can have moderate to high relative sediment resilience.

The September 2013 mesoscale flood had a recurrence interval on the order of tens to hundreds of years (*Yochum*, 2015), and much like the 1976 flood in HG, stripped many valleys of sediment (e.g., *Gartner et al.*, 2015; *Wicherski et al.*, 2017; *Yochum et al.*, 2017). The minimal recovery indicates that the mesoscale flood had low to moderate relative sediment resilience. The implication is that the relative sediment resilience in channels is generally lower after extreme floods as compared to fires and debris flows (e.g., *Rathburn et al.*, 2017).

Table 3.4: Estimated sediment recovery, disturbance recurrence interval (RI), and relative sediment resilience for Skin Gulch and Hill Gulch for the post-fire and flood-induced changes affecting each watershed over the past 40 years. Relative sediment resilience is defined as the estimated time for sediment recovery divided by the disturbance recurrence interval; a ratio less than one is defined as a *high* relative sediment resilience, while a ratio greater than one is defined as a *low* relative sediment resilience. n/a indicates not applicable.

Disturbance	Metric	Skin Gulch	Hill Gulch	Example references
1976 flood	Sediment recovery	n/a	10^2–10^3 years	*Nanson* (1986)
	Disturbance RI		10^2–10^3 years	*Jarrett and Costa* (1988); *Nanson* (1986)
	Rel. sed. resilience		Moderate	n/a
2012 High Park Fire	Sediment recovery	10^1 years	10^1 years	*Moody et al.* (2013)
	Disturbance RI	10^1–10^2 years	10^1–10^2 years	*Moody et al.* (2013)
	Rel. sed. resilience	Moderate–high	Moderate–high	n/a
2012 convective flood	Sediment recovery	10^1–10^2 years	n/a	*Elliott and Parker* (2001)
	Disturbance RI	10^2–10^3 years		*Cotrufo et al.* (2016); *Elliott and Parker* (2001)
	Rel. sed. resilience	Moderate–high		n/a
2013 mesoscale flood	Sediment recovery	Minimal	Minimal	*Rathburn et al.* (2017)
	Disturbance RI	10^1–10^2 years	10^1–10^2 years	*Gochis et al.* (2014); *Yochum* (2015)
	Rel. sed. resilience	Low–moderate	Low–moderate	n/a

It can be argued that at larger spatial scales wildfires in the western U.S.A. have limited geomorphic effects because of the inherent spatial scale of most fires and the threshold precipitation needed to produce significant runoff, erosion, and downstream deposition (*Kampf et al.*, 2016; *Laird and Harvey*, 1986). The larger scale effects of fires are limited by several factors. First, it is rare for a fire to burn the majority of a larger watershed—commonly they burn in the headwaters of multiple watersheds so not all of the post-fire effects are concentrated in a single watershed. Second, it is relatively rare for all of a watershed to burn at high and moderate severity, so the post-fire effects are diluted by the much lower contributions of runoff and sediment from unburned or low severity areas. Third, individual convective storms, which are commonly the dominant driver of post-fire runoff and erosion in the Rocky Mountains (*Moody and Martin*, 2009), typically cover a small area, so only small portions of a large fire will produce large amounts of runoff and erosion. In contrast, large floods like the 1976 Big Thompson flood and the 2013 mesoscale flood were caused by storms that covered much larger areas than a typical convective storm; they also had a much longer duration. The larger temporal and spatial scale of these causal rainfalls resulted in much larger accumulations of runoff, and much greater energy expenditures that then greatly altered the downstream channels and valley bottoms over a large area. The implication is that large, geomorphically effective floods appear to be more dominant than fires in terms of shaping downstream valleys in much of the Rocky Mountains.

The complex response observed in this study and documented by other researchers (e.g., *Cluer and Thorne*, 2014; *Laird and Harvey*, 1986; *Moody and Martin*, 2001a; *Phillips and Van Dyke*, 2016; *Schumm et al.*, 1984; *Simon and Hupp*, 1986) allow us to develop a state-and-transition model (STM) to conceptualize how the relative magnitudes of sediment supply and transport capacity induced by fires and floods influence channel evolution (Figure 3.21). Because channels do not always respond linearly to disturbance (*Lisenby et al.*, 2017) and their response can depend on their history of previous disturbances (*Brierley*, 2010), a STM allows for interpreting geomorphic changes based on empirical observations (*Phillips and Van Dyke*, 2017). I identify three states based first on the relative amount of sediment stored within the valley bottoms, and then whether

the watershed is unburned or burned. Unburned states with low valley fill are the least sensitive, while all burned states are inherently more sensitive, but the sensitivity varies with the amount of valley fill that is available and susceptible to erosion. Channels and valley bottoms transition between states according to the balance between sediment supply and transport capacity.

With respect to my two study watersheds, I posit that both SG and HG were in a similar unburned state with moderate to high valley fill prior to the 1976 Big Thompson flood. This flood decreased the valley fill in HG to low and greatly reduced its relative sensitivity (Figure 3.20). The HPF changed both watersheds from unburned to burned, increasing their sensitivity. The 2012 convective flood in lower SG caused a shift from moderate to high valley fill, increasing its sensitivity further, while HG did not have as much post-fire deposition. SG was therefore in a more sensitive state when it was hit by the 2013 mesoscale flood, but both watersheds ended up in a burned state with low valley fill. Over some decades to centuries the valley bottoms will slowly accumulate sediment. This slow shift from low to moderate to high valley fill will gradually increase their relative sensitivity unless they are subjected to another fire-flood sequence, or an exceptionally large flood. Knowing the history of a watershed *a priori* is therefore critical for understanding and predicting the potential for valley and channel changes to fires and floods.

3.6 Conclusions

Geomorphic changes were quantified in the channels and valley bottoms in two ~15 km^2 watersheds after the 2012 High Park Fire and subsequent floods. Post-fire summer convective thunderstorms caused extensive overland flow and hillslope erosion that delivered and deposited sediment into the downstream channels, particularly in the Skin Gulch watershed. The enhanced post-fire baseflows and spring snowmelt incised through these deposits, and the thunderstorms in the second summer deposited additional sediment and also reworked some of the lower-lying post-fire deposits. These relatively typical post-fire channel responses were interrupted 15 months after the fire by an extreme, long-duration flood that stripped the valleys of nearly all of the post-fire sediment as well as causing extensive erosion of some of the older valley bottom deposits. The channel

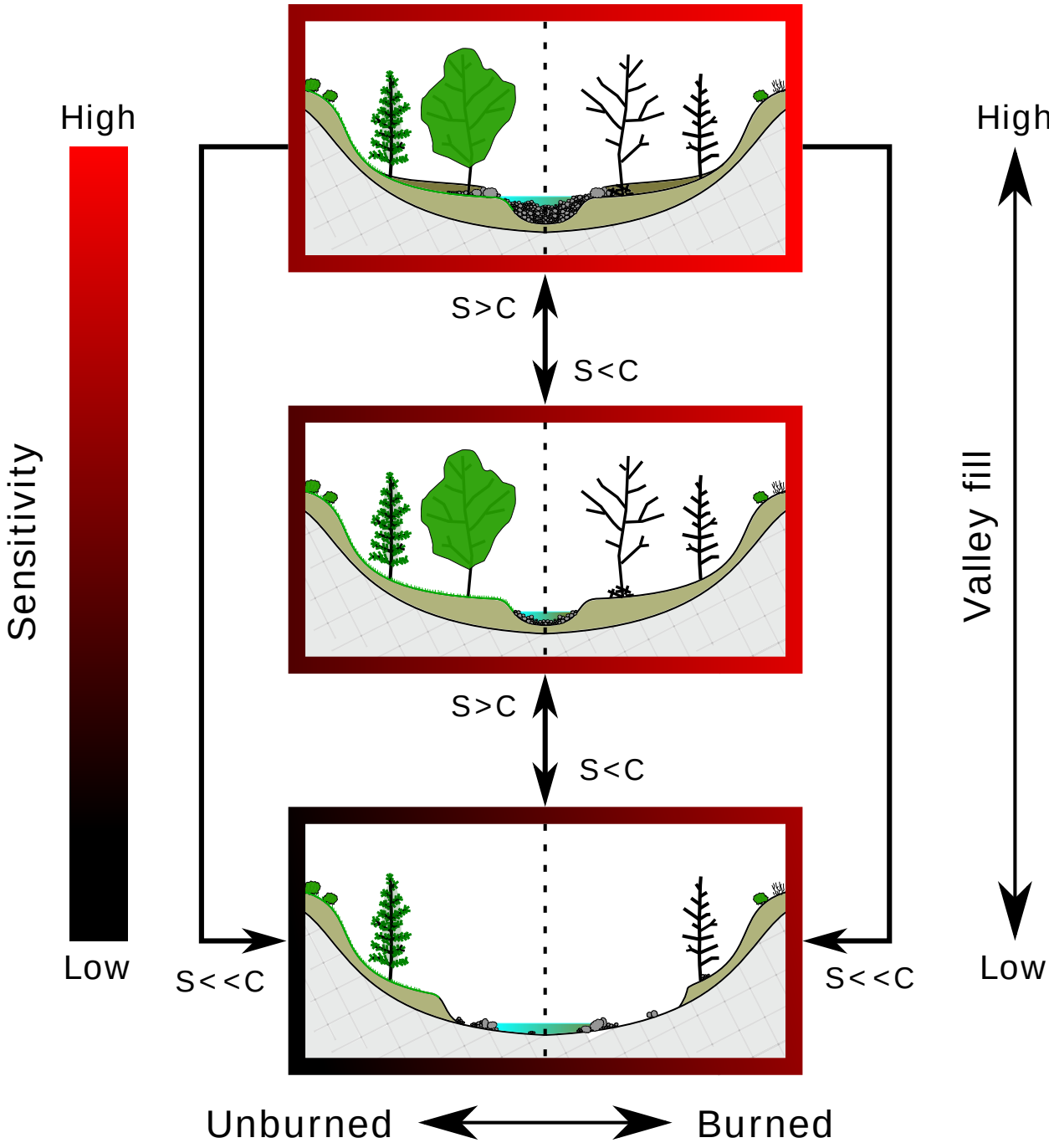

Figure 3.21: Conceptual state-and-transition model for the changing sensitivity of channels and valley bottoms to a high or moderate severity fire, increasing scour or deposition of valley fill, and a large erosional flood. Relative sensitivity is denoted by the edge color of the boxes surrounding each state. Transitions between states are governed by the relative balance between sediment transport capacity (C) and available sediment supply (S).

incision, widening, and coarsening was much more severe in Skin Gulch, which is attributed to 1) to the larger peak flow and correspondingly greater energy expenditure in SG stemming from the different spatial patterns of burn severity between the two watersheds, 2) the reduced sensitivity in Hill Gulch as a result of the channel and valley bottom erosion caused by an extreme flood in 1976, and 3) the increased sensitivity in Skin Gulch as a result of the post-fire deposition associated with the 2012 convective flood, which effectively loaded the gun for the subsequent erosion by the large mesoscale flood in September 2013.

The sequence of events and differences between watersheds led to the development of a state-and-transition model that relates the sensitivity of channel change to the amount of valley fill and whether a watershed is burned or unburned. Transitions between states depend on the relative sediment supply and transport capacity, with fires greatly increasing the sensitivity to downstream channel changes as a result of the upslope increases in runoff and erosion, and large erosive floods reducing future sensitivity to channel changes by removing the accumulated sediment and the associated coarsening of the stream channel and adjacent valley bottom. Additional downstream monitoring is needed in more watersheds with different disturbance histories, particularly to assess the larger-scale and longer-term effects of fires in different physiographic and climatic conditions. I conclude that the timing and sequence of different disturbances are critical control on the relative sensitivity of watersheds to downstream channel change, and that the extreme floods are more dominant at shaping downstream valleys than the effects of wildfires.

3.7 Supporting information

Additional supporting information is in Appendix C.

Chapter 4

Spatial and temporal patterns of sediment storage and erosion following a wildfire and extreme flood

4.1 Introduction

Wildfires alter the hydrologic response by creating conditions that can lead to greatly increased runoff and erosion rates. At plot to hillslope scales increased rates of runoff have been attributed to decreased canopy cover, ground cover and surface roughness, and increased soil sealing and soil water repellency (e.g., *Benavides-Solorio and MacDonald*, 2001; *Ebel et al.*, 2012; *Huffman et al.*, 2001; *Larsen and MacDonald*, 2007; *Larsen et al.*, 2009; *Onda et al.*, 2008; *Schmeer et al.*, 2018; *Stoof et al.*, 2012). At the hillslope scale these fire-induced changes increase a series of erosional processes, including rainsplash, sheetflow, rilling, gullying, landslides, and debris flows (e.g., *Benda and Dunne*, 1997; *Cannon et al.*, 2001; *Gabet and Dunne*, 2003; *Inbar et al.*, 1998; *Rengers et al.*, 2016; *Roering and Gerber*, 2005; *Wagenbrenner and Robichaud*, 2014). With increasing watershed scale channel erosion can become an important process (e.g., *Legleiter et al.*, 2003; *Meyer et al.*, 1992; *Wagenbrenner and Robichaud*, 2014), but the literature provides many more examples of post-fire depositional features such as alluvial fans, levees, debris jams, channel infilling, floodplain accretion, braided channels, reservoir filling, and a sediment superslug (e.g., *Moody*, 2017; *Moody and Martin*, 2001a; *Orem and Pelletier*, 2015; *Reneau et al.*, 2007; *Santi et al.*, 2008).

Considerable advances have been made in understanding post-wildfire runoff, erosion, and mass wasting at hillslope and small watershed scales (see *Moody et al.*, 2013; *Shakesby and Doerr*, 2006, and references within); however, the larger-scale effects of fires on flooding, water

Coauthors for this planned journal submission include P. A. Nelson and L. H. MacDonald.

quality, and sedimentation are often the most significant (*Doehring*, 1968; *Hamilton et al.*, 1954; *Moody and Martin*, 2001a, 2004; *Rhoades et al.*, 2011; *Writer et al.*, 2014). The problem is that post-fire estimates of downstream flooding, erosion, and sedimentation are not a simple sum of hillslope-scale processes. Most efforts to model post-fire runoff and erosion have focused at the hillslope scale, and include WEPP (e.g., *Elliot*, 2004; *Miller et al.*, 2011), RUSLE (*Renard et al.*, 1997), AGWA (*Goodrich et al.*, 2005), and ERMiT (*Robichaud et al.*, 2007). These models have been used as the basic building blocks for efforts to predict changes at the watershed scale (e.g., GeoWEPP; *Elliot et al.*, 2016; *Miller et al.*, 2011), but they do not include key mechanisms of sediment storage and erosion in channel networks greater than 1-100 ha. Scaling up from hillslopes can result in unreliable and inaccurate estimates of watershed-scale runoff and sediment production, deposition and delivery (e.g., *Moody and Kinner*, 2006; *Stoof et al.*, 2012). The majority of studies that have looked at larger scales quantify sediment delivery, not controls on the spatial changes within the watershed (e.g., *Orem and Pelletier*, 2015; *Pelletier and Orem*, 2014). Efforts to measure and better understand these larger-scale geomorphic changes are still hampered by the lack of high spatial- and temporal-resolution data over entire channel networks (*Moody et al.*, 2013).

To some extent the larger-scale effects of fires should be similar to observed patterns of erosion and deposition following large floods (e.g., *Wolman and Eiler*, 1958). In general, stream power—or gradients in stream power—and lateral confinement are the best predictors of the spatial patterns of erosion and deposition (e.g., *Fuller*, 2008; *Gartner et al.*, 2015; *Miller*, 1995; *Stoffel et al.*, 2016; *Surian et al.*, 2016; *Thompson and Croke*, 2013; *Yochum et al.*, 2017), although strong correlations are not always apparent (e.g., *Nardi and Rinaldi*, 2015). Total energy expenditure during floods (*Costa and O'Connor*, 1995) can be equally important as stream power and lateral confinement in estimating total sediment transport (e.g., *Wicherski et al.*, 2017). Studies on the geomorphic impacts of extreme floods have usually focused on changes that are largely erosional, but short-duration, high-energy floods also can cause substantial and long-lasting sediment deposition (e.g., Chapter 2; *Magilligan et al.*, 2015).

Post-fire hydrologic effects and geomorphic changes can be expected to diminish with increasing basin size because fires typically only burn a portion of larger watersheds (*Havel et al.*, 2018). In certain climatic regimes larger-scale effects also will decline because high-intensity convective storms, which are often the driving force of post-fire runoff and erosion (e.g., *Benavides-Solorio and MacDonald*, 2005; *Cannon et al.*, 2001; *Meyer et al.*, 1995; *Moody and Martin*, 2001a; *Morris and Moses*, 1987; *Wagenbrenner and Robichaud*, 2014), typically are concentrated in a small area.

New technologies, such as repeat airborne laser scanning (ALS), offer the potential to greatly improve the ability to quantify post-fire sediment storage and erosion over time and space across the watershed scale (sensu *Passalacqua et al.*, 2015). Decimeter-scale uncertainty for detecting elevation change means that this technique will be most useful in channels and valley bottoms where detectable changes are most likely. The goal is to relate the measured or expected volumetric changes to rainfall, burn severity, and geomorphic properties—a post-fire research need highlighted in *Moody et al.* (2013).

In June 2012 the High Park Fire (HPF) burned 350 km^2 of primarily montane forest just west of Fort Collins, Colorado, U.S.A. Within the HPF burn area I began intensively monitoring two similar $\sim$15 km^2 watersheds to quantify post-wildfire geomorphic changes (viz., Chapter 3). Subsequent rainfall-runoff floods caused a unique comparison between the two watersheds. One watershed was subjected to a very high intensity summer thunderstorm just one week after the fire was contained—this caused extensive downstream deposition that was not replicated in the other watershed. Fifteen months after burning an exceptionally large and long-duration mesoscale flood caused sustained high flows and erosion in both watersheds; which severely altered the expected post-fire trajectory of erosion and deposition. Two ALS datasets were collected before the mesoscale flood and three ALS datasets in the following two years. This unique collection of sequential ALS data allows us to quantify the geomorphic changes over time and space. The ALS differencing was validated and enhanced by intensive monitoring of 21 channel cross sections and longitudinal profiles in the two study watersheds (Chapter 3), estimating peak flows (Chapters 2 and 3), rainfall thresholds for runoff and sediment delivery (*Wilson et al.*, 2018), measured

hillslope-scale erosion rates (*Schmeer et al.*, 2018), and a more limited study of erosion rates and channel changes in 2013 (*Kampf et al.*, 2016). Together these data allow us to answer two key questions: 1) what are the spatial and temporal patterns of erosion and deposition following a wildfire and a large flood in small- to moderate-sized watersheds (0.1–15 km^2)? and 2) to what extent can these patterns be related to precipitation depths and intensities, burn severity, and valley and basin morphology?

4.2 Site description

Two proximate watersheds burned in the High Park fire, Skin Gulch (SG) and Hill Gulch (HG) were selected to investigate post-wildfire geomorphic changes (Figure 4.1). A control watershed was not chosen due to a lack of ALS data coverage outside the burn area. Both study watersheds drain north into the Cache la Poudre River. Elevations range from 1890 to 2580 m in SG and HG is slightly farther east and lower at 1740 to 2380 m (Table 4.1). Average terrain slopes and drainage density for SG and HG are very similar at 23% and 24%, and 2.5 and 2.3 km km^{-2}, respectively. The two watersheds have nearly identical hypsometric curves with the bulk of the elevations falling within mid-elevations, with some flatter areas in the upper portions of each watershed. Land cover is primarily uninhabited wildland with 81% and 89% evergreen forest in SG and HG, respectively (*Jin et al.*, 2013). SG is predominantly National Forest land, while HG is primarily privately owned. In each watershed there are several very small reservoirs that were presumably established as stock ponds.

Approximately 65% of each watershed was burned at moderate to high severity. In SG most of the area burned at moderate to high severity was in the upper headwaters, while in HG most of the moderate to high severity burn was at lower elevations (Figure 4.1). Straw and wood mulch were applied in 2012 and 2013 to approximately 6% and 18% of the hillslopes in SG and HG, respectively. The underlying geology is primarily schist with scattered rock outcrops (*Abbott*, 1970, 1976; *Braddock et al.*, 1988), and the soils are predominantly Redfeather sandy loams (*HPF BAER Report*, 2012; *Soil Survey Staff*, 2018). Headwater reaches range from wide shallow swales to steep

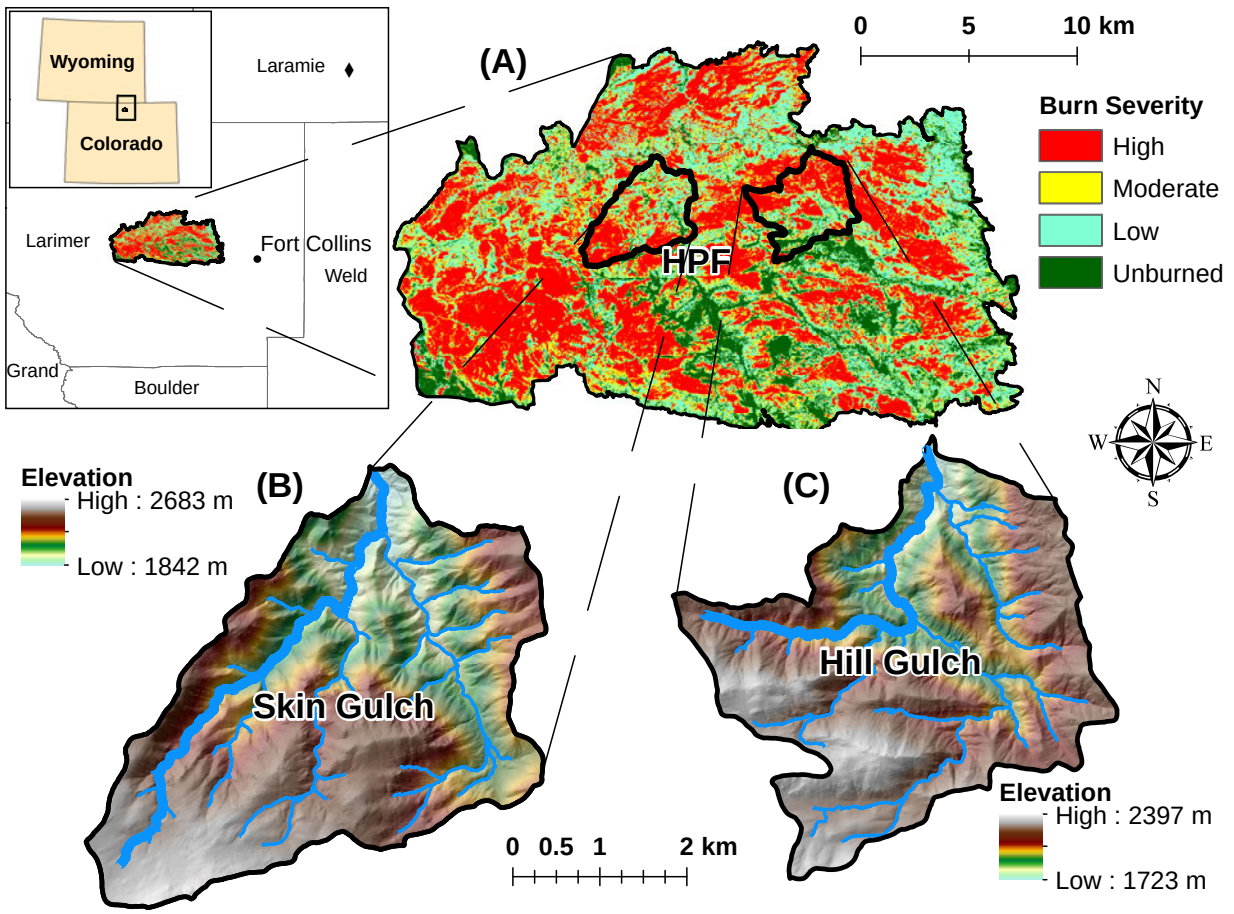

Figure 4.1: Location and burn severity of the (A) High Park Fire (HPF) in the Colorado Front Range of the western U.S., and elevations of (B) Skin Gulch and (C) Hill Gulch. The black diamond to the east of Laramie in (A) is the location of the KCYS Doppler radar station in Cheyenne, WY. The thick blue lines in each watershed represent the reach used to present longitudinal results in Figures 4.10 and 4.11.

and confined, while the middle reaches generally are steep and confined with scattered floodplain pockets, while the downstream reaches are wider with mostly continuous floodplains. Sediment is stored predominantly in the channel bed and in the floodplains. The area is characterized as semiarid with mean annual precipitation of 450-550 mm (PRISM Climate Group, Oregon State University, http://prism.oregonstate.edu). Summer precipitation is usually derived from convective thunderstorms, while spring and fall storms tend to be lower intensity frontal storms. Approximately one-third of the annual precipitation falls as snow.

Table 4.1: General watershed metrics for Skin Gulch and Hill Gulch.

Metric	Skin Gulch	Hill Gulch
Contributing area (km^2)	15.3	14.2
Elevation range (m)	1842-2683	1723-2397
Relief (m)	841	674
Mean slope (%)	23	24
Total stream length (km)	39	33
Drainage density (km km^{-2})	2.5	2.3
Elongation ratio	0.53	0.44

Streamflow in both watersheds was seasonal prior to burning, and the downstream mainstem channels were only about 1-2 m wide. After the fire streamflow increased and became perennial. One week after the fire had been contained a convective storm in SG generated large amounts of hillslope and upstream channel erosion, an estimated peak flow of nearly 30 m^3 s^{-1} km^{-2}, and extensive downstream deposition (Chapter 2); this event is referred to as the 'convective flood' throughout the paper. No comparable storm occurred in HG, but in September 2013 a large mesoscale storm caused widespread and prolonged high flows in both watersheds. Peak flows were estimated to be 2.3–5.7 m^3 s^{-1} km^{-2} in SG and 0.9–1.4 m^3 s^{-1} km^{-2} in HG, with the range of values depending primarily on whether the peak flow is estimated using pre- or post-flood topography (Chapters 2 and 3).

4.3 Methods

4.3.1 ALS preparation

In each of the four years after the fire an ALS dataset was collected over the entire burn area by the National Ecological Observatory Network (NEON) Airborne Observatory Platform. Each ALS dataset is referred to in this paper by the year and month of collection using the format of yyyymm, so the four NEON datasets are 201210, 201307, 201409, and 201506. A fifth ALS dataset, 201310, was collected by the U.S. Geological Survey (USGS) and Federal Emergency Management Agency (FEMA) in fall 2013 to help assess the damage caused by the September 2013 mesoscale flood. The four time periods between the five ALS datasets are referred to in this

paper as T1, T2, T3 and T4. The 201307 ALS data in SG had substantial alignment issues, so I used OPALS (Orientation and Processing of Airborne Laser Scanning software *Mandlburger et al.*, 2009) to improve the flightline alignment. Aerial photographs were collected in 2008 and point clouds covering my study watersheds were constructed from these images using structure-from-motion photogrammetry [unpublished data from S. Filippelli, Colorado State University, 2015]. Unfortunately these data did not allow for accurate volumetric differencing with respect to the first ALS dataset, because extensive vegetation cover hampered the measurement of bare-earth elevations over most of the study area.

For each ALS dataset the raw point clouds were merged, ground classified, and clipped to my two study watersheds using LAStools (*Isenburg*, 2015). Ground classification parameters included: a buffer of 50 m; a step size of 5 m; and an extra fine search for initial ground points. From these processed point clouds digital elevation models (DEMs) with 1 x 1 m pixels were created (*Isenburg*, 2015). Care was taken to align all ALS DEMs as closely as possible using a Python script to calculate the differences in slopes and aspects between each NEON DEM and that of the 201310 USGS/FEMA DEM (following the co-registration methodology from *Nuth and Kääb*, 2011). The resulting estimate of the XYZ translation required to rectify the location of the DEM was repeated until translation changes in X, Y, and Z were less than 1 cm, or the required shift for that iteration was less than 2% of the overall required shift. Each point cloud was shifted by the computed translation, and DEM rasters were recreated from the translated point clouds. Finally, the mean absolute error (MAE) between the rectified point clouds and locally collected total station and RTK-GNSS survey points was computed to determine the ALS accuracy for each dataset.

4.3.2 Valley bottom and contributing area delineation

I used FluvialCorridor, an ArcGIS Toolbox that extracts a number of riverscape features (*Roux et al.*, 2015), to delineate the valley bottoms in each watershed from the 201310 DEM. Defining a channel network is the first step, and for this I set a contributing area threshold of 0.1 km^2 based on local field surveys (*Henkle et al.*, 2011). The valley bottom was then computed and adjusted

using a number of user-controlled input parameters, such as an elevation threshold aggregation and disaggregation distances, buffer sizes, and smoothing tolerance. I adjusted these parameters until the valley bottom delineation satisfactorily matched aerial photographs and 2-m contour lines derived from the 201310 DEM.

Valley bottom polygons were segmented into 50-m long sections oriented in the downstream direction (see Figure 4.2 as an example), yielding 595 segments in SG and 559 segments in HG. FluvialCorridor had difficulty characterizing valley bottoms for the headwaters of several tributaries with gently sloping topography; 89 and 56 segments were removed in the headwaters of SG and HG, respectively, due to unrealistically wide valley widths. Another eight segments near the outlet of SG were excluded because the deposited sediment was repeatedly excavated by the state highway department (for example see Figure 10C in *Kampf et al.*, 2016). Seven more segments in lower SG were excluded during T4 due to channel realignment and rehabilitation efforts, and one more segment was excluded in lower HG during T4 due to the reconstruction of a house. A few other segments were removed from each watershed due to small reservoirs and unreliable ground classification. Ultimately 490 segments in SG and 484 segments in HG were used for summarizing morphometrics (see section 4.3.4) and for statistical analysis (see section 4.3.7).

Contributing area polygons were delineated for each segment using a looped Python script that uses the 'Hydrology' toolset and 'Raster to Polygon' tool in ArcGIS. The resulting polygons were used to determine mean total rainfall and area-maximum maximum 30-minute rainfall intensity for each segment (see section 4.3.3 for more detail). Percent contributing area burned at both high and moderate severity were determined for each segment using a burn severity (BS) map derived from RapidEye imagery and a multistage decision tree (*Stone*, 2015).

4.3.3 Precipitation

The amount and intensity of precipitation over the two study watersheds was determined from the National Weather Service WSR-88D Doppler radar in Cheyenne, WY, corrected with local daily rain gage data. I began by converting dual-polarized one-hour precipitation accumulation

(DAA) radar products into gridded precipitation estimates on a 0.5-km grid. For each day the precipitation was summed for each grid cell from 0700 to 0700 local time to match daily rain gage data. These radar estimates were then compared to the rain gage estimates to come up with a daily mean field bias (*Wright et al.*, 2014):

$$B_i = \frac{\sum G_{ij}}{\sum R_{ij}} \tag{4.1}$$

where B_{i} is the bias for day i, G_{ij} is the daily rainfall for day i and gage j, and R_{ij} is the summed 24-hour rainfall for day i and radar pixel containing j. Sources of gage data include four-inch diameter rain gages monitored by members of the Community Collaborative Rain, Hail & Snow (CoCoRaHS) Network (url: www.cocorahs.org), and tipping-bucket gages monitored by researchers at Colorado State University, the National Center for Atmospheric Research, and the U. S. Geological Survey. The number of rain gages used to compute the bias ranged from 36 to 97 depending on how many of the tipping-bucket gages were active and how many manual observations were recorded for a given day. These gages were located in and around my study watersheds, with the farthest gage being 40 km away.

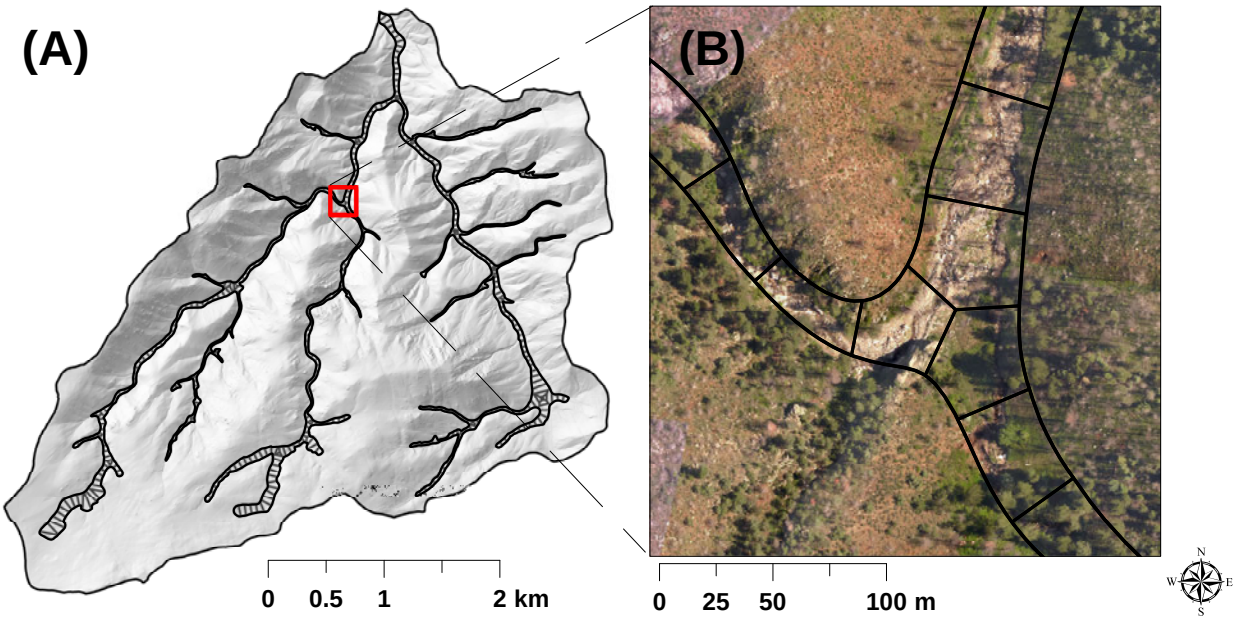

Figure 4.2: Delineated valleys in (A) Skin Gulch derived with the FluvialCorridor ArcGIS Toolbox, and (B) an example of how the valleys were segmented into 50-m lengths. Aerial imagery in (B) was collected at the same time as the 201506 ALS data.

Daily total rainfall and maximum 30-minute precipitation intensity (MI_{30}) were calculated from the bias-corrected DAA radar data for every 0.5-km grid cell across the HPF from October 2012 to November 2015. MI_{30} was chosen over other intensity intervals (e.g., MI_5, MI_{15}, etc.) because it correlates best with peak flood discharge (*Moody et al.*, 2013), and also is closely correlated with hillslope erosion rates from the HPF (*Schmeer et al.*, 2018). Since volume changes over the intervals between ALS datasets represent cumulative geomorphologic effects, daily rainfall was summed for each of the four time periods. In contrast, the maximum MI_{30} value between each ALS dataset was determined for each cell in each watershed. Finally, the mean total rainfall and the maximum MI_{30} was computed for the upstream area of each channel segment for each DoD. This meant that the maximum MI_{30} values for different cells within a given contributing area did not always occur in the same storm since the different summer thunderstorms were often very localized.

4.3.4 Topographic and hydraulic controls

A series of valley bottom, channel, and contributing area metrics, called morphometrics in this chapter, were estimated for each 50-m segment. These data were correlated to the calculated volume changes to help determine possible controls on the volumes of erosion, deposition, and net change. A series of Python scripts were written to clip, extract and compute morphometrics directly from the DEMs and/or a combination of outputs from FluvialCorridor (e.g., stream network, segment polygons, valley widths). Stream networks for each ALS dataset were created for each watershed, and channel slope (S) for each segment was calculated using a linear regression on streamline elevations extracted from each ALS dataset at one-meter intervals. Topographic curvature (ΔS) was quantified for each segment by calculating the slope of a linear regression where the channel slope of the segment and the two upstream segments were plotted against the distance upstream. A positive curvature indicates a decrease in slope, while a negative curvature indicates an increase in slope. Valley width (w_v) was computed at one-meter intervals along the valley centerline and an average width was calculated for each 50-m segment. Valley constriction

and expansion (Δw_{v}) was computed in the same way as ΔS. Since the resolution of the DEMs and aerial imagery were too coarse to accurately delineate the channels, channel width (w_{c}) was estimated from a regional downstream hydraulic geometry equation (*Bieger et al.*, 2015):

$$w_c = 1.24A^{0.435} \tag{4.2}$$

where A is the drainage area in km^2 and channel width is in m.

I defined channel confinement as the ratio of valley width to channel width (C_r). A number of studies use this metric to define whether a channel lies within a confined, partly confined, or unconfined valley (e.g., *Beechie et al.*, 2006; *Rinaldi et al.*, 2013). While these categories are helpful for determining the ability for a channel to meander, they are not applicable here because the channel segments are steep and predominately confined.

Unit stream power, a hydraulic control, is often a good predictor of erosion and deposition (e.g., *Baker and Costa*, 1987). Unit stream power is equal to:

$$\omega = \frac{\gamma Q S_f}{w_c} \tag{4.3}$$

where γ is the specific weight of water (N m^{-3}), Q is discharge (m^3 s^{-1}), and S_f is the friction slope (m m^{-1}). Because continuous stage or flow data was not available, and given the potential uncertainty in the regression equation for w_c, I used the ratio of channel slope to valley width ($\frac{S}{w_v}$) as a proxy for stream power. Downstream changes in the slope-width ratio ($\Delta\frac{S}{w_v}$) were computed in the same way as ΔS and Δw_{v}.

4.3.5 Valley change

DEMs of difference (DoDs) were computed using the geomorphic change detection (GCD) tool add-in for ArcGIS (gcd.joewheaton.org, version 6; *Wheaton et al.*, 2010). GCD uses a fuzzy inference system (FIS) to propagate spatially explicit DEM uncertainties, and consequently the uncertainties in the DoD. Spatially propagated errors are much more accurate than assuming a

uniform uncertainty, as the latter can drastically under- or over-estimate volumes of erosion and deposition (e.g., *Milan et al.*, 2011; *Wheaton et al.*, 2010).

Point quality, point density, and slope were included as membership functions in my FIS procedure. I assumed uniform point quality based on the accuracy of the ALS after adjustment (i.e., the MAE for each dataset). Point density was computed for each DEM pixel based on the point cloud, and each pixel slope was derived directly from the DEM. Pixels with elevation changes smaller than the spatially propagated errors were ignored, and the remaining values constitute the thresholded DoD. The GCD tool also calculates total volumes of erosion, deposition, and net change, along with the uncertainty for each volume estimate. The uncertainties in the total volumes of erosion and deposition are computed by multiplying individual error heights times the pixel area and summing these. Uncertainty in each net volume difference is propagated from the corresponding uncertainties in erosion and deposition. Using the thresholded DoDs and my own Python script I computed the volumes of erosion, deposition, and net change for each 50-m segment for each time period.

The sign and overall magnitude of ALS-derived volumetric changes for the 50-m segments were compared to the surveyed changes at 10 cross sections in SG and 11 cross sections in HG (see Chapter 3 for more information on the field data). The measured changes in cross-sectional area were multiplied by 50 m to obtain volumes that were then compared to the calculated ALS volume change for a given segment.

4.3.6 Removal of spurious vegetation artifacts

A visual check of the DoD results revealed the calculated volume changes were being affected by seasonal changes in leaf cover. For example, some locations had up to 3 m of deposition from fall to summer (i.e., 201210–201307, 201409–201506), and nearly identical amounts of erosion from summer to fall (i.e., 201307–201310). Vegetation issues were not immediately obvious in the 201310–201409 DoD, as both ALS datasets were collected in the fall. A raster-based algorithm was written to identify possible locations of spurious changes due to changes in the deciduous leaf

cover on a pixel-by-pixel basis for the DoDs that covered different seasons (i.e., T1, T2, and T4). This algorithm took the form:

$$\begin{aligned} if(DoD_{T1} - DoD_{T4} \leq \theta and DoD_{T4} + DoD_T2 \leq \theta and DoD_T2 + DoD_T1 \leq \theta), \\ or(DoD_{T1} - DoD_{T4} \leq \theta and DoD_{T4} + DoD_T2 \leq \theta), \\ or(DoD_{T1} - DoD_{T4} \leq \theta and DoD_{T2} + DoD_T1 \leq \theta), \\ or(DoD_{T4} + DoD_{T2} \leq \theta and DoD_{T2} + DoD_T1 \leq \theta), \\ then pixelvalue = 0, \\ else pixelvalue = 1 \end{aligned} \tag{4.4}$$

where $DoD_{T\#}$ refers to the DoD for a given time period (i.e., T1, T2, or T4), and θ is a threshold in meters. I used this algorithm to classify each pixel as a 0 or 1, with z indicating a seasonal vegetation artifact when at least two of the three DoDs showed a difference in elevation change that was less than or equal to 1-m (θ). This newly created raster of 1's and 0's was then multiplied on a cell-by-cell basis with each of the DEMs to exclude the seasonal vegetation artifacts, and the GCD tool was rerun to more accurately estimate the volume and uncertainty of geomorphic changes. Figure 4.3 shows an example of this vegetation filtering for a location in Skin Gulch that had around 1 to 3 m of deposition from fall 2012 to summer 2013, before filtering out vegetation-influenced pixels (Figure 4.3A), and around 1 to 3 m of erosion from summer 2013 to fall 2013 (Figure 4.3B). A site visit in September 2016 verified the lack of such large-scale geomorphic changes and confirmed a predominantly deciduous cover of narrowleaf cottonwood, Rocky Mountain maple, alders, chokecherry, and wild raspberries (Figure 4.3C).

4.3.7 Statistical analysis of controls on erosion and deposition

Pearson correlation coefficients were calculated for each time period and watershed between the different site factors and the calculated total erosion, total deposition and net volume changes

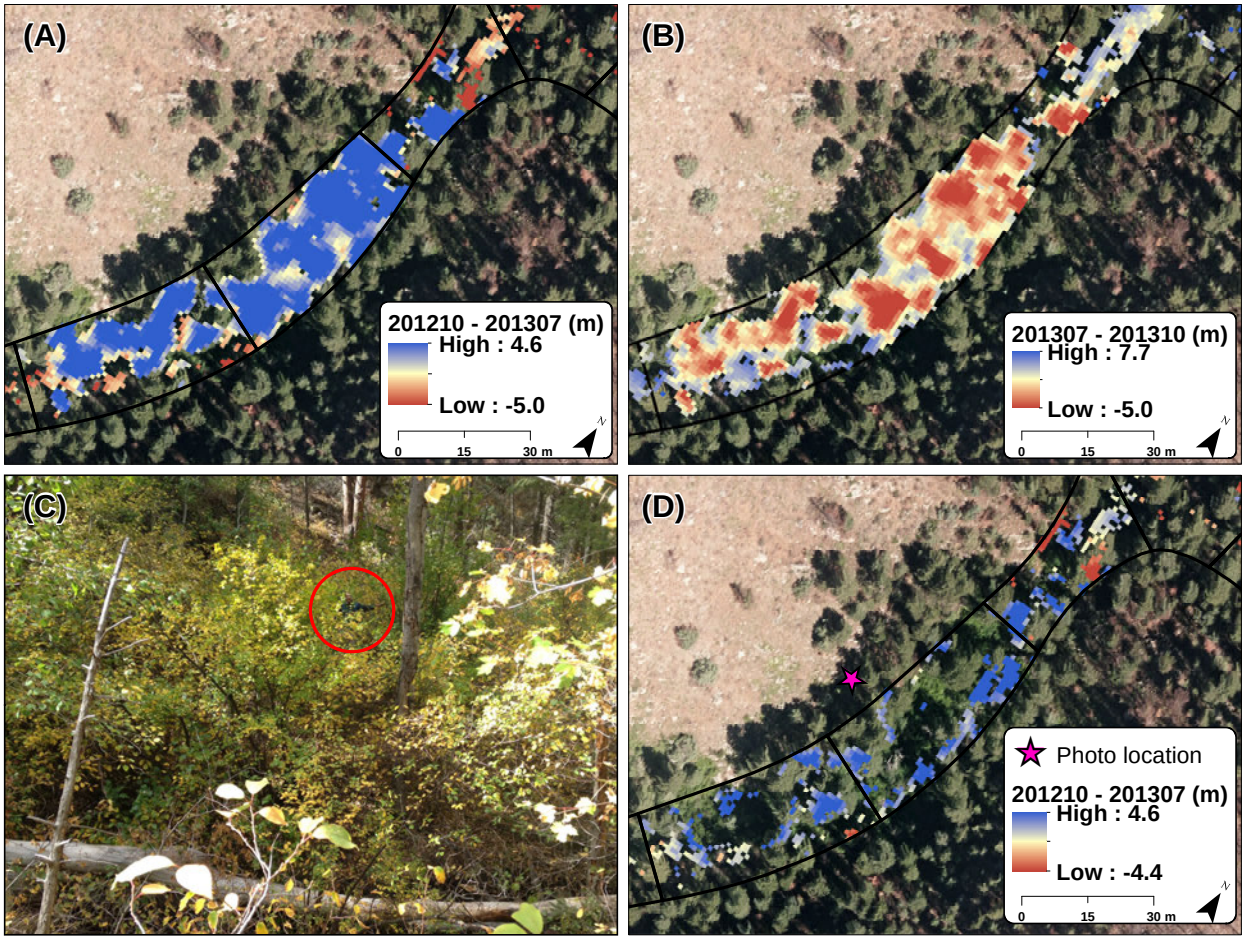

Figure 4.3: Seasonal changes in vegetation led to spurious deposition during fall to summer DoDs (A), and (B) spurious erosion in the summer to fall DoDs. The valley bottom in (A) and (B) includes several woody deciduous species along with some ponderosa pine (C). (D) shows the remaining change after using my raster-based algorithm to reduce the errors due to leaf out and leaf drop. Red circle in (C) identifies the upper half of a person standing in the understory, and the pink star in (D) represents the approximate location of the photo in (C).

in the 50-m segments. The different site factors were total rainfall, MI_{30}, percent of contributing area burned at high and/or moderate severity, and drainage network morphometrics (as explained in section 4.3.4). Since some of the morphometric variables changed from the beginning to the end of a given time period (i.e., S, ΔS, $\frac{S}{w_v}$, and $\Delta\frac{S}{w_v}$), I calculated the correlations for each time period using both the before and the after values. I found negligible differences in the strength of the correlations depending on whether I used the before or after values, so I only present the results for the before values. Normalizing the net volume changes by contributing area generally did

not improve the correlations, so these results also are not presented here. Correlations were also calculated after stratifying the data by channel slope (< or $\geq$ 4%) and contributing area (< or $\geq$ 4 km^2), but these results are not presented. I did not stratify the data by physiographic unit or lateral confinement as suggested by *Rinaldi et al.* (2013) and *Nardi and Rinaldi* (2015) because the stream type in my two study watersheds is predominantly classified as cascade (*Montgomery and Buffington*, 1997). It should be noted that a positive correlation indicates either increasing deposition or decreasing erosion with an increasing independent variable, while a negative correlation indicates decreasing deposition or increasing erosion. Although the data are not independent because erosion and deposition in upstream reaches influences downstream reaches. Auto-correlations of dependent variables generally fall below $r = 0.5$ within five segments upstream or downstream, and the correlations provide a useful metric for exploring relationships between watershed morphology and patterns of erosion and deposition. In the results I primarily focus on correlation coefficients that are greater than 0.32 and less than -0.32 (i.e., $R^2 > 0.10$).

4.4 Results

4.4.1 Precipitation

Total rainfall and maximum 30-minute intensities varied considerably between each DoD time period, but the values were relatively similar between and within the two watersheds (Figure 4.4; Table 4.2). The lowest amount of precipitation was in T1 with a mean of 174 mm for SG and 185 mm for HG (Figure 4.4A). This period also generally had the lowest MI30 other than a few very localized higher values (Figure 4.4B). The second period included the large mesoscale storm and the rainfall from this storm was distributed relatively evenly across both watersheds (*Kampf et al.*, 2016). For this three-month period the total rainfall ranged from 276 to 439 mm (Figure 4.4C). Rainfall intensities during T2 tended to have the highest MI_{30} values for any of the four periods as these ranged from 32 to 73 mm hr^{-1} in SG and 36-106 mm hr^{-1} in HG (Figure 4.4D), but closer inspection of the rain gage data shows that the higher values were due to convective summer thunderstorms prior to the lower-intensity mesoscale flood (*Kampf et al.*, 2016).

Table 4.2: Mean total rainfall (P) and mean maximum 30-min intensities (MI_{30}) for Skin Gulch and Hill Gulch for each time period (T1: 201210 to 201307, T2: 201307 to 201310, T3: 201310 to 201409, T4: 201409 to 201506). Ranges are in parentheses.

Time period	Months	Skin Gulch		Hill Gulch	
		P (mm)	MI_{30} (mm h^{-1})	P (mm)	MI_{30} (mm h^{-1})
T1	8	174 (156–234)	24 (11–85)	185 (175–205)	17 (13–32)
T2	3	366 (276–439)	49 (32–73)	327 (302–439)	49 (36–106)
T3	11	527 (441–634)	38 (23–63)	488 (443–559)	41 (21–71)
T4	9	340 (259–403)	30 (17–39)	397 (362–446)	38 (26–58)

The third period of nearly a year generally had the greatest total rainfall of 441 to 634 mm (Figure 4.4E), but lower MI_{30} values of 21 to 71 mm hr^{-1} (Figure 4.4F; Table 4.2). Again the variation in maximum MI_{30} values was greater than the variation in total rainfall, and this is due to the high spatial variability in the summer thunderstorms. Total rainfall during the fourth time period was lower than T2 and T3 at 259 to 446 mm (Figure 4.4G), and mean MI30 values were also lower at about only 30 mm $hr^{-1}$for SG and 38 mm $hr^{-1}$for HG (Figure 4.4H; Table 4.2), indicating a smaller potential for inducing channel geomorphic change.

4.4.2 ALS data accuracy and valley morphometrics

Point density increased with each ALS dataset from a minimum of just under 1.2 pts/m^2 in the first ALS dataset to over 3.5 pts/m^2 for the last dataset in Skin Gulch and the next to last dataset in Hill Gulch (Table 4.3). Mean absolute errors (MAE) of the final ALS point clouds in each watershed were only 9-13 cm, except for the MAEs of 23 and 15 cm for the first and second ALS datasets in HG, respectively (Table 4.3).

A comparison of the volume changes calculated from cross section data and the calculated volume changes from the ALS data for the corresponding segments generally fall along a 1:1 line except for one comparison for the second period in Skin Gulch and sevaral comparison for the first time period in Hill Gulch (Figure 4.5). The differences between these two datasets should not be too surprising given that the measured cross-section change was extrapolated to the entire 50-m segment. The main point is that the general agreement in the sign and magnitude of the ALS

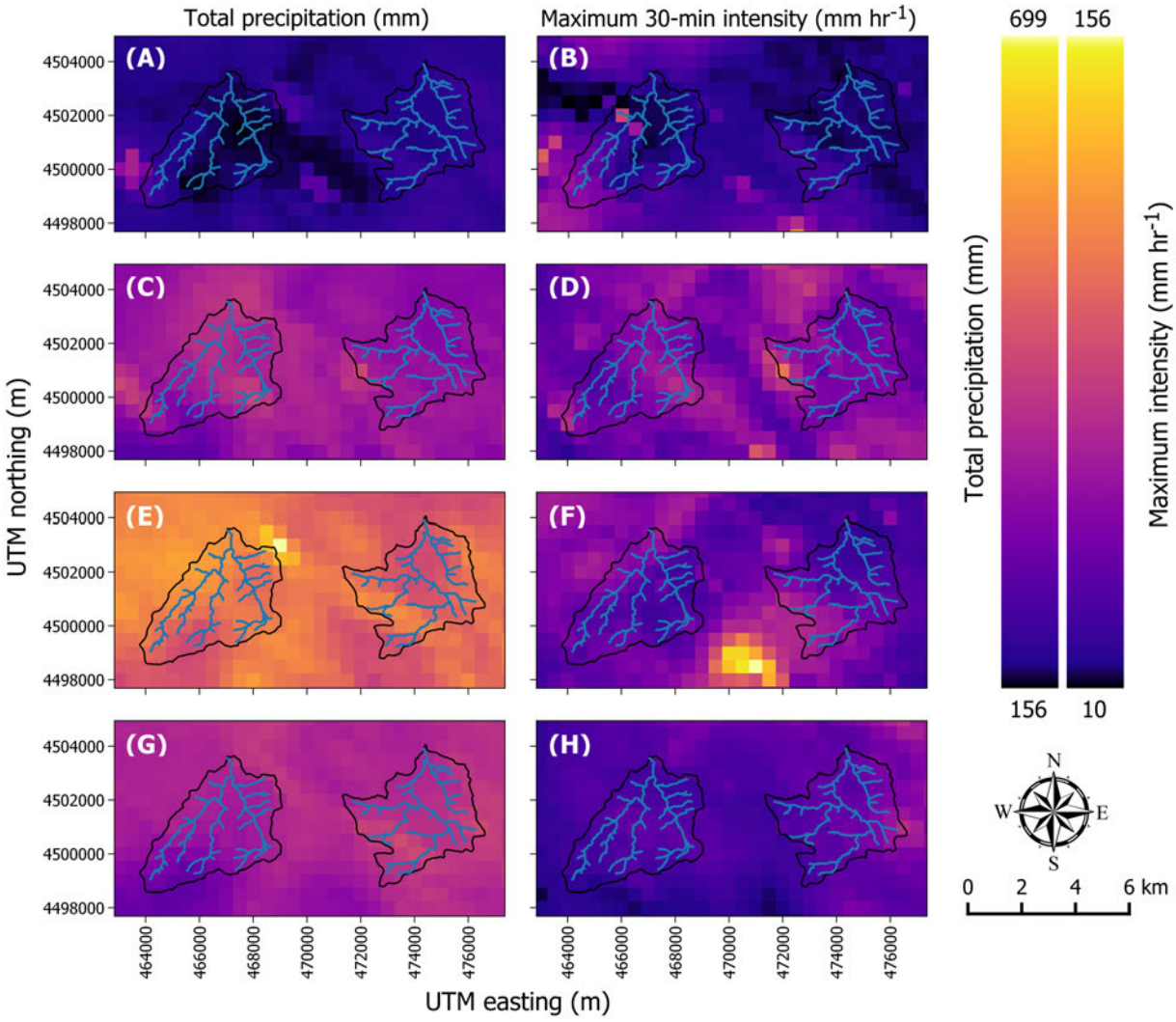

Figure 4.4: Total rainfall (mm) and maximum 30-minute intensity (mm hr^{-1}) for the time periods between each successive DoD for: (A, B) 201210 to 201307; (C, D) 201307 to 201310; (E, F) 201310 to 201409; and (G, H) 201409 to 201506. Within each panel Skin Gulch is the watershed on the left and Hill Gulch is to the right.

differencing and measured cross-section change indicates that my ALS differencing is producing reasonable results.

The inherent comparability of SG and HG is further confirmed by the generally similar spatial distributions and trends in channel slopes, valley widths, and confinement ratios (Figure 4.6). For the 490 segments in SG and 484 segments in HG used in my analyses 86% and 73% had channel slopes greater than 0.065 m m^{-1}, respectively, and were classified as cascade according to *Mont-*

Table 4.3: Point density and average mean absolute error (MAE) for each ALS dataset for Skin Gulch and Hill Gulch, respectively. MAE was determined by the elevation difference between total station and RTK-GNSS survey points and interpolated ALS points.

ALS dataset	Skin Gulch		Hill Gulch	
	Point density (pts/m^2)	MAE (cm)	Point density (pts/m^2)	MAE (cm)
201210	1.16	12	1.18	23
201307	2.00	11	2.21	15
201310	3.01	11	2.78	9
201409	3.27	12	3.82	10
201506	3.67	13	2.21	13

gomery and Buffington (1997). In SG and HG, respectively, 13% and 22% of the segments had channel slopes of 0.03 to 0.065 m m^{-1}, which would be classified as step-pool, and less than 2% and 5% of the segments had channel slopes less than 0.03 m m^{-1}, and were classified as either pool-riffle or plane bed (*Montgomery and Buffington*, 1997). The few channels with slopes less than 0.03 m/m are primarily in a few headwater areas, near tributaries, and towards the outlet of each watershed (Figure 4.6).

Valley widths tended to increase downstream, with the exception of certain headwater locations where FluvialCorridor had difficulty characterizing the valley bottoms, while confinement ratios tended to decrease downstream (Figure 4.6). Approximately 80% of the valley widths in each watershed were between 10 and 40 m. Confinement ratios in the two watersheds were relatively similar with about 75% of the valley bottoms having values between 10 and 35, about 20% were greater than 35, and no segments were less than 5.

4.4.3 Spatial and temporal erosion and deposition volumes

T1 (201210–201307) included both spring snowmelt and some summer thunderstorms in 2013, and during this period there were considerable variations in the spatial patterns of deposition and erosion within and between the two watersheds (Figures 4.7-4.11; see also Figures D.1–D.4). In SG there was more deposition than erosion, which resulted in a net volume difference of 7,900 m^3 (Figure 4.7A). Little erosion or deposition occurred in the headwaters during this time period, especially in the westward flowing channels in the easternmost part of the watershed (Figure 4.8A).

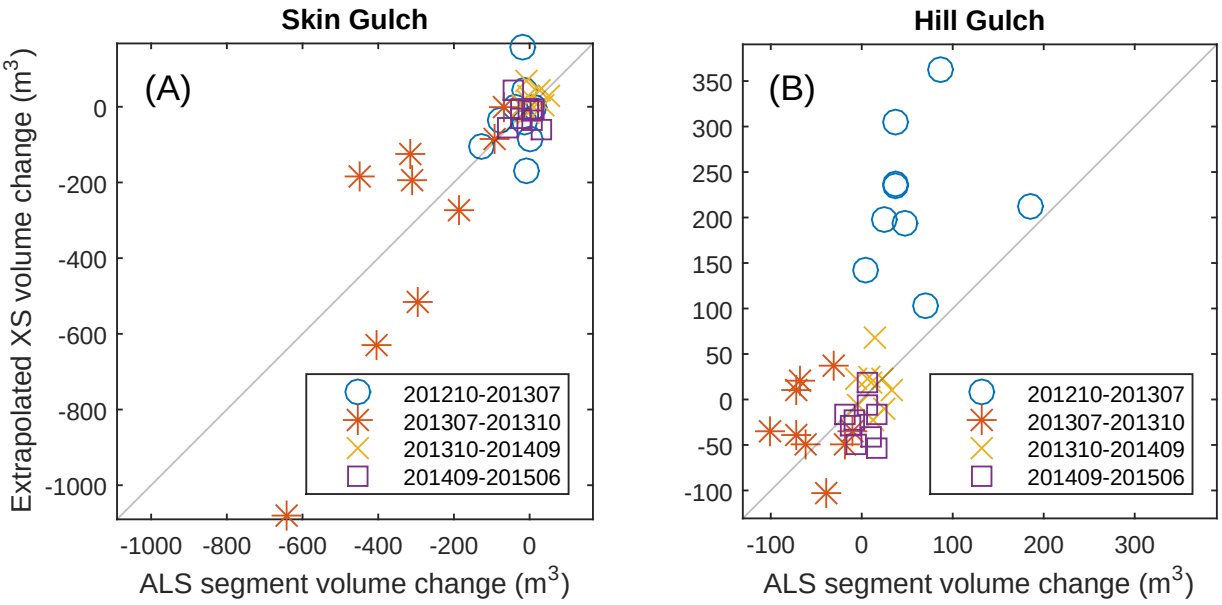

Figure 4.5: Comparison of the extrapolated cross section (XS) volume change and the ALS segment volume change for (A) Skin Gulch and (B) Hill Gulch. Diagonal lines are the 1:1 relationship.

In the middle portions of SG deposition was predominant (Figure 4.8A), and this was particularly evident on the main stem about 4-5 km above the outlet (Figure 4.10B). Lower in the watershed there was net erosion and only limited deposition (Figures 4.8A and 4.10B). This erosion in the lower watershed was due primarily to snowmelt incising through the large amounts of sediment that had been deposited during the previous summer (Figure 4.12). In particular the greatest erosion of 130 m^3 was just downstream of a confluence about 2 km from the outlet (Figures 4.10B and 4.12), which is a result of substantial deposition associated with a large convective flood just after the fire (see reference to confluence and XS6 in Chapters 2 and 3). This location also coincides with a decrease in channel slope and widening of the main valley (Figure 4.10A). In general, however, there was not a clear association between the amounts of erosion or deposition and morphometric characteristics for this time period in SG, because the first ALS dataset in fall 2012 was collected only after there had been extensive hillslope erosion and downstream deposition.

In HG there was 19,000 m^3 of net deposition during T1, mostly in the main channels about 2-4 km above the watershed outlet (Figures 4.7B, 4.9A, and 4.11B). This deposition is where the

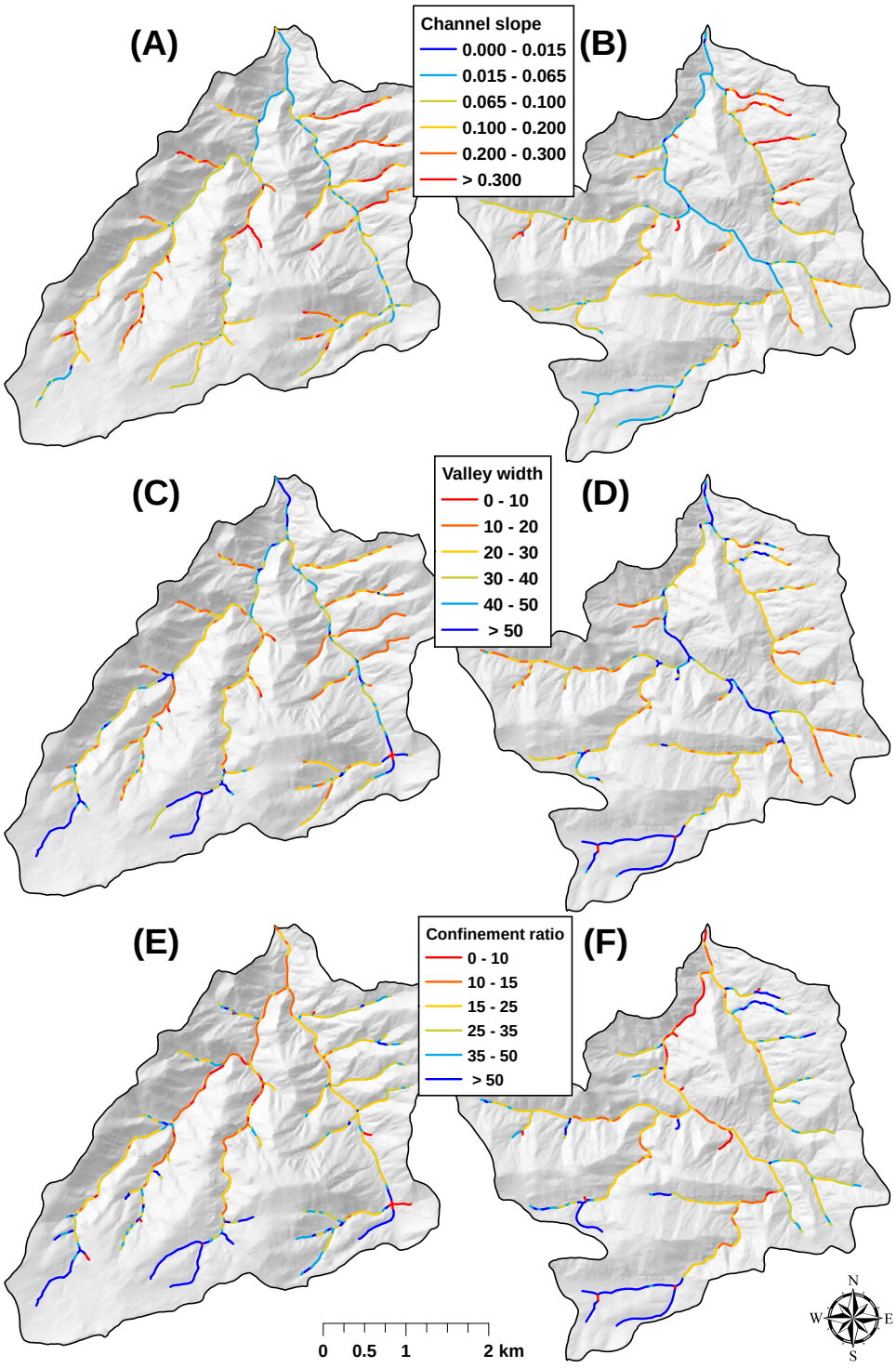

Figure 4.6: Spatial distribution of channel slopes averaged across all ALS datasets (A, B), valley widths (C, D), and confinement ratios (E, F) in Skin Gulch (left) and Hill Gulch (right).

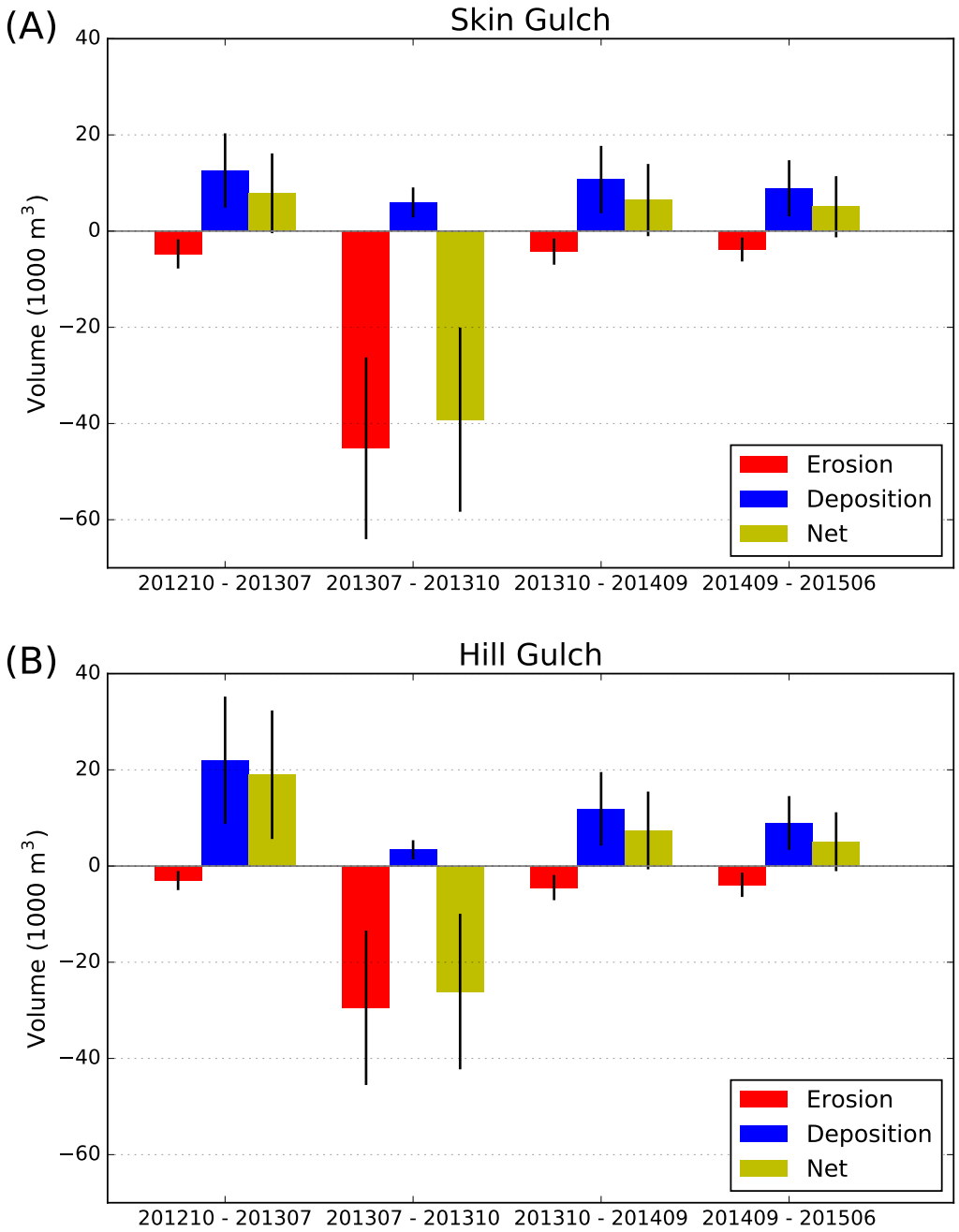

Figure 4.7: Total valley erosion, deposition, and net volume change for each time period for (A) Skin Gulch, and (B) Hill Gulch. Black vertical bars indicate the uncertainty in the volume estimates.

channel slopes generally decrease to less than ~0.10 and valley widths increase to more than ~30 m (Figures 4.5 and 4.11). Peak deposition of nearly 300 m^3 was in a segment about 2.5 km from the outlet, which is where the valley width abruptly increases to nearly 75 m and the slope drops below 0.05 (Figure 4.11). Similar to SG, the headwaters in HG had only minor erosion or deposition and there was a distinct lack of geomorphic changes in the westward-flowing channels in the easternmost portion of the watershed (Figure 4.9A). Aerial imagery and soils data (*Soil Survey Staff*, 2018) indicate that these areas are steeper with a greater density of exposed rock outcrops, suggesting shallower soils. These characteristics, combined with the steep narrow channels, would reduce the amount of available sediment to be eroded and also provide less space for deposition.

In September 2013, 15 months after the fire and during T2, the mesoscale flood resulted in widespread and often dramatic erosion in SG (Figure 4.13; Chapters 2 and 3). Erosion in the SG headwaters was mild compared to the extensive channel changes in the middle and downstream reaches (Figures 4.8B, and 4.10C). In the middle reaches channel incision was common, especially where the valley was more narrow (Figures 4.5, and 4.13D, 4.13E and 4.13F). Channel widening and a few avulsions occurred in the downstream reaches where the valley was wide enough to contain a more continuous floodplain (Figures 4.5, 4.13B, and 4.13C). Many of the segments with the greatest erosion were in areas where there was more sediment available to be eroded. These locations included floodplain pockets (e.g., ~2.5 km, ~2.9 km and ~3.5 km from the outlet), tributary junctions (e.g., ~1.4, ~2.0 km and ~3.7 km from the outlet), colluvial deposits from hollows (e.g., ~1.8 km from the outlet), and deposition from a combination of processes (e.g., ~0.6 km and ~1.0 km from the outlet). The pre-fire sediment is believed to have been deposited over centuries and millennia (*Cotrufo et al.*, 2016), while the extensive hillslope erosion in summer 2012 and 2013 added considerably more sediment (Chapters 2 and 3). These post-fire deposits along with substantial amounts of the pre-fire sediment were largely washed away during the mesoscale flood (Figure 4.10).

The greatest erosion in SG during T2 was at ~1.8 km from the outlet where over 1,800 m^3 of sediment was removed (Figure 4.13B and 4.13C); the four segments upstream from this location

also experienced substantial erosion, which was due in part to the particularly large amounts of deposition from the large convective flood that occurred just after the fire (see reference to confluence and XS6 in Chapters 2 and 3; Figures 4.8B, 4.10C and 4.12). Up to 4.4 m of incision occurred near a confluence in the middle reaches of the watershed (Figure 4.14). Overall the total erosion in SG during T2 was 3.6 times larger than the total deposition during T1, with this large difference being due to the fact that most of the post-fire sediment was deposited in summer 2012, before the first ALS survey. Similar to T1, there was little to no geomorphic changes during T2 in the westward-flowing channels in the easternmost part of each watershed (Figure 4.8B).

During T2 HG also experienced widespread erosion (Figures 4.8B and 4.9B; Chapters 2 and 3), but the net volume change was only two-thirds of the net volume change in SG (Figure 4.7). Similar to SG, the greatest erosion in HG was in locations where more long-term pre-fire sediment had been stored; these include floodplain pockets (e.g., ~2.4 km, ~3.7 km and ~4.7 km), tributary junctions (e.g., ~2.2 km and ~3.3 km), and colluvial deposits from hollows (e.g., ~4.4 km; Figures 4.11 and 4.15). Substantial erosion also occurred where the hillsides constricted the valley width to less than 20 m; for example, there was over 800 m^3 and 1300 m^3 of erosion around 3.4–3.5 km and 3.8–4.0 km from the outlet, respectively (Figure 4.11C). Similar to T1 there was little to no geomorphic changes in the westward flowing channels in the easternmost part of the watershed (Figure 4.9B).

The pattern of erosion during T2 closely mirrored the depositional patterns from T1 (Figures 4.10 and 4.11), and this was particularly true for HG because of the greater deposition recorded during T1. For example, there was 2,300 m^3 of deposition in the valley bottom in HG between 2 and 3 km upstream of the outlet during T1, and this large amount of deposition was where the slope decreases to around 0.04 m m^{-1} and the valley width increases to 55 m, resulting in decreased slope-width ratio. During T2 this same reach experienced 2,700 m^3 of erosion.

During T3 the patterns of erosion, deposition, and net change in both watersheds were similar in direction and location to T1 but smaller in magnitude (Figure 4.7). The magnitudes of change were more similar between the two watersheds in T3 than in T1 because there was no undocu-

mented erosion or deposition. During T3 erosion in the southeastern headwaters in SG resulted in deposition at small alluvial fans (Figure 4.8C). Additional deposition again occurred about 4-5 km from the outlet on the mainstem (Figure 4.10D), while farther downstream there was a more equal balance between erosion and deposition (Figure 4.8C). The greatest erosion in SG occurred at a confluence around 3.7 km from the outlet where there was bank sloughing, which was largely a result of the channel incision and bank oversteepening that took place during the mesoscale flood in the previous time period (Figures 4.10D and 4.14). A few segments with steep slopes and rock outcrops at the edge of the valley margin had large erroneous erosion estimates. Errors in estimating the location and elevation of the ground on steep slopes were primarily due to ALS interpolation error and horizontal displacement error (*Hodgson and Bresnahan*, 2004). For example, the segment with the greatest erosion of 170 m^3 at 2.1 km from the outlet was due to a 10+ m rock outcrop (Figures 4.8C and 4.10D); this outcrop can be seen in the far left background of Figures 4.12C and 4.12D. Another segment on the eastern part of the watershed with large erroneous erosion was also due to a large rock outcrop (Figure 4.8C).

In HG during T3 there was more consistent deposition from the headwaters to the outlet (Figure 4.9). The total volume changes in HG were slightly greater than in SG, but this difference is much smaller than the 2-3-fold difference between SG and HG in T1 (Figure 4.7). The largest estimated volumes of deposition were in the headwaters, presumably due to hillslope erosion, and in the lowest portion of the watershed where sediment was reworked from spring snowmelt and summer thunderstorms (Figure 4.9C). Many of the pixels of deposition on the floodplains appear to be due to inaccurate ground elevations in thick vegetation. The segments with the greatest erosion were scattered throughout the watershed (Figure 4.9C), and many of the pixels composing these segments appear to have inaccurate ground elevations in thick vegetation and steep rocky sections.

The magnitude of total net volume change in T4 was less than any of the other time periods (Figure 4.7). The overall pattern in both watersheds—like in T1 and T3—was deposition with very little erosion and a net volume change of just over 5,000 m^3.

The similarity in total erosion, total deposition, and net volume changes between the two watersheds indicate that the summer thunderstorms, hillslope erosion, downstream deposition, and erosion due to snowmelt were the primary drivers of change in the channels and valley bottoms, but absolute magnitudes in the third year after burning were less (Figure 4.7). As with the other time periods there generally were minimal changes in the headwaters of each watershed (Figures 4.8-4.11). The majority of the large volumetric changes were in the middle and lower portions of both watersheds. Again, however, many of the pixels showing the most change appear to be artifacts of either unreliably determined ground points in thick vegetation or the effects of steep slopes and rock outcrops.

To summarize, the calculated volume changes for SG and HG were similar in their direction over the four time periods, as well as roughly similar trends in magnitude (Figure 4.7). Net volume changes in T1, T3, and T4 for both channel networks were positive, indicating that the primary effect of the fire and subsequent rainstorms was erosional at the hillslope scale and depositional at scales larger than a few km^2. Over these three time periods both watersheds showed a decrease in the amount of geomorphic change over time, particularly in HG, as the net volume change dropped from 19,000 m^3 in the first period to just over 7,000 m^3 and 5,000 m^3 in the third and fourth periods, respectively (Figure 4.7B). In SG the net volumes over these same time periods showed a smaller decrease from nearly 8,000 m^3 in T1 to over 6,000 m^3 and then 5,000 m^3 in T3 and T4, respectively (Figure 4.7A). Total deposition over all four time periods was just over 38,000 m^3 in SG and just over 46,000 m^3 in HG, while total erosion over all four time periods was similar with nearly 58,000 m^3 in SG and nearly 41,000 m^3 in HG. Seventy-eight percent and 72% of the total erosion in SG and HG, respectively, took place during T2 as a result of the September 2013 mesoscale flood. This means that in the absence of the highly unusual mesoscale flood the HPF would ultimately have caused extensive net deposition at scales greater than a few km^2.

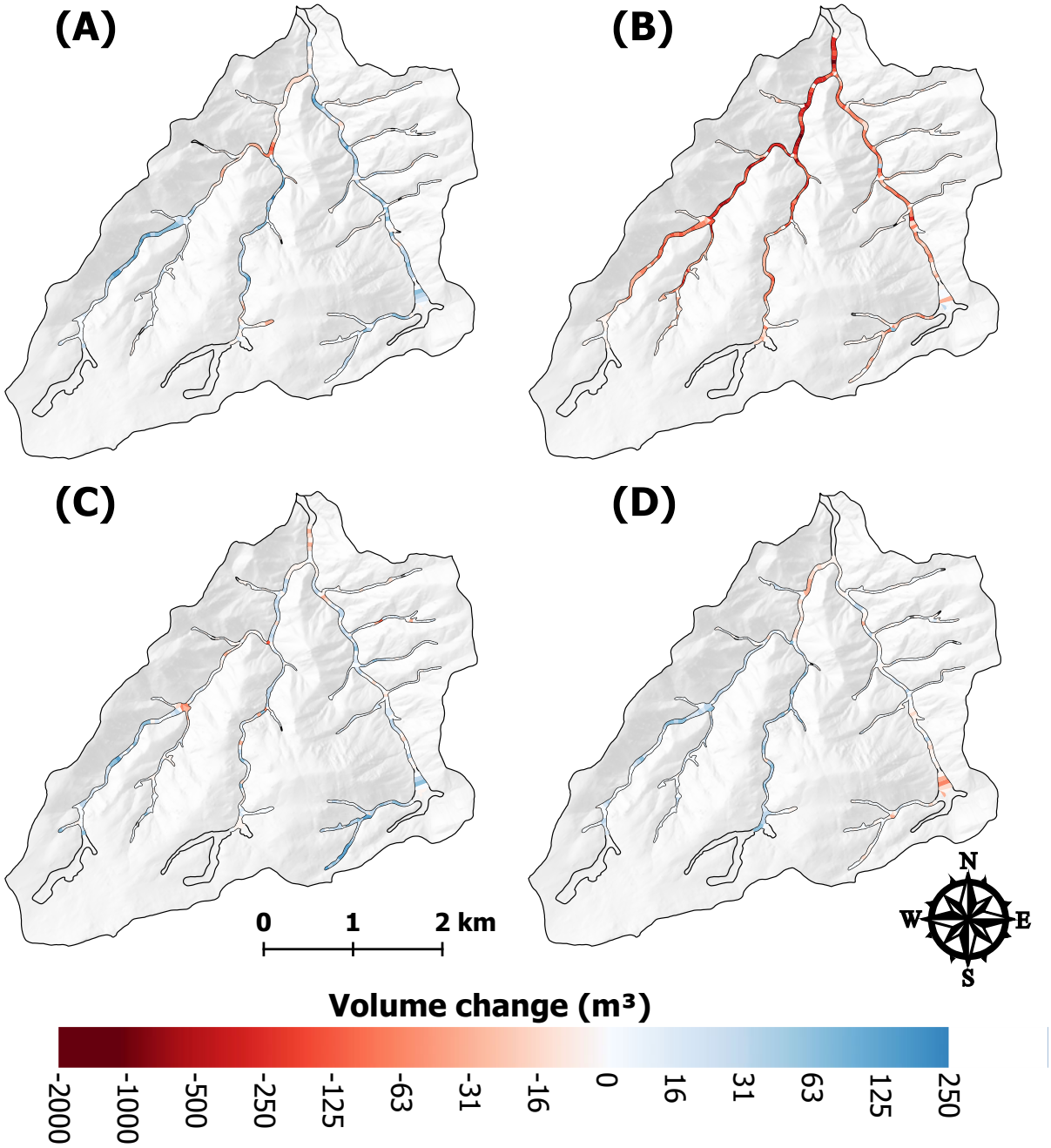

Figure 4.8: Net volume differences for each valley bottom segment in Skin Gulch for (A) 201210–201307, (B) 201307–201310, (C) 201310–201409, and (D) 201409–201506. Calculated volumes are not reported for the transparent segments due to unrealistically wide valley widths, repeat excavations, or the ground surface could not be reliably determined.

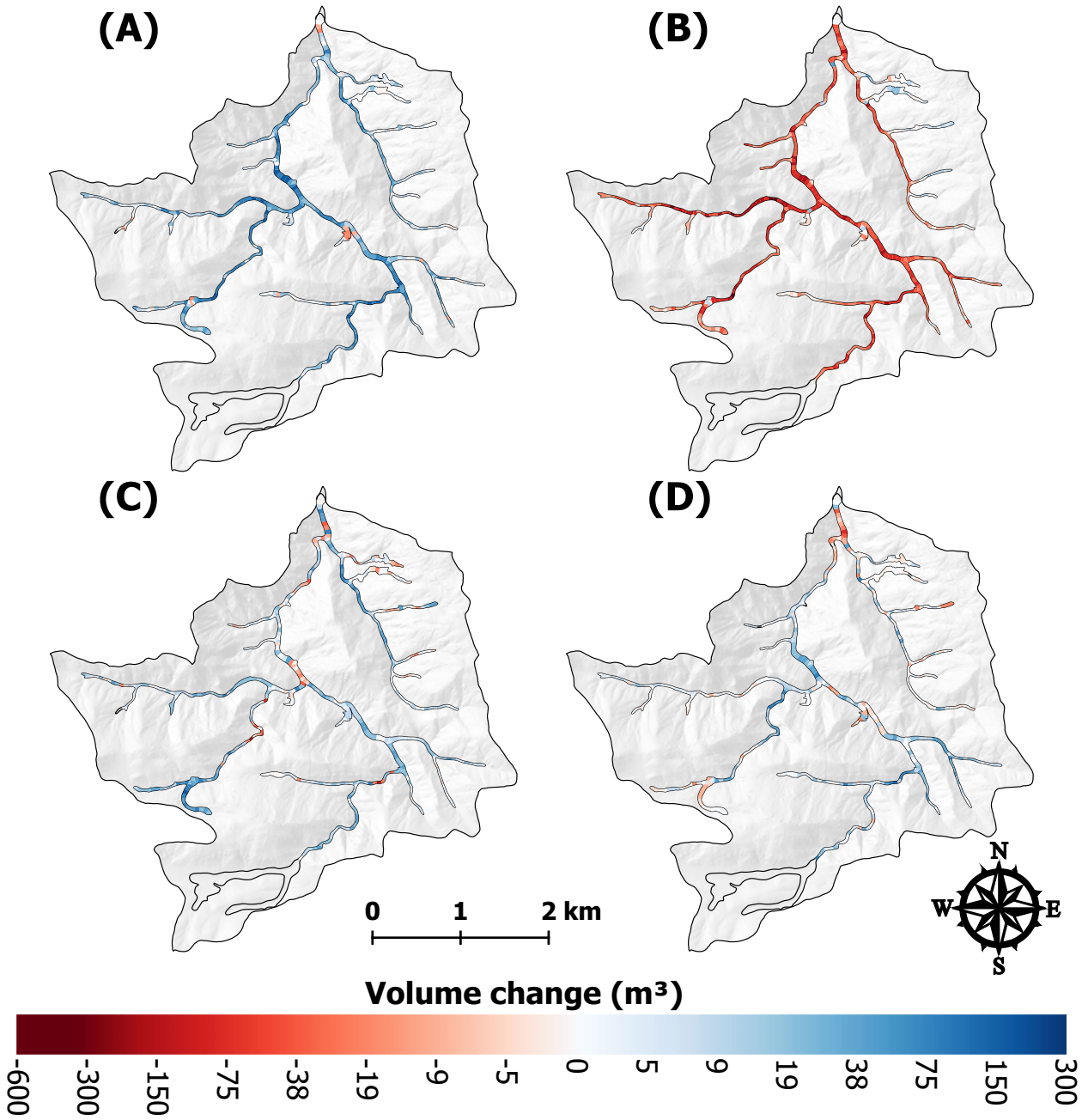

Figure 4.9: Net volume differences for each valley bottom segment in Hill Gulch for (A) 201210–201307, (B) 201307–201310, (C) 201310–201409, and (D) 201409–201506. Calculated volumes are not reported for the transparent segments due to unrealistically wide valley widths, repeat excavations, or the ground surface could not be reliably determined.

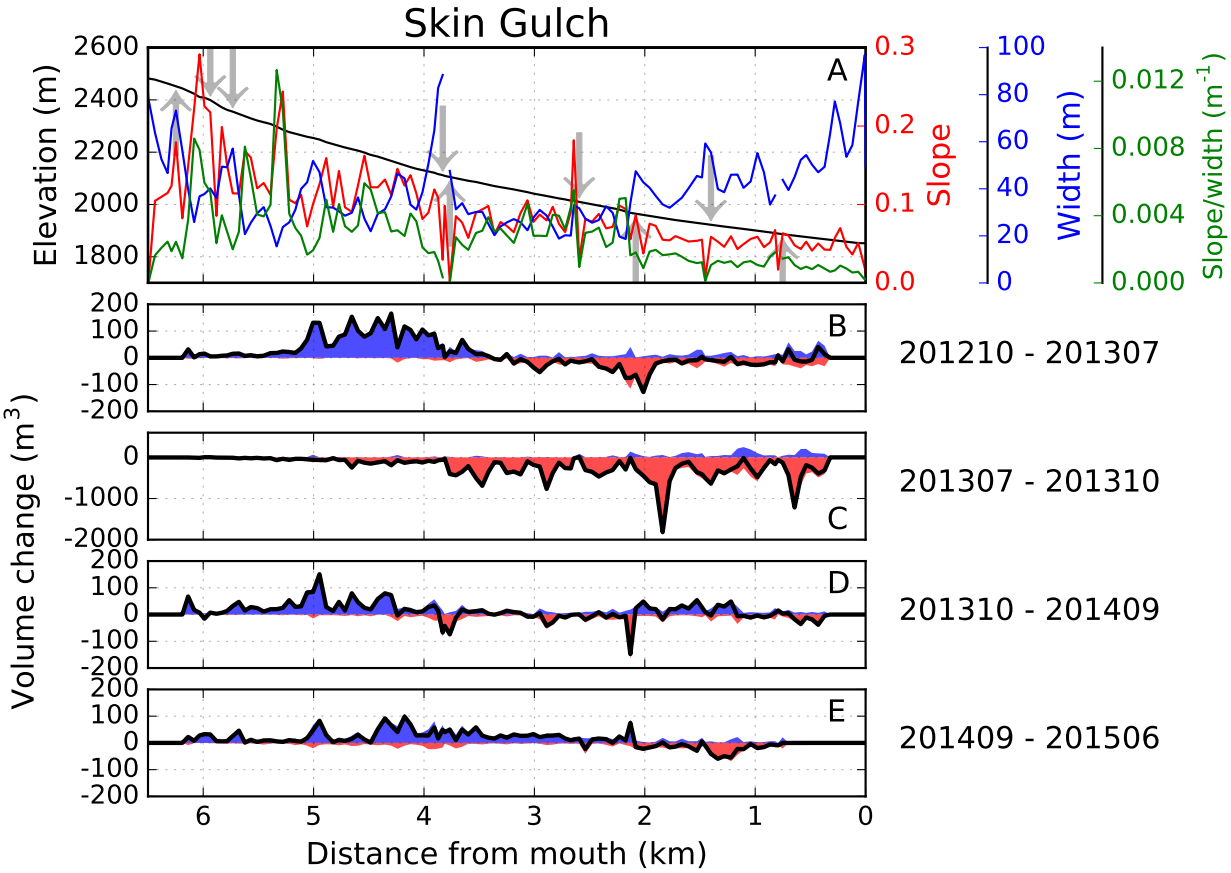

Figure 4.10: Longitudinal distributions in Skin Gulch of (A) elevation, channel slope, valley width and slope/width, and the corresponding change in volume for (B) 201210–201307, (C) 201307–201310, (D) 201310–201409, and (E) 201409–201506. Up and down arrows in (A) represent tributaries that enter the main channel from the right and left, respectively. Blue and red areas in (B)–(E) are deposition and erosion, respectively, and the black line is net volume change. Removal of excess sediment and restoration activities means that the data for the lowest 400 m were excluded for all time periods, and for the lower 700 m in (E).

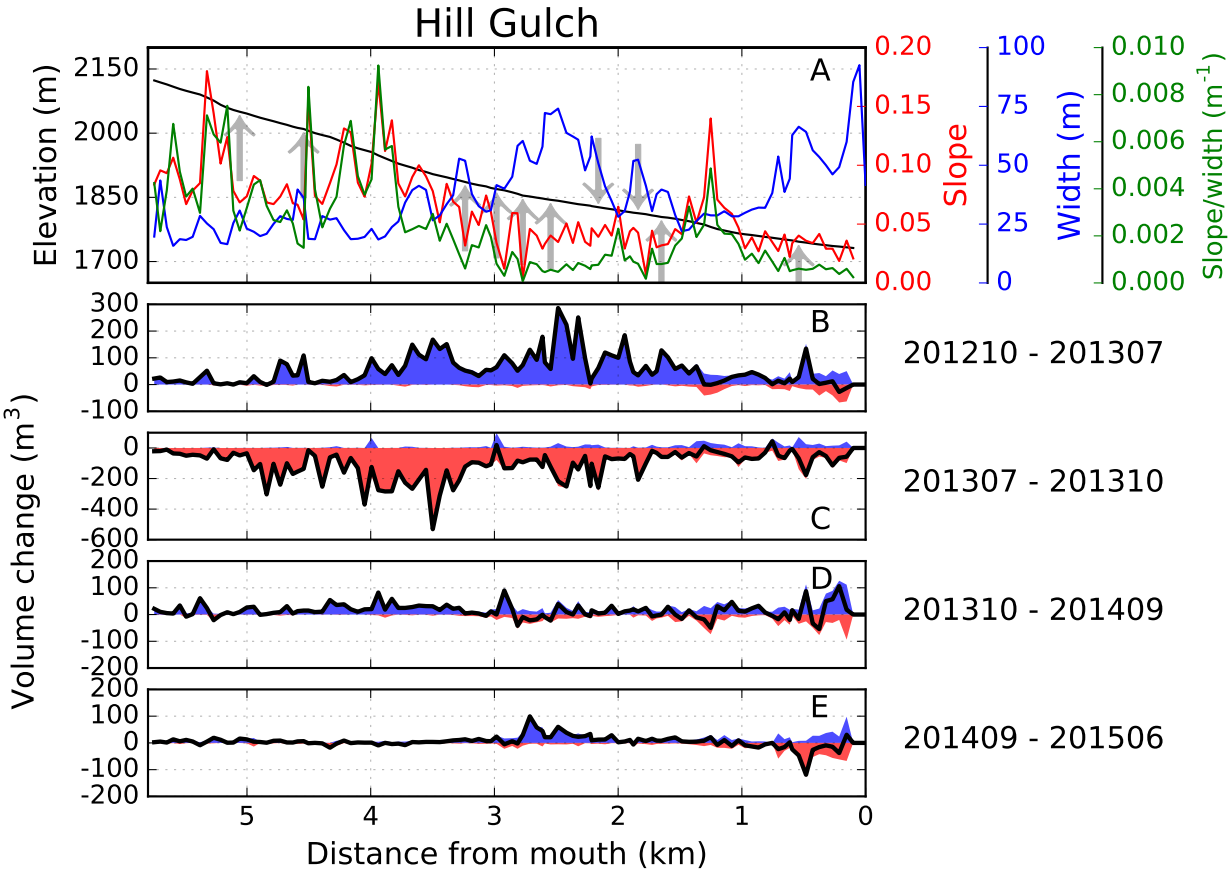

Figure 4.11: Longitudinal distributions in Hill Gulch of (A) elevation, channel slope, valley width and flood power, and the corresponding change in volume for (B) 201210–201307, (C) 201307–201310, (D) 201310–201409, and (E) 201409–201506. Up and down arrows in (A) represent tributaries that enter the main channel from the right and left, respectively. Blue and red areas in (B)–(E) are deposition and erosion, respectively, and the black line is net volume change.

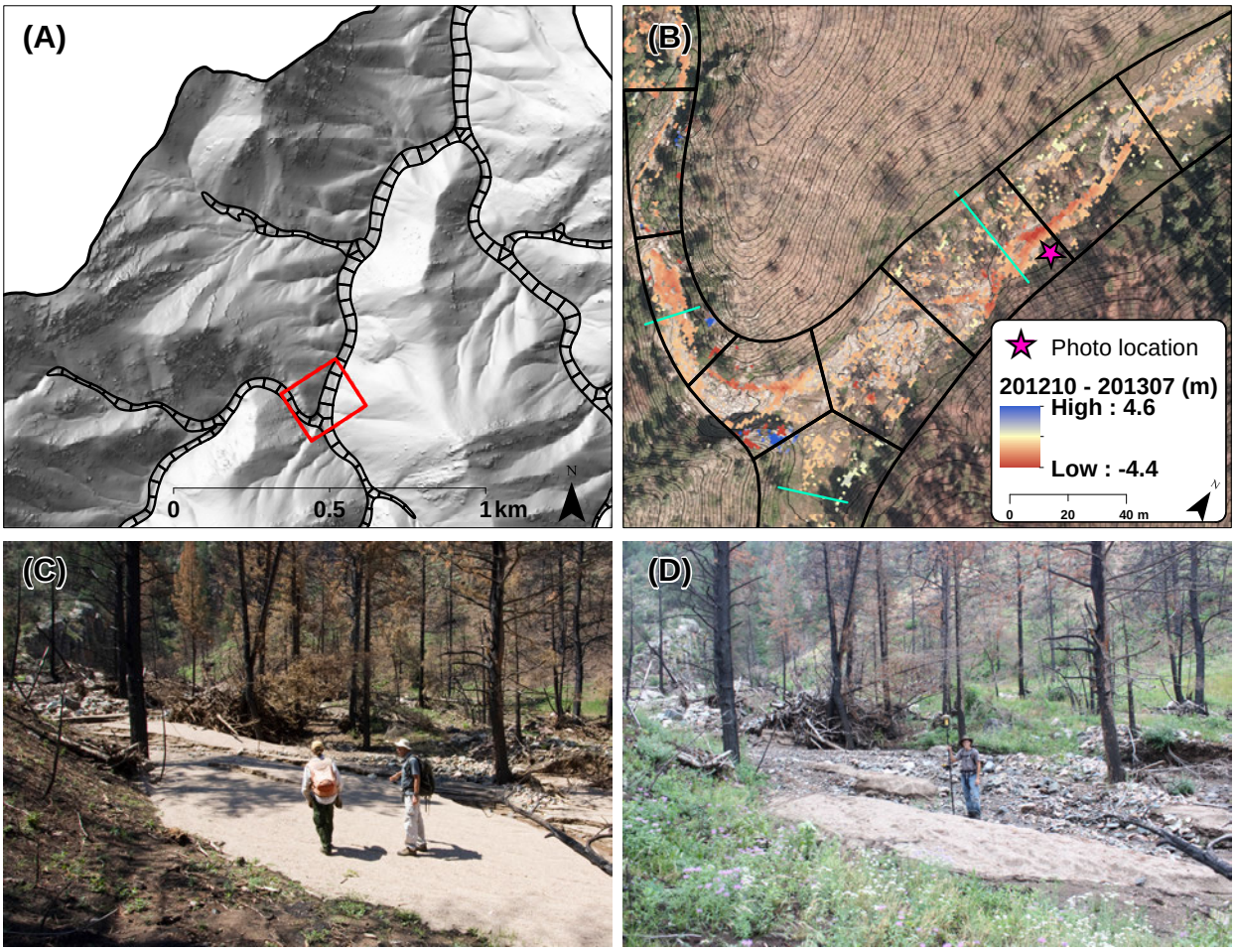

Figure 4.12: Illustration of channel incision and widening in Skin Gulch during T1 as a result of summer thunderstorms followed by snowmelt. The red square in (A) shows the location of the valley bottom segments in (B), and the red star in (B) shows the location of the photos in (C) and (D). Green lines in (B) represent surveyed cross sections, and contour intervals are 1 m (thin lines) and 5 m (thick lines). The photo in (C) was taken on 11 August 2012 and shows the extensive deposition that occurred in the first two months after the fire. (D) shows the same location after spring snowmelt. Maximum erosion was ~1.0 m near the photo location.

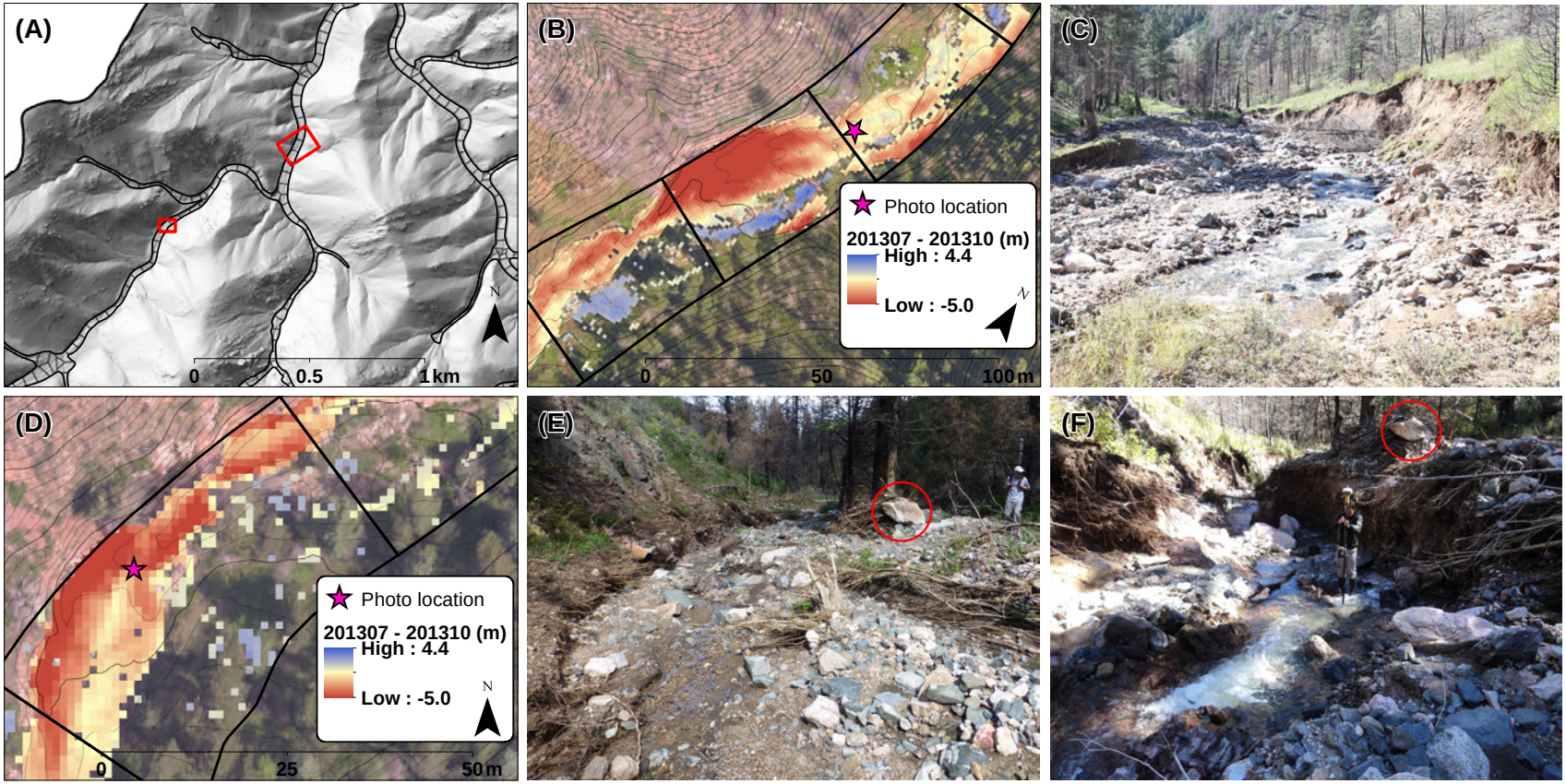

Figure 4.13: Illustration of channel incision and widening in Skin Gulch during T2 caused primarily by the mesoscale flood. The red square in (A) shows the location of the valley bottom segments in (B) and (D), the red star in (B) shows the location of the photo in (C), and the red star in (D) shows the location of the photos in (E) and (F). The photos in (C), (E), and (F) were taken on 24 September 2013, 3 September 2012, and 26 September 2013, respectively, and highlight the extensive erosion that occurred during the mesoscale flood. The rock circled in red can be seen in both (E) and (F), and the person holding a 2-m survey rod in (F) provides scale. Contour intervals in (B) and (D) are 1 m (thin lines) and 5 m (thick lines).

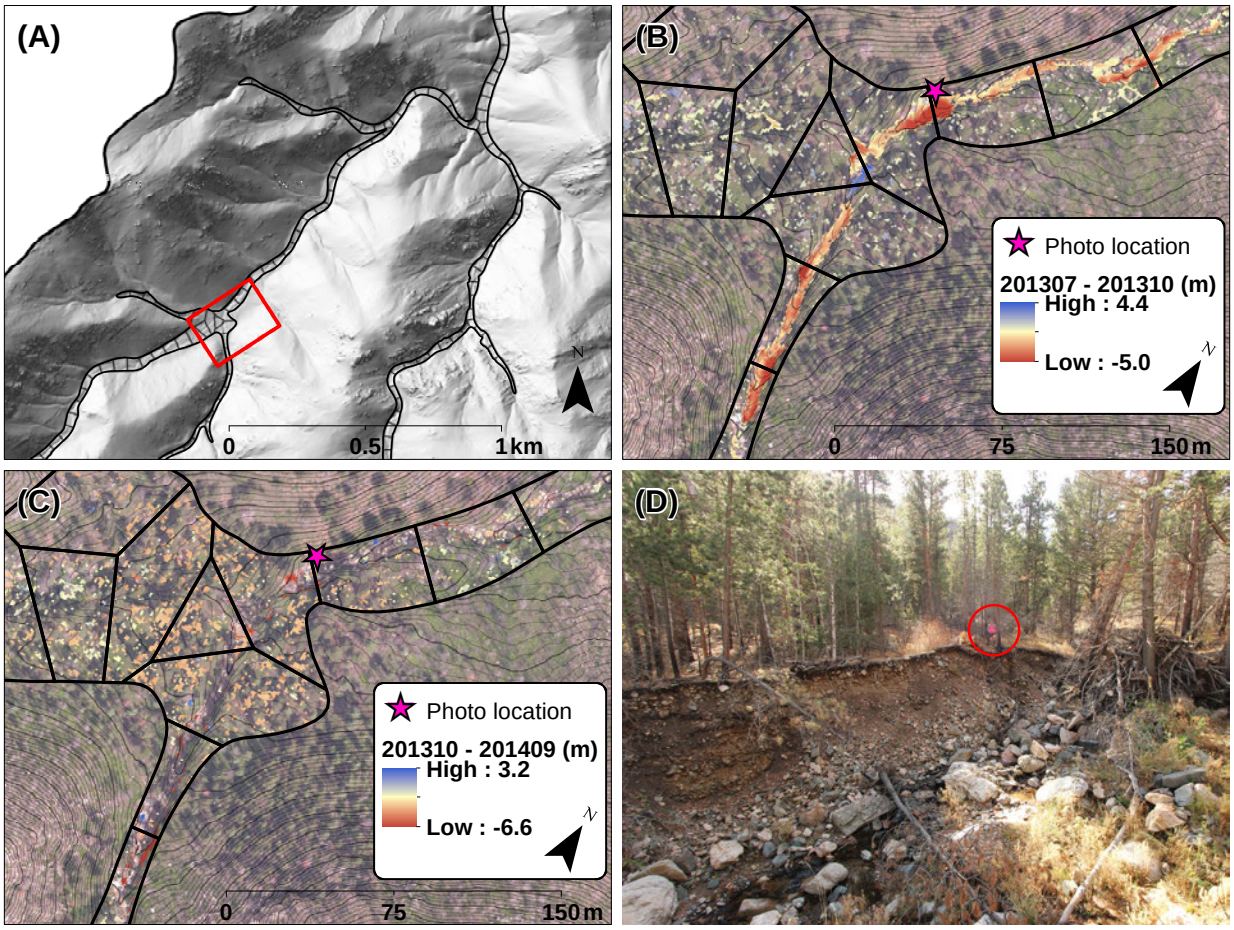

Figure 4.14: Close-up of the elevation change at a tributary junction in Skin Gulch as outlined by the red box in (A). (B) shows the extensive valley bottom erosion and associated elevated changes during T2 due primarily to the mesoscale flood, (C) shows the additional elevation changes during T3 due to bank sloughing. The red star in (B) and (C) shows the location of the photo in (D) that was taken on 25 October 2015, and this shows the extreme magnitude of the channel incision and bank erosion due to the fire and flood; for scale the person on top of the bank is circled in red. Contour intervals in (B) and (C) are 1 m (thin lines) and 5 m (thick lines).

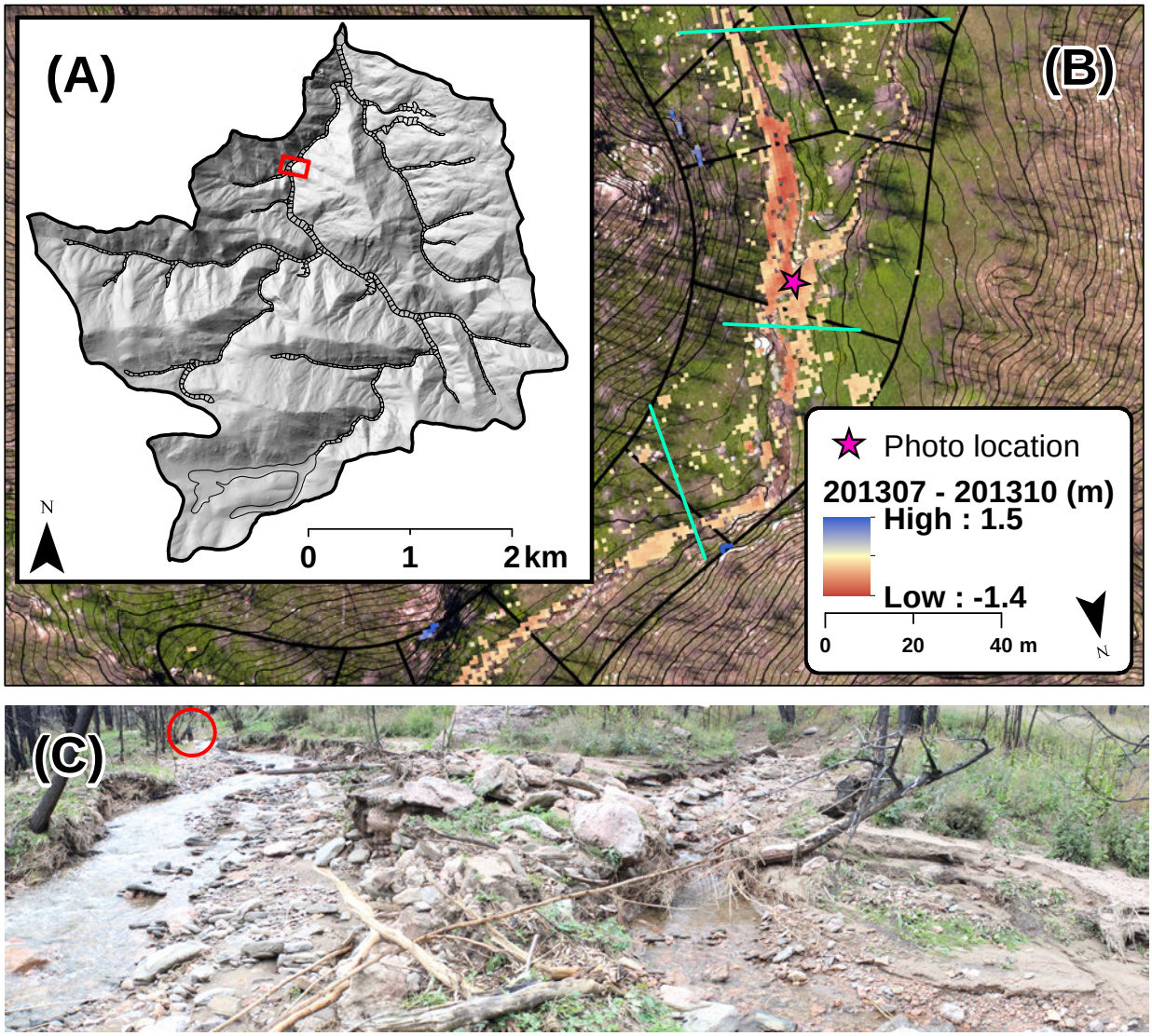

Figure 4.15: Illustration of channel incision and widening in Hill Gulch during T2 due primarily to the mesoscale flood. The red square in (A) shows the location of the valley bottom segments in (B), and the red star in (B) shows the location of the photo in (C). Note that the area mapped in (B) is reversed in orientation with south at the top to better orient with the photo in (C). Green lines in (B) represent surveyed cross sections, and the contour intervals in (B) are 1 m (thin lines) and 5 m (thick lines). The photo in (C) was taken on 22 September 2013. Maximum erosion in this reach was 1.4 m in (B). A person holding a 2-m survey rod in (C) is circled in red to provide scale.

4.4.4 Statistical analysis of controls on erosion and deposition

Pearson correlation coefficients between independent variables indicate that several of the metrics are highly correlated (Figure 4.16; Tables 4.4 and 4.5). For example, the highest cross-correlation was between percent area burned at high severity, and moderate and high severity (0.99 for both watersheds). The strength of this correlation implies that these variables are nearly linearly related. Because of these high correlations percent area burned at high severity, slope-area ratio, and channel width were removed from further analysis. Change in slope-width ratio and confinement ratio were additionally removed because of their dependency on other removed metrics.

Correlation coefficients (r) between net volume change in each segment and the corresponding morphometric variables varied greatly between metrics and across time periods (Figure 4.16). Appendix D presents the r values, p-values, and regression slopes for all comparisons between each independent and dependent variable for each time period and each watershed. Appendix D also includes the correlation values when the data are stratified by channel slope and contributing area (Tables D.3 and D.4; Figures D.5 and D.6). Correlations are reported to show the direction of the relationship, with a positive correlation indicating that increasing values of the independent variable were associated with either decreasing erosion or increasing deposition. Inversely, a negative correlation indicated that increasing values of the independent variable were associated with either increasing erosion or decreasing deposition. The following sections summarize the key results for each time period, in chronological order.

In SG the absolute correlations ($|r|$) for net volume change during T1 never exceeded 0.17 (Figure 4.16; Table D.1), and this was primarily a result of the paucity of large floods and generally limited geomorphic change during this period (Figures 4.8A and 4.10B). The ALS data for T1 did not include the deposition from the large convective flood that occurred in SG shortly after the fire, but did include the removal of some of this material by subsequent spring runoff (Chapters 2 and 3). Hence, the correlations were substantially greater when segment-scale erosion volumes were the dependent variable (Figure 4.16). The greatest correlations with erosion were contributing area (r = -0.56), MI_{30} (r = -0.42), and channel slope (r = 0.33). These results indicate that much

of the erosion occurred in the lower gradient, wider downstream reaches. Correlations between the independent variables and deposition were generally greater than for net volume change, but the correlations were much less than for erosion (Figure 4.16). I posit that the correlations for deposition and net volume change in SG would have been greater had the first ALS dataset captured the extensive post-fire deposition in the first summer after burning.

The geomorphic changes observed during T1 included deposition from smaller convective thunderstorms, and channel erosion due to elevated baseflow (Figure 4.12). Further investigation of the scatterplots indicate these processes transitioned from primarily deposition at contributing areas less than about 4–5 km^2 to erosion at contributing areas greater than about 4–5 km^2 (Figure 4.17). This suggests that the smaller convective thunderstorms have limited impact on larger watershed scales, while elevated baseflow can cause channel changes at the larger watershed scales, if bed sediment is available.

Table 4.4: Pearson correlation coefficients (r) for the independent variables used in our statistical analysis in Skin Gulch.

r	S	ΔS	A	w_{v}	Δw_{v}	$\frac{S}{w_v}$	$\Delta \frac{S}{w_v}$	w_{c}	C_{r}	P	MI_{30}	BS_{m}	BS_{h}	$BS_{\mathrm{m+h}}$
S	-	-	-	-	-	-	-	-	-	-	-	-	-	-
ΔS	0.33	-	-	-	-	-	-	-	-	-	-	-	-	-
A	-0.54	0.03	-	-	-	-	-	-	-	-	-	-	-	-
w_{v}	-0.48	-0.08	0.37	-	-	-	-	-	-	-	-	-	-	-
Δw_{v}	0.00	-0.16	-0.02	0.41	-	-	-	-	-	-	-	-	-	-
$\frac{S}{w_v}$	0.88	0.27	-0.48	-0.62	-0.17	-	-	-	-	-	-	-	-	-
$\Delta \frac{S}{w_v}$	0.15	0.68	0.05	-0.20	-0.52	0.32	-	-	-	-	-	-	-	-
w_{c}	-0.65	0.02	0.94	0.42	-0.04	-0.59	0.06	-	-	-	-	-	-	-
C_{r}	0.21	-0.08	-0.44	0.41	0.46	-0.03	-0.31	-0.54	-	-	-	-	-	-
P	0.00	-0.05	0.04	0.06	0.04	0.02	-0.06	0.00	0.08	-	-	-	-	-
MI_{30}	-0.40	0.04	0.59	0.30	-0.04	-0.38	0.03	0.64	-0.28	0.32	-	-	-	-
BS_{m}	0.16	-0.07	0.05	-0.14	0.07	0.24	-0.10	0.01	-0.11	0.17	0.00	-	-	-
BS_{h}	-0.16	0.07	0.02	0.13	-0.10	-0.23	0.10	0.08	0.02	-0.08	0.14	-0.84	-	-
$BS_{\mathrm{m+h}}$	-0.15	0.06	0.05	0.12	-0.10	-0.21	0.09	0.10	-0.01	-0.04	0.17	-0.74	0.99	-

Table 4.5: Pearson correlation coefficients (r) for the independent variables used in my statistical analysis in Hill Gulch.

r	S	ΔS	A	w_{v}	Δw_{v}	$\frac{S}{w_v}$	$\Delta \frac{S}{w_v}$	w_{c}	C_{r}	P	MI_{30}	BS_{m}	BS_{h}	$BS_{\mathrm{m+h}}$
S	-	-	-	-	-	-	-	-	-	-	-	-	-	-
ΔS	0.31	-	-	-	-	-	-	-	-	-	-	-	-	-
A	-0.45	0.01	-	-	-	-	-	-	-	-	-	-	-	-
w_{v}	-0.33	-0.12	0.47	-	-	-	-	-	-	-	-	-	-	-
Δw_{v}	-0.05	-0.21	0.03	0.45	-	-	-	-	-	-	-	-	-	-
$\frac{S}{w_v}$	0.88	0.35	-0.43	-0.55	-0.18	-	-	-	-	-	-	-	-	-
$\Delta \frac{S}{w_v}$	0.18	0.80	0.03	-0.20	-0.44	0.36	-	-	-	-	-	-	-	-
w_{c}	-0.54	0.01	0.96	0.47	0.02	-0.51	0.03	-	-	-	-	-	-	-
C_{r}	0.34	-0.12	-0.41	0.37	0.33	0.06	-0.24	-0.53	-	-	-	-	-	-
P	0.03	0.02	-0.10	-0.01	-0.03	0.02	0.03	-0.10	0.08	-	-	-	-	-
MI_{30}	-0.41	0.02	0.52	0.29	0.01	-0.39	0.03	0.55	-0.26	0.33	-	-	-	-
BS_{m}	-0.42	0.00	0.17	0.16	0.03	-0.37	0.02	0.22	-0.12	0.18	0.43	-	-	-
BS_{h}	0.42	-0.04	-0.27	-0.25	0.00	0.39	-0.05	-0.35	0.16	-0.27	-0.50	-0.82	-	-
$BS_{\mathrm{m+h}}$	0.39	-0.05	-0.28	-0.26	0.01	0.37	-0.05	-0.36	0.17	-0.28	-0.49	-0.73	0.99	-

Overall the correlations in HG for T1 were slightly stronger in HG than in SG (Figure 4.16). The correlations for net volume change showed that deposition increased with increasing channel width (r = 0.40) and erosion increased with percent area burned at high or moderate and high severity (r = -0.37; Table D.2). Deposition again was more strongly correlated with the independent variables than net volume change or erosion. This improvement is likely due to the greater magnitudes of deposition in the middle and lower reaches in HG relative to SG (Figure 4.9); the highest correlations with deposition were for contributing area (r = 0.35), MI_{30} (r = 0.34), and BS_m and BS_{m+h} (r = 0.33 and -0.42, respectively; Table D.2).

Correlations for T2 were generally stronger than for any of the other three time periods, and this was primarily due to the substantial and consistent erosion resulting from the large mesoscale flood (Chapters 2 and 3; Figure 4.16). In SG three metrics had r > 0.32 or < -0.32 with net volume change, and these included channel slope (r = 0.35), contributing area (r = -0.63), and MI_{30} (r = -0.36; Table D.1). These results indicate increasing erosion in the downstream direction and nearly 40% of the variance in the amount of net change can be explained by A alone. Using erosion as the dependent variable generally improved correlations, and the highest correlation for any variable for any time period was between contributing area and erosion for T2 in SG (r = -0.71; Table D.1). In contrast, using deposition as the dependent variable generally decreased correlations (Figure 4.16).

As in SG, the correlations during T2 in HG were generally better than for the other three time periods (Figure 4.16). The correlations for HG were not as high as for SG and this can be attributed to the lower volume changes in HG compared to SG (Figure 4.7). In HG two metrics had r > 0.32 or < -0.32 with net volume change, and these included channel slope (r = 0.35) and MI_{30} (r = -0.33). Similar to SG, the correlations in HG generally improved when erosion was the dependent variable and decreased when deposition was the dependent variable (Figure 4.16).

Overall the volume changes in T2 were similar in magnitude but opposite in sign as the volume changes in T1 (Figures 4.10 and 4.11). Plots of the net volume changes for T2 against the net volume changes for T1 show that for both watersheds much of the data plot along a line with a slope

of -1 (Figure 4.18). This indicates that for many segments the erosion from the mesoscale flood was approximately equal to the post-fire volume deposited in T1. However, the overall R^2 value was near zero in SG because a number of segments had much more erosion in T2 than deposition in T1; these points plot well below the regression line and are shown in red in Figure 4.18A. These segments are almost exclusively downstream of areas burned at high severity and subjected to the high intensity July 2012 convective storm (Figures 4.12 and 4.18B). These segments had very large volumes of deposition just after the fire (Chapter 2), but these were prior to the collection of the first ALS dataset and hence not quantified. The shift in correlations from negative to positive, or vice versa, between T1 and T2 are particularly notable for channel slope (r = -0.14 in T1 and 0.35 in T2) and valley width (r = 0.13 in T1 and -0.17 in T2; Figure 4.16).

The mirroring of deposition in T1 and erosion in T2 was even more similar for HG than in SG (Figure 4.11). Segment-scale net volume changes in T2 versus T1 also have a much stronger relationship (R^2 = 0.40), but again there is a cluster of points below the 1:-1 line (Figure 4.18C). The number and absolute magnitude of the differences between these points and the 1:-1 line is smaller than in SG, and these segments are almost exclusively in a major tributary that drains an area burned at high severity (Figure 4.18D). Field obserations indicate that this area also was subjected to deposition prior to the first ALS dataset (see Figure 3.9 in Chapter 3), but this deposition was not nearly as substantial as the deposition in SG. Excluding these points from the regression increases the R^2 to 0.64, indicating an even closer relationship between the volumes of segment-scale deposition in T1 and erosion in T2. These results show that the magnitude and spatial pattern of the segment-scale erosional response in each watershed in T2 was directly related to the volume and distribution of post-fire sediment deposition in T1. As in SG, many of the correlations in HG shifted from negative to positive, or vice versa, between T1 and T2 (Table D.2), including channel slope (r = -0.25 in T1 and 0.35 in T2), contributing area (r = 0.28 in T1 and -0.24 in T2), and MI_{30} (r = 0.29 in T1 and -0.33 in T2; Figure 4.16).

In T3 and T4 the correlations between the independent variables and the volume changes were generally low in both watersheds (Figure 4.16). The lower correlations can be attributed to the

much lower amounts of erosion and deposition (Figure 4.7). The directions of the correlations were generally the same for T3 and T4 as they were for T1, as these periods were primarily depositional. In SG the only correlations with net change that had an $r > 0.32$ or < -0.32 ($R^2 > 0.10$) were percent area burned at moderate severity (r = -0.35) in T3 and total rainfall (r = -0.33) in T4 (Figure 4.16). The limited correlations > 0.33 or < -0.33 for total erosion and total deposition suggest that spring high flows continued to erode the raw channel enlarged by the mesoscale flood. In HG none of the independent variables explained much more than 8% of the variation in net volume change (Table D.2). Independent variables also were only weakly correlated with the erosion and deposition volumes in T3 and T4. The only three correlations with an $r > 0.33$ or < -0.33 were for increasing segment-scale erosion with increasing contributing area (r = -0.49) and valley width (r = -0.38), and decreasing deposition with increasing percent area burned at moderate and high severity (r = -0.38).

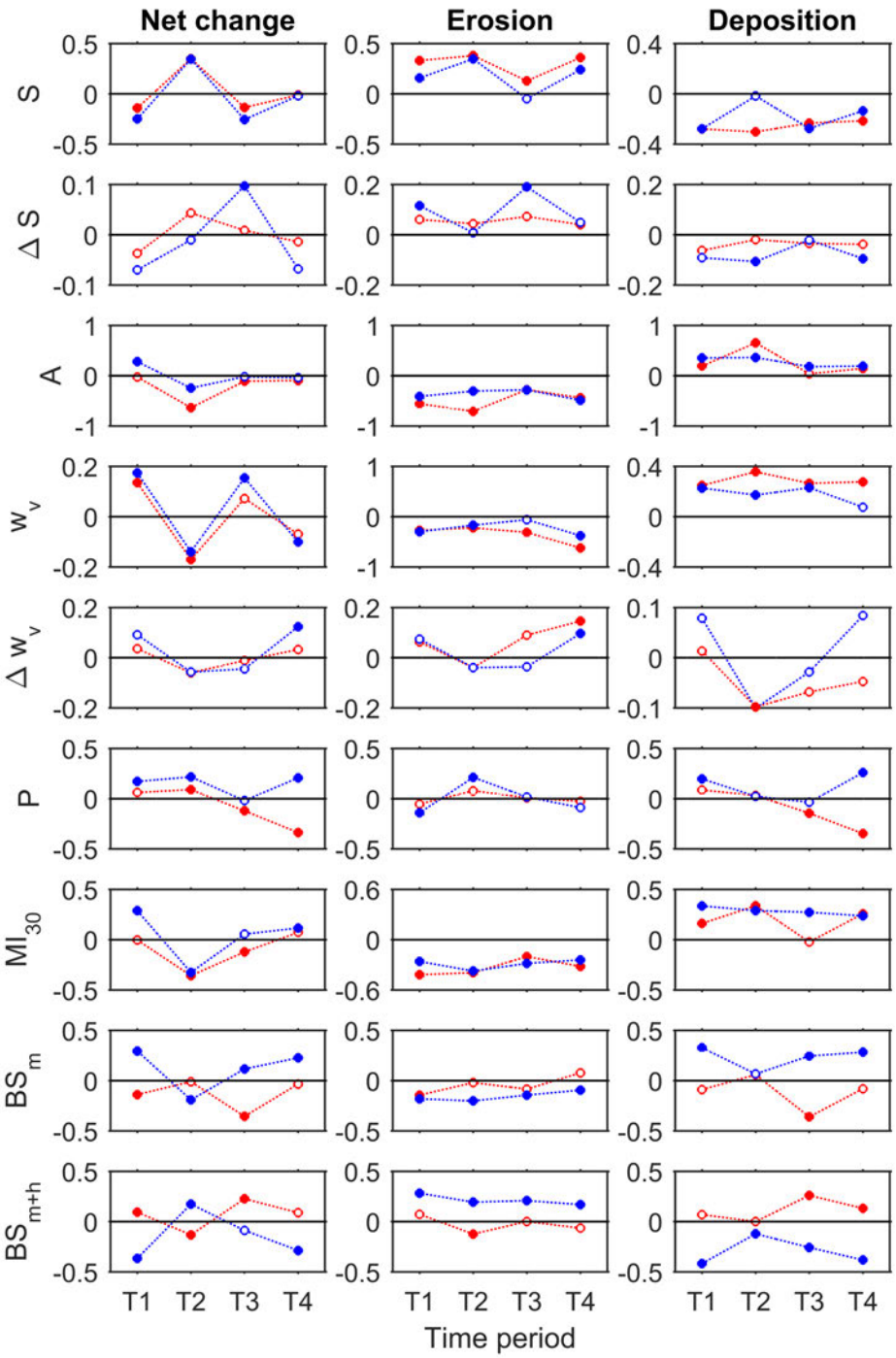

Figure 4.16: Correlation coefficients for Skin Gulch (red dashed lines) and Hill Gulch (blue dashed lines) for each time period between the independent metrics and the dependent variables of net volume change, total erosion, and total deposition. Time periods (T#) are for 201210–201307, 201307–201310, 201310–201409, and 201409–201506, respectively. Independent variables include channel slope (S), ΔS, contributing area (A), valley width (w_{v}), change in valley width (Δw_{v}), total rainfall (P), maximum 30-minute intensity (MI_{30}), percent burned at moderate severity (BS_{m}), and percent burned at moderate-to-high severity ($BS_{\mathrm{m+h}}$). Filled circles indicate significant correlations, p-value ≤ 0.05.

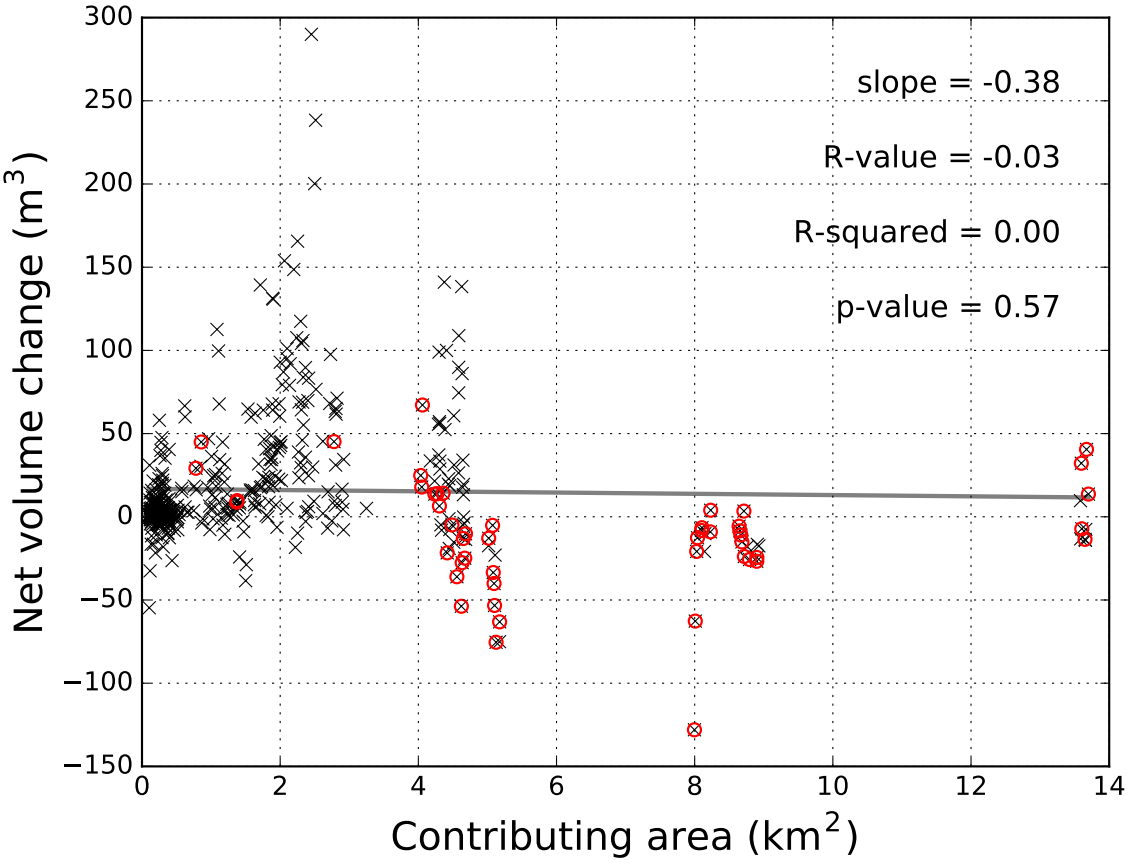

Figure 4.17: Scatterplot during T1 of Skin Gulch of net volume changes versus contributing area. Red circles correspond to the segments highlighted in Figure 4.18.

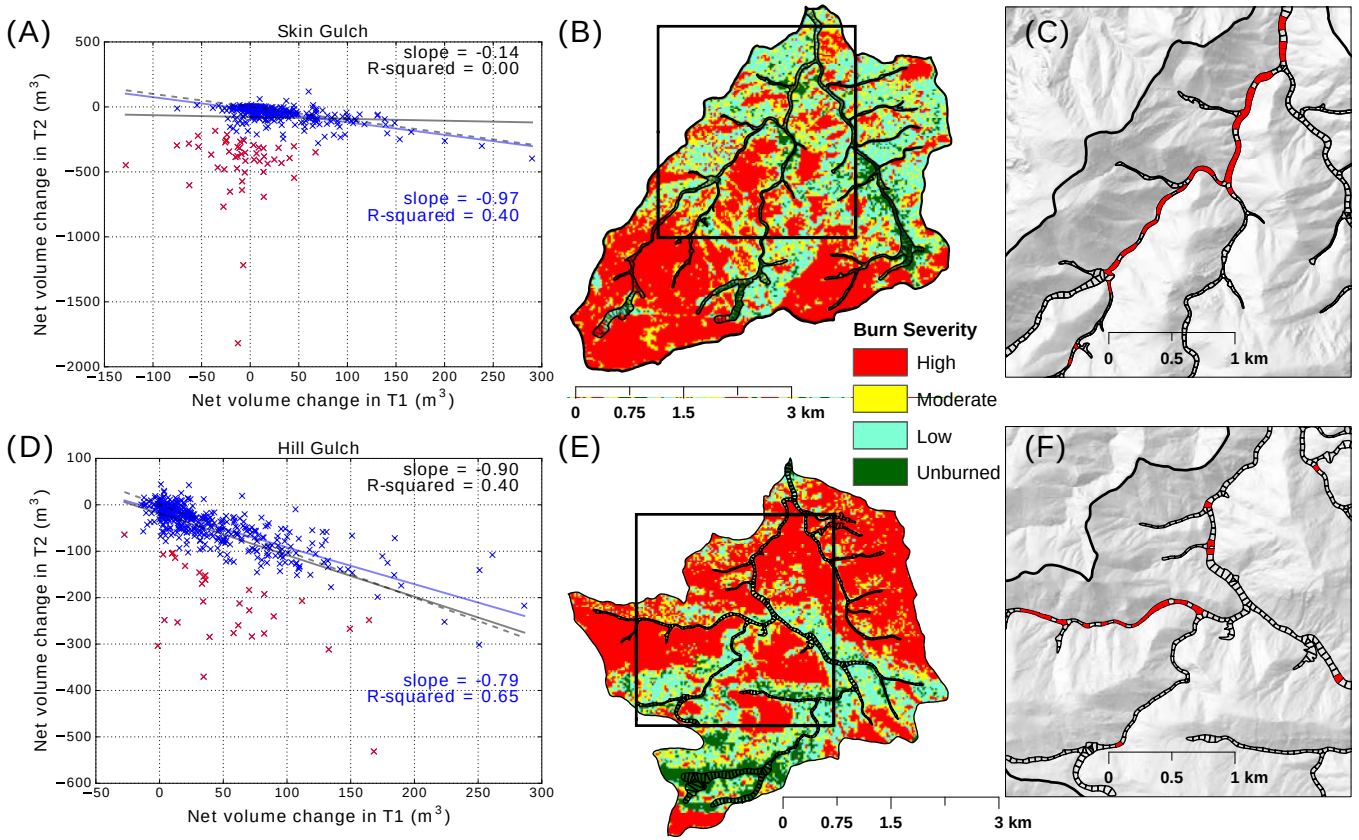

Figure 4.18: Regression of the net volume change for each 50-m segment for T2 (the period including the large erosional mesoscale flood; 201307–201310) against the net volume change for T1 (the depositional period of 201210–201307) for (A) Skin Gulch and (D) Hill Gulch. The red x's in (A) and (D) are the segments with much more erosion in T2 than deposition in T1, causing them to deviate substantially from the dashed -1:1 line. The regression line and statistics for all of the data are shown in black, while the regression line and statistics in blue are for the truncated data after removing the red data points. (B) and (E) are burn severity maps of Skin Gulch and Hill Gulch, respectively, and the black boxes show the valley bottom segments in (C) and (F). The red segments in (C) and (F) are the red data points in (A) and (D).

4.5 Discussion

4.5.1 Mechanisms of watershed scale post-fire erosion and deposition

As rainfall intensities exceed infiltration rates (e.g., *Cammeraat*, 2004; *Kampf et al.*, 2016) the greatly enhanced hillslope runoff causes rapid expansion and incision of the headwater channels (*Wohl*, 2013). The increased runoff and increased connectivity transports eroded sediment down the hillslopes into the channel network (e.g., *Prosser and Williams*, 1998; *Schmeer et al.*, 2018). The finer particles from hillslopes and channel erosion are readily transported downstream as suspended load. In contrast, the coarse sand and larger particles are usually transported much shorter distances as bedload (e.g., *Moody and Martin*, 2001a; *Reneau et al.*, 2007), and deposited in the wider, lower gradient reaches (e.g., *Anderson*, 1976; *Doehring*, 1968; *Meyer et al.*, 1995; *Moody and Martin*, 2009).

The sediment transported into the Cache la Poudre River after the High Park Fire greatly increased turbidities and suspended sediment concentrations (*Writer et al.*, 2014), but the sediment inputs generally did not alter the channel morphology of the mainstem other than at a few confluences. Field data and observations both showed that fine sands, silts and clays did not comprise much of the post-fire deposits in the valley bottoms, so the topographic changes quantified by the ALS differencing primarily reflect the delivery, deposition, and possible subsequent movement of the coarser bedload particles.

The relatively recent technology for differencing high-resolution topographic data allows detailed, spatially-explicit calculations of erosion and deposition. This study was relatively unique in terms of being able to compare five ALS datasets, and the resulting map of valley bottom changes shows spatial and temporal complexity (sensu *Schumm*, 1973). Despite this variability the DEMs of difference clearly documented net deposition in both study watersheds in T1, T3, and T4 after the HPF. This illustrates that—other than the mesoscale flood—post-fire effects were contributing to a net increase in valley sediment fill 3–4 years after burning (Figure 4.7; see also Figure 3.21 from Chapter 3). The preponderance of deposition over erosion is a typical post-fire response (e.g., *Moody and Martin*, 2001a; *Morris and Moses*, 1987; *Swanson*, 1981; *Wagenbrenner et al.*,

2006). Highly accurate surveyed cross sections and longitudinal profiles in the same two watersheds, which represent only some portions of the entire watersheds, showed limited changes in T3 and T4 (Chapter 3). In contrast, the ALS differencing covered the entire channel network, but has higher uncertainty due to alignment issues, horizontal displacement errors, interpolation errors, and errors associated with vegetation. Thus, the combination of these two data sets highlights the importance of collecting data at different spatial and temporal scales.

Both the field data (Chapter 3) and the ALS differencing showed smaller geomorphic changes in T3 and T4, and this is due to several factors. Some of these include the the stripping and coarsening of the channel and valley bottoms due to the mesoscale flood, the ongoing hillslope vegetation recovery, reduction in headwater channel length (*Wohl and Scott*, 2017), and paucuty of large convective storms. The presence and regrowth of riparian vegetation also can exert strong control on the hydraulics and patterns of erosion and deposition following fire (e.g., *Pettit and Naiman*, 2007), although in SG the delayed riparian vegetation regrowth following the fire and mesocale flood was not as important as other factors. These factors, when combined with the reduction in sediment inputs from hillslope erosion (*Schmeer et al.*, 2018), indicate a sharp decline in channel geomorphic response and imply reduced sensitivity to further convective thunderstorms, increased baseflows, and spring snowmelt (e.g., Chapter 3; *Brunsden and Thornes*, 1979; *Fryirs*, 2017; *Phillips and Van Dyke*, 2016; *Rathburn et al.*, 2017; *Thomas*, 2001).

Patterns of post-fire erosion and deposition are not uniform, and since the uncertainty of the ALS differencing was generally around 25 cm this technique is not able to pick up small changes. ALS differencing instead is most able to detect the larger elevation changes at tributary junctions and in larger channels and valley bottoms. In SG and HG most of the largest geomorphic changes occurred in downstream locations where channel slopes were generally less than ~10% and valley widths were greater than ~30 m. The general trend of deposition at and near confluences (Figure 4.12; see also Figure 3.9 in Chapter 3) corroborates previous research (e.g., *Benda et al.*, 2003; *Nardi and Rinaldi*, 2015), however, my observations along with other researchers indicate that there were few large debris flows after the High Park Fire and September 2013 mesoscale storm

(*Coe et al.*, 2014). Because deposition tends to be spread out over wide areas, while erosion is generally very localized, the elevation differences associated with deposition may fall below the elevation uncertainty more often than in erosional areas. This difference in physical processes and the associated uncertainty in quantifying elevation differences means there is potential in underestimating deposition volumes.

4.5.2 Uncertainty, errors, and methodological issues in DEM differencing

Errors associated with DEM differencing need to be minimized to accurately detect and quantify geomorphic changes, particularly in smaller streams. My experience with ALS datasets of varying quality over time provides useful insights into best practices for using repeat ALS data to document geomorphic changes after wildfires or other disturbances. First, ALS data collection must happen as soon as possible following the disturbance, particularly in post-fire landscapes because these are extremely sensitive to runoff, erosion, and channel change from even relatively small rainstorms (e.g., *Moody et al.*, 2013; *Shakesby and Doerr*, 2006). Second, high-resolution topography should be repeated at a sufficiently high temporal resolution to capture the effects of discrete storms and floods, or at least seasonally in order to distinguish and understand the relative effects of different driving forces (e.g., summer thunderstorms versus snowmelt). Recent advances in the use of drones rather than airplanes should greatly facilitate more frequent lidar data collection (e.g., *Tulldahl and Larsson*, 2014). Drone-based structure-from-motion (SfM) photogrammetry is another and increasingly popular alternative to lidar (e.g., *Smith et al.*, 2016).

Third, differencing of repeat high-resolution topographic data often require translational rectification to better match the different datasets and thereby increase the accuracy of change detection. In this study the ALS data required vertical and horizontal translation to more accurately estimate elevation change. Since manual adjustments are laborious and non-repeatable, an automated approach to co-register the point clouds greatly facilitated my methodology *Nuth and Kääb* (2011). This approach, along with the availability of highly accurate RTK-GNSS field data (Chapter 3), reduced the vertical uncertainties of the ALS data to 10-15 cm, with a maximum of 23 cm. Fourth,

ALS data should be collected at low altitudes with narrow flight pass widths, low scan angles, and with good ground control to improve the quality and density of the raw point clouds.

Automated GIS tools allow for quick and easy characterization of the channel and adjacent topography; examples include FluvialCorridor (e.g., *Roux et al.*, 2015), River Bathymetry Toolkit (e.g., *McKean et al.*, 2009), TerEx (*Stout and Belmont*, 2014), V-BET (*Gilbert et al.*, 2016), and the Valley Confinement Algorithm (*Nagel et al.*, 2014). Users should be aware of the limitations of these tools. FluvialCorridor provides objective valley bottom delineations that can be used over large spatial domains and facilitates longitudinal segmentation of the channel and valley bottom, but the tool occasionally had trouble identifying valley margins. This meant that the delineated valley area sometimes included steep slopes (e.g., rock outcrops), and it is the slope breaks associated with these steep slopes that can cause errors in the volume estimates (e.g., *Bangen et al.*, 2016; *Heritage et al.*, 2009; *Milan et al.*, 2011; *Wheaton et al.*, 2010). The inaccuracies in identifying the valley margins meant there were higher elevation points within a given segment, which inhibited the accurate calculation of the valley bottom slopes. Fifth, manually delineating the valley bottom may be necessary to avoid errors associated with an automated process, especially if the area of interest extends into steep mountainous terrain.

Techniques for computing elevation differences directly from point clouds in steep slopes are improving (e.g., *Lague et al.*, 2013), but simple volume computation from point cloud differencing is still in its infancy (*Passalacqua et al.*, 2015). In this study I initially tried to compute volumes of erosion and deposition directly from the point clouds, but switched because previous research has shown that raster-based approaches, as opposed to mesh differencing, are better for lower density point clouds as they result in lower volume uncertainty (*Hartzell et al.*, 2015). Raster-based differencing also has a mature suite of tools to calculate spatially-varying uncertainties. Sixth, incorporating spatially-varying uncertainties rather than uniform uncertainty improves the accuracy of volume change estimates (e.g., *Milan et al.*, 2011; *Wheaton et al.*, 2010).

A key problem in this study was that the varied seasonal timing of the ALS data acquisition resulted in large errors due to comparing ALS data with leaf on versus leaf off. I developed an

algorithm to remove unrealistically large elevation change due to changes in canopy cover. This reduced the mean the mean calculated total erosion, total deposition, and net volume differences by 46% (s.d = 16%), 54% (s.d. = 15%), and 22% (s.d. = 33%), respectively (total volumes before and after vegetation removal are in Appendix D). In T3, however, the net volumes increased by 11% in SG and 25% in HG; the increase in net volume is due to the reduction in total erosion being less than the reduction in total deposition. Even with the use of this algorithm, a careful inspection of the DoDs and aerial imagery showed several places and times where the vegetation removal algorithm did not successfully identify the ground identification errors resulting from changes in the vegetation heights between ALS datasets (e.g., Figure 4.3D). Seventh, to avoid similar issues repeat ALS data should be collected at similar times of the year, preferably during leaf-off. Eighth, visual checks of DoDs are critical to catch random errors, which can be mistaken as volumes of real geomorphic changes (e.g., *Lane et al.*, 2004).

4.5.3 Controls on spatial and temporal patterns of geomorphic change

The linear regression results showed that different rainfall depths and intensities, burn severity, and valley and basin morphology were correlated with post-fire volume changes, however, no metric consistently had strong correlations. Because some processes and/or topographic controls are more important in some parts of the watershed than in others, better relationships could potentially be attained by parsing the valley into more discrete geomorphic units prior to statistical analysis (channel, floodplain, terrace, etc.; e.g., *Weber and Pasternack*, 2017). Despite the noise in the data logical results still provide insight into the controls on spatial and temporal channel and valley changes. In particular, channel changes were consistently greatest at larger contributing areas, and at floodplain pockets, tributary junctions, and colluvial deposits. The greater volume changes were primarily associated with the deposition in T1 and the erosion in T2. Correlations in T3 and T4 generally were lower than in T1 and T2. This decrease in the strength of correlations is due in part to the lower magnitude of erosion and deposition as the watersheds recovered, but also due to the reduced sensitivity to channel change caused by the mesoscale flood. Therefore, a key take-home

message is that the geomorphic changes in the channels and valleys of the study watersheds are largely controlled by sediment availability.

The assertion about sediment availability controlling the locations of geomorphic changes is further illustrated by the large amount of erosion during T2 that followed from the post-fire deposition (Figure 4.18; Chapters 2 and 3). The importance of storage availability can also be seen in scatter plots of net volume change versus slope (Figure 4.19), where little change occurred in segments with slopes greater than about 0.2 m m^{-1}, or about 11%. Much of the bed in steep channels like these is composed of large, generally immobile sediment, and hence in-channel storage of more transportable sediment is limited (e.g., *Yager et al.*, 2012). Sediment the size of large boulders has an estimated residence time on the order of 1,000 years in this region (*Wohl et al.*, 2017). Following the 2013 flood *Yochum et al.* (2017) noted that channels with a slope greater than about 3% were more resistant to geomorphic changes due to armoring and bedforms formed by large grain sizes and instream wood. Over varying time scales, and throughout the channel network, fires and floods influence the rates of sediment supply and sediment transport capacity, which ultimately leads to fluctuations in valley fill (see Figure 3.21 in Chapter 3). Therefore it may be more important to quantify where and how much sediment is available in the valleys of mountain catchments for determining the potential for geomorphic changes (e.g., *Carling and Beven*, 1989), rather than the spatial distribution of hydraulic and morphometric controls.

Downstream gradient in stream power is often highly correlated with areas of erosion and deposition (e.g., *Gartner et al.*, 2015; *Yochum et al.*, 2017), but to my surprise none of the gradient metrics (i.e., ΔS, Δw_v, $\Delta \frac{S}{w_v}$) correlated well with net volume, total erosion, or total deposition. Most of the largest volume changes occurred in segments where gradients in morphometrics were approximately zero, resulting in low correlation coefficients. The results again suggest spatial and temporal variations in sediment supply, due to hillslope sediment inputs or in-channel processes, may be more important for understanding the potential for erosion or deposition than local gradients in slope or valley width.

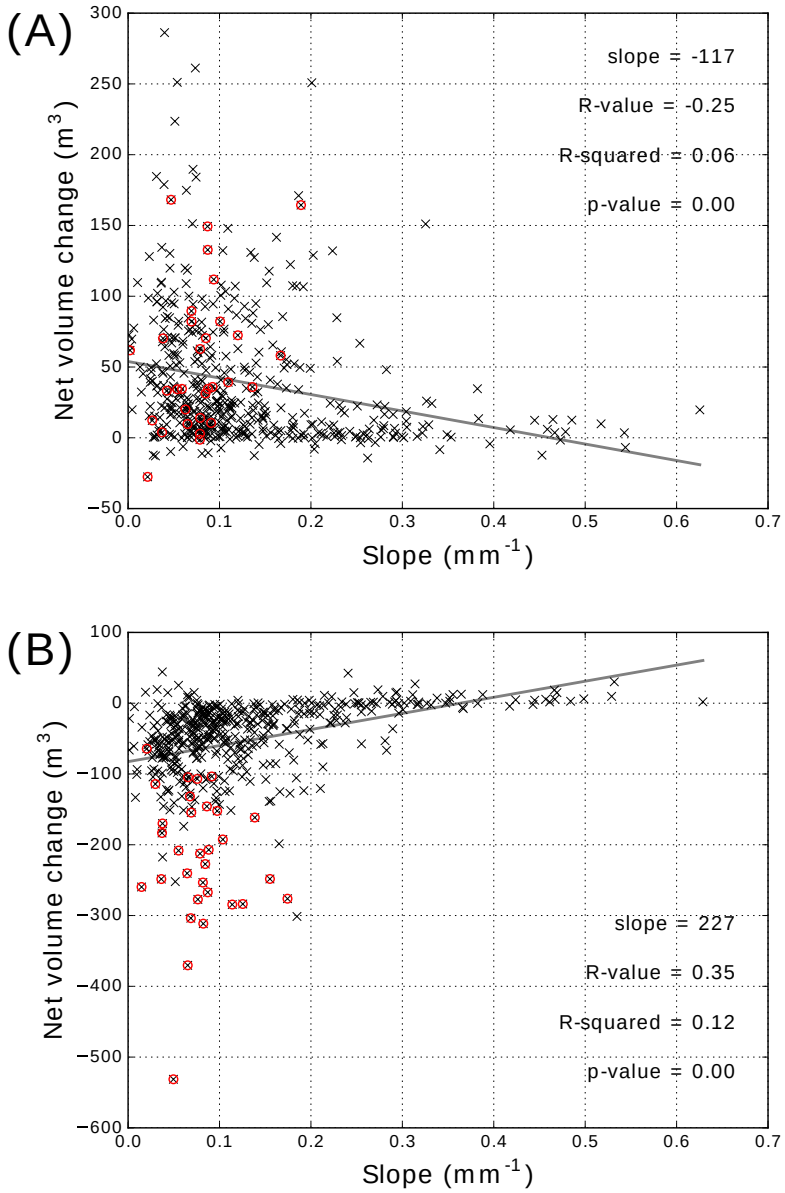

Figure 4.19: Scatterplot during of Hill Gulch for net volume change versus slope for (A) T1 and (B) T2. Red circles correspond to the segments highlighted in Figure 4.18.

Using erosion or deposition as the dependent variable generally did not improve correlations greatly compared to net volume change; however, there were some metrics whose importance increased with a change in dependent variable. For example, 50% of the total erosion in SG during T2 was explained by contributing area. Similarly, correlations for contributing area substantially improved in SG during T1 as much of the erosion in the lower gradient, wider downstream reaches

was caused by spring snowmelt. Using deposition as the dependent variable generally did not improve correlations, with few exceptions. For example, most correlations using deposition were improved in HG during T1 as the ALS differencing captured much of the downstream trend of post-fire deposition. The implication is that quantifying the controls on post-fire geomorphic changes is limited by the uncertainty in the elevation differencing and the magnitude of volume changes.

Additional research is needed to couple hillslope erosion estimate to watershed-scale sediment delivery and geomorphic changes. My analysis showed that valley morphometrics can help explain spatial variations in erosion due to large floods, and to a much lesser extent, the deposition from hillslope and upstream sediment production as indexed by burn severity and rainfall. Thus, I speculate that localized deposition, which in this environment is most frequently caused by localized thunderstorms (e.g., *Kampf et al.*, 2016; *Wagenbrenner and Robichaud*, 2014), may correlate better with characteristics of the adjacent and convergent hillslopes that are directly connected to the valley rather than valley and basin morphometrics. A relatively complete sediment budget can be created (sensu *Vericat et al.*, 2017) when estimates of hillslope sediment delivery to the channel network (e.g., *Schmeer et al.*, 2018) are coupled with spatially explicit estimates of valley volume changes. The combination of hillslope sediment production and channel change data, along with burn severity, basin morphometrics, and storm-specific precipitation depths and intensities can improve our understanding of the mechanisms driving post-fire erosion processes across scales.

Results from this study suggest that the potential for storing and attenuating floodwaters and sediment after wildfire can vary between watersheds or across different portions of a single watershed. Therefore, the risk for local residents and downstream water users will depend on the specific characteristics of the upstream burned area. After fires considerable funds are spent to reduce hillslope erosion risks (e.g., *Robichaud et al.*, 2000). My research helps suggest where burned area emergency rehabilitation teams might focus critical post-fire rehabilitation efforts. If ecosystems and infrastructure concerns are within or very near the burned area, then rehabilitation efforts should be locally focused to reduce peak flows and sediment deposition. However, if water users much farther downstream are the primary concern, then post-fire treatments might best be

focused on those sub-watersheds with a relatively steep and narrow valley that drain directly to the mainstem river. Once ash and suspended sediment are introduced to the channel network these are typically transported downstream rather than stored, and if these constituents are the primary concern then rehabilitation efforts should focus on rapidly increasing the amount of ground cover on the hillslopes. Understanding controls on geomorphic changes, and identifying probable locations of stored sediment, can help prioritize areas for post-fire hillslope rehabilitation treatments, and identify those valley bottoms with the greatest potential for post-fire sediment erosion and deposition.

4.6 Conclusions

Fires can induce tremendous amounts of overland flow and hillslope erosion, and these can cause profound erosion and deposition throughout the channel network. This study analyzed post-fire changes in the channels and valley bottoms in two 15 km^2 watersheds for three years after the 2012 High Park Fire. Field observations and a detailed analysis of channel and valley bottom changes from differencing five sequential airborne laser scanning datasets show the primary effect of the fire was deposition following summer thunderstorms with smaller amounts of incision from spring runoff. This sequence was interrupted by a very unusual and large sustained flood in September 2013, 15 months after the fire, that eroded nearly all of the post-fire deposition along with much of the pre-fire valley bottom deposits. In the following two years there was much less deposition as the hillslopes recovered, and much less erosion as most of the available sediment had been removed by the September 2013 mesoscale flood.

Correlations were generally low, but results still suggest that precipitation depths and intensities, percent area burned at high and moderate severity, and valley and basin morphology can help identify areas of potentially greater geomorphic change, and therefore higher sensitivity. Most importantly, the results indicate that areas with greater sediment availability are locations where there is the greatest potential for geomorphic change. These locations include segments with channel slopes less than about 11%, but also locations of floodplain pockets, tributary junctions, colluvial

deposits, and in particular where the valley width is wide enough for more continuous floodplain development.

My experience processing ALS datasets provides useful insights into best practices for using repeat ALS data to document geomorphic changes after wildfires or other disturbances across small- to moderate-sized watersheds (0.1–15 km^2). The ALS data should be collected as soon as possible following the disturbance and preferably with a high enough temporal scale to understand the relative effects of different driving forces. When possible ALS data should be collected at similar times of the year, preferably during leaf-off, to avoid vegetation artifacts due to thick canopy cover. Ground control is crucial for improving the accuracy of the data. Using an automated approach to co-register the point clouds can greatly improve the accuracy of the ALS differencing, and incorporating spatially-varying uncertainties rather than uniform uncertainty improves the accuracy of volume change estimates.

Future research should be aimed at investigating post-fire sediment routing from hillslopes through channel networks, geomorphic changes at shorter temporal scales, and relationships between geomorphic changes and specific geomorphic units (e.g., channel, floodplain, pools, bars, etc.). Our ability to rigorously address these research needs is rapidly increasing as repeat high resolution topographic data become more readily available. The results presented here identify valley bottom reaches with higher sensitivity to geomorphic change, and can help inform future post-fire hillslope runoff and erosion mitigation efforts.

4.7 Supporting information

Additional supporting information is in Appendix D.

Bibliography

Abbott, J. T. (1970), Geology of Precambrian rocks and isotope geochemistry of shear zones in the Big Narrows area, northern Front Range, Colorado, *US Geological Survey, Open-File Report OF-70-1*.

Abbott, J. T. (1976), Geologic map of the Big Narrows quadrangle, Larimer County, Colorado, *US Geological Survey, Geologic Quadrangle Map GQ-1323*.

Anderson, H. W. (1976), Fire effects on water supply, floods, and sedimentation, in *Proceedings Tall Timbers Fire Ecology Conference*, pp. 249–260.

Anderson, S. W., S. P. Anderson, and R. S. Anderson (2015), Exhumation by debris flows in the 2013 Colorado Front Range storm, *Geology*, *43*(5), 391–394, doi:10.1130/G36507.1.

Arcement, G. J., and V. R. Schneider (1989), Guide for selecting Manning's roughness coefficients for natural channels and flood plains.

Asahi, K., Y. Shimizu, J. Nelson, and G. Parker (2013), Numerical simulation of river meandering with self-evolving banks, *Journal of Geophysical Research: Earth Surface*, *118*(4), 2208–2229, doi:10.1002/jgrf.20150.

Baker, V., and J. Costa (1987), Flood power, in *Catastrophic Flooding*, edited by V. Baker and J. Costa, pp. 1–21, Allen and Unwin.

Baker, V. R. (1977), Stream-channel response to floods, with examples from central Texas, *Geological Society of America Bulletin*, *88*(8), 1057–1071, doi:10.1130/0016-7606(1977)88<1057:SRTFWE>2.0.CO;2.

Bangen, S., J. Hensleigh, P. McHugh, and J. Wheaton (2016), Error modeling of DEMs from topographic surveys of rivers using fuzzy inference systems, *Water Resources Research*, *52*(2), 1176–1193, doi:10.1002/2015WR018299.

Barnes, H. H. (1967), Roughness characteristics of natural channels, *US Geological Survey Water-Supply Paper 1849*.

Beechie, T. J., M. Liermann, M. M. Pollock, S. Baker, and J. Davies (2006), Channel pattern and river-floodplain dynamics in forested mountain river systems, *Geomorphology*, *78*(1-2), 124–141, doi:10.1016/j.geomorph.2006.01.030.

Benavides-Solorio, J., and L. H. MacDonald (2001), Post-fire runoff and erosion from simulated rainfall on small plots, Colorado Front Range, *Hydrological Processes*, *15*(15), 2931–2952, doi:10.1002/hyp.383.

Benavides-Solorio, J., and L. H. MacDonald (2005), Measurement and prediction of post-fire erosion at the hillslope scale, Colorado Front Range, *International Journal of Wildland Fire*, *14*(4), 457–474, doi:10.1071/WF05042.

Benda, L., and T. Dunne (1997), Stochastic forcing of sediment routing and storage in channel networks, *Water Resources Research*, *33*(12), 2865–2880, doi:10.1029/97WR02387.

Benda, L., D. Miller, P. Bigelow, and K. Andras (2003), Effects of post-wildfire erosion on channel environments, Boise River, Idaho, *Forest Ecology and Management*, *178*(1), 105–119, doi:10.1016/S0378-1127(03)00056-2.

Berg, P., C. Moseley, and J. O. Haerter (2013), Strong increase in convective precipitation in response to higher temperatures, *Nature Geoscience*, *6*(3), 181–185, doi:10.1038/ngeo1731.

Bieger, K., H. Rathjens, P. M. Allen, and J. G. Arnold (2015), Development and evaluation of bankfull hydraulic geometry relationships for the physiographic regions of the United States, *JAWRA Journal of the American Water Resources Association*, *51*(3), 842–858.

Braddock, W. A., J. T. Abbott, J. J. Connor, and G. A. Swann (1988), Geologic map of the Poudre Park quadrangle, Larimer County, Colorado, *US Geological Survey, Geologic Quadrangle Map GQ-1620*.

Brierley, G. J. (2010), Landscape memory: the imprint of the past on contemporary landscape forms and processes, *Area*, *42*(1), 76–85, doi:10.1111/j.1475-4762.2009.00900.x.

Brogan, D. J., P. A. Nelson, and L. H. MacDonald (2017), Reconstructing extreme post-wildfire floods: a comparison of convective and mesoscale events, *Earth Surface Processes and Landforms*, *42*, 2505–2522, doi:10.1002/esp.4194.

Brunsden, D., and J. Thornes (1979), Landscape sensitivity and change, *Transactions of the Institute of British Geographers*, pp. 463–484, doi:10.2307/622210.

Cammeraat, E. L. (2004), Scale dependent thresholds in hydrological and erosion response of a semi-arid catchment in southeast Spain, *Agriculture, Ecosystems & Environment*, *104*(2), 317–332, doi:10.1016/j.agee.2004.01.032.

Campo, J., V. Andreu, E. Gimeno-García, O. González, and J. L. Rubio (2006), Occurrence of soil erosion after repeated experimental fires in a Mediterranean environment, *Geomorphology*, *82*(3-4), 376–387, doi:10.1016/j.geomorph.2006.05.014.

Canfield, H. E., C. J. Wilson, L. J. Lane, K. J. Crowell, and W. A. Thomas (2005), Modeling scour and deposition in ephemeral channels after wildfire, *Catena*, *61*(2), 273–291, doi:10.1016/j.catena.2005.03.013.

Cannon, S. H. (2001), Debris-flow generation from recently burned watersheds, *Environmental & Engineering Geoscience*, *7*(4), 321–341, doi:10.2113/gseegeosci.7.4.321.

Cannon, S. H., R. M. Kirkham, and M. Parise (2001), Wildfire-related debris-flow initiation processes, Storm King Mountain, Colorado, *Geomorphology*, *39*(3), 171–188, doi:10.1016/S0169-555X(00)00108-2.

Cannon, S. H., J. E. Gartner, M. G. Rupert, J. A. Michael, A. H. Rea, and C. Parrett (2010), Predicting the probability and volume of postwildfire debris flows in the intermountain western United States, *GSA Bulletin*, *122*(1-2), 127–144, doi:10.1130/B26459.1.

Carling, P., and K. Beven (1989), The hydrology, sedimentology and geomorphological implications of floods: an overview, *in Floods: Hydrological, Sedimentological and Geomorphological Implications. John Wiley & Sons New York. 1989. p 1-9.*

Chmura, D. J., P. D. Anderson, G. T. Howe, C. A. Harrington, J. E. Halofsky, D. L. Peterson, D. C. Shaw, and J. B. S. Clair (2011), Forest responses to climate change in the northwestern United States: ecophysiological foundations for adaptive management, *Forest Ecology and Management*, *261*(7), 1121–1142, doi:10.1016/j.foreco.2010.12.040.

Chow, V. T. (1959), *Open-channel hydraulics*, McGraw-Hill Book Co; New York, 680pp.

Cifelli, R., N. Doesken, P. Kennedy, L. D. Carey, S. A. Rutledge, C. Gimmestad, and T. Depue (2005), The community collaborative rain, hail, and snow network: Informal education for scientists and citizens, *Bulletin of the American Meteorological Society*, *86*(8), 1069–1077, doi: 10.1175/BAMS-86-8-1069.

Clow, D. W. (2010), Changes in the timing of snowmelt and streamflow in Colorado: a response to recent warming, *Journal of Climate*, *23*(9), 2293–2306, doi:10.1175/2009JCLI2951.1.

Cluer, B., and C. Thorne (2014), A stream evolution model integrating habitat and ecosystem benefits, *River Research and Applications*, *30*(2), 135–154, doi:10.1002/rra.2631.

Coe, J. A., J. W. Kean, J. W. Godt, R. L. Baum, E. S. Jones, D. J. Gochis, and G. S. Anderson (2014), New insights into debris-flow hazards from an extraordinary event in the Colorado Front Range, *GSA Today*, *24*(10), 4–10, doi:0.1130/GSATG214A.1.

Collins, L. M., and B. Ketcham (2001), Fluvial geomorphic response of a northern California coastal stream to wildfire, *Vision Fire - Lessons Learned from the 1995 fire*, pp. 59–79.

Costa, J. E. (1987), Hydraulics and basin morphometry of the largest flash floods in the conterminous United States, *Journal of hydrology*, *93*(3-4), 313–338, doi:10.1016/0022-1694(87) 90102-8.

Costa, J. E. (1988), Rheologic, geomorphic and sedimentologic differentiation of water floods, hyperconcentrated flows and debris flows, *in Flood Geomorphology*, pp. 113–122.

Costa, J. E., and J. E. O'Connor (1995), Geomorphically effective floods, *Natural and anthropogenic influences in fluvial geomorphology*, pp. 45–56, doi:10.1029/GM089p0045.

Cotrufo, M. F., C. M. Boot, S. Kampf, P. A. Nelson, D. J. Brogan, T. Covino, M. L. Haddix, L. H. MacDonald, S. Rathburn, S. Ryan-Bukett, et al. (2016), Redistribution of pyrogenic carbon from hillslopes to stream corridors following a large montane wildfire, *Global Biogeochemical Cycles*, *30*(9), 1348–1355, doi:10.1002/2016GB005467.

Dalrymple, T., and M. A. Benson (1967), *Measurement of peak discharge by the slope-area method*, US Government Printing Office.

de Vente, J., J. Poesen, M. Arabkhedri, and G. Verstraeten (2007), The sediment delivery problem revisited, *Progress in Physical Geography*, *31*(2), 155–178, doi:10.1177/0309133307076485.

DeBano, L. F., D. G. Neary, and P. F. Ffolliott (1998), *Fire effects on ecosystems*, 159–196 pp., John Wiley & Sons.

Dethier, D. P., W. Ouimet, P. R. Bierman, D. H. Rood, and G. Balco (2014), Basins and bedrock: Spatial variation in 10Be erosion rates and increasing relief in the southern Rocky Mountains, USA, *Geology*, *42*(2), 167–170, doi:10.1130/G34922.1.

Dingman, S. L., and K. P. Sharma (1997), Statistical development and validation of discharge equations for natural channels, *Journal of Hydrology*, *199*(1-2), 13–35, doi:10.1016/S0022-1694(96)03313-6.

Doehring, D. O. (1968), The effect of fire on geomorphic processes in the San Gabriel Mountains, California, *Rocky Mountain Geology*, *7*(1), 43–65.

Dunham, J. B., M. K. Young, R. E. Gresswell, and B. E. Rieman (2003), Effects of fire on fish populations: landscape perspectives on persistence of native fishes and nonnative fish invasions, *Forest Ecology and Management*, *178*(1), 183–196, doi:10.1016/S0378-1127(03)00061-6.

Eaton, B., R. Moore, and T. Giles (2010), Forest fire, bank strength and channel instability: the 'unusual' response of Fishtrap Creek, British Columbia, *Earth Surface Processes and Landforms*, *35*(10), 1167–1183, doi:10.1002/esp.1946.

Eaton, B. C., and T. R. Giles (2009), Assessing the effect of vegetation-related bank strength on channel morphology and stability in gravel-bed streams using numerical models, *Earth Surface Processes and Landforms*, *34*(5), 712–724, doi:10.1002/esp.1768.

Ebel, B. A., and B. B. Mirus (2014), Disturbance hydrology: challenges and opportunities, *Hydrol. Process*, *28*(19), 5140–5148, doi:10.1002/hyp.10256.

Ebel, B. A., J. A. Moody, and D. A. Martin (2012), Hydrologic conditions controlling runoff generation immediately after wildfire, *Water Resources Research*, *48*(3), doi:10.1029/2011WR011470.

Elliot, W. J. (2004), WEPP internet interfaces for forest erosion prediction, *Journal of the American Water Resources Association*, *40*, 299–309, doi:10.1111/J.1752-1688.2004.TB01030.X.

Elliot, W. J., M. E. Miller, and N. Enstice (2016), Targeting forest management through fire and erosion modelling, *International Journal of Wildland Fire*, *25*(8), 876–887, doi:10.1071/WF15007.

Elliott, J. G., and R. S. Parker (2001), Developing a post-fire flood chronology and recurrence probability from alluvial stratigraphy in the Buffalo Creek watershed, Colorado, USA, *Hydrological Processes*, *15*(15), 3039–3051, doi:10.1002/hyp.390.

Erskine, W., and M. Saynor (1996), Effects of catastrophic floods on sediment yields in southeastern Australia, in *Erosion and Sediment Yield: Global and Regional Perspectives: Proceedings of an International Symposium*, 236, p. 381, IAHS.

Ferguson, R. (2007), Flow resistance equations for gravel-and boulder-bed streams, *Water Resources Research*, *43*(5), doi:10.1029/2006WR005422.

Ferguson, R. (2010), Time to abandon the Manning equation?, *Earth Surface Processes and Landforms*, *35*(15), 1873–1876, doi:10.1002/esp.2091.

Flannigan, M. D., M. A. Krawchuk, W. J. de Groot, B. M. Wotton, and L. M. Gowman (2009), Implications of changing climate for global wildland fire, *International journal of wildland fire*, *18*(5), 483–507, doi:10.1071/WF08187.

Florsheim, J. L., E. A. Keller, and D. W. Best (1991), Fluvial sediment transport in response to moderate storm flows following chaparral wildfire, Ventura County, southern California, *Geological Society of America Bulletin*, *103*(4), 504–511, doi:10.1130/0016-7606(1991)103<0504:FSTIRT>2.3.CO;2.

Foster, M. A., R. S. Anderson, C. E. Wyshnytzky, W. B. Ouimet, and D. P. Dethier (2015), Hillslope lowering rates and mobile-regolith residence times from in situ and meteoric 10Be analysis, Boulder Creek Critical Zone Observatory, Colorado, *Bulletin*, *127*(5-6), 862–878, doi:10.1130/B31115.1.

Friedman, J. M., and V. J. Lee (2002), Extreme floods, channel change, and riparian forests along ephemeral streams, *Ecological Monographs*, *72*(3), 409–425, doi:10.2307/3100097.

Fryirs, K. (2013), (Dis)Connectivity in catchment sediment cascades: a fresh look at the sediment delivery problem, *Earth Surface Processes and Landforms*, *38*(1), 30–46, doi:10.1002/esp.3242.

Fryirs, K. A. (2017), River sensitivity: A lost foundation concept in fluvial geomorphology, *Earth Surface Processes and Landforms*, *42*(1), 55–70, doi:10.1002/esp.3940.

Fuller, I. C. (2008), Geomorphic impacts of a 100-year flood: Kiwitea Stream, Manawatu catchment, New Zealand, *Geomorphology*, *98*(1), 84–95, doi:10.1016/j.geomorph.2007.02.026.

Gabet, E. J., and T. Dunne (2003), Sediment detachment by rain power, *Water Resources Research*, *39*(1), doi:10.1029/2001WR000656.

Gardner, T. W. (1983), Experimental study of knickpoint and longitudinal profile evolution in cohesive, homogeneous material, *Geological Society of America Bulletin*, *94*(5), 664–672, doi: 10.1130/0016-7606(1983)94<664:ESOKAL>2.0.CO;2.

Gartner, J. D., W. B. Dade, C. E. Renshaw, F. J. Magilligan, and E. M. Buraas (2015), Gradients in stream power influence lateral and downstream sediment flux in floods, *Geology*, *43*(11), 983–986, doi:10.1130/G36969.1.

Gary, H. L. (1975), Watershed management problems and opportunities for the Colorado Front Range ponderosa pine zone: The status of our knowledge, *US Department of Agriculture, Forest Service, Rocky Mountain Forest and Range Experiment Station. RM-RP-139*, *139*, 32.

Germanoski, D. (2002), The importance of event sequencing on the geomorphic impact of wildfire in the central great basin, in *Geological Society of America Abstracts with Programs*, vol. 34, p. 319.

Gilbert, J. T., W. W. Macfarlane, and J. M. Wheaton (2016), The Valley Bottom Extraction Tool (V-BET): A GIS tool for delineating valley bottoms across entire drainage networks, *Computers & Geosciences*, *97*, 1–14, doi:10.1016/j.cageo.2016.07.014.

Gochis, D., R. Schumacher, K. Friedrich, N. Doesken, M. Kelsch, J. Sun, K. Ikeda, D. Lindsey, A. Wood, B. Dolan, S. Matrosov, A. Newman, K. Mahoney, S. Rutledge, R. Johnson, P. Kucera, P. Kennedy, D. Sempere-Torres, M. Steiner, R. Roberts, J. Wilson, W. Yu, V. Chandrasekar, R. Rasmussen, A. Anderson, and B. Brown (2014), The great Colorado flood of September 2013: Bulletin of the American Meteorological Society, *Bulletin of the American Meteorological Society*.

Goodrich, D., H. E. Canfield, I. S. Burns, D. Semmens, S. Miller, M. Hernandez, L. Levick, D. Guertin, and W. Kepner (2005), Rapid post-fire hydrologic watershed assessment using the

AGWA GIS-based hydrologic modeling tool, in *Managing Watersheds for Human and Natural Impacts: Engineering, Ecological, and Economic Challenges*, pp. 1–12.

Grant, G. E. (1997), Critical flow constrains flow hydraulics in mobile-bed streams: A new hypothesis, *Water Resources Research*, *33*(2), 349–358, doi:10.1029/96WR03134.

Hamilton, E., J. Horton, P. Rowe, and L. Reimann (1954), Fire-flood sequences on the San Dimas Experimental Forest, *Forest Service - U.S. Department of Agriculture, California Forest and Range Experiment Station, Technical Paper No. 6*.

Hartzell, P. J., P. J. Gadomski, C. L. Glennie, D. C. Finnegan, and J. S. Deems (2015), Rigorous error propagation for terrestrial laser scanning with application to snow volume uncertainty, *Journal of Glaciology*, *61*(230), 1147–1158, doi:10.3189/2015JoG15J031.

Havel, A., A. Tasdighi, and M. Arabi (2018), Assessing the long-term hydrologic response to wildfires in mountainous regions, *Hydrology and Earth System Sciences*, doi:10.5194/hess-2017-604.

Henkle, J. E., E. Wohl, and N. Beckman (2011), Locations of channel heads in the semiarid Colorado Front Range, USA, *Geomorphology*, *129*(3), 309–319.

Heritage, G. L., D. J. Milan, A. R. Large, and I. C. Fuller (2009), Influence of survey strategy and interpolation model on DEM quality, *Geomorphology*, *112*(3-4), 334–344, doi:10.1016/j.geomorph.2009.06.024.

Hey, R. D. (1979), Flow resistance in gravel-bed rivers, *Journal of the Hydraulics Division*, *105*(4), 365–379.

Hicks, N. S., J. A. Smith, A. J. Miller, and P. A. Nelson (2005), Catastrophic flooding from an orographic thunderstorm in the central Appalachians, *Water Resources Research*, *41*(12), doi:10.1029/2005WR004129.

Hodgson, M. E., and P. Bresnahan (2004), Accuracy of airborne LiDAR-derived elevation, *Photogrammetric Engineering & Remote Sensing*, *70*(3), 331–339, doi:10.14358/PERS.70.3.331.

Hohner, A. K., K. Cawley, J. Oropeza, R. S. Summers, and F. L. Rosario-Ortiz (2016), Drinking water treatment response following a Colorado wildfire, *Water research*, *105*, 187–198, doi:10.1016/j.watres.2016.08.034.

Holling, C. S. (1996), Engineering resilience versus ecological resilience, *Engineering within ecological constraints*, *31*(1996), 32.

Hooke, J. (2015), Variations in flood magnitude–effect relations and the implications for flood risk assessment and river management, *Geomorphology*, *251*, 91–107, doi:10.1016/j.geomorph.2015.05.014.

House, P. K., and P. A. Pearthree (1995), A geomorphologic and hydrologic evaluation of an extraordinary flood discharge estimate: Bronco Creek, Arizona, *Water Resources Research*, *31*(12), 3059–3073, doi:10.1029/95WR02428.

HPF BAER Report (2012), High Park Fire Burned Area Emergency Response (BAER) Report, Department of Transportation, Larimer County, Natural Resources Conservation Service, U.S. Forest Service, 25 pp.

Hsu, L., N. J. Finnegan, and E. E. Brodsky (2011), A seismic signature of river bedload transport during storm events, *Geophysical Research Letters*, *38*(13), doi:10.1029/2011GL047759.

Huffman, E. L., L. H. MacDonald, and J. D. Stednick (2001), Strength and persistence of fire-induced soil hydrophobicity under ponderosa and lodgepole pine, Colorado Front Range, *Hydrological Processes*, *15*(15), 2877–2892, doi:10.1002/hyp.379.

Hyde, K., S. W. Woods, and J. Donahue (2007), Predicting gully rejuvenation after wildfire using remotely sensed burn severity data, *Geomorphology*, *86*(3-4), 496–511, doi:10.1016/j.geomorph.2006.10.012.

Inbar, M., M. i. Tamir, and L. Wittenberg (1998), Runoff and erosion processes after a forest fire in Mount Carmel, a Mediterranean area, *Geomorphology*, *24*(1), 17–33, doi:10.1016/S0169-555X(97)00098-6.

Isenburg, M. (2015), LAStools - fast tools to catch reality, accessed: 2015-05-13.

Jarrett, R. D. (1984), Hydraulics of high-gradient streams, *Journal of Hydraulic Engineering*, *110*(11), 1519–1539, doi:10.1061/(ASCE)0733-9429(1984)110:11(1519).

Jarrett, R. D. (1987a), Errors in slope-area computations of peak discharges in mountain streams, *Journal of Hydrology*, *96*(1-4), 53–67, doi:10.1016/0022-1694(87)90143-0.

Jarrett, R. D. (1987b), Roughness coefficients of large floods, in *Irrigation Systems for the 21st Century*, pp. 32–40, American Society of Civil Engineers.

Jarrett, R. D., and J. E. Costa (1988), Evaluation of the flood hydrology in the Colorado Front Range using precipitation, streamflow, and paleoflood data for the Big Thompson River basin, *US Geological Survey Water-Resources Investigations Report 87-4117*.

Jarrett, R. D., and J. E. Costa (2006), 1976 Big Thompson Flood, Colorado - Thirty Years Later, *US Geological Survey Fact Sheet 2006-3095*, Accessed: 2015-01-29.

Jarrett, R. D., and J. F. England (2002), Reliability of paleostage indicators for paleoflood studies, *Ancient Floods, Modern Hazards*, pp. 91–109, doi:10.1029/WS005p0091.

Jin, S., L. Yang, P. Danielson, C. Homer, J. Fry, and G. Xian (2013), A comprehensive change detection method for updating the National Land Cover Database to circa 2011, *Remote Sensing of Environment*, *132*, 159–175, doi:10.1016/j.rse.2013.01.012.

Johansen, M. P., T. E. Hakonson, and D. D. Breshears (2001), Post-fire runoff and erosion from rainfall simulation: contrasting forests with shrublands and grasslands, *Hydrological processes*, *15*(15), 2953–2965, doi:10.1002/hyp.384.

Johnson, A. (2016), Snowmelt and rainfall runoff in burned and unburned catchments at the intermittent-persistent snow transition, Colorado Front Range, Master's thesis, Department of Ecosystem Science and Sustainability. Colorado State University, Fort Collins, CO, 81 pp.

Julien, P. Y. (2010), *Erosion and sedimentation*, Cambridge University Press.

Kampf, S. K., D. J. Brogan, S. Schmeer, L. H. MacDonald, and P. A. Nelson (2016), How do geomorphic effects of rainfall vary with storm type and spatial scale in a post-fire landscape?, *Geomorphology*, *273*, 39–51, doi:10.1016/j.geomorph.2016.08.001.

Kaufmann, M. R., L. Huckaby, and P. Gleason (2000), Ponderosa pine in the Colorado Front Range: long historical fire and tree recruitment intervals and a case for landscape heterogeneity, in *Proceedings of the Joint Fire Science Conference and Workshop: Crossing the millennium: integrating spatial technologies and ecological principles for a new age in fire management*, pp. 153–160.

Klemeš, V. (1983), Conceptualization and scale in hydrology, *Journal of hydrology*, *65*(1-3), 1–23, doi:10.1016/0022-1694(83)90208-1.

Kochel, R. C. (1988), Geomorphic impact of large floods: review and new perspectives on magnitude and frequency, *Flood Geomorphology. John Wiley & Sons New York. 1988. p 169-187. 9 fig, 2 tab, 43 ref. NSF Grant EAR 77-23025.*

Krajewski, W. F., A. Kruger, J. A. Smith, R. Lawrence, C. Gunyon, R. Goska, B.-C. Seo, P. Domaszczynski, M. L. Baeck, M. K. Ramamurthy, et al. (2011), Towards better utilization of NEXRAD data in hydrology: An overview of Hydro-NEXRAD, *Journal of hydroinformatics*, *13*(2), 255–266, doi:10.2166/hydro.2010.056.

Krapesch, G., C. Hauer, and H. Habersack (2011), Scale orientated analysis of river width changes due to extreme flood hazards, *Natural Hazards and Earth System Sciences*, *11*(8), 2137, doi:10.5194/nhess-11-2137-2011.

Kunze, M. D., and J. D. Stednick (2006), Streamflow and suspended sediment yield following the 2000 Bobcat fire, Colorado, *Hydrological Processes*, *20*(8), 1661–1681, doi:10.1002/hyp.5954.

Lague, D., N. Brodu, and J. Leroux (2013), Accurate 3D comparison of complex topography with terrestrial laser scanner: Application to the Rangitikei canyon (NZ), *ISPRS Journal of Photogrammetry and Remote Sensing*, *82*, 10–26, doi:10.1016/j.isprsjprs.2013.04.009.

Laird, J., and M. Harvey (1986), Complex-response of a chaparral drainage basin to fire, in *Drainage Basin Sediment Delivery*, edited by R. Hadley, 159, pp. 165–183, International Association of Hydrological Sciences, Albuquerque, NM.

Lane, S. N., S. C. Reid, R. M. Westaway, and D. M. Hicks (2004), Remotely sensed topographic data for river channel research: the identification, explanation and management of error, in *Spatial Modelling of the Terrestrial Environment*, edited by D. N. Kelly R, Barr S, pp. 113–136, John Wiley & Sons, Ltd: West Sussex, UK.

Larsen, I. J., and L. H. MacDonald (2007), Predicting postfire sediment yields at the hillslope scale: Testing RUSLE and Disturbed WEPP, *Water Resources Research*, *43*(11).

Larsen, I. J., L. H. MacDonald, E. Brown, D. Rough, M. J. Welsh, J. H. Pietraszek, Z. Libohova, J. de Dios Benavides-Solorio, and K. Schaffrath (2009), Causes of post-fire runoff and erosion: water repellency, cover, or soil sealing?, *Soil Science Society of America Journal*, *73*(4), 1393–1407, doi:10.2136/sssaj2007.0432.

Lee, A. J., and R. I. Ferguson (2002), Velocity and flow resistance in step-pool streams, *Geomorphology*, *46*(1-2), 59–71, doi:10.1016/S0169-555X(02)00054-5.

Legleiter, C. J., R. L. Lawrence, M. A. Fonstad, W. A. Marcus, and R. Aspinall (2003), Fluvial response a decade after wildfire in the northern yellowstone ecosystem: a spatially explicit analysis, *Geomorphology*, *54*(3), 119–136, doi:10.1016/S0169-555X(02)00332-X.

Legleiter, C. J., P. C. Kyriakidis, R. R. McDonald, and J. M. Nelson (2011), Effects of uncertain topographic input data on two-dimensional flow modeling in a gravel-bed river, *Water Resources Research*, *47*(3), doi:10.1029/2010WR009618.

Limerinos, J. T. (1970), Determination of the Manning coefficient from measured bed roughness in natural channels, *US Geological Survey Water-Supply Paper 1898-B*.

Lisenby, P., J. Croke, and K. Fryirs (2017), Geomorphic effectiveness: A linear concept in a non-linear world, *Earth Surface Processes and Landforms*, doi:10.1002/esp.4096.

Littell, J. S., D. McKenzie, D. L. Peterson, and A. L. Westerling (2009), Climate and wildfire area burned in western US ecoprovinces, 1916–2003, *Ecological Applications*, *19*(4), 1003–1021, doi:10.1890/07-1183.1.

Liu, Y., S. L. Goodrick, and J. A. Stanturf (2013), Future U.S. wildfire potential trends projected using a dynamically downscaled climate change scenario, *Forest Ecology and Management*, *294*, 120–135, doi:0.1016/j.foreco.2012.06.049.

Lukas, J., K. Wolter, K. Mahoney, J. Barsugli, N. Doesken, W. Ryan, I. Rangwala, B. Livneh, E. Gordon, M. Hoerling, et al. (2013), Severe flooding on the Colorado Front Range, September 2013: A preliminary assessment from the CIRES Western Water Assessment at the University of Colorado, *CIRES Western Water Assessment at the University of Colorado, NOAA ESRL Physical Science Division, and the CSU Colorado Climate Center*.

Lumbroso, D., and E. Gaume (2012), Reducing the uncertainty in indirect estimates of extreme flash flood discharges, *Journal of Hydrology*, *414*, 16–30, doi:0.1016/j.jhydrol.2011.08.048.

MacDonald, L. H., and J. D. Stednick (2003), Forests and water: A state-of-the-art review for Colorado, *Colorado Water Resources Research Institute Completion Report*, (196).

Magilligan, F. J. (1992), Thresholds and the spatial variability of flood power during extreme floods, *Geomorphology*, *5*(3-5), 373–390, doi:10.1016/0169-555X(92)90014-F.

Magilligan, F. J., J. D. Phillips, L. A. James, and B. Gomez (1998), Geomorphic and sedimentological controls on the effectiveness of an extreme flood, *The Journal of Geology*, *106*(1), 87–96, doi:10.1086/516009.

Magilligan, F. J., E. Buraas, and C. Renshaw (2015), The efficacy of stream power and flow duration on geomorphic responses to catastrophic flooding, *Geomorphology*, *228*, 175–188, doi:10.1016/j.geomorph.2014.08.016.

Mandlburger, G., J. Otepka, W. Karel, W. Wagner, and N. Pfeifer (2009), Orientation and processing of airborne laser scanning data (OPALS)–Concept and first results of a comprehensive ALS software, *International archives of the photogrammetry, remote sensing and spatial information sciences*, *38*(3/W8), 55–60.

Marcus, W. A., K. Roberts, L. Harvey, and G. Tackman (1992), An evaluation of methods for estimating Manning's n in small mountain streams, *Mountain Research and Development*, pp. 227–239, doi:10.2307/3673667.

McKean, J., D. Nagel, D. Tonina, P. Bailey, C. W. Wright, C. Bohn, and A. Nayegandhi (2009), Remote sensing of channels and riparian zones with a narrow-beam aquatic-terrestrial LIDAR, *Remote Sensing*, *1*(4), 1065–1096, doi:10.3390/rs1041065.

Mejía, A. I., and G. E. Moglen (2010), Spatial distribution of imperviousness and the space-time variability of rainfall, runoff generation, and routing, *Water Resources Research*, *46*(7), doi:10.1029/2009WR008568.

Meyer, G. A., S. G. Wells, R. C. Balling Jr, and A. T. Jull (1992), Response of alluvial systems to fire and climate change in Yellowstone National Park, *Nature*, *357*(6374), 147, doi:10.1038/357147a0.

Meyer, G. A., S. G. Wells, and A. J. T. Jull (1995), Fire and alluvial chronology in Yellowstone National Park: climatic and intrinsic controls on Holocene geomorphic processes, *Geologi-*

cal Society of America Bulletin, *107*(10), 1211–1230, doi:10.1130/0016-7606(1995)107<1211:FAACIY>2.3.CO;2.

Milan, D. J., G. L. Heritage, A. R. Large, and I. C. Fuller (2011), Filtering spatial error from DEMs: Implications for morphological change estimation, *Geomorphology*, *125*(1), 160–171, doi:10.1016/j.geomorph.2010.09.012.

Miller, A. J. (1990a), Flood hydrology and geomorphic effectiveness in the central Appalachians, *Earth Surface Processes and Landforms*, *15*(2), 119–134, doi:10.1002/esp.3290150203.

Miller, A. J. (1990b), Fluvial response to debris associated with mass wasting during extreme floods, *Geology*, *18*(7), 599–602, doi:{10.1130/0091-7613(1990)018\<0599:FRTDAW\>âĂŃ2.3.CO;2}.

Miller, A. J. (1995), Valley morphology and boundary conditions influencing spatial patterns of flood flow, *Natural and anthropogenic influences in fluvial geomorphology*, pp. 57–81, doi:10.1029/GM089p0057.

Miller, M. E., L. H. MacDonald, P. R. Robichaud, and W. J. Elliot (2011), Predicting post-fire hillslope erosion in forest lands of the western United States, *International Journal of Wildland Fire*, *20*(8), 982–999, doi:10.1071/WF09142.

Montgomery, D. R., and J. M. Buffington (1997), Channel-reach morphology in mountain drainage basins, *Geological Society of America Bulletin*, *109*(5), 596–611, doi:10.1130/0016-7606(1997)109<0596:CRMIMD>2.3.CO;2.

Moody, J. A. (2016), Estimates of peak flood discharge for 21 sites in the Front Range in Colorado in response to extreme rainfall in September 2013, *US Geological Survey Scientific Investigation Report, 2016-5003*, doi:10.3133/sir20165003.

Moody, J. A. (2017), Residence times and alluvial architecture of a sediment superslug in response to different flow regimes, *Geomorphology*, doi:10.1016/j.geomorph.2017.04.012.

Moody, J. A., and B. A. Ebel (2012), Hyper-dry conditions provide new insights into the cause of extreme floods after wildfire, *Catena*, *93*, 58–63, doi:10.1016/j.catena.2012.01.006.

Moody, J. A., and D. A. Kinner (2006), Spatial structures of stream and hillslope drainage networks following gully erosion after wildfire, *Earth Surface Processes and Landforms*, *31*(3), 319–337, doi:10.1002/esp.1246.

Moody, J. A., and D. A. Martin (2001a), Initial hydrologic and geomorphic response following a wildfire in the Colorado Front Range, *Earth Surface Processes and Landforms*, *26*(10), 1049–1070, doi:10.1002/esp.253.

Moody, J. A., and D. A. Martin (2001b), Post-fire, rainfall intensity–peak discharge relations for three mountainous watersheds in the western USA, *Hydrological processes*, *15*(15), 2981–2993, doi:10.1016/j.geomorph.2007.05.011.

Moody, J. A., and D. A. Martin (2004), Wildfire impacts on reservoir sedimentation in the western United States, in *Proceedings of the Ninth International Symposium on River Sedimentation*, pp. 1095–1102, Tsinghua University Press China.

Moody, J. A., and D. A. Martin (2009), Synthesis of sediment yields after wildland fire in different rainfall regimes in the western United States, *International Journal of Wildland Fire*, *18*(1), 96–115, doi:10.1071/WF07162.

Moody, J. A., D. A. Martin, S. L. Haire, and D. A. Kinner (2008a), Linking runoff response to burn severity after a wildfire, *Hydrological Processes*, *22*(13), 2063–2074, doi:10.1002/hyp.6806.

Moody, J. A., D. A. Martin, and S. H. Cannon (2008b), Post-wildfire erosion response in two geologic terrains in the western USA, *Geomorphology*, *95*(3-4), 103–118, doi:10.1016/j.geomorph.2007.05.011.

Moody, J. A., R. A. Shakesby, P. R. Robichaud, S. H. Cannon, and D. A. Martin (2013), Current research issues related to post-wildfire runoff and erosion processes, *Earth-Science Reviews*, *122*, 10–37.

Morris, S. E., and T. A. Moses (1987), Forest fire and the natural soil erosion regime in the Colorado Front Range, *Annals of the Association of American Geographers*, *77*(2), 245–254, doi: 10.1111/j.1467-8306.1987.tb00156.x.

Morvan, H., D. Knight, N. Wright, X. Tang, and A. Crossley (2008), The concept of roughness in fluvial hydraulics and its formulation in 1D, 2D and 3D numerical simulation models, *Journal of Hydraulic Research*, *46*(2), 191–208, doi:10.1080/00221686.2008.9521855.

Mrokowska, M. M., P. Rowiński, and M. B. Kalinowska (2014), Notes on the estimation of resistance to flow during flood wave propagation, *Hydrology and Earth System Sciences Discussions*, *11*(12), 13,311–13,352.

Nagel, D., J. Buffington, S. Parkes, S. Wenger, and J. Goode (2014), A landscape scale valley confinement algorithm: Delineating unconfined valley bottoms for geomorphic, aquatic, and riparian applications, *US Dept of Agriculture, Forest Service, RMRS-GTR 321, Fort Collins, CO*, p. 42, doi:10.2737/RMRS-GTR-321.

Nanson, G. C. (1986), Episodes of vertical accretion and catastrophic stripping: a model of disequilibrium flood-plain development, *Geological Society of America Bulletin*, *97*(12), 1467–1475, doi:10.1130/0016-7606(1986)97<1467:EOVAAC>2.0.CO;2.

Nardi, L., and M. Rinaldi (2015), Spatio-temporal patterns of channel changes in response to a major flood event: the case of the Magra River (central–northern Italy), *Earth Surface Processes and Landforms*, *40*(3), 326–339, doi:10.1002/esp.3636.

Neary, D. G., G. J. Gottfried, and P. F. Ffolliott (2003), Post-wildfire watershed flood responses, in *Proceedings of the 2nd International Fire Ecology Conference, American Meteorological Society*, vol. 1B7.

Nelson, J. M., J. P. Bennett, and S. M. Wiele (2003), Flow and sediment-transport modeling, *Tools in fluvial geomorphology*, *18*, 539–576.

Nelson, J. M., Y. Shimizu, T. Abe, K. Asahi, M. Gamou, T. Inoue, T. Iwasaki, T. Kakinuma, S. Kawamura, I. Kimura, et al. (2016), The international river interface cooperative: Public domain flow and morphodynamics software for education and applications, *Advances in Water Resources*, *93*, 62–74, doi:10.1016/j.advwatres.2015.09.017.

Newson, M. (1980), The geomorphological effectiveness of floods–a contribution stimulated by two recent events in mid-Wales, *Earth Surface Processes*, *5*(1), 1–16, doi:10.1002/esp.3760050102.

Nuth, C., and A. Kääb (2011), Co-registration and bias corrections of satellite elevation data sets for quantifying glacier thickness change, *The Cryosphere*, *5*(1), 271, doi:10.5194/tc-5-271-2011.

O'Connor, J. E., and J. E. Costa (2004), Spatial distribution of the largest rainfall-runoff floods from basins between 2.6 and 26,000 km2 in the United States and Puerto Rico, *Water Resources Research*, *40*(1), doi:10.1029/2003WR002247.

Onda, Y., W. E. Dietrich, and F. Booker (2008), Evolution of overland flow after a severe forest fire, Point Reyes, California, *Catena*, *72*(1), 13–20, doi:10.1016/j.catena.2007.02.003.

Orem, C. A., and J. D. Pelletier (2015), Quantifying the time scale of elevated geomorphic response following wildfires using multi-temporal LiDAR data: An example from the Las Conchas fire, Jemez Mountains, New Mexico, *Geomorphology*, *232*, 224–238.

Parsons, A. J., J. Wainwright, R. E. Brazier, and D. M. Powell (2006), Is sediment delivery a fallacy?, *Earth Surface Processes and Landforms*, *31*(10), 1325–1328, doi:10.1002/esp.1395.

Passalacqua, P., P. Belmont, D. M. Staley, J. D. Simley, J. R. Arrowsmith, C. A. Bode, C. Crosby, S. B. DeLong, N. F. Glenn, S. A. Kelly, et al. (2015), Analyzing high resolution topography for advancing the understanding of mass and energy transfer through landscapes: A review, *Earth-Science Reviews*, *148*, 174–193, doi:10.1016/j.earscirev.2015.05.012.

Pausas, J. G., J. Llovet, A. Rodrigo, and R. Vallejo (2009), Are wildfires a disaster in the Mediterranean basin?–A review, *International Journal of Wildland Fire*, *17*(6), 713–723, doi: 10.1071/WF07151.

Pelletier, J. D., and C. A. Orem (2014), How do sediment yields from post-wildfire debris-laden flows depend on terrain slope, soil burn severity class, and drainage basin area? Insights from airborne-LiDAR change detection, *Earth Surface Processes and Landforms*, *39*(13), 1822–1832, doi:10.1002/esp.3570.

Perica, S., D. Martin, S. Pavlovic, I. Roy, M. S. Laurent, C. Trypaluk, D. Unruh, M. Yekta, and G. Bonnin (2013), NOAA Atlas 14: Precipitation-frequency atlas of the United States, *U.S. Department of Commerce, National Oceanic and Atmospheric Administration, and National Weather Service, Silver Spring, MD.*

Pettit, N. E., and R. J. Naiman (2007), Fire in the riparian zone: characteristics and ecological consequences, *Ecosystems*, *10*(5), 673–687, doi:10.1007/s10021-007-9048-5.

Phillips, J. D., and C. Van Dyke (2016), Principles of geomorphic disturbance and recovery in response to storms, *Earth Surface Processes and Landforms*, doi:10.1002/esp.3912.

Phillips, J. D., and C. Van Dyke (2017), State-and-transition models in geomorphology, *CATENA*, *153*, 168–181, doi:10.1016/j.catena.2017.02.009.

Pierce, J. L., G. A. Meyer, and A. T. Jull (2004), Fire-induced erosion and millennial-scale climate change in northern ponderosa pine forests, *Nature*, *432*(7013), 87, doi:10.1038/nature03058.

Pierson, T. C. (2005), Hyperconcentrated flowâĂŤtransitional process between water flow and debris flow, in *Debris-flow hazards and related phenomena*, pp. 159–202, Springer.

Pierson, T. C., and J. E. Costa (1987), A rheologic classification of subaerial sediment-water flows, *Debris flows/avalanches: process, recognition, and mitigation. Reviews in Engineering Geology*, *7*, 1–12.

Pietraszek, J. (2006), Controls on post-fire erosion at the hillslope scale, Master's thesis, Department of Forest, Rangeland, and Watershed Stewardship. Colorado State University, Fort Collins, CO, 124 pp.

Poff, N. L., J. D. Allan, M. B. Bain, J. R. Karr, K. L. Prestegaard, B. D. Richter, R. E. Sparks, and J. C. Stromberg (1997), The natural flow regime, *BioScience*, *47*(11), 769–784.

Prosser, I. P., and L. Williams (1998), The effect of wildfire on runoff and erosion in native Eucalyptus forest, *Hydrological processes*, *12*(2), 251–265, doi:10.1002/(SICI)1099-1085(199802)12:2<251::AID-HYP574>3.0.CO;2-4.

Rathburn, S. L., S. M. Shahverdian, and S. E. Ryan (2017), Post-disturbance sediment recovery: Implications for watershed resilience, *Geomorphology*, doi:10.1016/j.geomorph.2017.08.039.

Reid, D. E., and E. J. Hickin (2008), Flow resistance in steep mountain streams, *Earth Surface Processes and Landforms*, *33*(14), 2211–2240, doi:10.1002/esp.1682.

Renard, K. G., G. R. Foster, G. A. Weesies, D. K. McCool, and D. C. Yoder (1997), *Predicting soil erosion by water: a guide to conservation planning with the Revised Universal Soil Loss Equation (RUSLE)*, US Government Printing Office Washington, DC.

Reneau, S. L., D. Katzman, G. A. Kuyumjian, A. Lavine, and D. V. Malmon (2007), Sediment delivery after a wildfire, *Geology*, *35*(2), 151–154, doi:10.1130/G23288A.1.

Rengers, F., G. Tucker, J. Moody, and B. Ebel (2016), Illuminating wildfire erosion and deposition patterns with repeat terrestrial lidar, *Journal of Geophysical Research: Earth Surface*, *121*(3), 588–608, doi:10.1002/2015JF003600.

Rhoades, C. C., D. Entwistle, and D. Butler (2011), The influence of wildfire extent and severity on streamwater chemistry, sediment and temperature following the Hayman Fire, Colorado, *International Journal of Wildland Fire*, *20*(3), 430–442, doi:10.1071/WF09086.

Rinaldi, M., N. Surian, F. Comiti, and M. Bussettini (2013), A method for the assessment and analysis of the hydromorphological condition of Italian streams: the Morphological Quality Index (MQI), *Geomorphology*, *180*, 96–108, doi:10.1016/j.geomorph.2012.09.009.

Robichaud, P. R., J. L. Beyers, and D. G. Neary (2000), Evaluating the effectiveness of postfire rehabilitation treatments, USDA Forest Service, RMRS-GTR-63, Fort Collins, CO.

Robichaud, P. R., W. J. Elliot, F. B. Pierson, D. E. Hall, and C. A. Moffet (2007), Predicting post-fire erosion and mitigation effectiveness with a web-based probabilistic erosion model, *Catena*, *71*(2), 229–241, doi:10.1016/j.catena.2007.03.003.

Rocca, M. E., P. M. Brown, L. H. MacDonald, and C. M. Carrico (2014), Climate change impacts on fire regimes and key ecosystem services in Rocky Mountain forests, *Forest Ecology and Management*, *327*, 290–305, doi:10.1016/j.foreco.2014.04.005.

Roering, J. J., and M. Gerber (2005), Fire and the evolution of steep, soil-mantled landscapes, *Geology*, *33*(5), 349–352, doi:10.1130/G21260.1.

Roux, C., A. Alber, M. Bertrand, L. Vaudor, and H. Piégay (2015), "FluvialCorridor": A new ArcGIS toolbox package for multiscale riverscape exploration, *Geomorphology*, *242*, 29–37, doi:10.1016/j.geomorph.2014.04.018.

Santi, P. M., J. D. Higgins, S. H. Cannon, J. E. Gartner, et al. (2008), Sources of debris flow material in burned areas, *Geomorphology*, *96*(3), 310–321, doi:10.1016/j.geomorph.2007.02.022.

Schick, A. (1974), Formation and obliteration of desert stream terraces-a conceptual analysis, *Geomorphology*, *21*, 88–105.

Schmeer, S. R. (2014), Post-fire erosion response and recovery, High Park Fire, Colorado, Master's thesis, Department of Ecosystem Science and Sustainability. Colorado State University, Fort Collins, CO, 153 pp.

Schmeer, S. R., S. K. Kampf, L. H. MacDonald, J. Hewitt, and C. Wilson (2018), Empirical models of annual post-fire erosion on mulched and unmulched hillslopes, *CATENA*, *163*, 276–287, doi: 10.1016/j.catena.2017.12.029.

Schumm, S. A. (1973), Geomorphic thresholds and complex response of drainage systems, *Fluvial geomorphology*, *6*, 69–85.

Schumm, S. A. (1979), Geomorphic thresholds: the concept and its applications, *Transactions of the Institute of British Geographers*, pp. 485–515.

Schumm, S. A. (1998), *To Interpret the Earth: Ten ways to be wrong*, Cambridge University Press.

Schumm, S. A., and R. W. Lichty (1963), Channel widening and flood-plain construction along Cimarron River in southwestern Kansas, US Geological Survey Professional Paper 352-D.

Schumm, S. A., M. D. Harvey, and C. C. Watson (1984), *Incised channels: morphology, dynamics, and control*, Water Resources Publications.

Scott, D. F., and D. B. Van Wyk (1990), The effects of wildfire on soil wettability and hydrological behaviour of an afforested catchment, *Journal of hydrology*, *121*(1), 239–256, doi: 10.1016/0022-1694(90)90234-O.

Scott, D. N., D. J. Brogan, K. B. Lininger, D. M. Schook, E. E. Daugherty, M. S. Sparacino, and A. I. Patton (2016), Evaluating survey instruments and methods in a steep channel, *Geomorphology*, *273*, 236–243, doi:10.1016/j.geomorph.2016.08.020.

Shahverdian, S. M. (2015), Controls on post-High Park Fire channel response, South Fork Cache la Poudre Basin, Colorado, Master's thesis, Department of Geosciences. Colorado State University, Fort Collins, CO, 104 pp.

Shakesby, R. A., and S. H. Doerr (2006), Wildfire as a hydrological and geomorphological agent, *Earth-Science Reviews*, *74*(3), 269–307.

Simon, A., and C. R. Hupp (1986), Channel evolution in modified Tennessee channels, pp. 71–82, Fourth Federal Interagency Sedimentation Conference, Las Vegas, NV.

Smith, H. G., G. J. Sheridan, P. N. Lane, P. Nyman, and S. Haydon (2011), Wildfire effects on water quality in forest catchments: a review with implications for water supply, *Journal of Hydrology*, *396*(1), 170–192, doi:10.1016/j.jhydrol.2010.10.043.

Smith, J. A., M. L. Baeck, K. L. Meierdiercks, P. A. Nelson, A. J. Miller, and E. J. Holland (2005a), Field studies of the storm event hydrologic response in an urbanizing watershed, *Water Resources Research*, *41*(10), doi:10.1029/2004WR003712.

Smith, J. A., A. J. Miller, M. L. Baeck, P. A. Nelson, G. T. Fisher, and K. L. Meierdiercks (2005b), Extraordinary flood response of a small urban watershed to short-duration convective rainfall, *Journal of Hydrometeorology*, *6*(5), 599–617, doi:10.1175/JHM426.1.

Smith, M., J. Carrivick, and D. Quincey (2016), Structure from motion photogrammetry in physical geography, *Progress in Physical Geography*, *40*(2), 247–275, doi:10.1177/0309133315615805.

Smith, M. W., N. J. Cox, and L. J. Bracken (2007), Applying flow resistance equations to overland flows, *Progress in Physical Geography*, *31*(4), 363–387.

Soil Survey Staff (2018), Natural Resources Conservation Service, United States Department of Agriculture. Web Soil Survey, Accessed: 2018-01-25.

Stoffel, M., B. Wyżga, and R. A. Marston (2016), Floods in mountain environments: A synthesis, *Geomorphology*, *272*, 1–9, doi:10.1016/j.geomorph.2016.07.008.

Stone, B. (2015), Mapping burn severity, pine beetle infestation, and their interaction at the High Park Fire, Master's thesis, Graduate Degree Program in Ecology. Colorado State University, Fort Collins, CO, 90 pp.

Stoof, C. R., R. Vervoort, J. Iwema, E. Van den Elsen, A. Ferreira, and C. Ritsema (2012), Hydrological response of a small catchment burned by experimental fire, *Hydrology and Earth System Sciences*, *16*(2), 267, doi:10.5194/hess-16-267-2012.

Stout, J. C., and P. Belmont (2014), TerEx Toolbox for semi-automated selection of fluvial terrace and floodplain features from lidar, *Earth Surface Processes and Landforms*, *39*(5), 569–580, doi:10.1002/esp.3464.

Strahler, A. N. (1964), Quantitative geomorphology of drainage basins and channel networks, in *Handbook of Applied Hydrology*, edited by V. Chow, pp. 4–39, McGraw-Hill.

Surian, N., M. Righini, A. Lucía, L. Nardi, W. Amponsah, M. Benvenuti, M. Borga, M. Cavalli, F. Comiti, L. Marchi, et al. (2016), Channel response to extreme floods: insights on controlling factors from six mountain rivers in northern Apennines, Italy, *Geomorphology*, *272*, 78–91, doi:10.1016/j.geomorph.2016.02.002.

Swanson, F. J. (1981), Fire and geomorphic processes, in *Fire Regime and Ecosystem Properties*, edited by H. Mooney, T. Bonnicksen, N. Christensen, J. Lotan, and W. Reiners, pp. 401–444, United States Department of Agriculture Forest Service General Technical Report WO-26.

Tabacchi, E., J. Steiger, D. Corenblit, M. T. Monaghan, and A.-M. Planty-Tabacchi (2009), Implications of biological and physical diversity for resilience and resistance patterns within Highly Dynamic River Systems, *Aquatic Sciences-Research Across Boundaries*, *71*(3), 279–289, doi:10.1007/s00027-009-9195-1.

Thomas, M. F. (2001), Landscape sensitivity in time and space – an introduction, *Catena*, *42*(2), 83–98, doi:10.1016/S0341-8162(00)00133-8.

Thompson, C., and J. Croke (2013), Geomorphic effects, flood power, and channel competence of a catastrophic flood in confined and unconfined reaches of the upper Lockyer valley, southeast Queensland, Australia, *Geomorphology*, *197*, 156–169, doi:10.1016/j.geomorph.2013.05.006.

Tonina, D., and K. Jorde (2013), Hydraulic modelling approaches for ecohydraulic studies: 3D, 2D, 1D and non-numerical models, *Ecohydraulics: An integrated approach*, pp. 31–74, doi: 10.1002/9781118526576.ch3.

Tulldahl, H. M., and H. Larsson (2014), Lidar on small UAV for 3D mapping, in *Electro-Optical Remote Sensing, Photonic Technologies, and Applications VIII; and Military Applications in Hyperspectral Imaging and High Spatial Resolution Sensing II*, International Society for Optics and Photonics, Amsterdam, Netherlands, doi:10.1117/12.2068448.

Veblen, T. T., T. Kitzberger, and J. Donnegan (2000), Climatic and human influences on fire regimes in ponderosa pine forests in the Colorado Front Range, *Ecological Applications*, *10*(4), 1178–1195, doi:10.1890/1051-0761(2000)010[1178:CAHIOF]2.0.CO;2.

Vericat, D., J. M. Wheaton, and J. Brasington (2017), Revisiting the morphological approach: Opportunities and challenges with repeat high-resolution topography, in *Gravel-Bed Rivers: Process and Disasters*, pp. 121–155, John Wiley & Sons.

Wagenbrenner, J., L. MacDonald, and D. Rough (2006), Effectiveness of three post-fire rehabilitation treatments in the Colorado Front Range, *Hydrological Processes*, *20*(14), 2989–3006, doi:10.1002/hyp.6146.

Wagenbrenner, J. W., and P. R. Robichaud (2014), Post-fire bedload sediment delivery across spatial scales in the interior western United States, *Earth Surface Processes and Landforms*, *39*(7), 865–876, doi:10.1002/esp.3488.

Walling, D. (1977), Assessing the accuracy of suspended sediment rating curves for a small basin, *Water Resources Research*, *13*(3), 531–538, doi:10.1029/WR013i003p00531.

Walling, D. E. (1983), The sediment delivery problem, *Journal of hydrology*, *65*(1), 209–237, doi:10.1016/0022-1694(83)90217-2.

Webb, R. H., and R. D. Jarrett (2002), One-dimensional estimation techniques for discharges of paleofloods and historical floods, *Ancient Floods, Modern Hazards*, pp. 111–125, doi:10.1029/WS005p0111.

Weber, M. D., and G. B. Pasternack (2017), Valley-scale morphology drives differences in fluvial sediment budgets and incision rates during contrasting flow regimes, *Geomorphology*, *288*, 39–51, doi:10.1016/j.geomorph.2017.03.018.

Westerling, A. L., H. G. Hidalgo, D. R. Cayan, and T. W. Swetnam (2006), Warming and earlier spring increase western U.S. forest wildfire activity, *Science*, *313*(5789), 940–943, doi:10.1126/science.1128834.

Wheaton, J. M., J. Brasington, S. E. Darby, and D. A. Sear (2010), Accounting for uncertainty in DEMs from repeat topographic surveys: improved sediment budgets, *Earth Surface Processes and Landforms*, *35*(2), 136–156, doi:10.1002/esp.1886.

Wicherski, W., D. P. Dethier, and W. B. Ouimet (2017), Erosion and channel changes due to extreme flooding in the Fourmile Creek catchment, Colorado, *Geomorphology*, doi:10.1016/j.geomorph.2017.03.030.

Wilson, C., S. K. Kampf, J. W. Wagenbrenner, and L. H. MacDonald (2018), Rainfall thresholds for post-fire runoff and sediment delivery from plot to watershed scales, *Forest Ecology and Management*, *430*, 346–356, doi:10.1016/j.foreco.2018.08.025.

Wohl, E. (2013), Migration of channel heads following wildfire in the Colorado Front Range, USA, *Earth Surface Processes and Landforms*, *38*(9), 1049–1053, doi:10.1002/esp.3429.

Wohl, E., and D. N. Scott (2017), Transience of channel head locations following disturbance, *Earth Surface Processes and Landforms*, *42*, doi:10.1002/esp.4124.

Wohl, E., B. P. Bledsoe, R. B. Jacobson, N. L. Poff, S. L. Rathburn, D. M. Walters, and A. C. Wilcox (2015), The natural sediment regime in rivers: broadening the foundation for ecosystem management, *BioScience*, *65*(4), 358–371, doi:10.1093/biosci/biv002.

Wohl, E., S. Rathburn, S. Chignell, K. Garrett, D. Laurel, B. Livers, A. Patton, R. Records, M. Richards, D. M. Schook, et al. (2017), Mapping longitudinal stream connectivity in the North St. Vrain Creek watershed of Colorado, *Geomorphology*, *277*, 171–181, doi:10.1016/j.geomorph.2016.05.004.

Wohl, E. E. (1998), Uncertainty in flood estimates associated with roughness coefficient, *Journal of Hydraulic Engineering*, *124*(2), 219–223.

Wohl, E. E., and P. P. Pearthree (1991), Debris flows as geomorphic agents in the Huachuca Mountains of southeastern Arizona, *Geomorphology*, *4*(3-4), 273–292, doi:10.1016/0169-555X(91)90010-8.

Wolman, M. G. (1954), A method of sampling coarse river-bed material, *EOS, Transactions American Geophysical Union*, *35*(6), 951–956, doi:10.1029/TR035i006p00951.

Wolman, M. G., and J. P. Eiler (1958), Reconnaissance study of erosion and deposition produced by the flood of August 1955 in Connecticut, *EOS, Transactions American Geophysical Union*, *39*(1), 1–14, doi:10.1029/TR039i001p00001.

Wolman, M. G., and R. Gerson (1978), Relative scales of time and effectiveness of climate in watershed geomorphology, *Earth Surface Processes and Landforms*, *3*(2), 189–208, doi:10.1002/esp.3290030207.

Wolman, M. G., and J. P. Miller (1960), Magnitude and frequency of forces in geomorphic processes, *The Journal of Geology*, *68*(1), 54–74, doi:10.1086/626637.

Wondzell, S. M., and J. G. King (2003), Postfire erosional processes in the Pacific Northwest and Rocky Mountain regions, *Forest Ecology and Management*, *178*(1), 75–87.

Wright, D. B., J. A. Smith, G. Villarini, and M. L. Baeck (2014), Long-term high-resolution radar rainfall fields for urban hydrology, *JAWRA Journal of the American Water Resources Association*, *50*(3), 713–734, doi:10.1111/jawr.12139.

Writer, J. H., A. Hohner, J. Oropeza, A. Schmidt, K. M. Cawley, F. L. Rosario-Ortiz, et al. (2014), Water treatment implications after the high Park wildfire, Colorado, *J. Am. Water Works Assoc*, *106*(4), E189–E199, doi:10.5942/jawwa.2014.106.0055.

Yager, E. M., W. Dietrich, J. W. Kirchner, and B. McArdell (2012), Patch dynamics and stability in steep, rough streams, *Journal of Geophysical Research: Earth Surface*, *117*(F2), doi:10.1029/2011JF002253.

Yochum, S. E. (2015), Colorado Front Range flood of 2013: peak flows and flood frequencies, in *3rd Joint Federal Interagency Conference on Sedimentation and Hydrologic Modeling*, pp. 537–548.

Yochum, S. E., F. Comiti, E. Wohl, G. C. David, and L. Mao (2014), *Photographic guidance for selecting flow resistance coefficients in high-gradient channels*, United States Department of Agriculture, Forest Service, Rocky Mountain Research Station.

Yochum, S. E., J. S. Sholtes, J. A. Scott, and B. P. Bledsoe (2017), Stream power framework for predicting geomorphic change: The 2013 Colorado Front Range flood, *Geomorphology*, doi:10.1016/j.geomorph.2017.03.004.

Zrnić, D., and A. Ryzhkov (1996), Advantages of rain measurements using specific differential phase, *Journal of Atmospheric and Oceanic Technology*, *13*(2), 454–464, doi:10.1175/1520-0426(1996)013<0454:AORMUS>2.0.CO;2.

Appendix A

Supporting information for Chapter 1

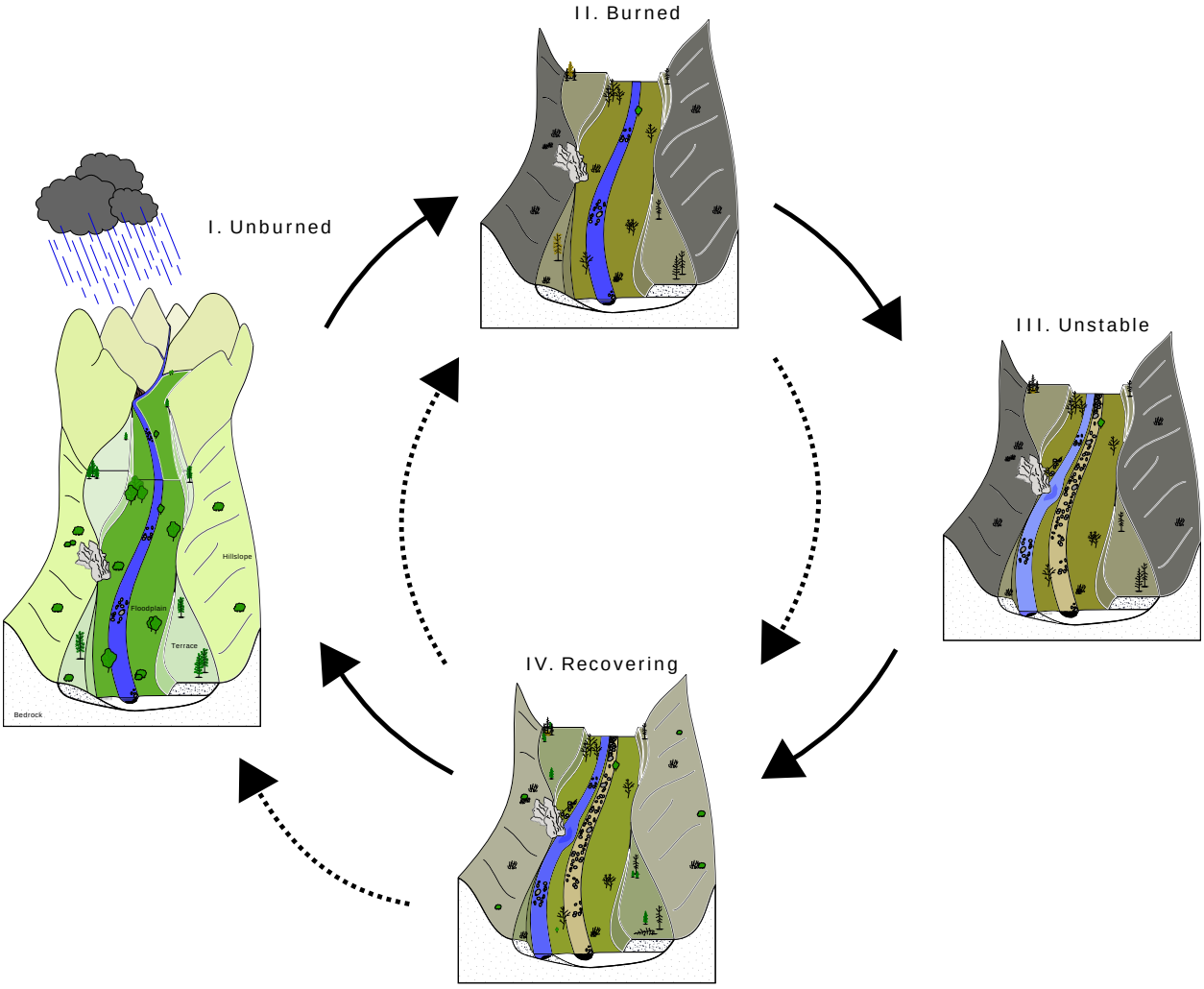

Figure A.1: Conceptual post-fire geomorphic response illustrated as four primary states: I. Unburned; II. Burned; III. Unstable; and IV. Recovering. Transitions between states are a function of burning, rainfall, runoff, and vegetation recovery (arrows with solid lines). Watersheds can deviate from this idealized cycle, and three potential deviations are highlighted (arrows with dashed lines). First, it is possible for a burned watershed to skip the unstable state if there is insufficient precipitation to cause substantial erosion (II $\rightarrow$ IV; e.g. *Eaton et al.*, 2010; *Prosser and Williams*, 1998). Second, a recovering watershed could burn again or have areas burn that were not burned in the previous fire before the watershed fully recovers (IV $\rightarrow$ II; sensu *Campo et al.*, 2006). Third, the combination of a stand-replacing fire and climate change or a lack of seed source could cause a long-term change in vegetation type (IV $\rightarrow$ I; e.g. *Pierce et al.*, 2004).

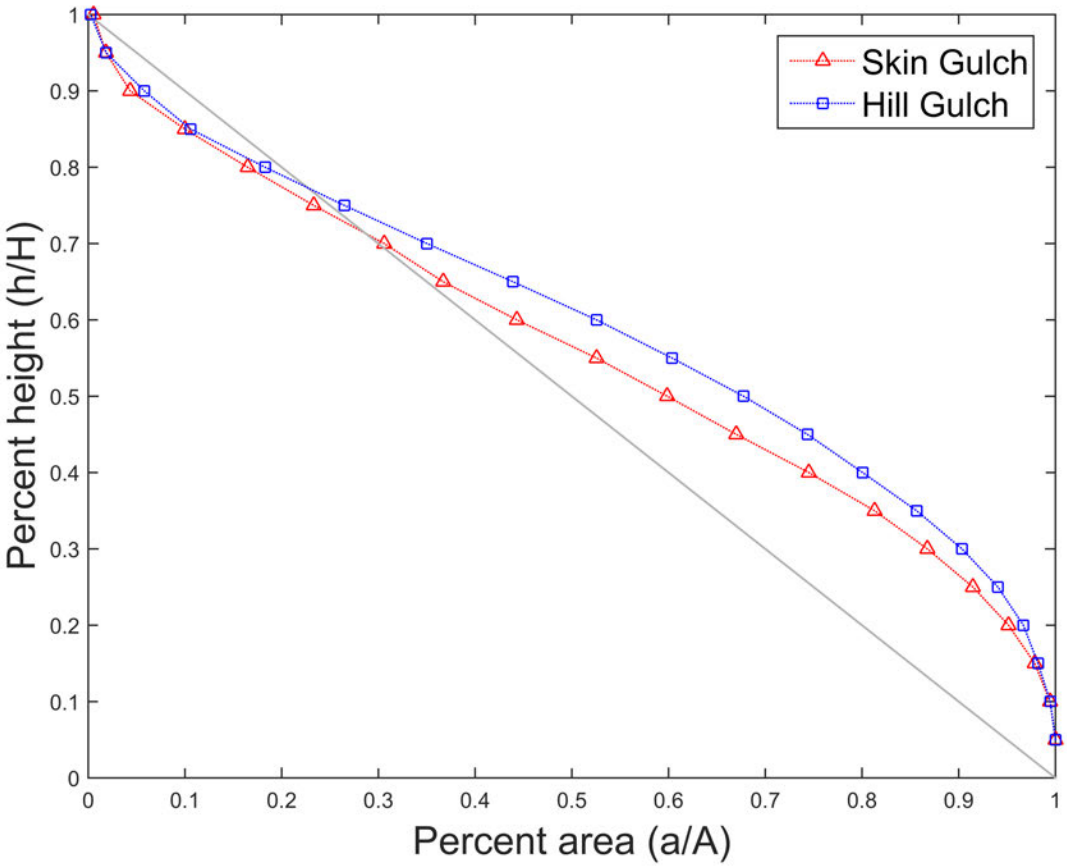

Figure A.2: Hypsometric curves for Skin Gulch (red) and Hill Gulch (blue).

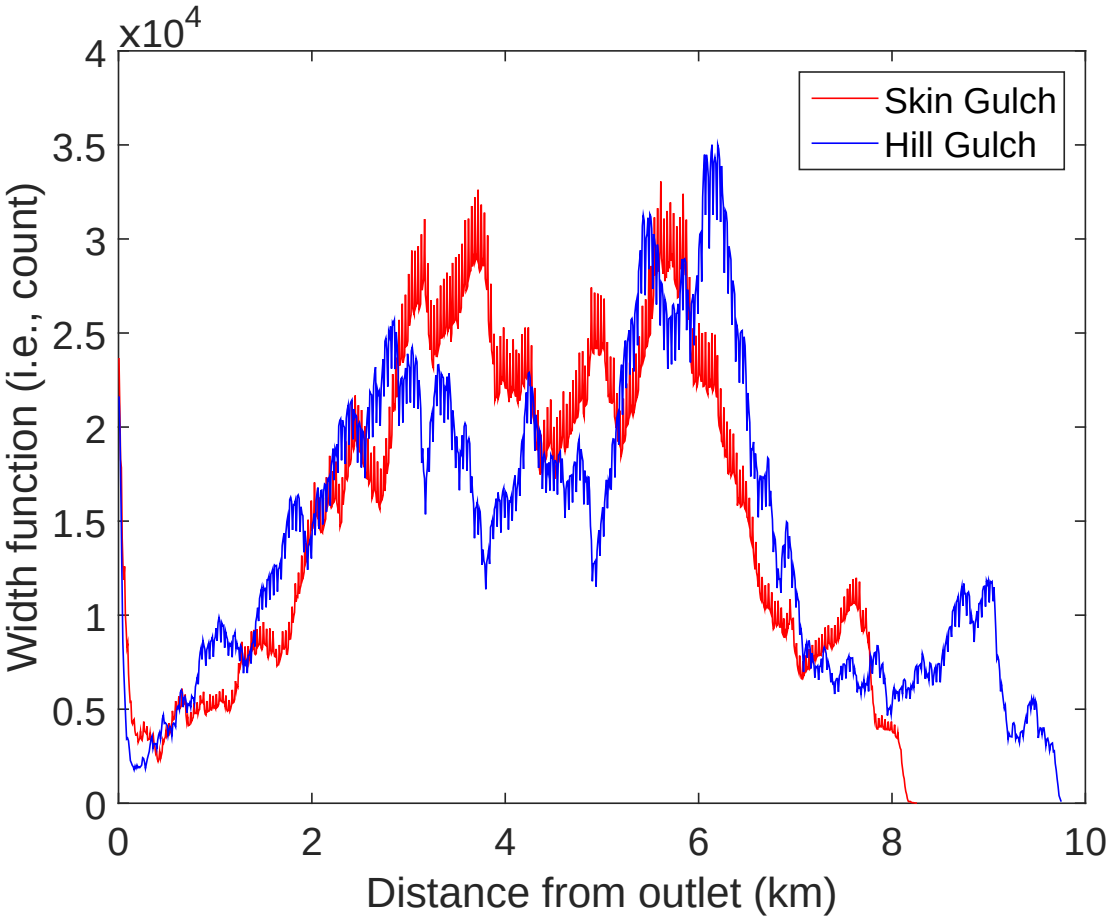

Figure A.3: Width function curves for Skin Gulch (red) and Hill Gulch (blue).

Appendix B

Supporting information for Chapter 2

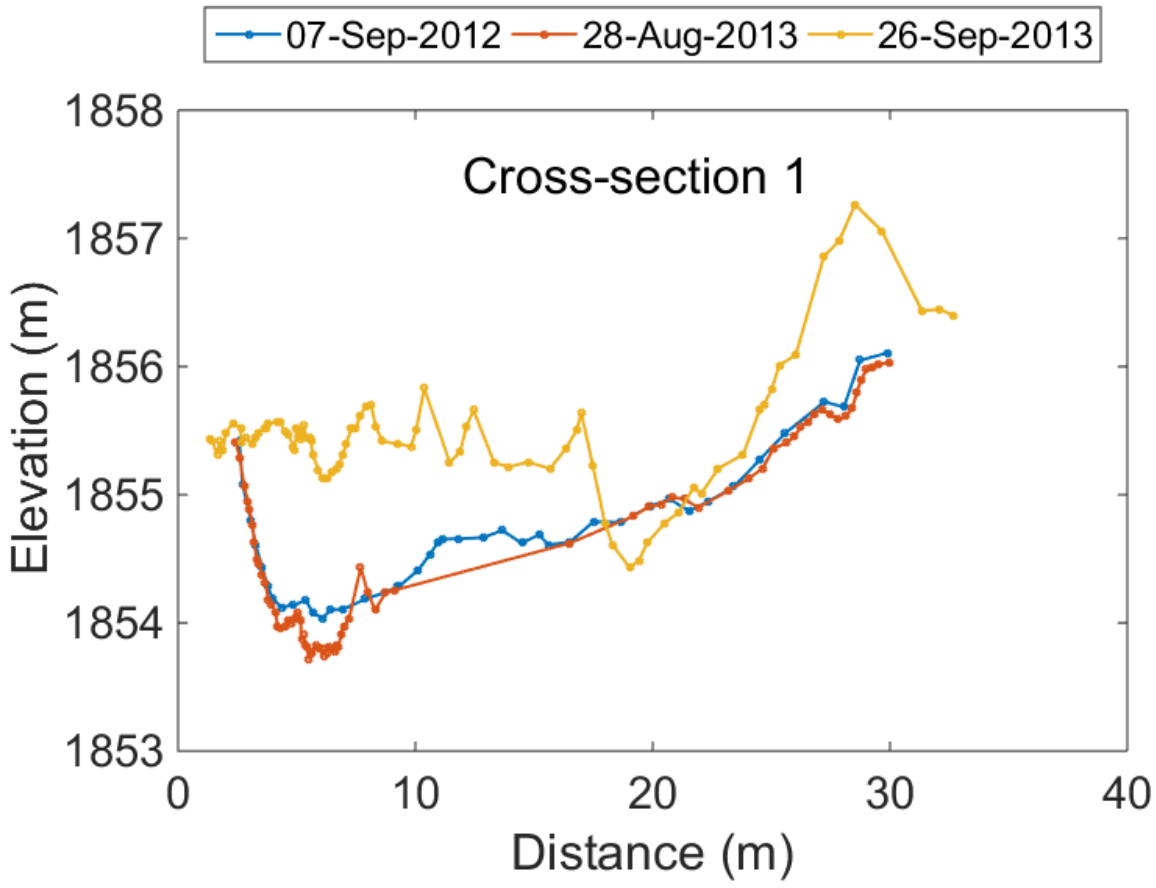

Figure B.1: Plot of cross section 1 in Skin Gulch as surveyed in fall 2012, pre-2013 flood, and post-2013 flood. Much of the post-2013 flood topography was disturbed by excavation due to deposition on the neighboring county highway.

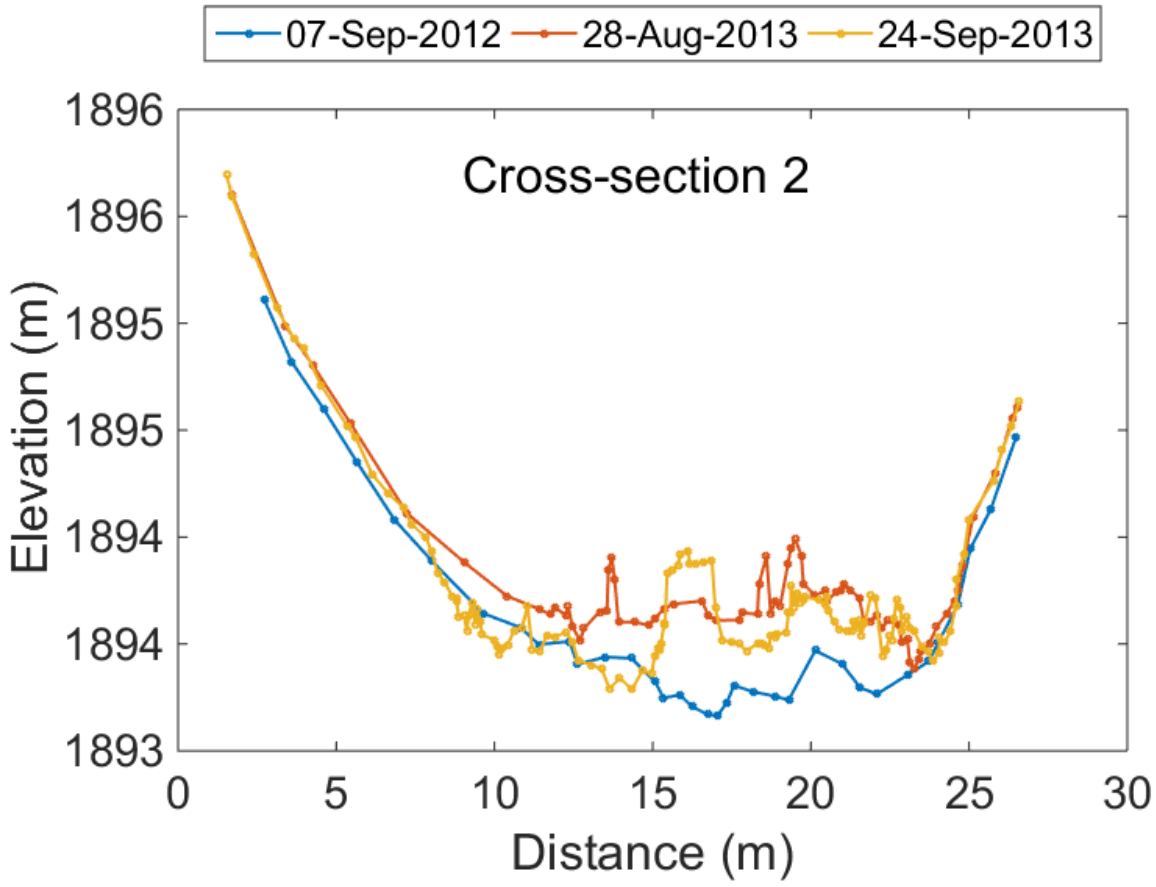

Figure B.2: Plot of cross section 2 in Skin Gulch as surveyed in fall 2012, pre-2013 flood, and post-2013 flood.

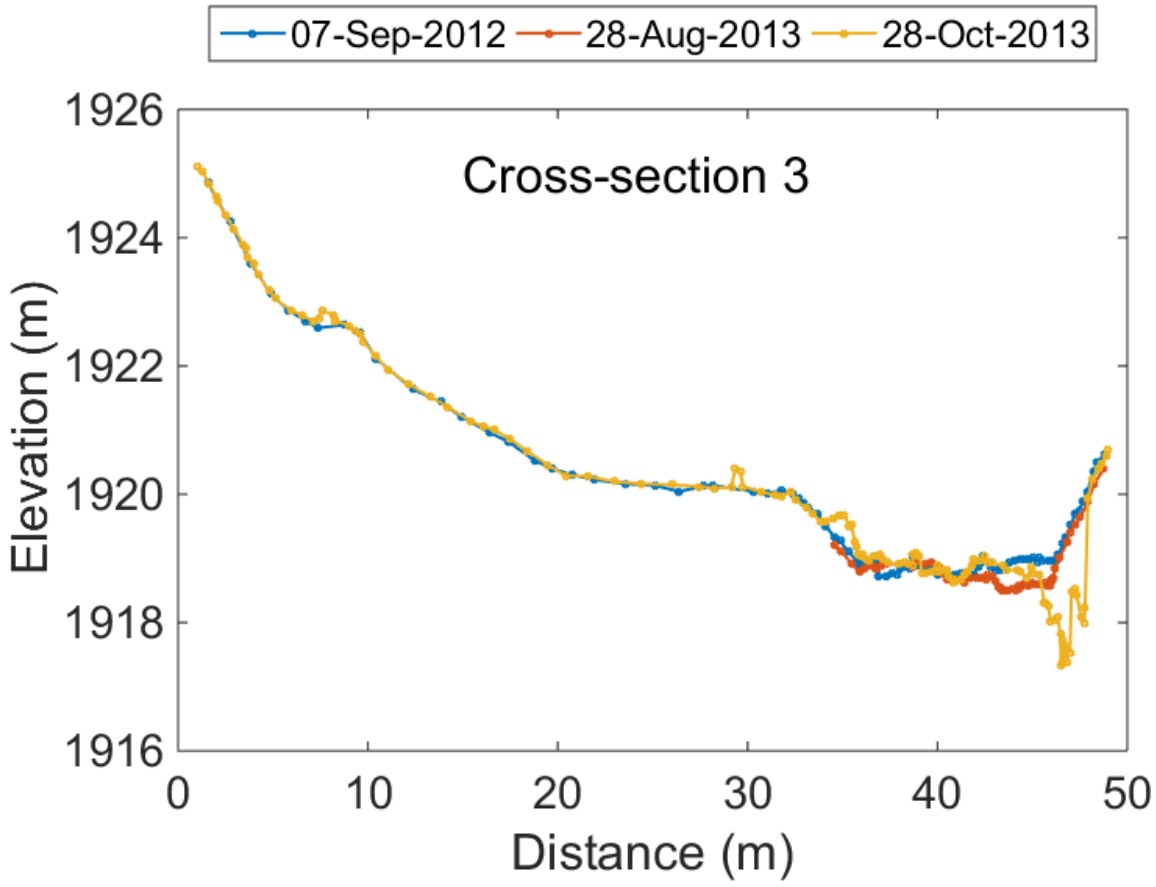

Figure B.3: Plot of cross section 3 in Skin Gulch as surveyed in fall 2012, pre-2013 flood, and post-2013 flood.

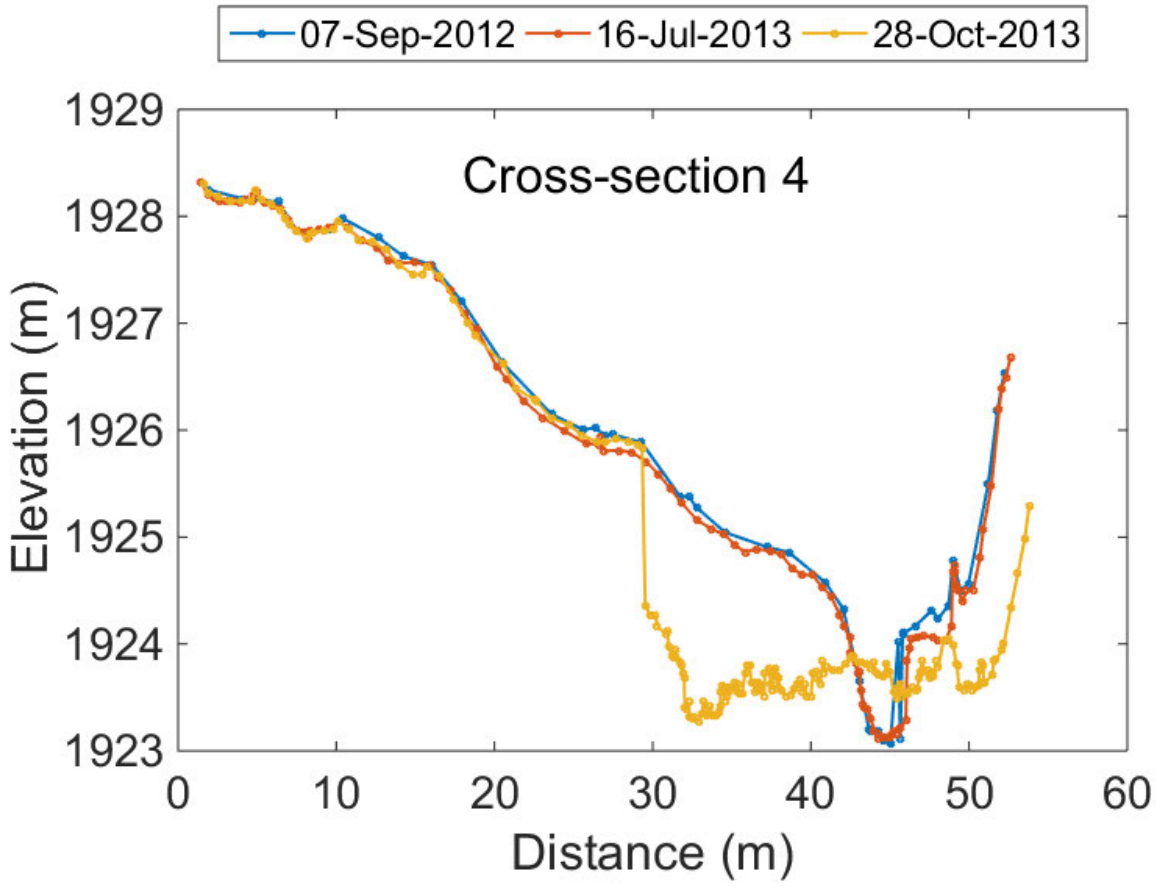

Figure B.4: Plot of cross section 4 in Skin Gulch as surveyed in fall 2012, pre-2013 flood, and post-2013 flood.

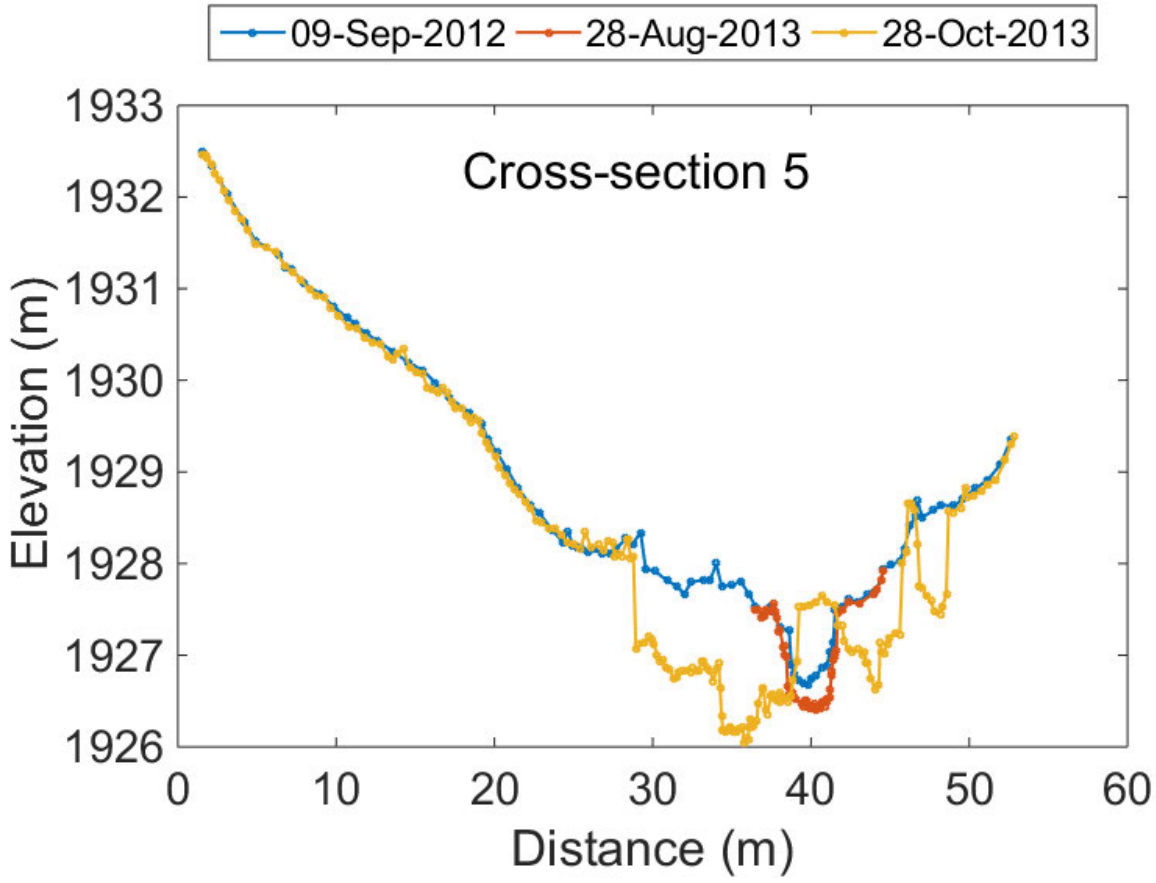

Figure B.5: Plot of cross section 5 in Skin Gulch as surveyed in fall 2012, pre-2013 flood, and post-2013 flood.

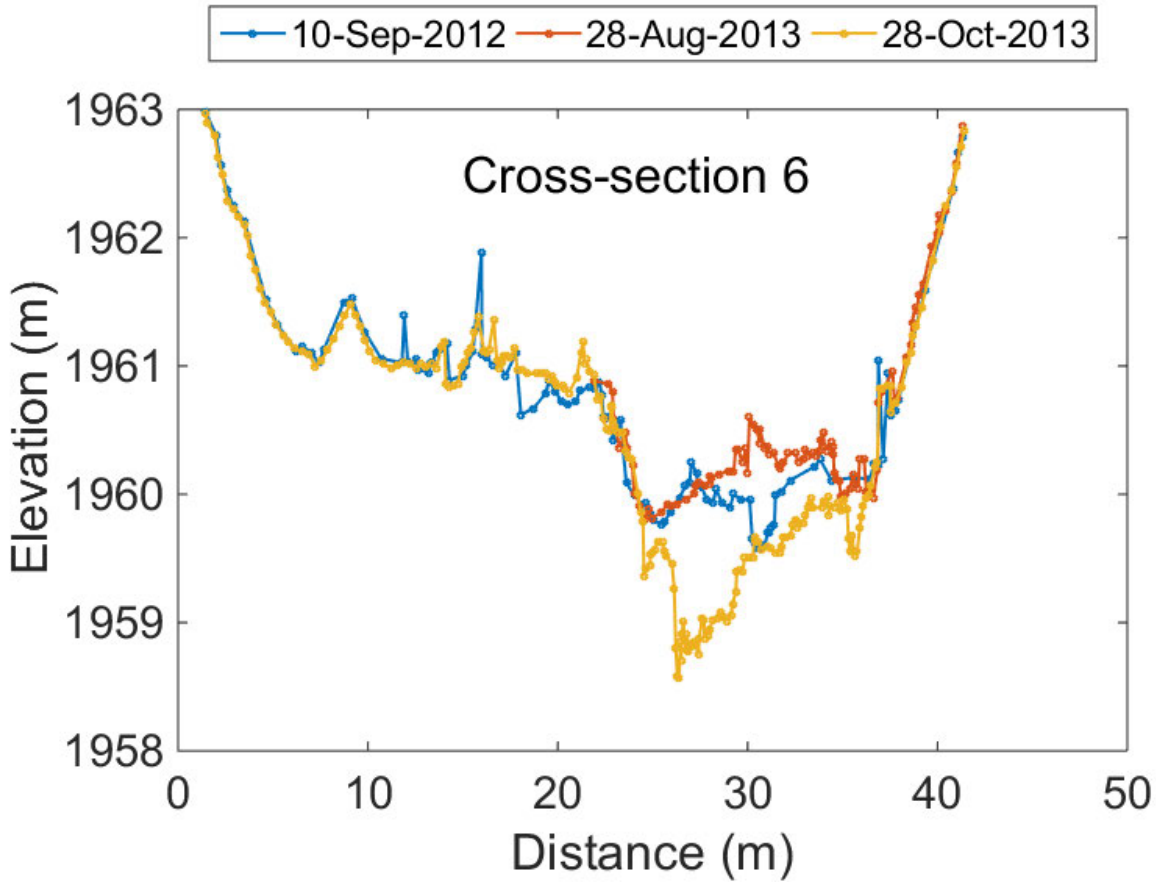

Figure B.6: Plot of cross section 6 in Skin Gulch as surveyed in fall 2012, pre-2013 flood, and post-2013 flood.

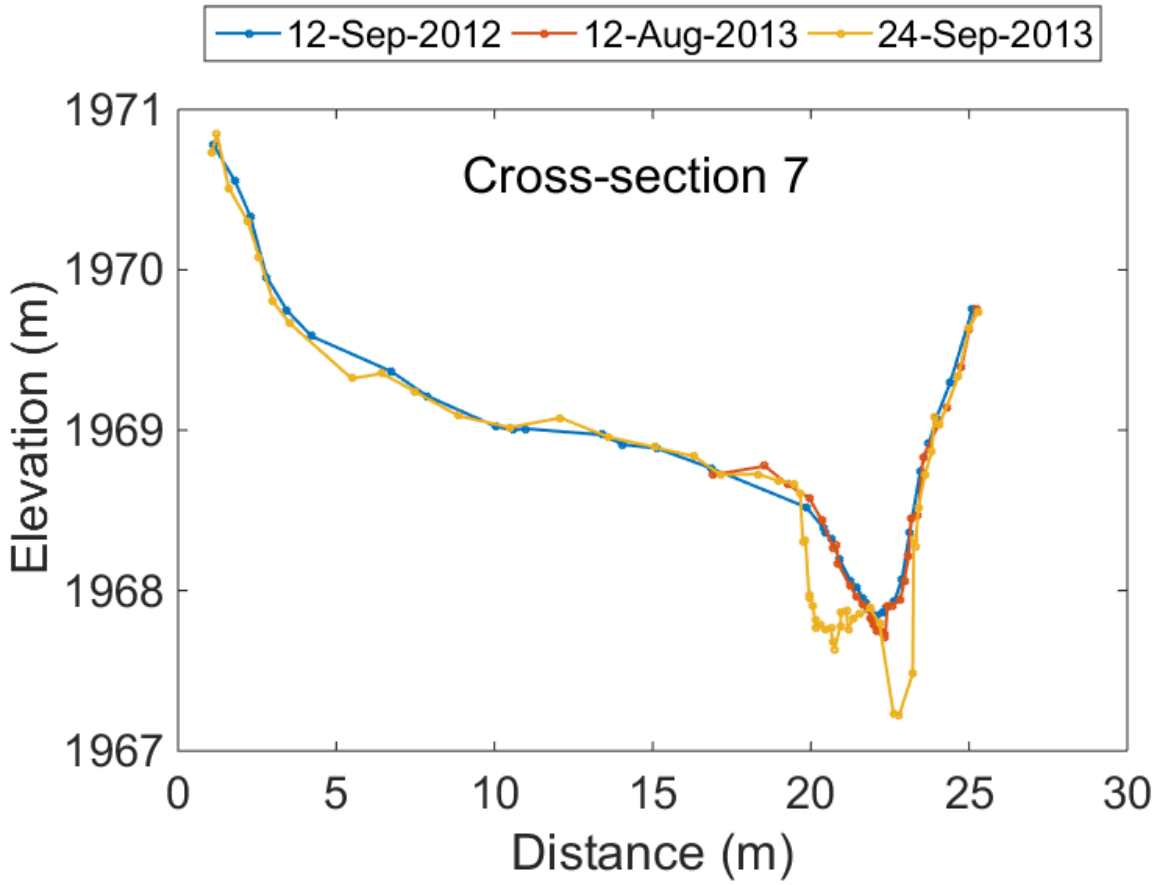

Figure B.7: Plot of cross section 7 in Skin Gulch as surveyed in fall 2012, pre-2013 flood, and post-2013 flood.

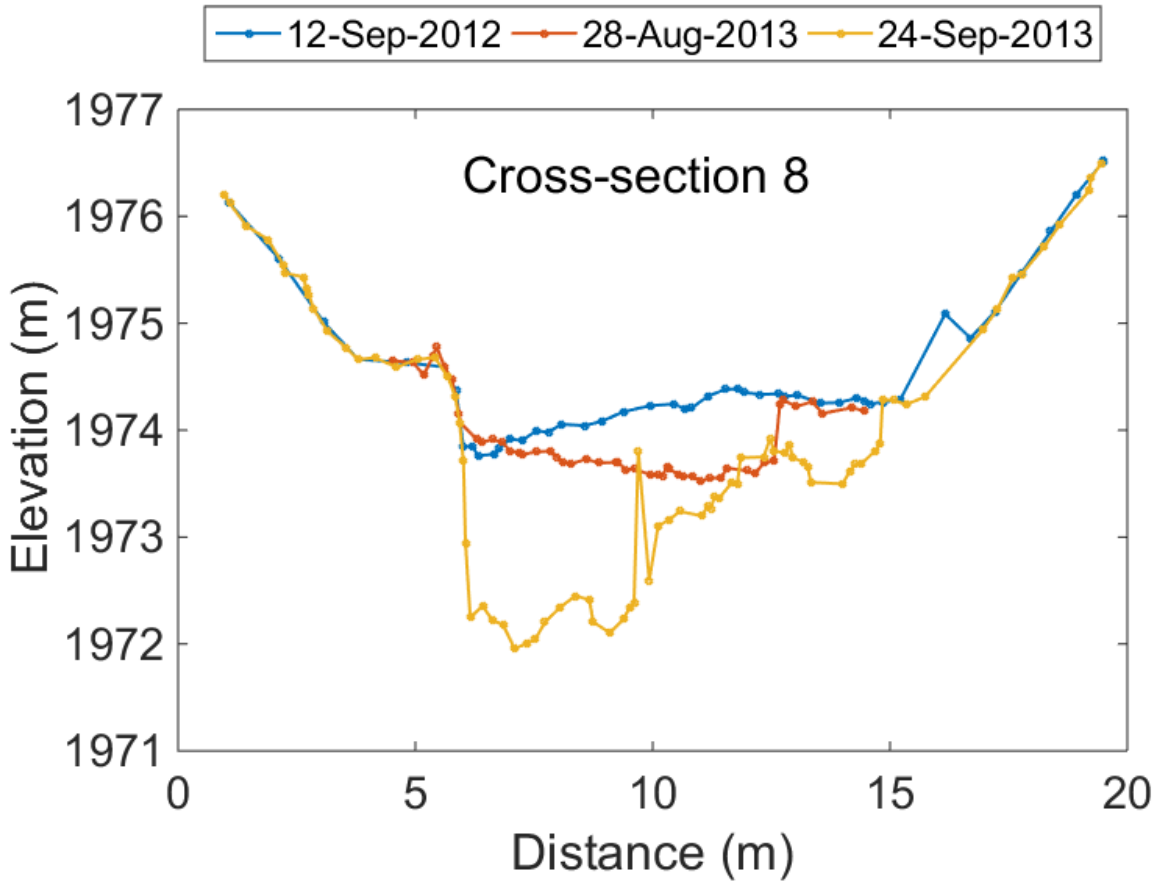

Figure B.8: Plot of cross section 8 in Skin Gulch as surveyed in fall 2012, pre-2013 flood, and post-2013 flood.

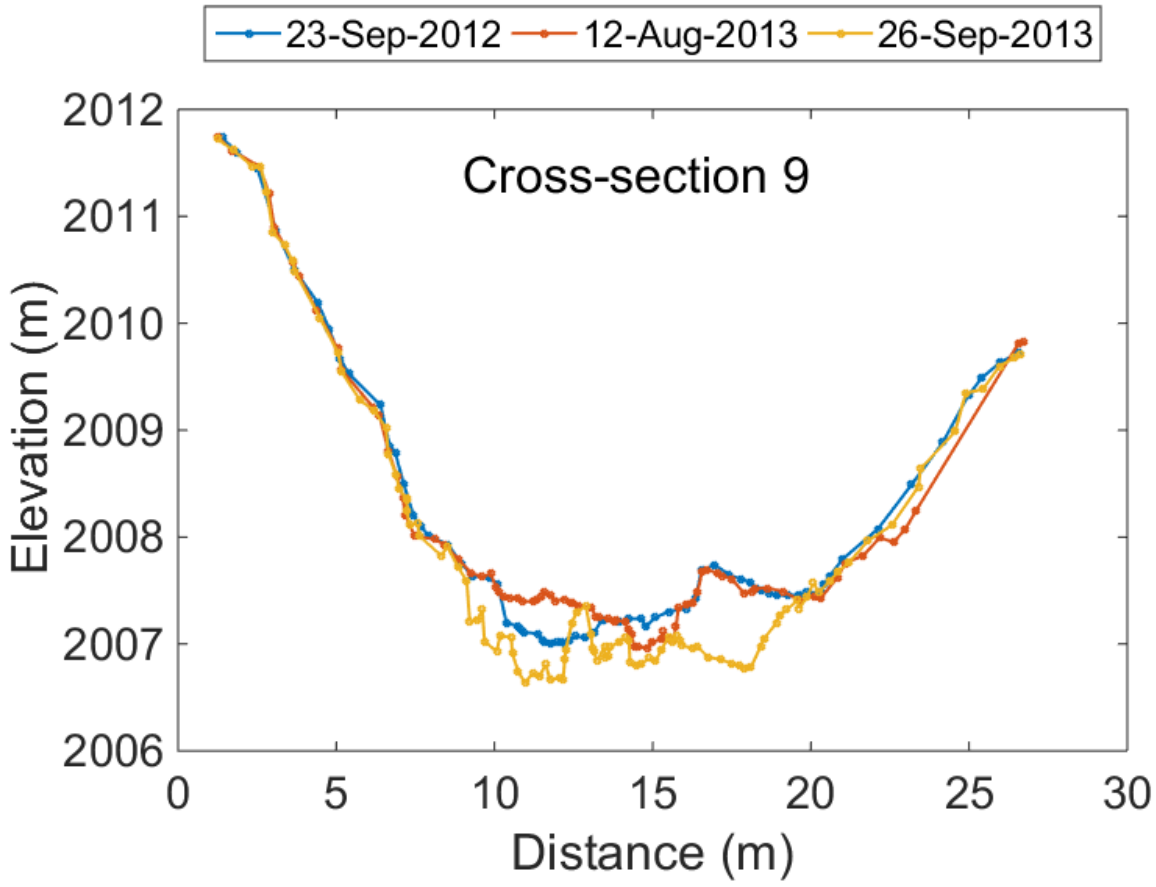

Figure B.9: Plot of cross section 9 in Skin Gulch as surveyed in fall 2012, pre-2013 flood, and post-2013 flood.

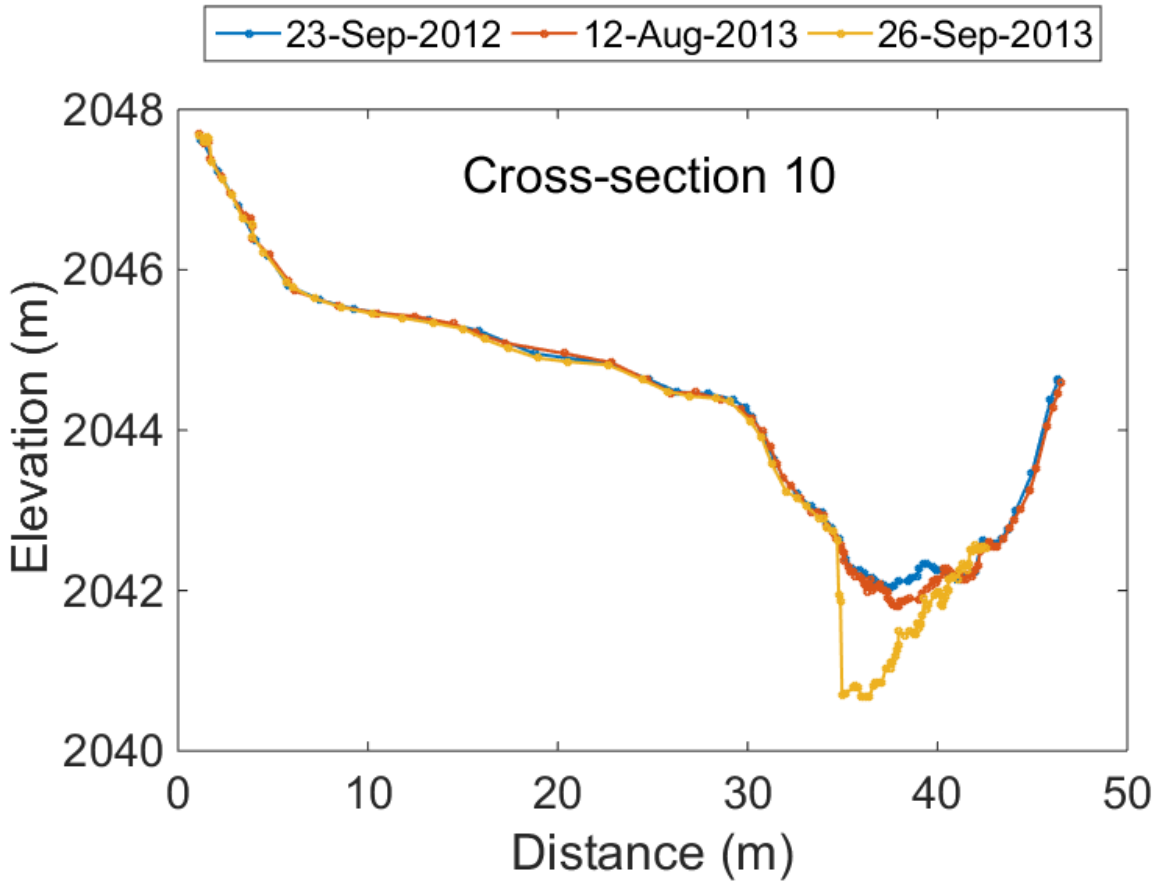

Figure B.10: Plot of cross section 10 in Skin Gulch as surveyed in fall 2012, pre-2013 flood, and post-2013 flood.

Appendix C

Supporting information for Chapter 3

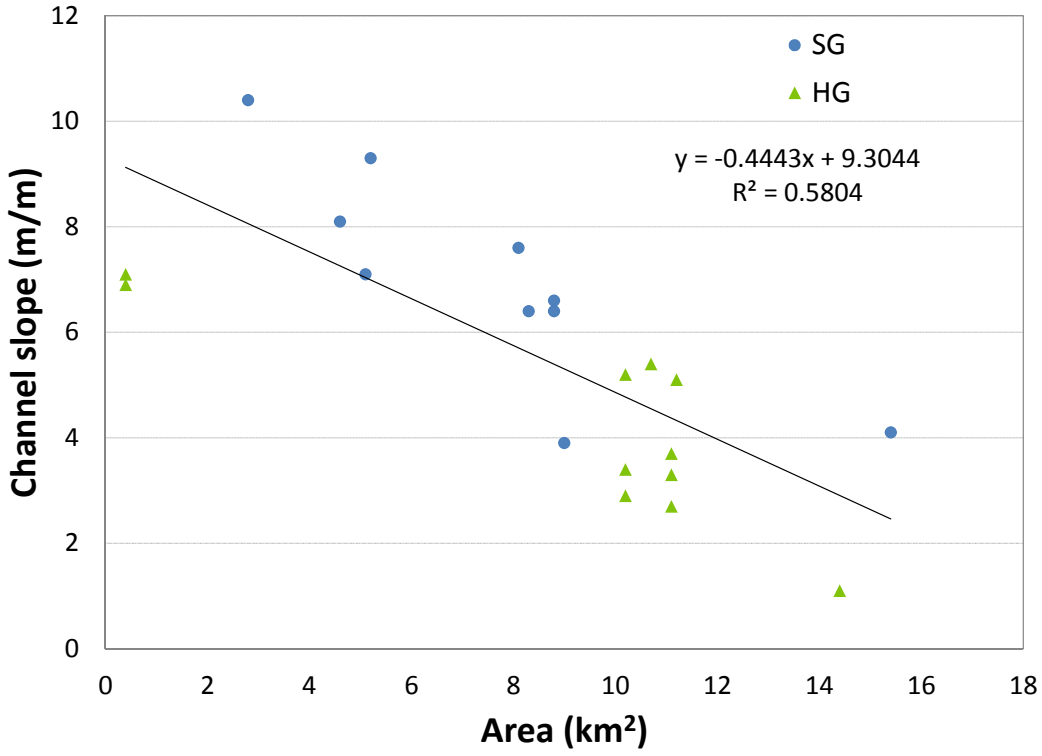

Figure C.1: Channel slope against contributing drainage area for the cross sections in Skin Gulch (blue circles) and Hill Gulch (green triangles).

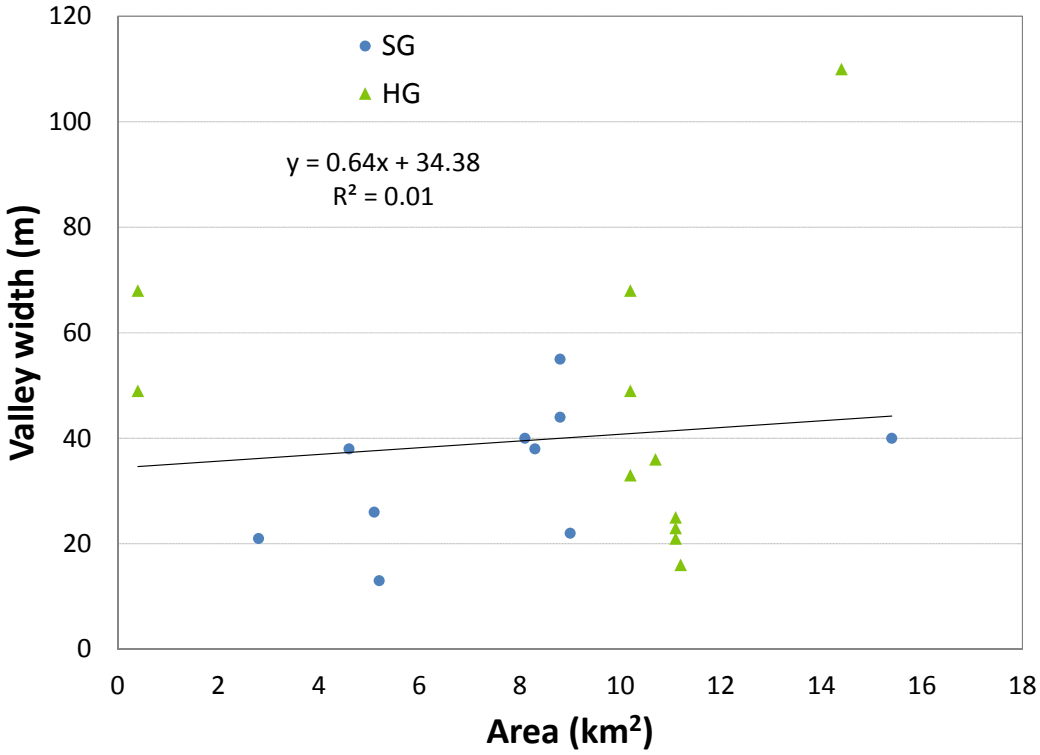

Figure C.2: Valley width against contributing drainage area for the cross sections in Skin Gulch (blue circles) and Hill Gulch (green triangles).

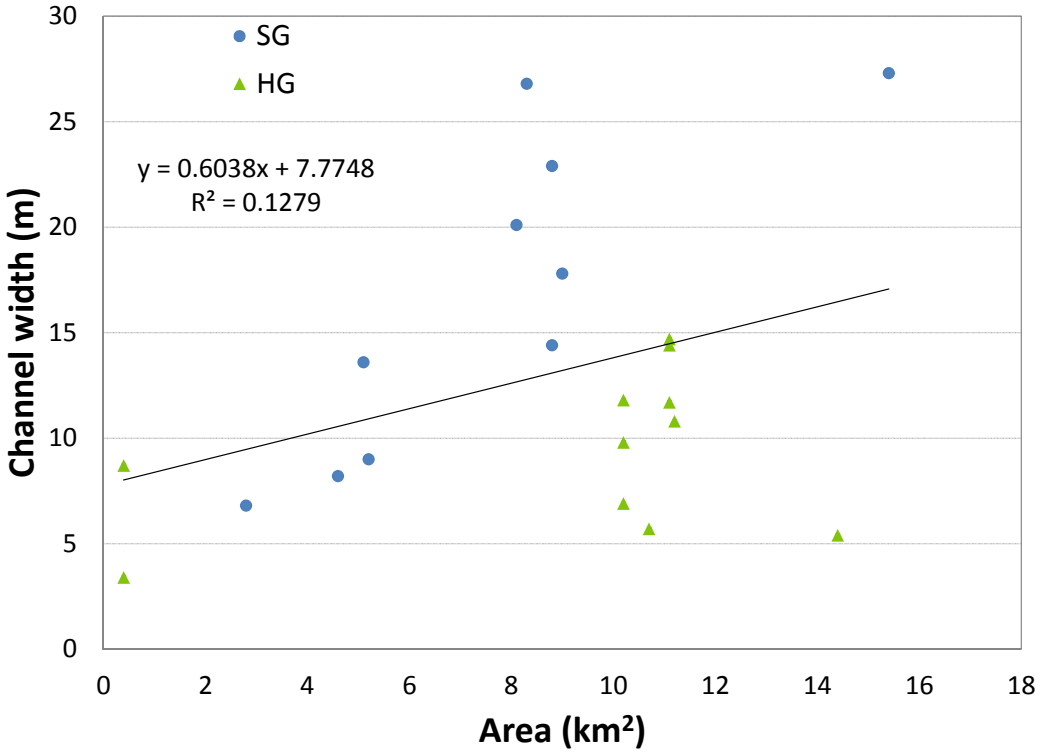

Figure C.3: Channel width against contributing drainage area for the cross sections in Skin Gulch (blue circles) and Hill Gulch (green triangles).

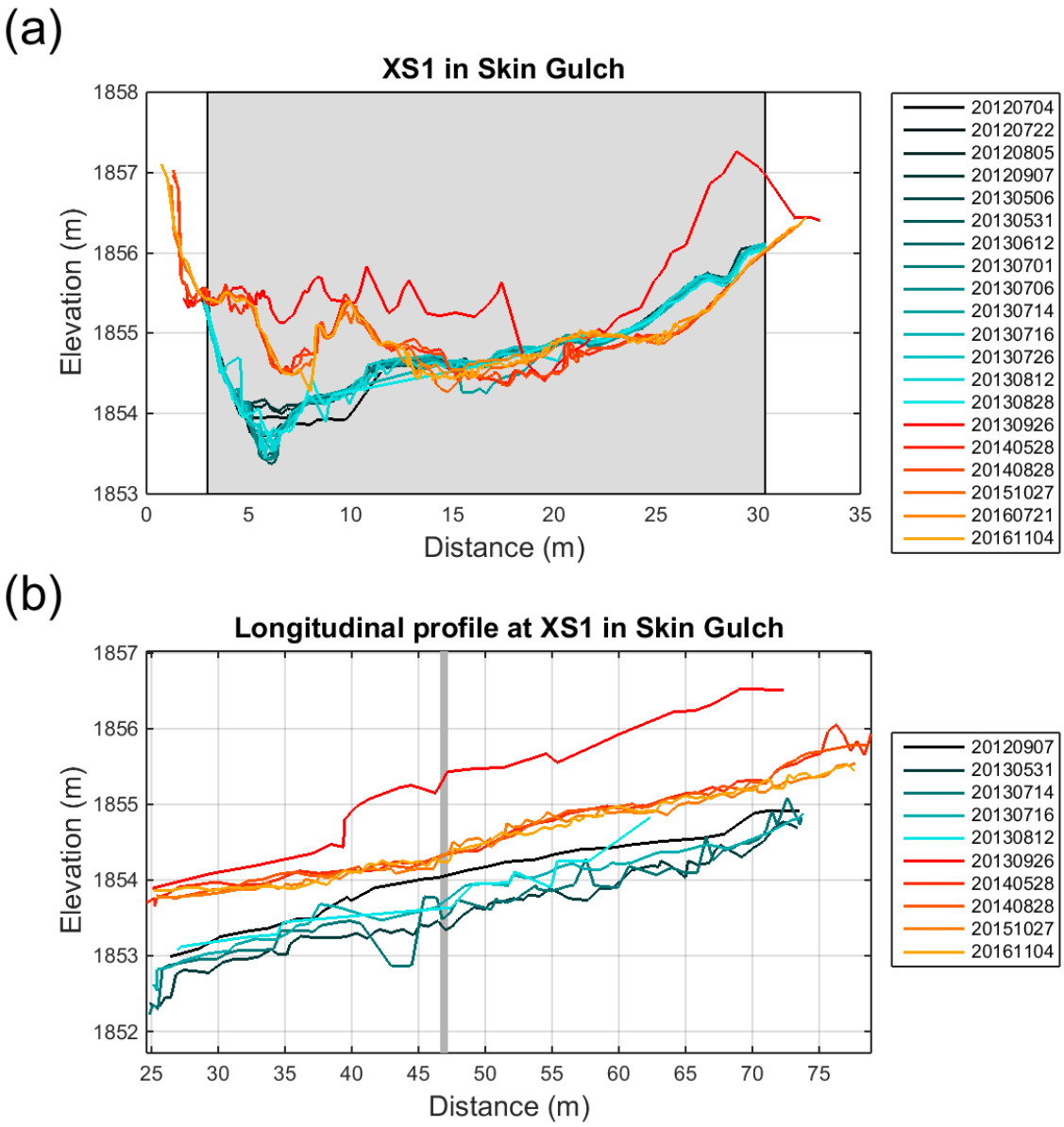

Figure C.4: Plots over the entire monitoring period of (a) cross section one in Skin Gulch and (b) the corresponding longitudinal profile. Gray shaded box in (a) delineates the active channel and the vertical line in (b) shows the location of the cross section.

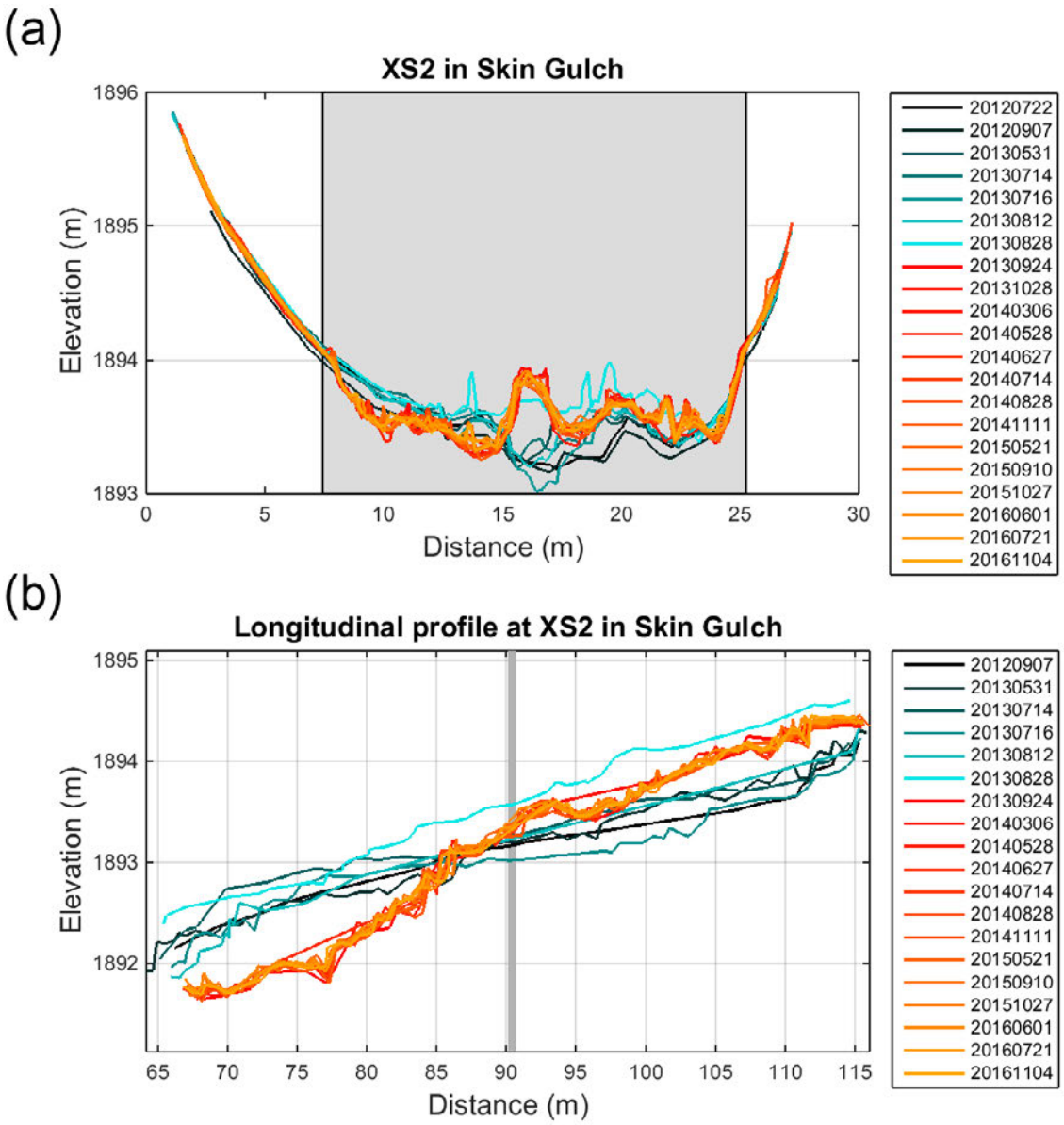

Figure C.5: Plots over the entire monitoring period of (a) cross section two in Skin Gulch and (b) the corresponding longitudinal profile. Gray shaded box in (a) delineates the active channel and the vertical line in (b) shows the location of the cross section.

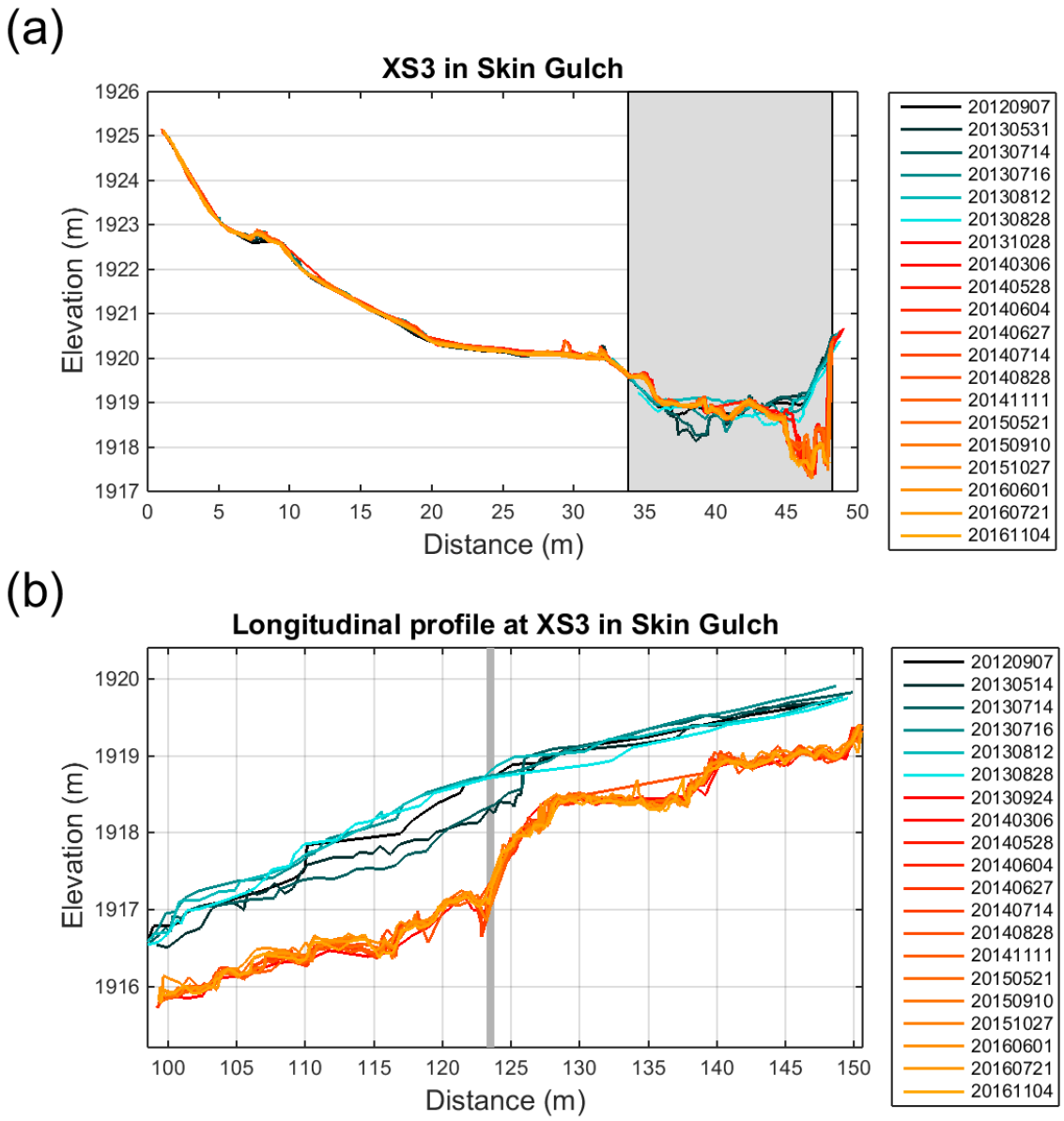

Figure C.6: Plots over the entire monitoring period of (a) cross section three in Skin Gulch and (b) the corresponding longitudinal profile. Gray shaded box in (a) delineates the active channel and the vertical line in (b) shows the location of the cross section.

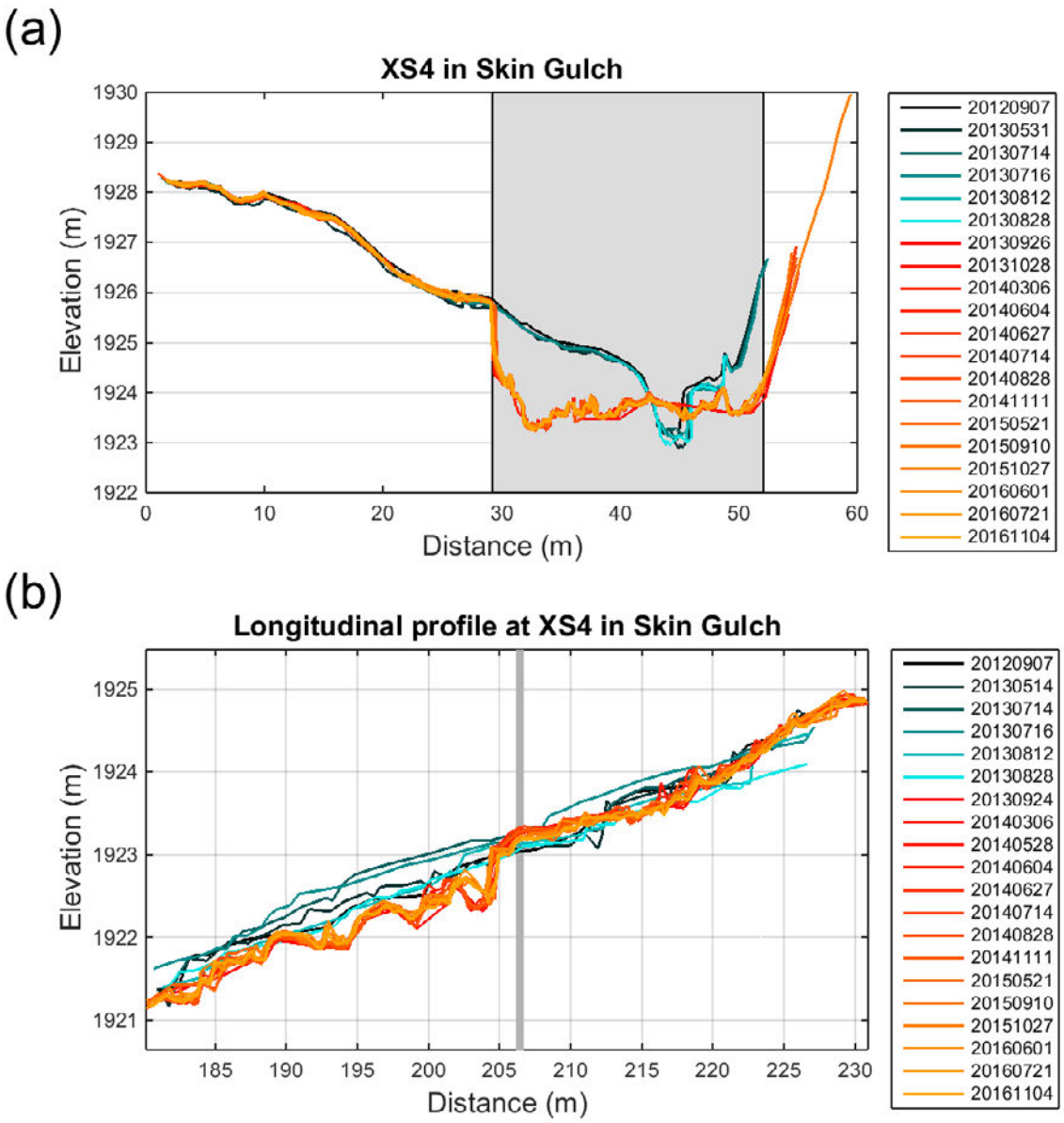

Figure C.7: Plots over the entire monitoring period of (a) cross section four in Skin Gulch and (b) the corresponding longitudinal profile. Gray shaded box in (a) delineates the active channel and the vertical line in (b) shows the location of the cross section.

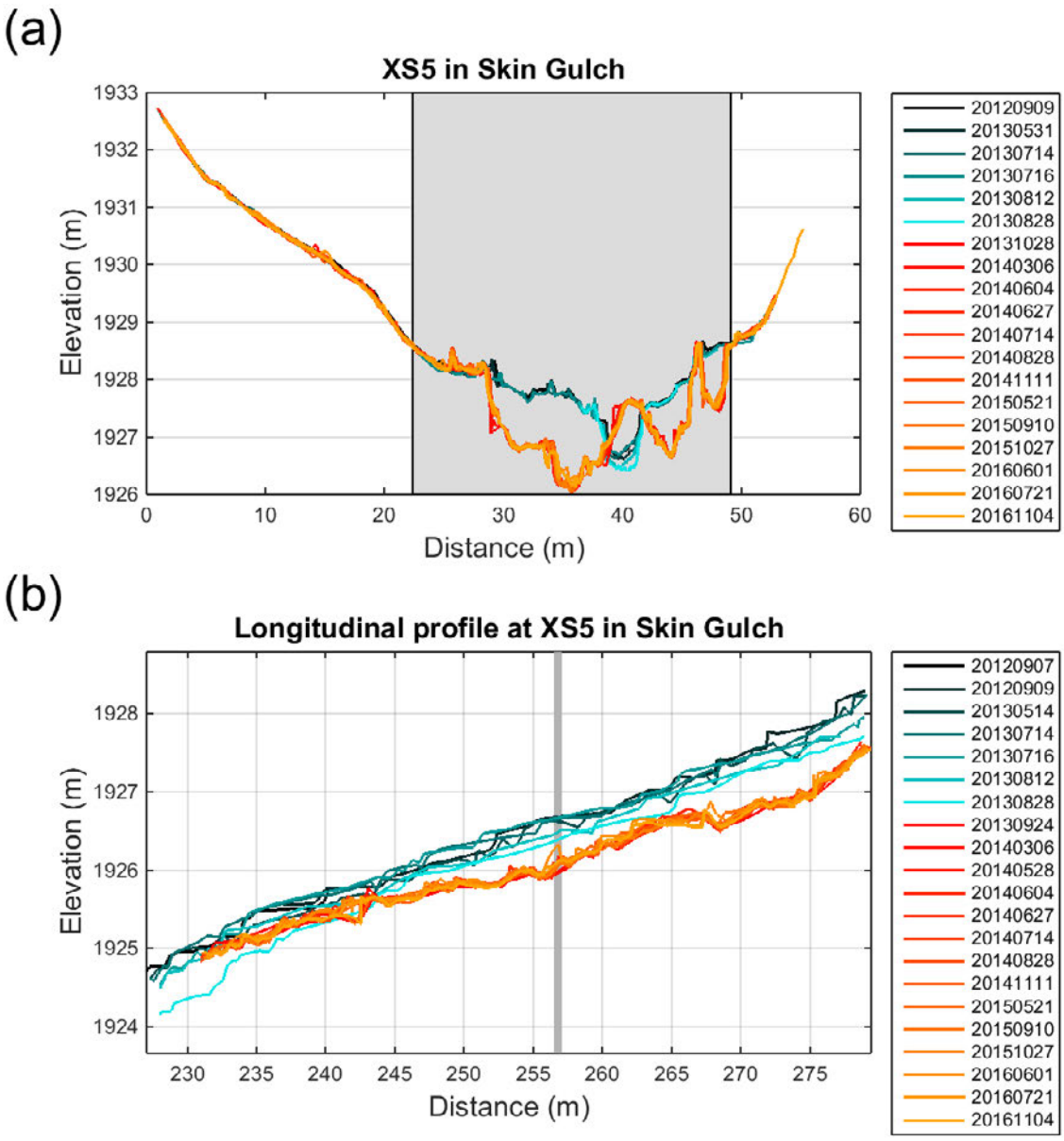

Figure C.8: Plots over the entire monitoring period of (a) cross section five in Skin Gulch and (b) the corresponding longitudinal profile. Gray shaded box in (a) delineates the active channel and the vertical line in (b) shows the location of the cross section.

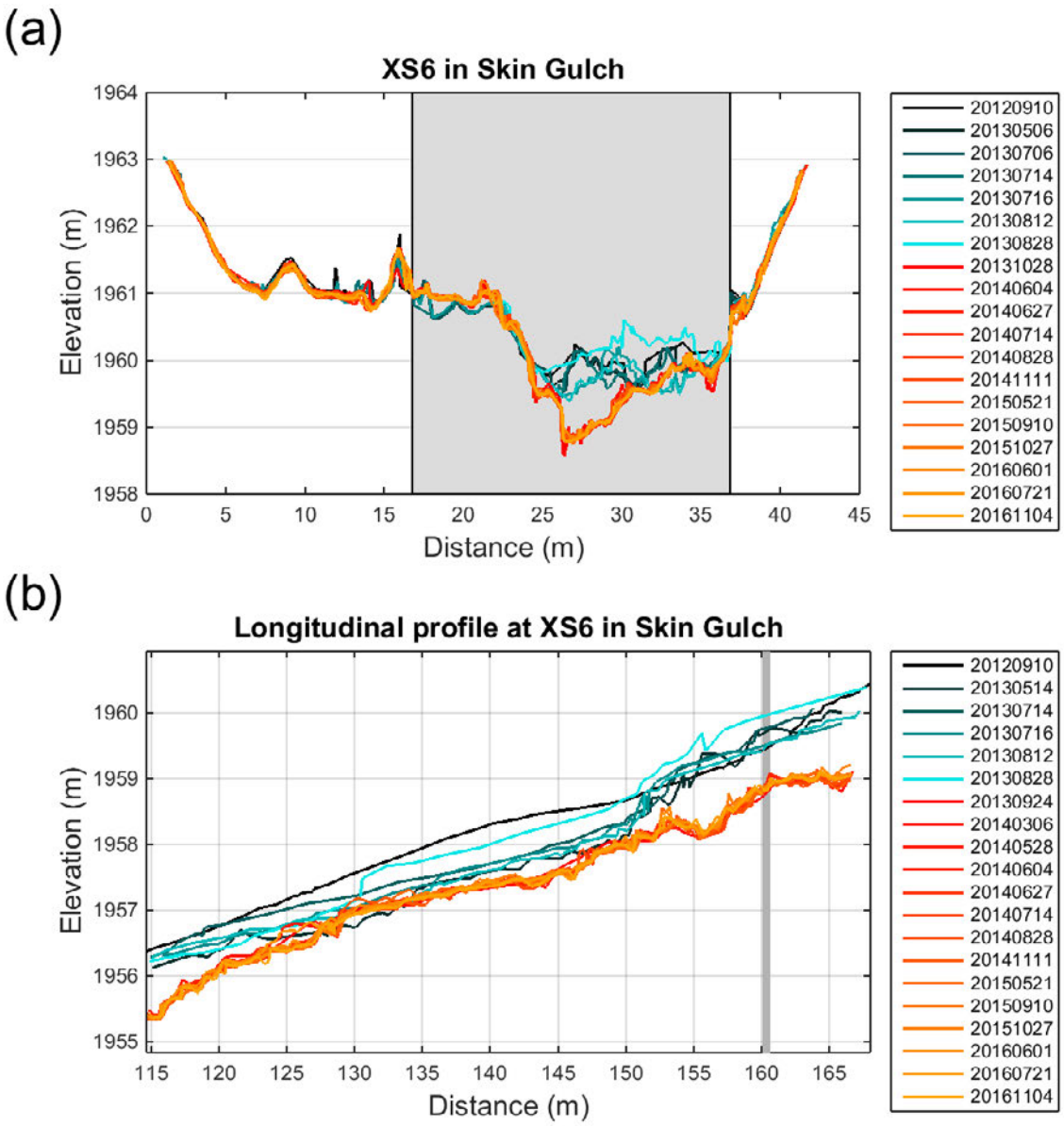

Figure C.9: Plots over the entire monitoring period of (a) cross section six in Skin Gulch and (b) the corresponding longitudinal profile. Gray shaded box in (a) delineates the active channel and the vertical line in (b) shows the location of the cross section.

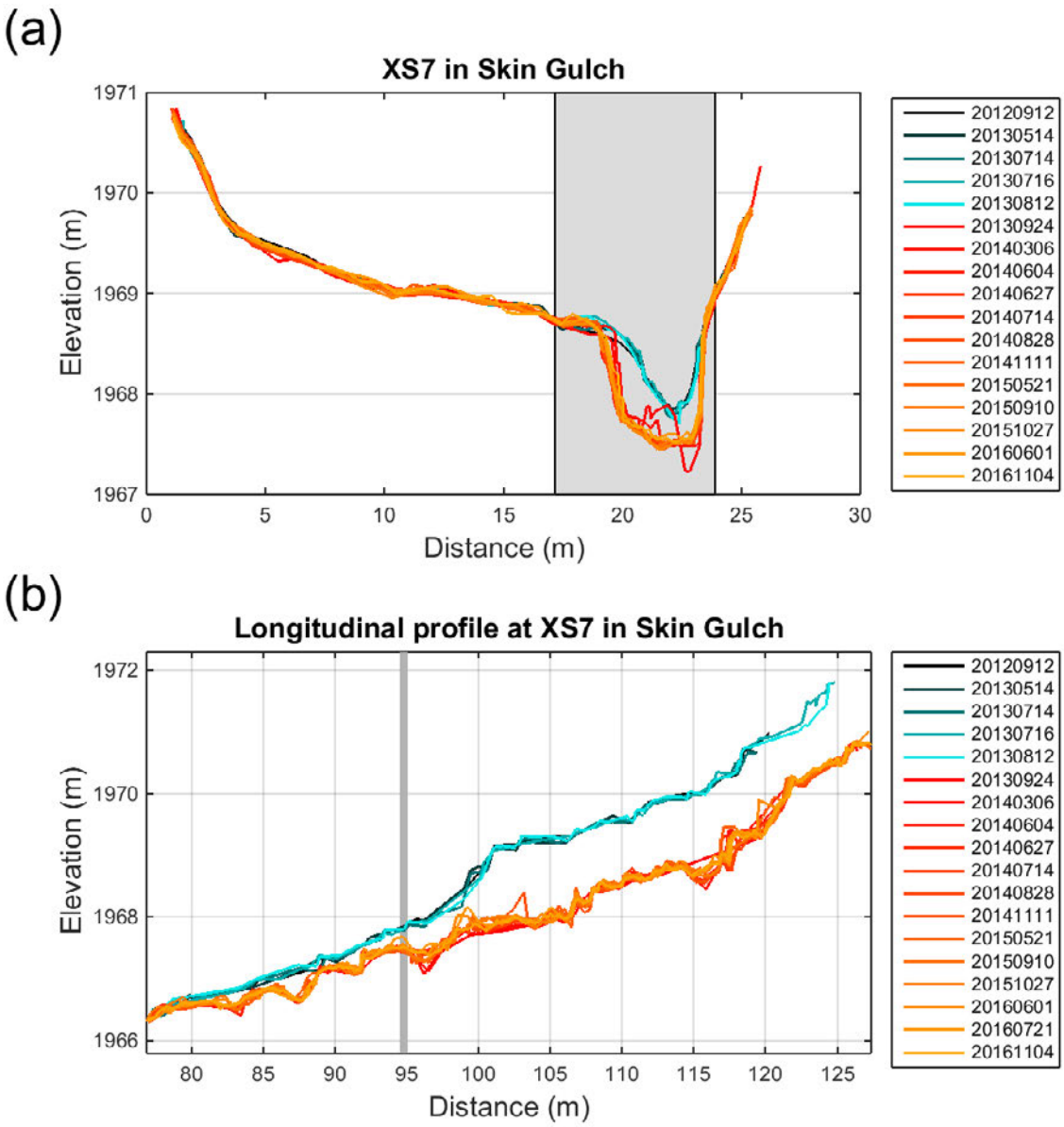

Figure C.10: Plots over the entire monitoring period of (a) cross section seven in Skin Gulch and (b) the corresponding longitudinal profile. Gray shaded box in (a) delineates the active channel and the vertical line in (b) shows the location of the cross section.

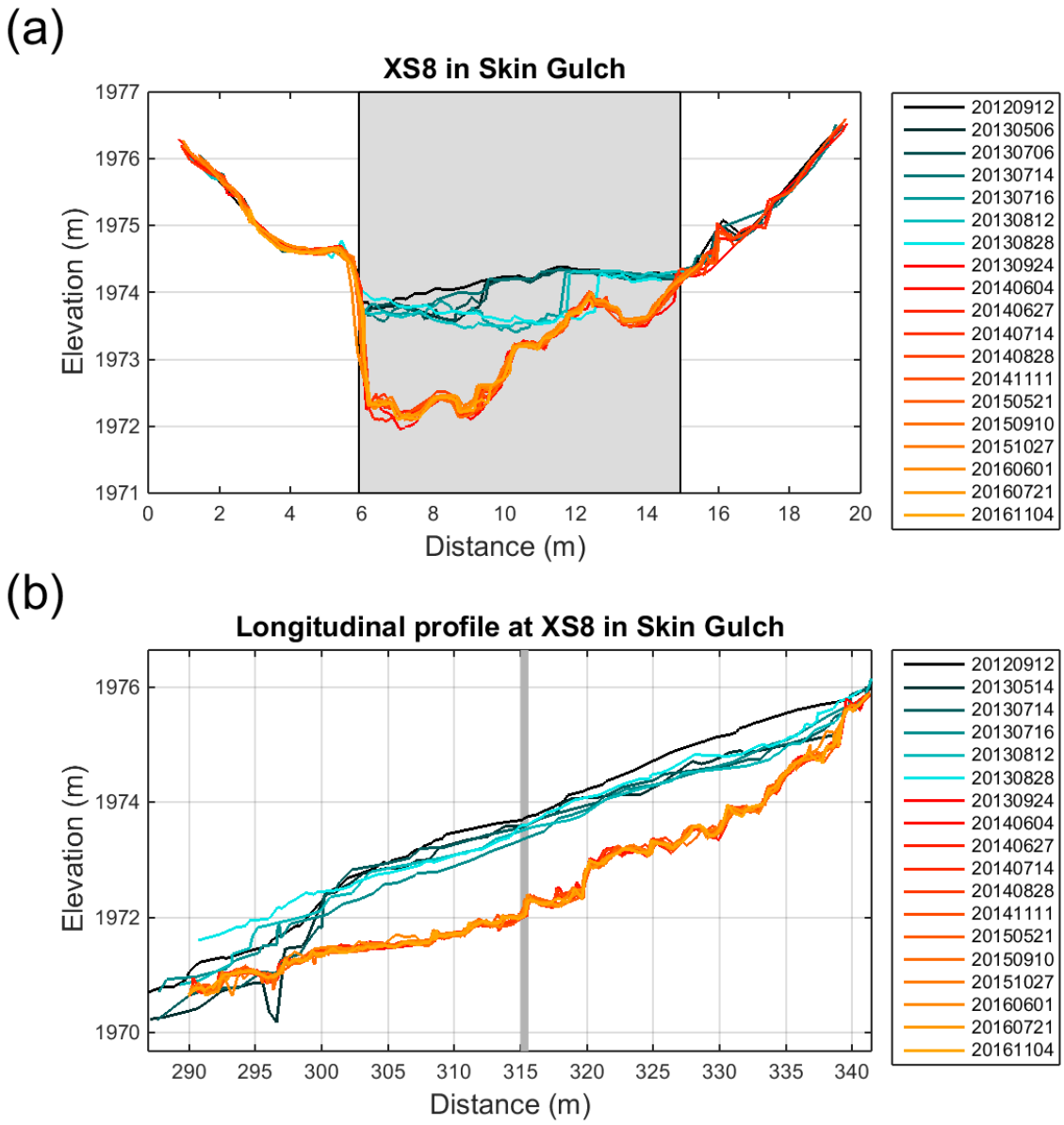

Figure C.11: Plots over the entire monitoring period of (a) cross section eight in Skin Gulch and (b) the corresponding longitudinal profile. Gray shaded box in (a) delineates the active channel and the vertical line in (b) shows the location of the cross section.

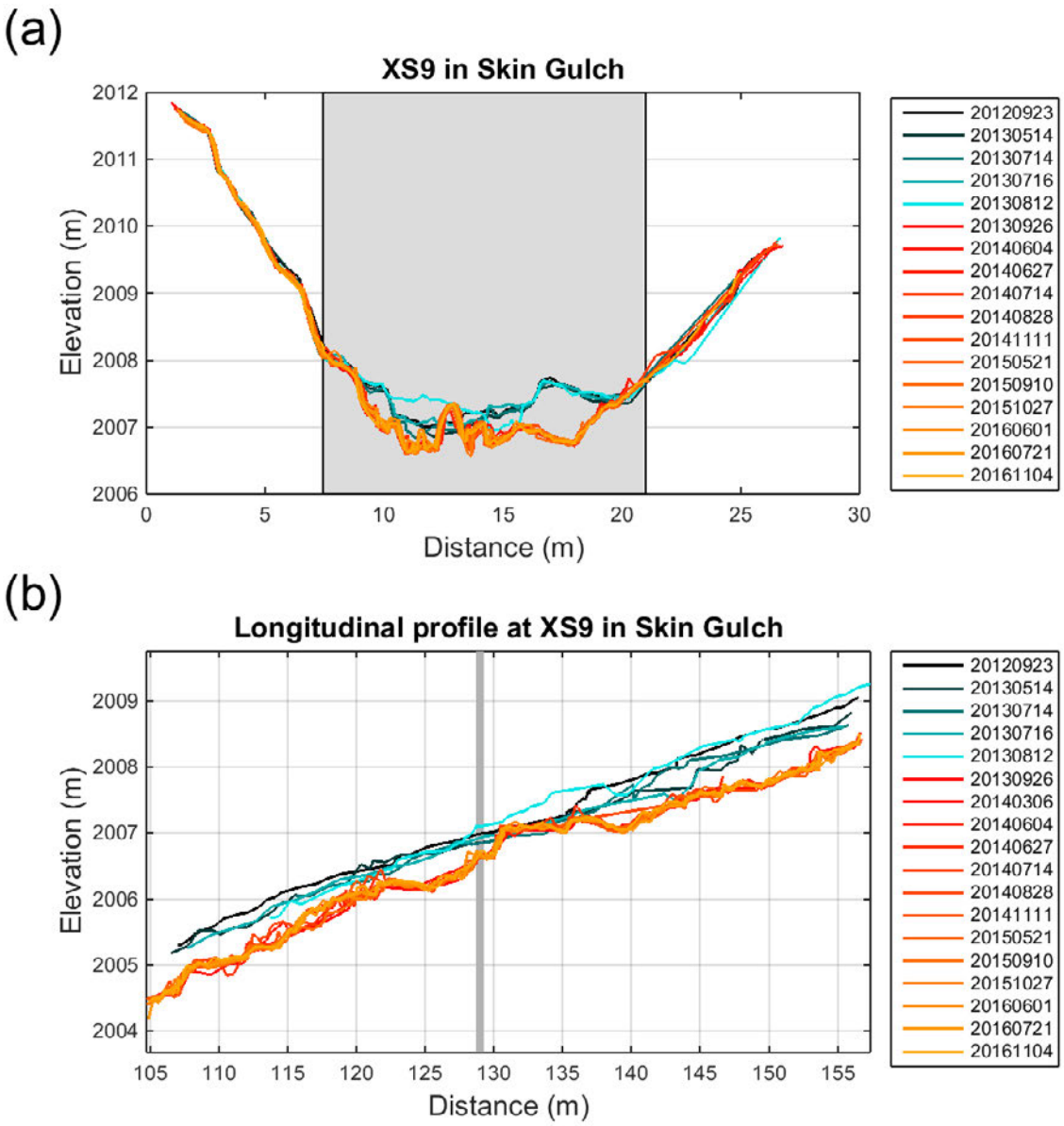

Figure C.12: Plots over the entire monitoring period of (a) cross section nine in Skin Gulch and (b) the corresponding longitudinal profile. Gray shaded box in (a) delineates the active channel and the vertical line in (b) shows the location of the cross section.

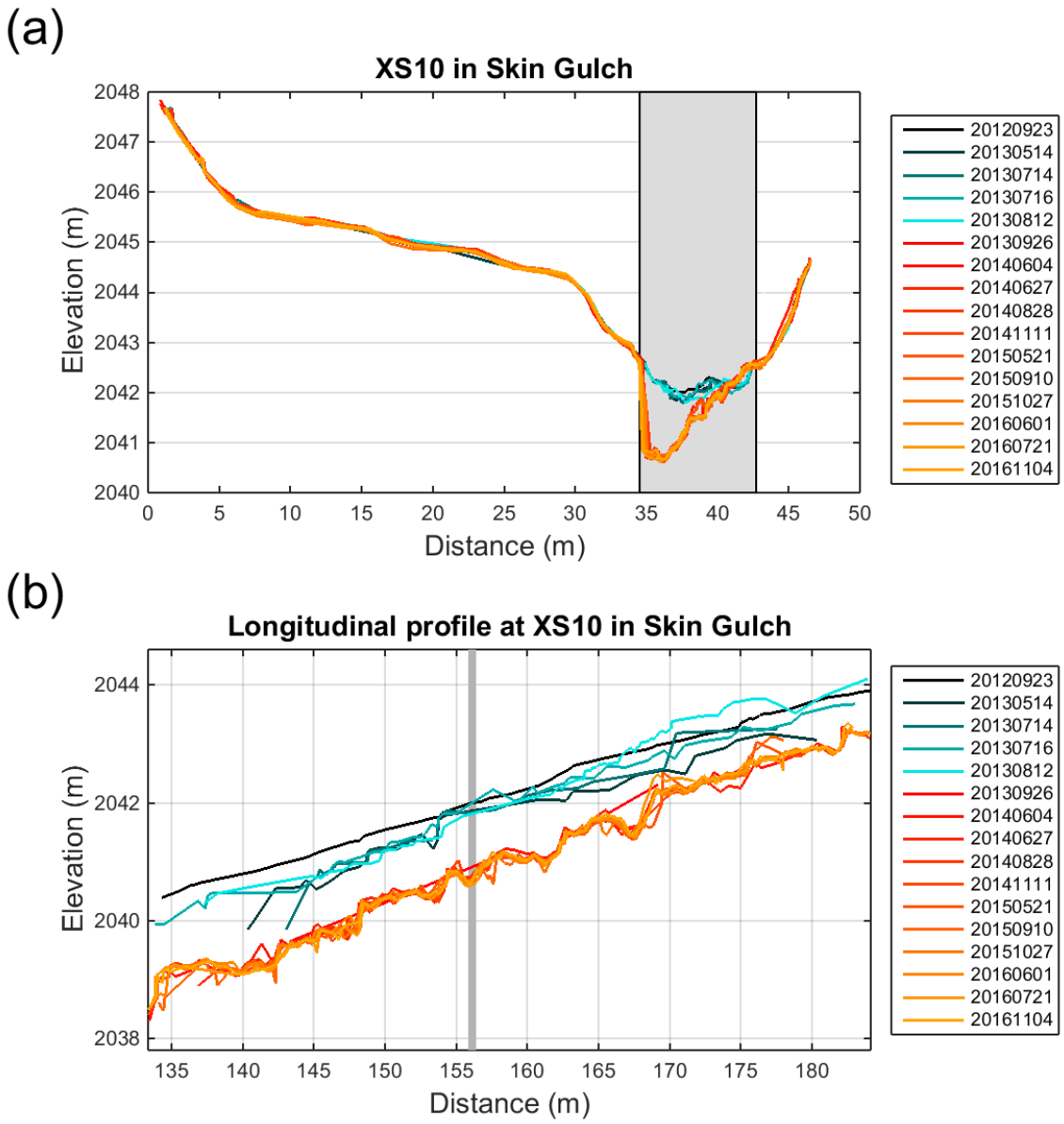

Figure C.13: Plots over the entire monitoring period of (a) cross section ten in Skin Gulch and (b) the corresponding longitudinal profile. Gray shaded box in (a) delineates the active channel and the vertical line in (b) shows the location of the cross section.

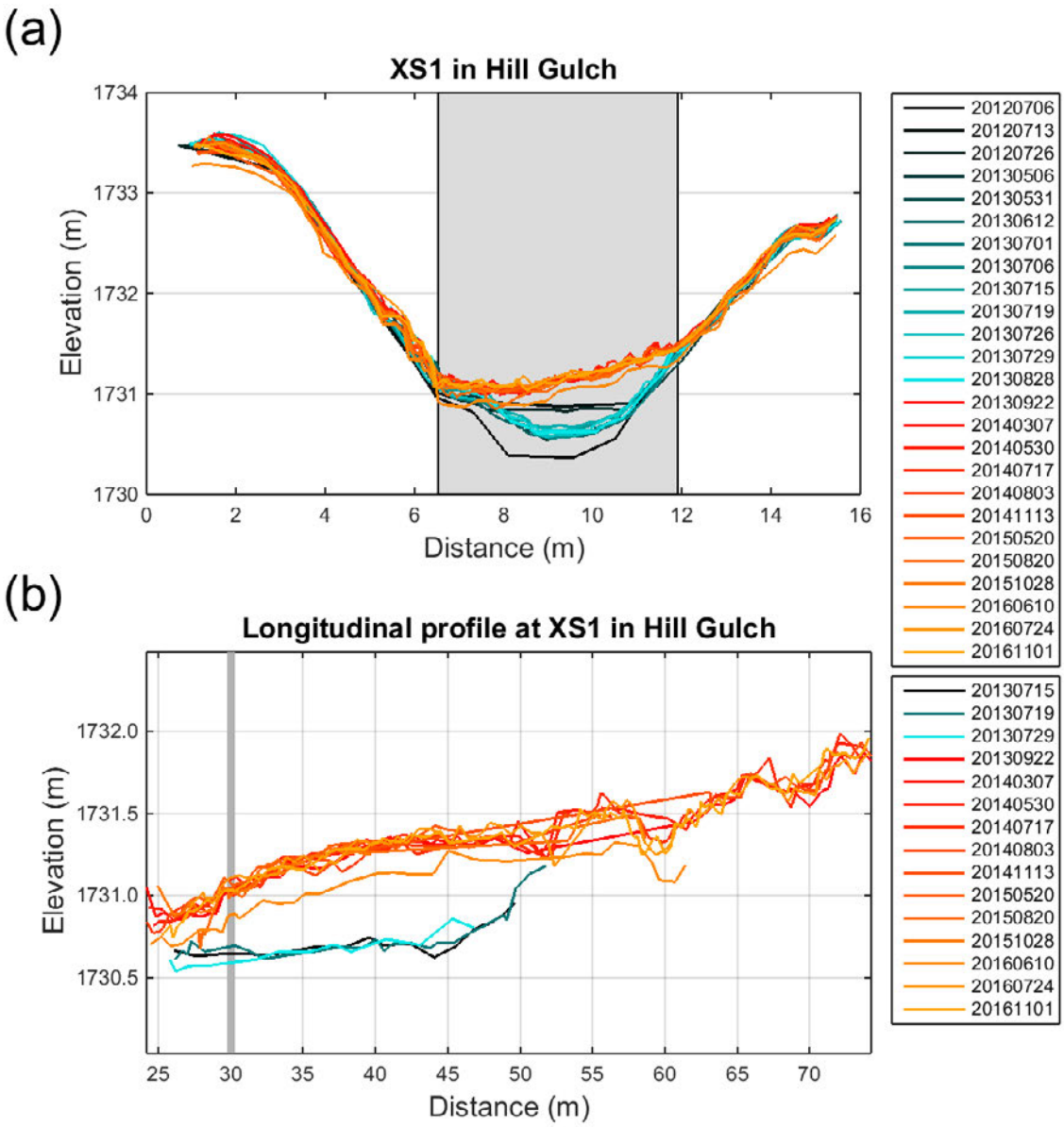

Figure C.14: Plots over the entire monitoring period of (a) cross section one in Hill Gulch and (b) the corresponding longitudinal profile. Gray shaded box in (a) delineates the active channel and the vertical line in (b) shows the location of the cross section.

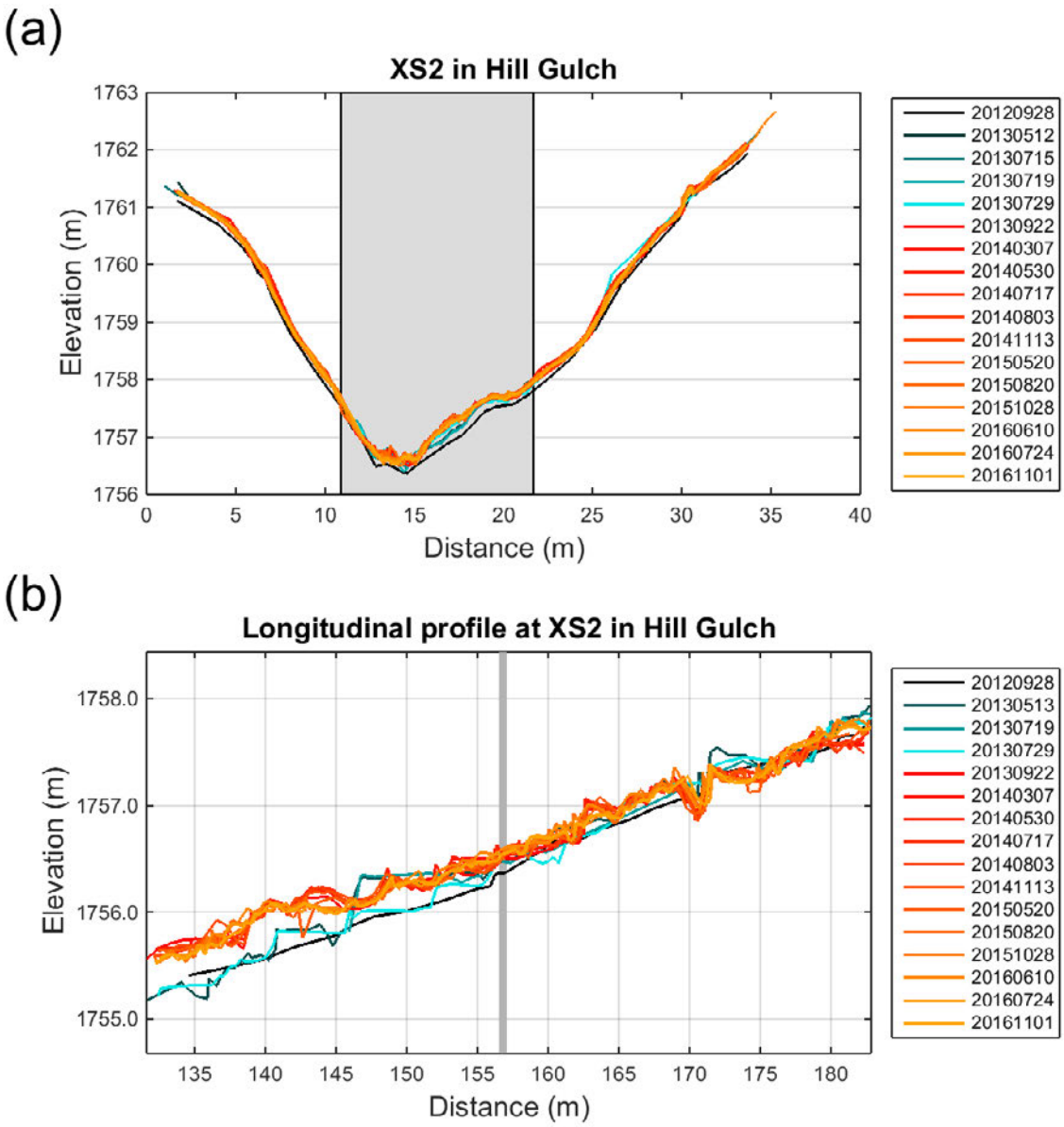

Figure C.15: Plots over the entire monitoring period of (a) cross section two in Hill Gulch and (b) the corresponding longitudinal profile. Gray shaded box in (a) delineates the active channel and the vertical line in (b) shows the location of the cross section.

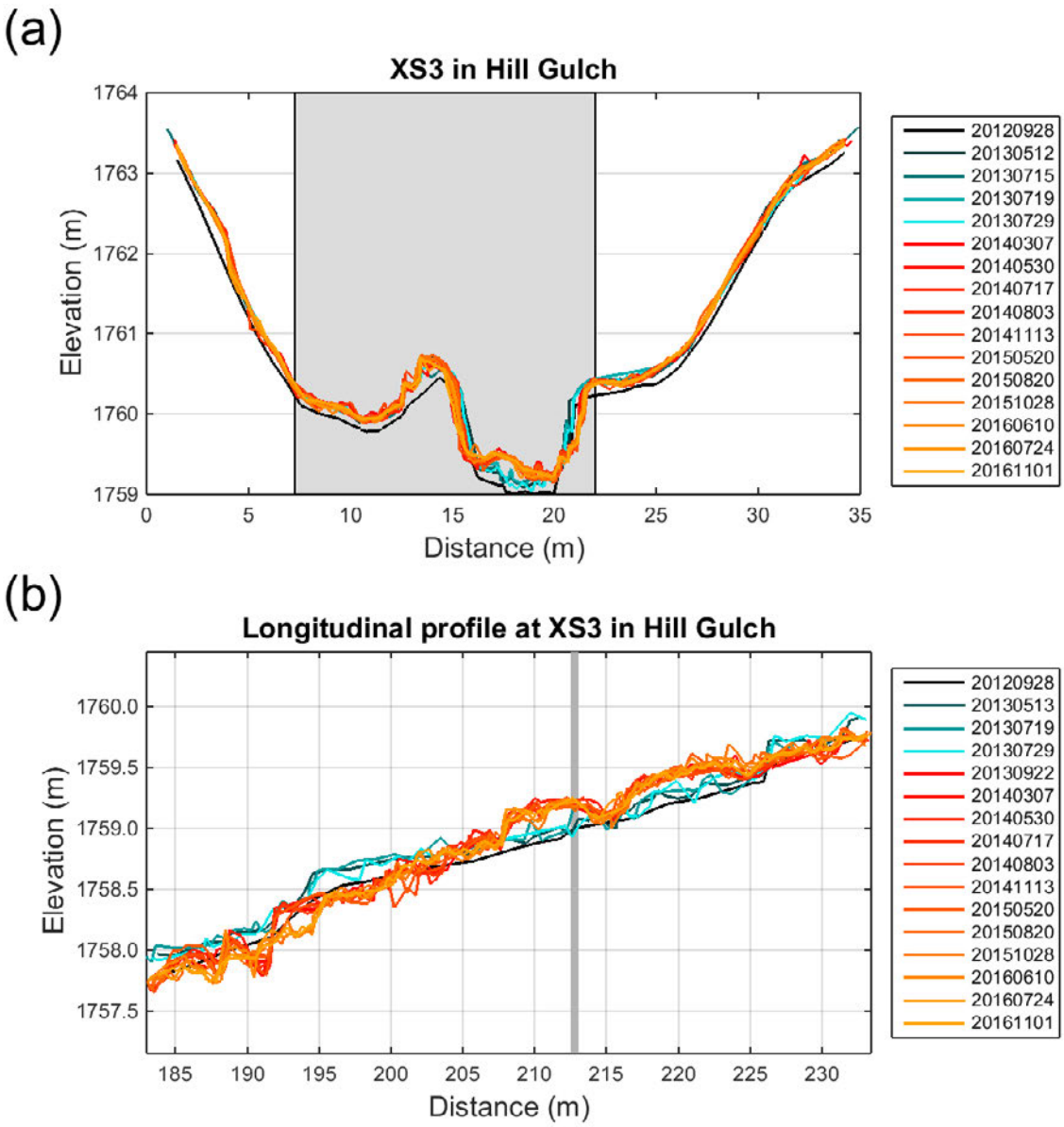

Figure C.16: Plots over the entire monitoring period of (a) cross section three in Hill Gulch and (b) the corresponding longitudinal profile. Gray shaded box in (a) delineates the active channel and the vertical line in (b) shows the location of the cross section.

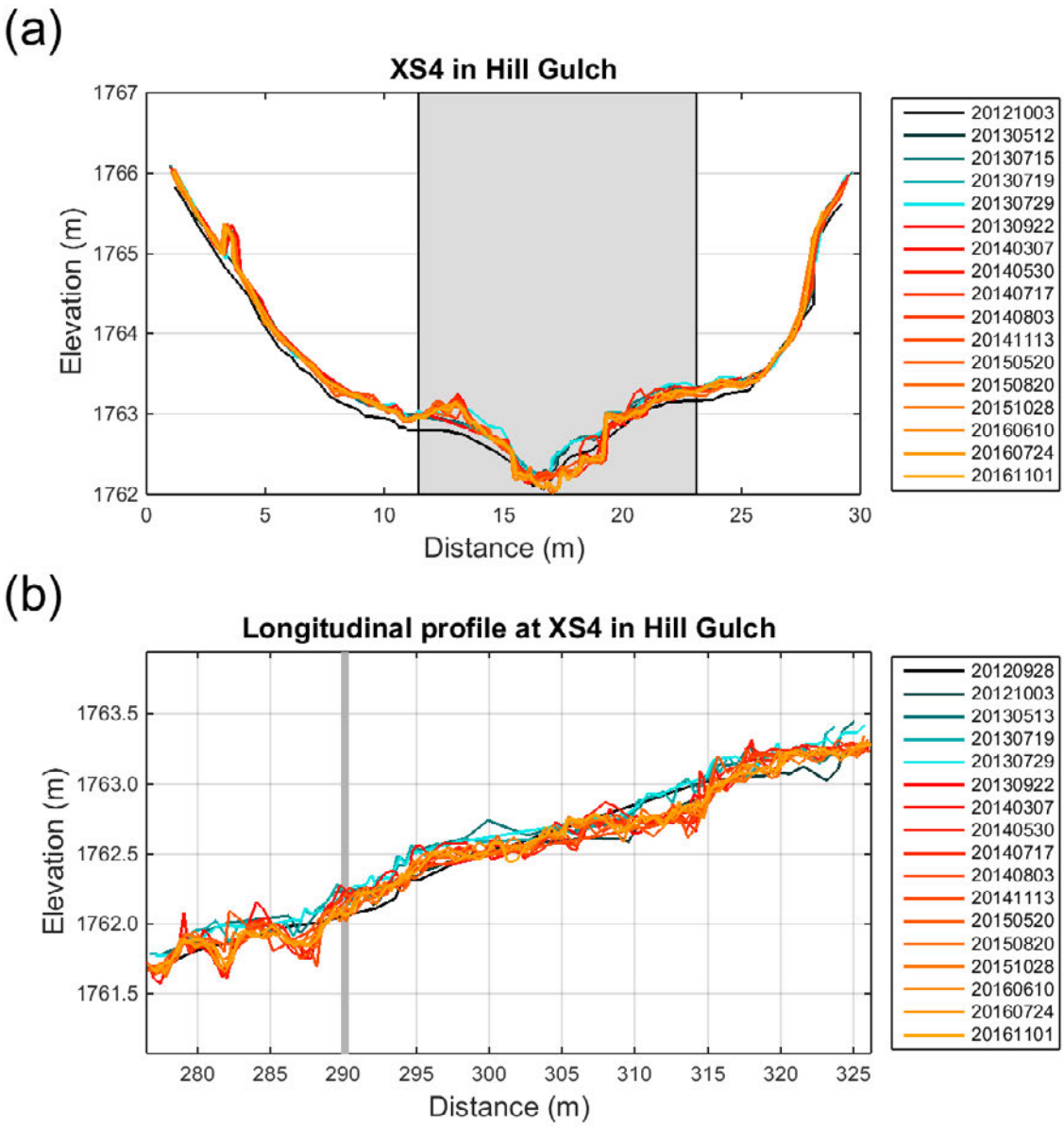

Figure C.17: Plots over the entire monitoring period of (a) cross section four in Hill Gulch and (b) the corresponding longitudinal profile. Gray shaded box in (a) delineates the active channel and the vertical line in (b) shows the location of the cross section.

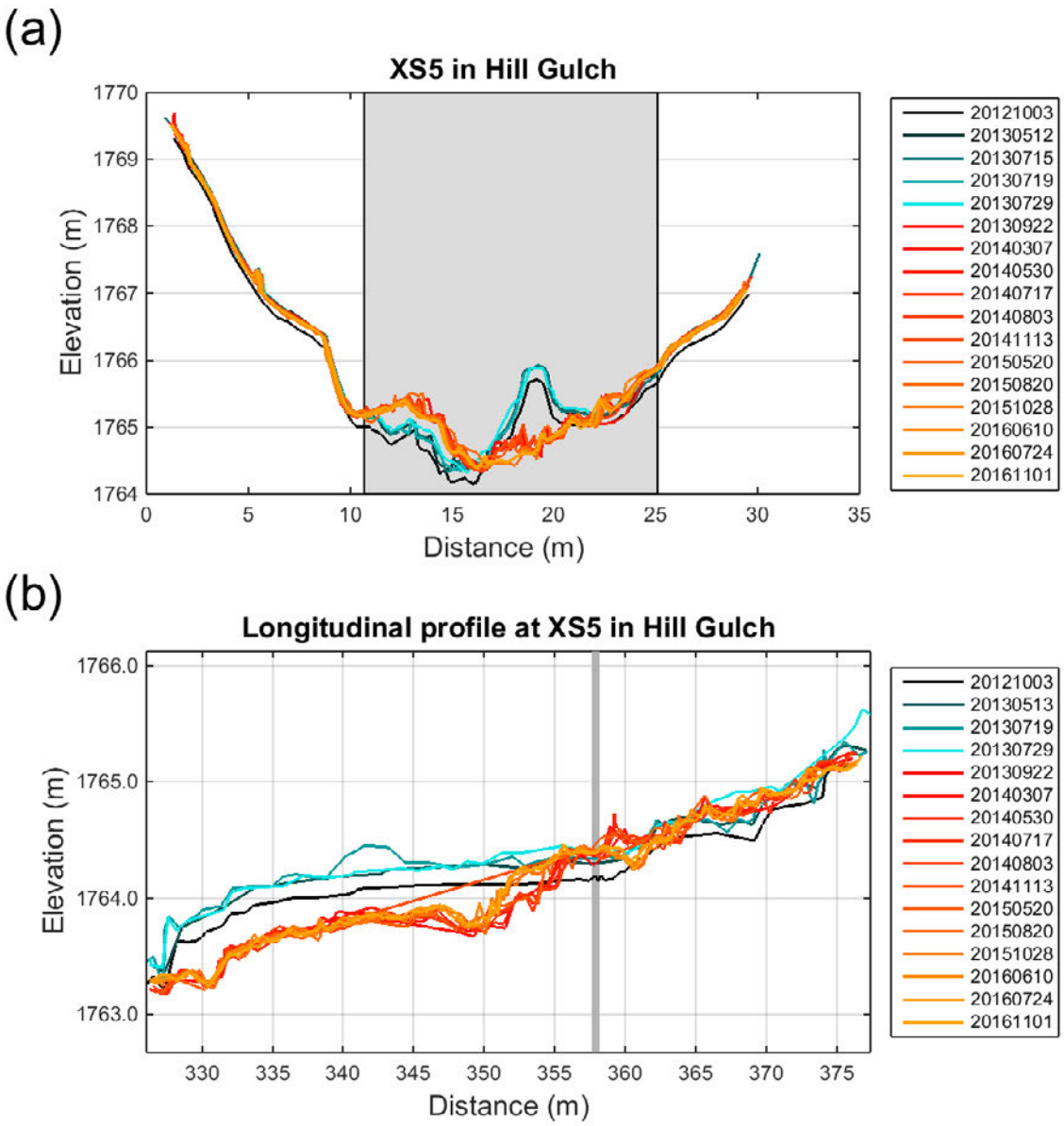

Figure C.18: Plots over the entire monitoring period of (a) cross section five in Hill Gulch and (b) the corresponding longitudinal profile. Gray shaded box in (a) delineates the active channel and the vertical line in (b) shows the location of the cross section.

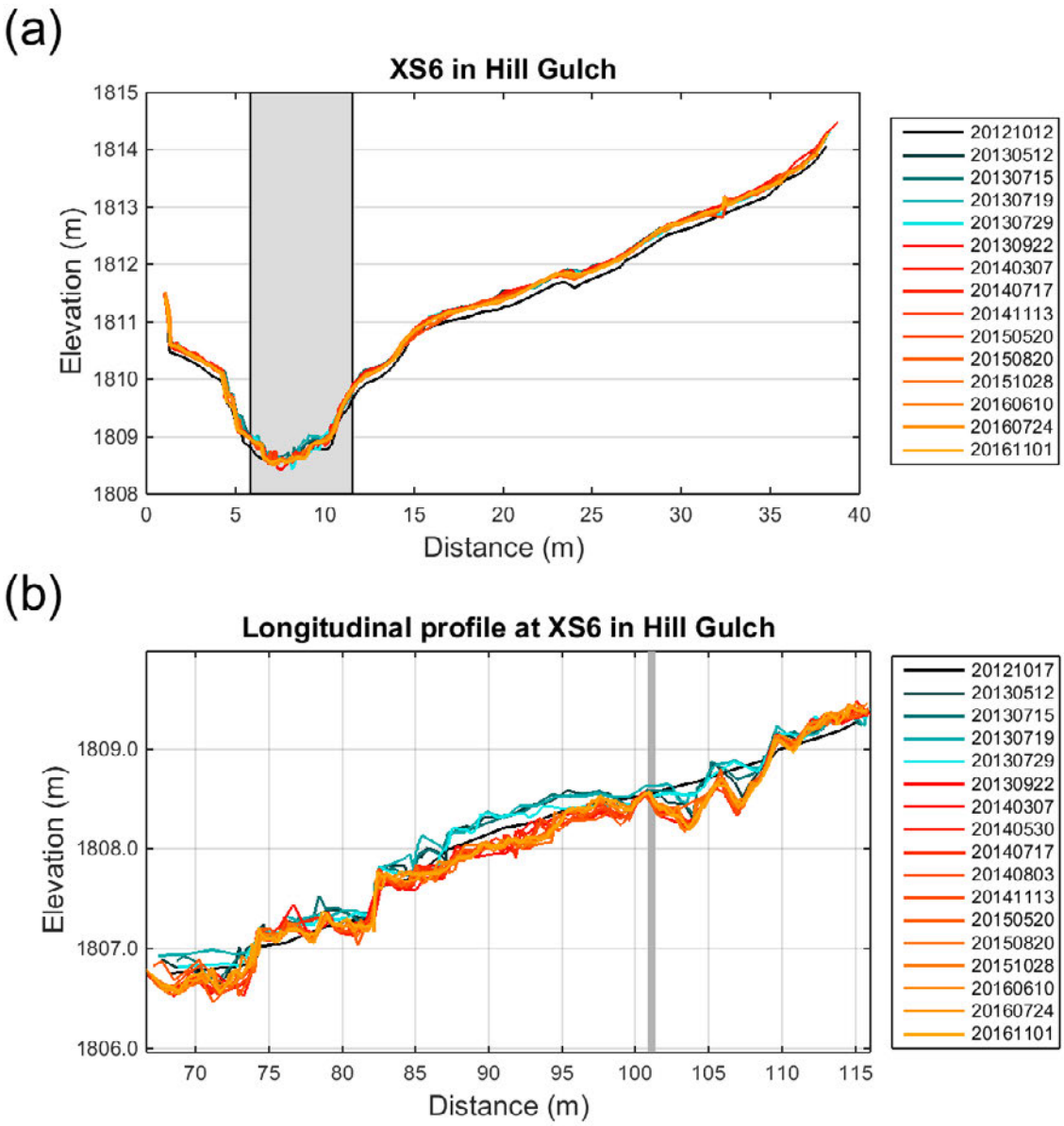

Figure C.19: Plots over the entire monitoring period of (a) cross section six in Hill Gulch and (b) the corresponding longitudinal profile. Gray shaded box in (a) delineates the active channel and the vertical line in (b) shows the location of the cross section.

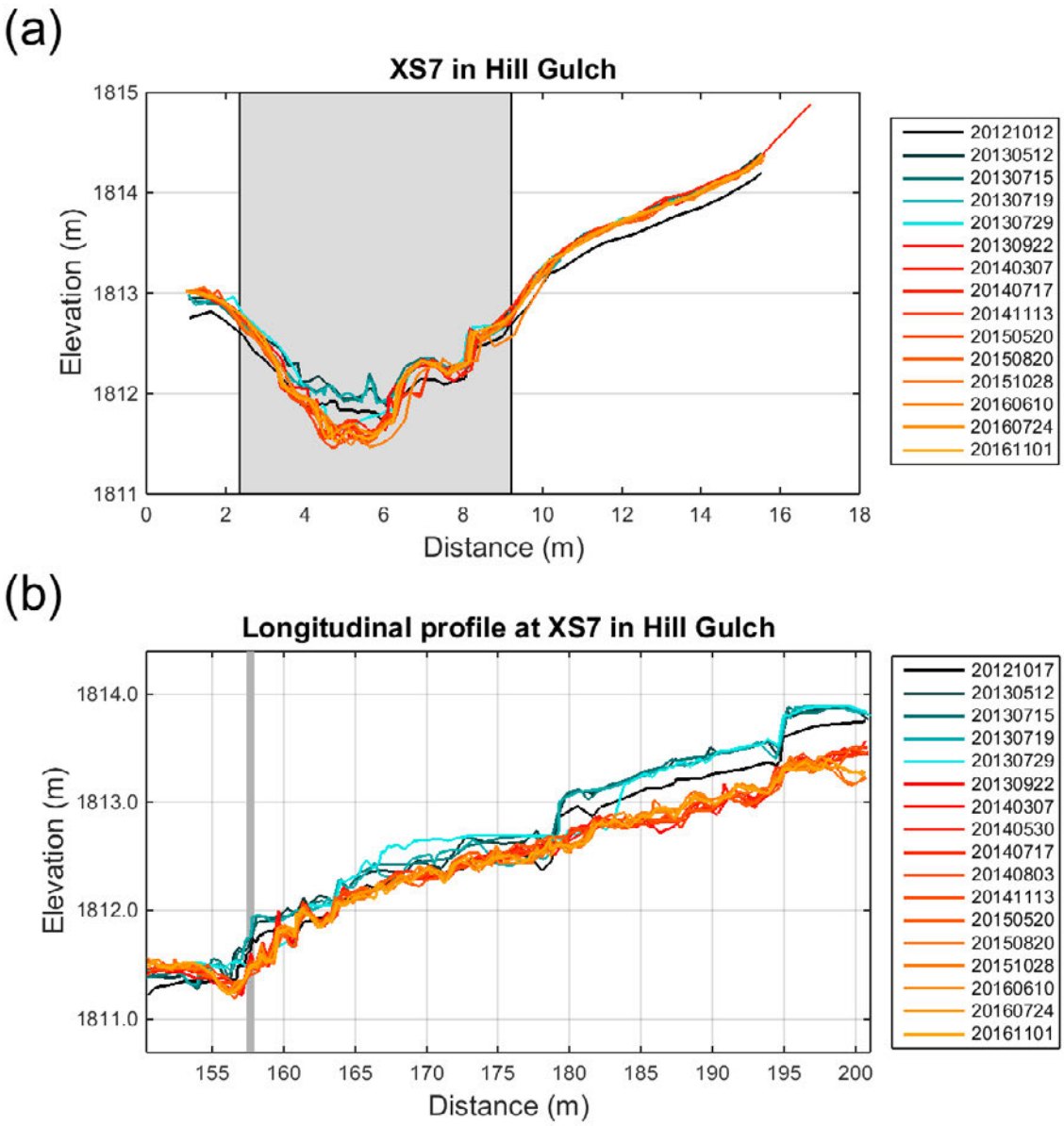

Figure C.20: Plots over the entire monitoring period of (a) cross section seven in Hill Gulch and (b) the corresponding longitudinal profile. Gray shaded box in (a) delineates the active channel and the vertical line in (b) shows the location of the cross section.

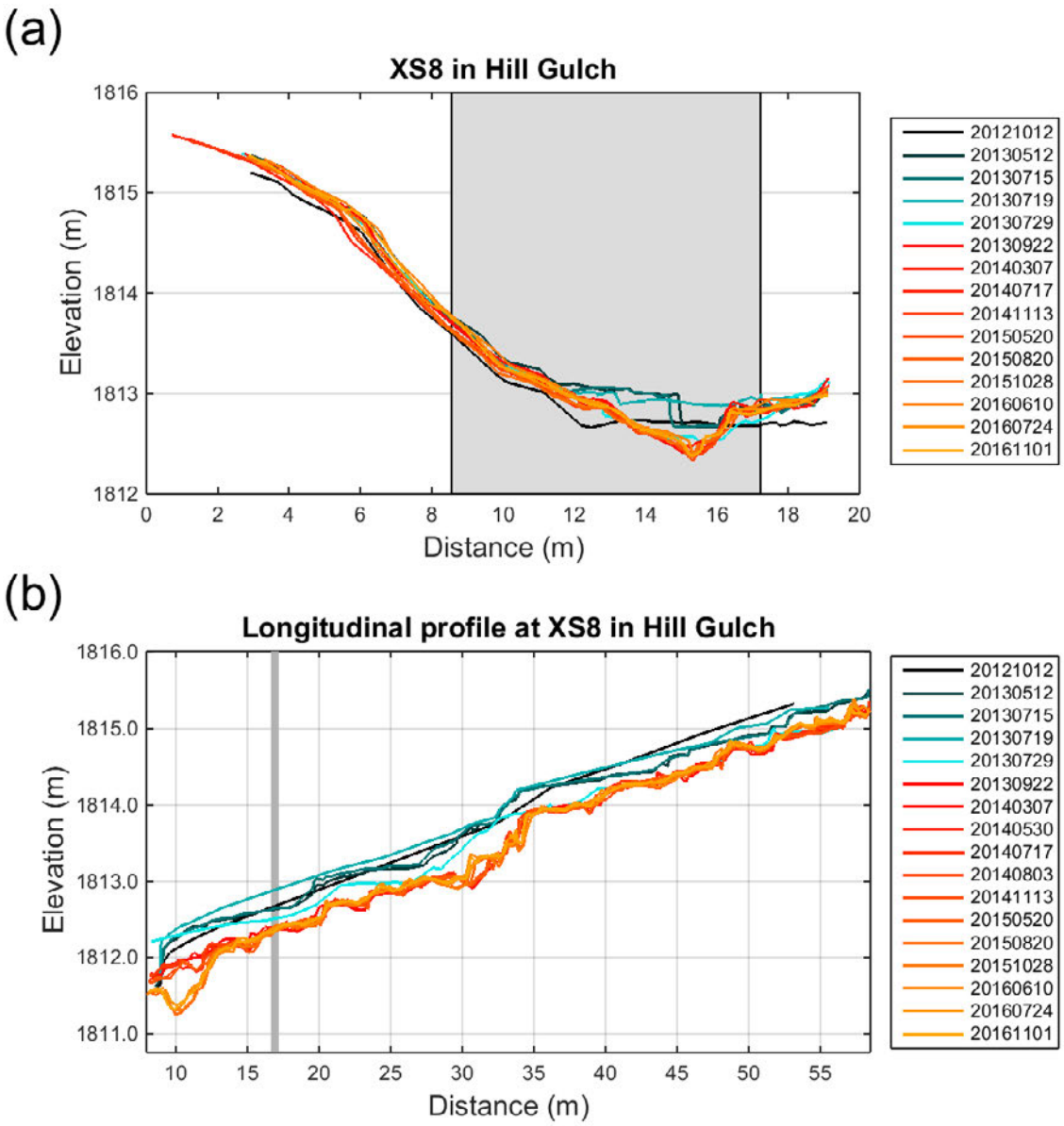

Figure C.21: Plots over the entire monitoring period of (a) cross section eight in Hill Gulch and (b) the corresponding longitudinal profile. Gray shaded box in (a) delineates the active channel and the vertical line in (b) shows the location of the cross section.

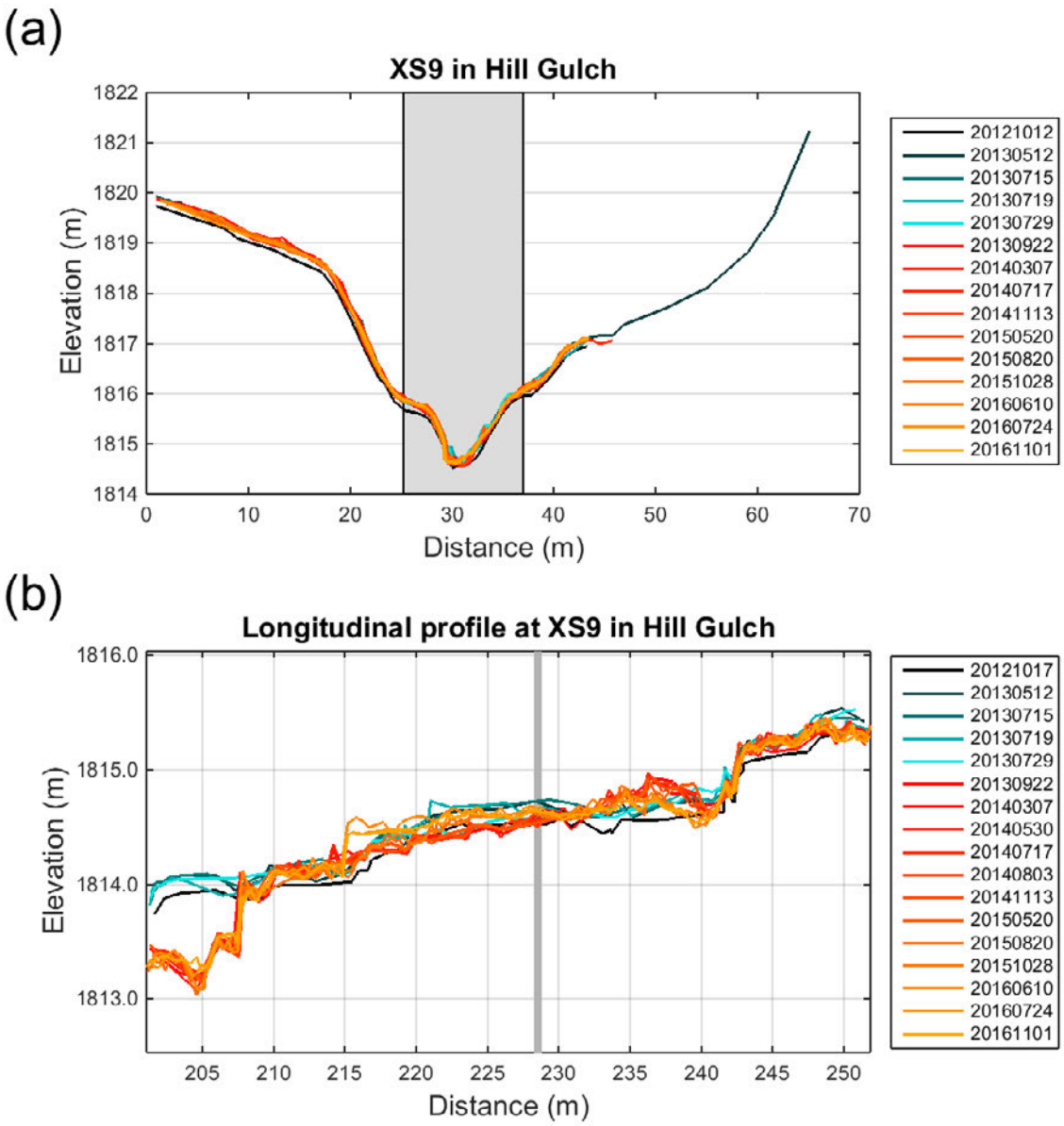

Figure C.22: Plots over the entire monitoring period of (a) cross section nine in Hill Gulch and (b) the corresponding longitudinal profile. Gray shaded box in (a) delineates the active channel and the vertical line in (b) shows the location of the cross section.

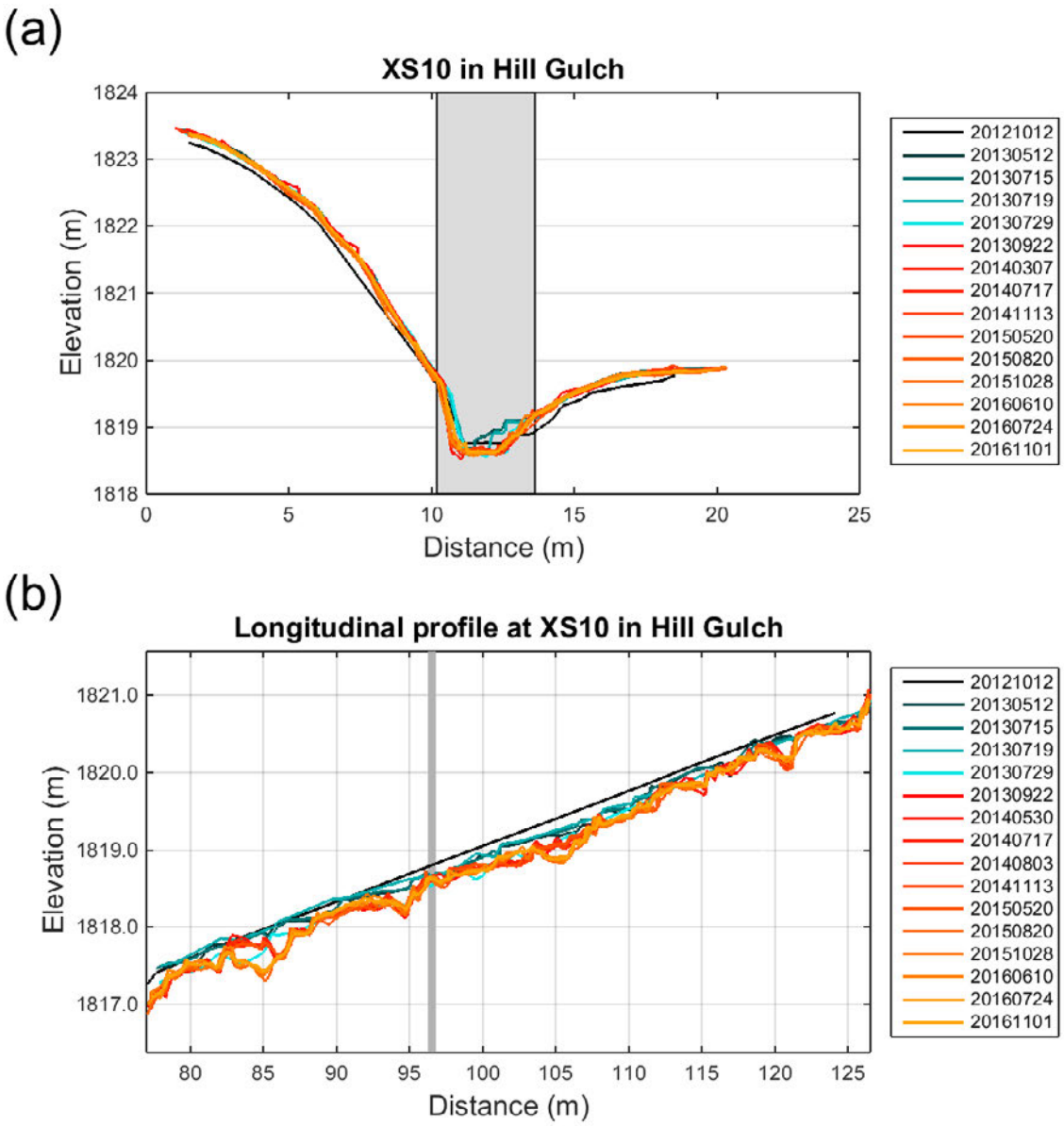

Figure C.23: Plots over the entire monitoring period of (a) cross section ten in Hill Gulch and (b) the corresponding longitudinal profile. Gray shaded box in (a) delineates the active channel and the vertical line in (b) shows the location of the cross section.

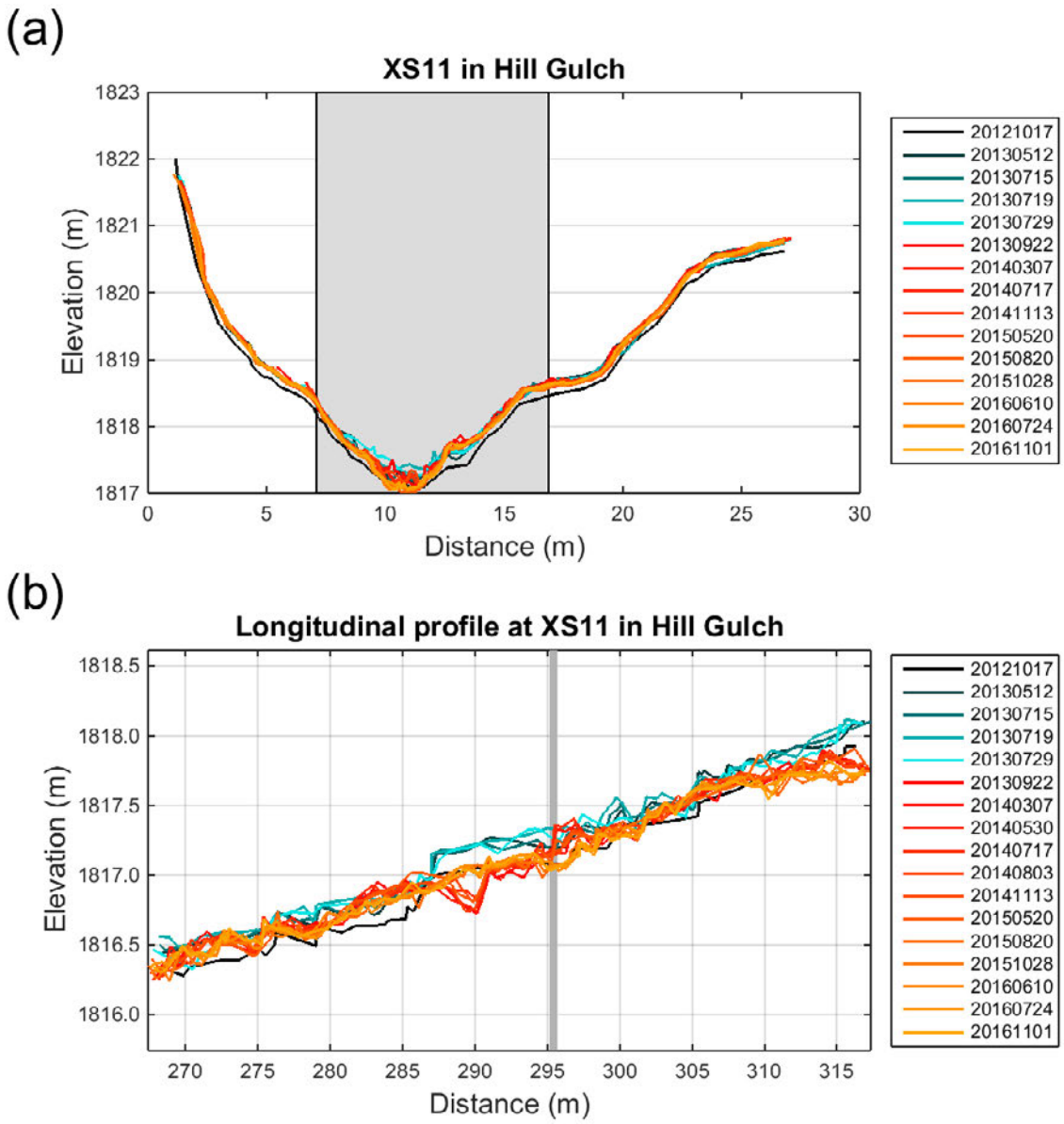

Figure C.24: Plots over the entire monitoring period of (a) cross section eleven in Hill Gulch and (b) the corresponding longitudinal profile. Gray shaded box in (a) delineates the active channel and the vertical line in (b) shows the location of the cross section.

Figure C.25: Photos showing the removal of riparian vegetation by locals at cross section one in Hill Gulch on (a) 6 July 2012 and (b) 27 July 2012.

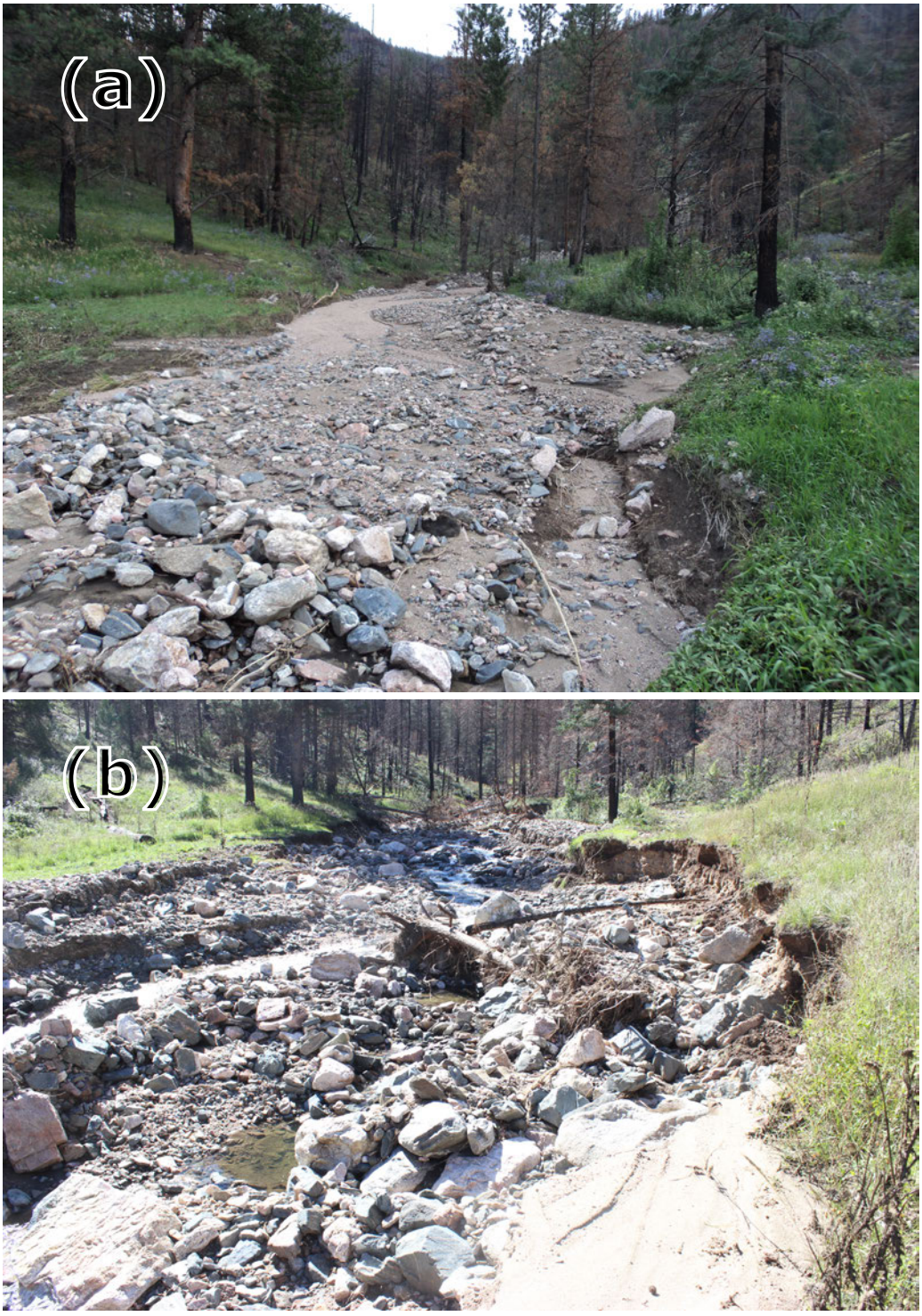

Figure C.26: Paired photos looking upstream in Skin Gulch approximately 80 m downstream from cross section six on (a) 28 August 2013 and (b) 24 September 2013 showing the incision and widening due to the mesoscale flood.

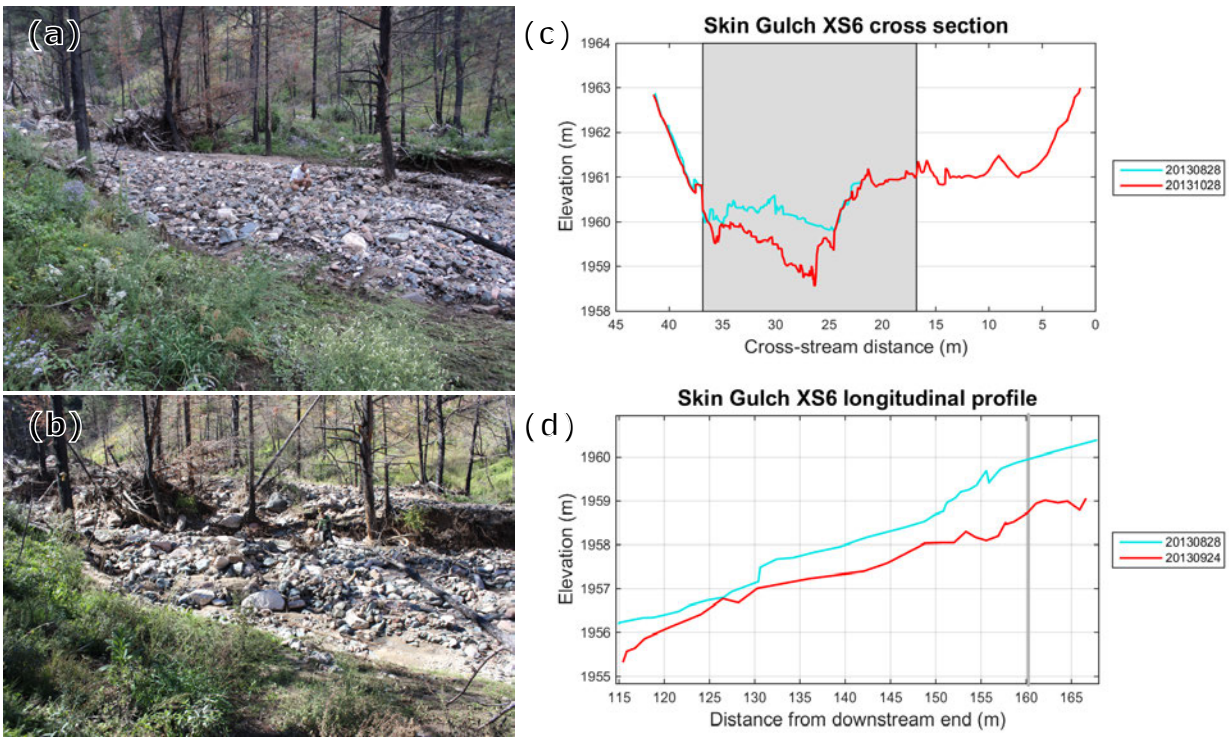

Figure C.27: Oblique photos looking upstream from below cross section six in Skin Gulch on (a) 28 August 2013 and (b) 24 September 2013 showing the incision and widening due to the mesoscale flood. (c) is the cross section and (d) is the longitudinal profile just before the flood (blue line) and after the flood (red line). The cross section in (c) is plotted looking upstream to match the perspective in the photos. A person in (a) and a different person in (b) provides scale, those people are standing at the location of cross section six.

Figure C.28: Paired photos looking up-valley, approximately 300 m upstream from cross section one in Hill Gulch on (a) August 1976, (b) 22 September 2013, and (c) 24 September 2016.

Figure C.29: Paired photos looking upstream, approximately 50 m downstream from cross section two in Hill Gulch on (a) August 1976, (b) 29 July 2013, (c) 22 September 2013, and (d) 24 September 2016.

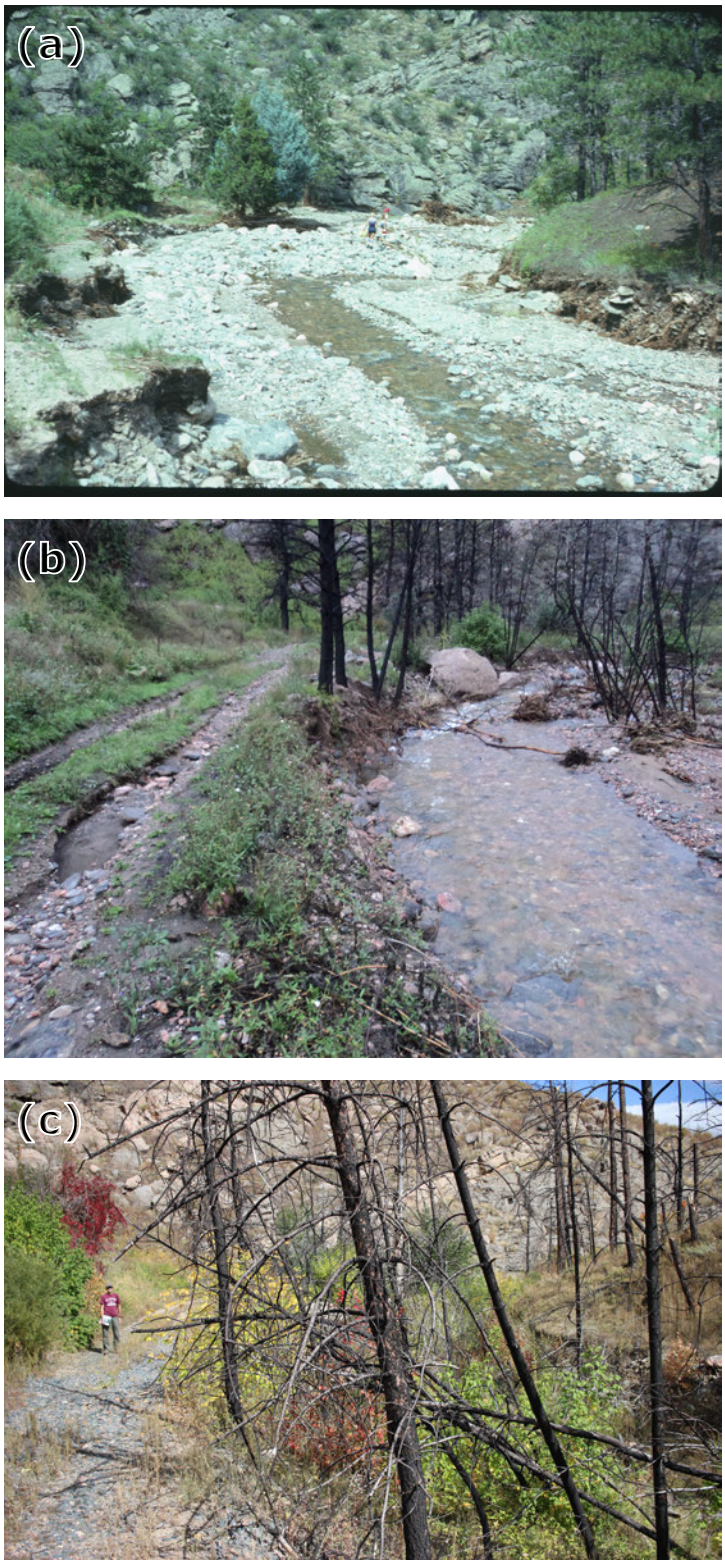

Figure C.30: Paired photos looking downstream, approximately 50 m downstraem from cross section two in Hill Gulch on (a) August 1976, (b) 22 September 2013, and (c) 24 September 2016.

Figure C.31: Paired photos looking downstream from cross sectio two in Hill Gulch on (a) August 1976, (b) 29 July 2013, (c) 22 September 2013, and (d) 20 May 2015.

Appendix D

Supporting information for Chapter 4

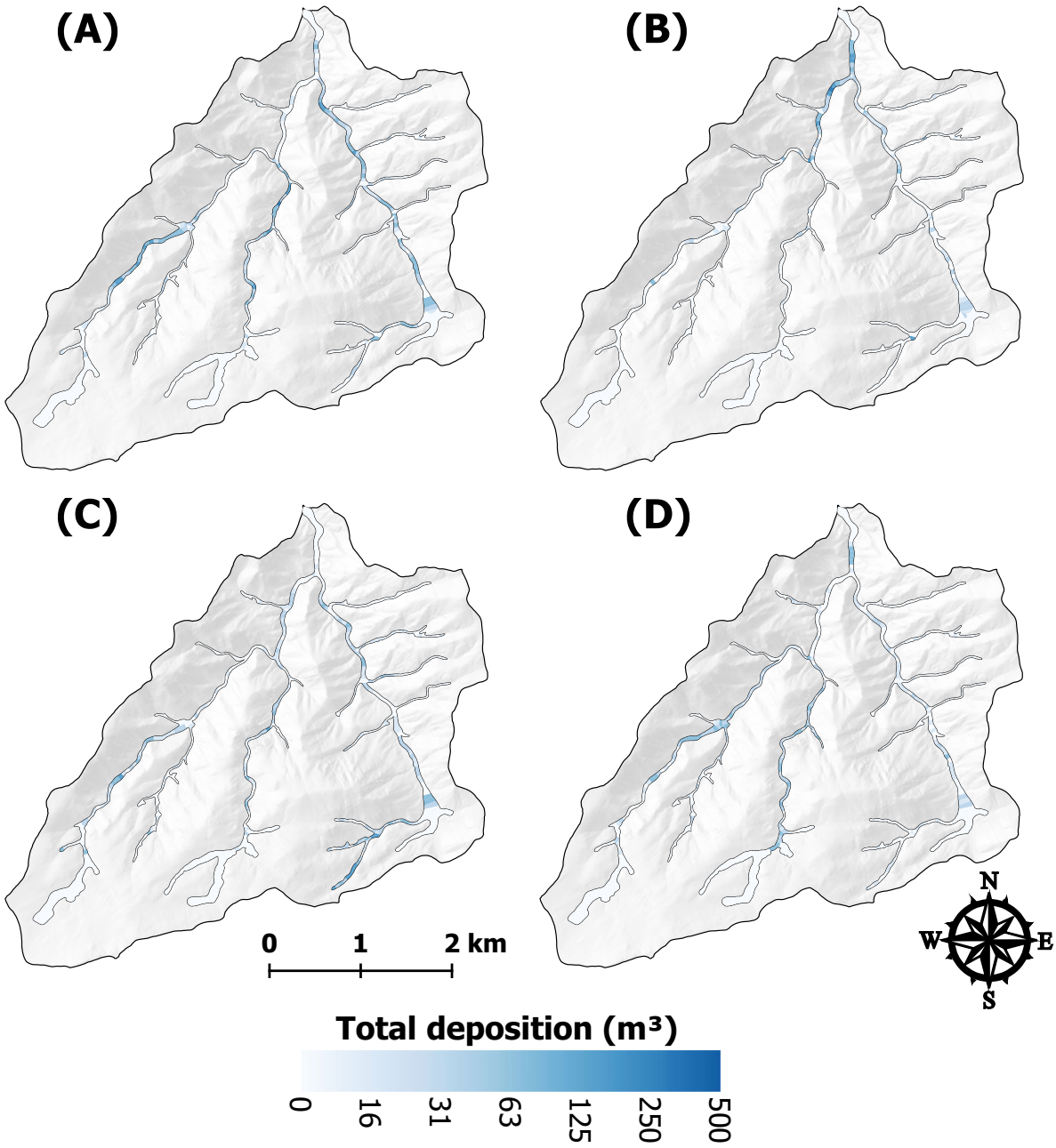

Figure D.1: Total deposition for each valley bottom segment in Skin Gulch for (A) 201210–201307, (B) 201307–201310, (C) 201310–201409, and (D) 201409–201506. Calculated volumes are not reported for the transparent segments due to unrealistically wide valley widths, repeat excavations, or the ground surface could not be reliably determined.

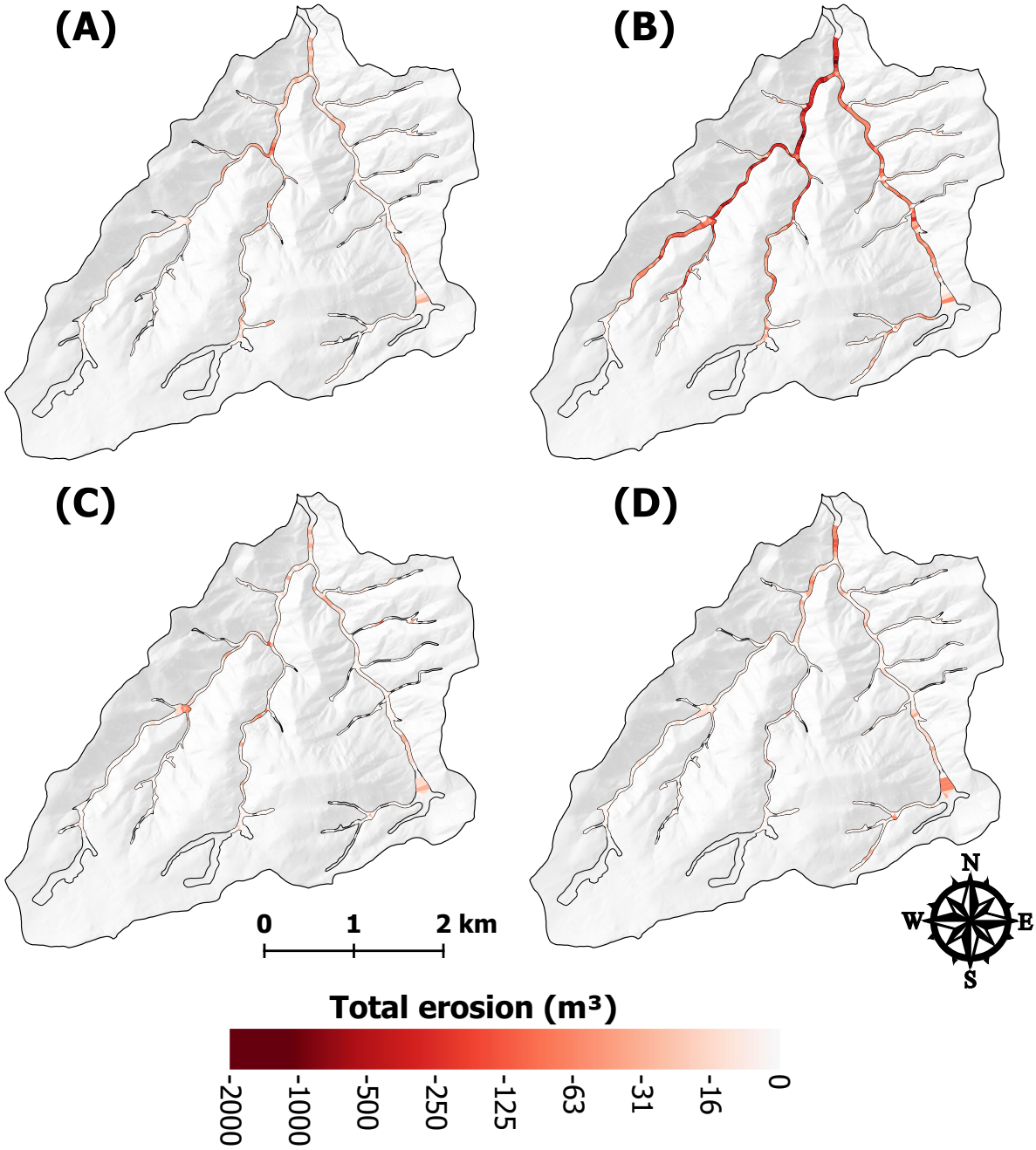

Figure D.2: Total erosion for each valley bottom segment in Skin Gulch for (A) 201210–201307, (B) 201307–201310, (C) 201310–201409, and (D) 201409–201506. Calculated volumes are not reported for the transparent segments due to unrealistically wide valley widths, repeat excavations, or the ground surface could not be reliably determined.

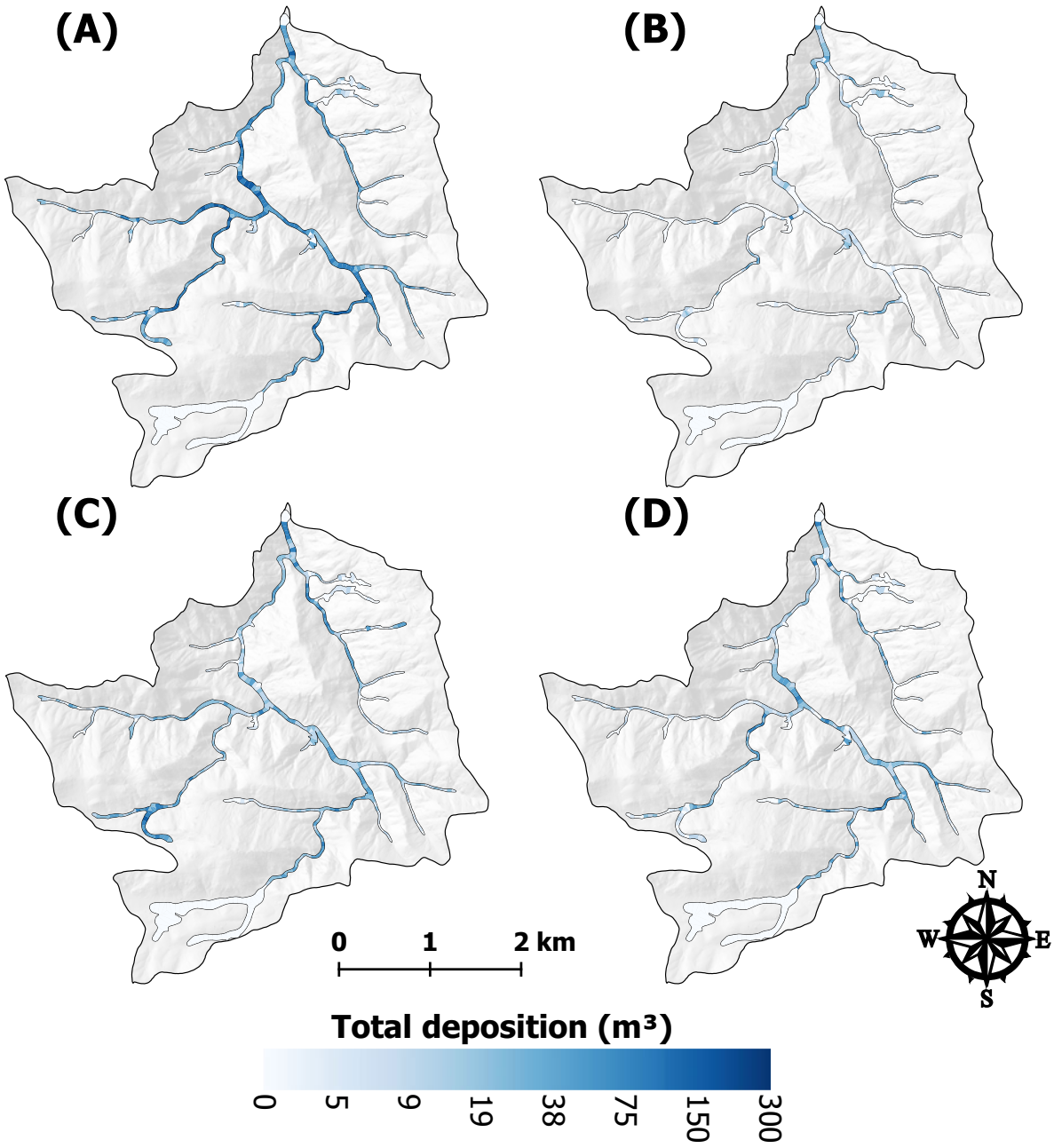

Figure D.3: Total deposition for each valley bottom segment in Hill Gulch for (A) 201210–201307, (B) 201307–201310, (C) 201310–201409, and (D) 201409–201506. Calculated volumes are not reported for the transparent segments due to unrealistically wide valley widths, repeat excavations, or the ground surface could not be reliably determined.

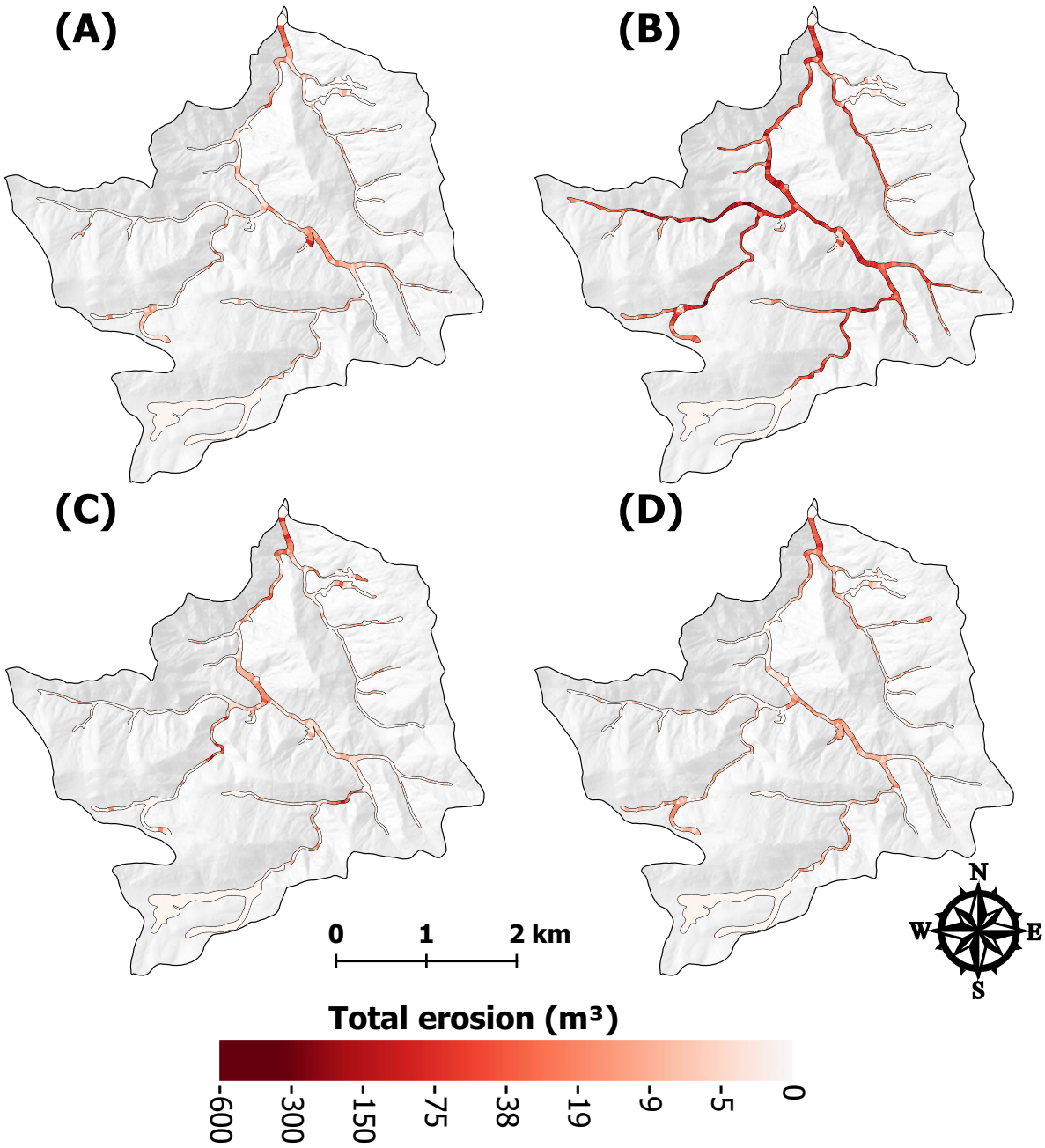

Figure D.4: Total erosion for each valley bottom segment in Hill Gulch for (A) 201210–201307, (B) 201307–201310, (C) 201310–201409, and (D) 201409–201506. Calculated volumes are not reported for the transparent segments due to unrealistically wide valley widths, repeat excavations, or the ground surface could not be reliably determined.

Table D.1: Correlation coefficients (r) for Skin Gulch between the the independent geomorphic, hydraulic, precipitation, and burn severity metrics and the dependent variables of net volume change, total erosion, and total deposition (n = 490). Independent variables include channel slope (S), ΔS, contributing area (A), valley width (w_{v}), change in valley width (Δw_{v}), $\frac{S}{w_v}$, $\Delta \frac{S}{w_v}$, channel width (w_{c}), confinement ratio (C_{r}), rainfall depth (P), maximum 30-min intensity (MI_{30}), and percent area burned at moderate severity (BS_{m}), high severity (BS_{h}) and moderate-to-high severity ($BS_{\mathrm{m+h}}$). Correlations in bold indicate $P \leq 0.05$.

Metrics	Net volume change				Total erosion				Total deposition			
	T1	T2	T3	T4	T1	T2	T3	T4	T1	T2	T3	T4
S	**-0.14**	**0.35**	**-0.14**	-0.01	**0.33**	**0.38**	**0.13**	**0.36**	**-0.28**	**-0.30**	**-0.23**	**-0.21**
ΔS	-0.03	0.03	0.02	-0.02	0.06	0.03	0.07	0.02	-0.06	-0.01	-0.02	-0.04
A	-0.03	**-0.63**	**-0.11**	**-0.10**	**-0.56**	**-0.71**	**-0.27**	**-0.44**	**0.19**	**0.65**	0.04	**0.14**
w_{v}	**0.13**	**-0.17**	0.07	-0.07	**-0.27**	**-0.22**	**-0.31**	**-0.62**	**0.25**	**0.36**	**0.26**	**0.28**
Δw_{v}	0.04	-0.06	-0.01	0.03	0.06	-0.04	0.09	**0.14**	0.02	**-0.10**	-0.07	-0.05
$\frac{S}{w_v}$	**-0.17**	**0.31**	**-0.16**	-0.05	**0.31**	**0.34**	**0.17**	**0.38**	**-0.30**	**-0.28**	**-0.28**	**-0.27**
$\Delta \frac{S}{w_v}$	-0.05	0.06	0.01	0.00	0.03	0.06	0.05	0.01	-0.07	-0.02	-0.02	-0.01
w_{c}	**0.10**	**-0.62**	-0.08	0.03	**-0.57**	**-0.68**	**-0.33**	**-0.45**	**0.33**	**0.57**	**0.10**	**0.29**
C_{r}	**-0.10**	**0.35**	**0.09**	**-0.15**	**0.24**	**0.35**	0.07	-0.06	**-0.20**	**-0.16**	0.06	**-0.13**
P	0.06	0.09	**-0.12**	**-0.33**	-0.05	0.08	0.01	-0.02	0.08	0.03	**-0.15**	**-0.34**
MI_{30}	0.00	**-0.36**	**-0.13**	0.07	**-0.42**	**-0.39**	**-0.20**	**-0.32**	**0.16**	**0.34**	-0.03	**0.26**
BS_{m}	**-0.14**	-0.01	**-0.35**	-0.04	**-0.14**	-0.02	-0.08	0.08	-0.09	0.06	**-0.36**	-0.08
BS_{h}	**0.11**	**-0.10**	**0.27**	0.08	**0.10**	**-0.09**	0.02	-0.07	0.08	-0.01	**0.30**	**0.13**
$BS_{\mathrm{m+h}}$	**0.09**	**-0.13**	**0.22**	0.09	0.07	**-0.12**	0.00	-0.06	0.07	0.00	**0.26**	**0.13**

Table D.2: Correlation coefficients (r) for Hill Gulch between the independent geomorphic, hydraulic, precipitation, and burn severity metrics and the dependent variables of net volume change, total erosion and total deposition (n = 484). Independent variables include channel slope (S), ΔS, contributing area (A), valley width (w_{v}), change in valley width (Δw_{v}), $\frac{S}{w_v}$, $\Delta\ \frac{S}{w_v}$, channel width (w_{c}), confinement ratio (C_{r}), rainfall depth (P), maximum 30-min intensity (MI_{30}), and percent area burned at moderate severity (BS_{m}), high severity (BS_{h}) and moderate-to-high severity ($BS_{\mathrm{m+h}}$). Correlations in bold indicate $P \leq 0.05$.

Metrics	Net volume change				Total erosion				Total deposition			
	T1	T2	T3	T4	T1	T2	T3	T4	T1	T2	T3	T4
S	**-0.25**	**0.35**	**-0.26**	-0.02	**0.16**	**0.35**	-0.05	**0.24**	**-0.28**	-0.02	**-0.28**	**-0.14**
ΔS	-0.07	-0.01	**0.10**	-0.07	**0.12**	0.01	**0.19**	0.05	-0.09	**-0.11**	-0.02	**-0.09**
A	**0.28**	**-0.24**	-0.02	-0.04	**-0.41**	**-0.31**	**-0.28**	**-0.49**	**0.35**	**0.36**	**0.18**	**0.19**
w_{v}	**0.17**	**-0.14**	**0.15**	**-0.10**	**-0.30**	**-0.17**	-0.06	**-0.38**	**0.23**	**0.17**	**0.23**	0.08
Δw_{v}	0.09	-0.06	-0.04	**0.12**	0.07	-0.04	-0.04	**0.10**	0.08	**-0.10**	-0.03	0.08
$\frac{S}{w_v}$	**-0.25**	**0.32**	**-0.29**	0.01	**0.17**	**0.32**	-0.06	**0.27**	**-0.29**	-0.03	**-0.31**	**-0.12**
$\Delta\ \frac{S}{w_v}$	-0.07	0.01	**0.09**	-0.06	**0.11**	0.02	**0.17**	0.02	-0.09	-0.06	-0.01	-0.07
w_{c}	**0.40**	**-0.36**	0.02	0.05	**-0.40**	**-0.42**	**-0.29**	**-0.46**	**0.47**	**0.34**	**0.23**	**0.28**
C_{r}	**-0.31**	**0.33**	0.08	**-0.21**	**0.11**	**0.35**	**0.18**	**0.10**	**-0.33**	**-0.11**	-0.03	**-0.27**
P	**0.17**	**0.22**	-0.02	**0.21**	**-0.14**	**0.21**	0.02	-0.09	**0.20**	0.02	-0.04	**0.26**
MI_{30}	**0.29**	**-0.33**	0.06	**0.12**	**-0.26**	**-0.37**	**-0.28**	**-0.24**	**0.34**	**0.29**	**0.27**	**0.24**
BS_{m}	**0.29**	**-0.19**	**0.12**	**0.23**	**-0.18**	**-0.20**	**-0.14**	**-0.09**	**0.33**	0.07	**0.25**	**0.28**
BS_{h}	**-0.37**	**0.19**	**-0.10**	**-0.29**	**0.27**	**0.20**	**0.20**	**0.16**	**-0.42**	**-0.12**	**-0.27**	**-0.38**
$BS_{\mathrm{m+h}}$	**-0.37**	**0.17**	-0.09	**-0.29**	**0.28**	**0.19**	**0.21**	**0.17**	**-0.42**	**-0.12**	**-0.26**	**-0.38**

Table D.3: Correlation coefficients (r) between the independent geomorphic, hydraulic, precipitation, and burn severity metrics and net volume change, stratified by S (channel slope) < 4% and $S \geq 4\%$. Independent variables include channel slope (S), ΔS, contributing area (A), valley width (w_{v}), change in valley width (Δw_{v}), $\frac{S}{w_v}$, $\Delta \frac{S}{w_v}$, channel width (w_{c}), confinement ratio (C_{r}), rainfall depth (P), maximum 30-min intensity (MI_{30}), and percent area burned at moderate severity (BS_{m}), high severity (BS_{h}) and moderate-to-high severity ($BS_{\text{m+h}}$). Correlations in bold indicate $P \leq 0.05$.

Metrics	Skin Gulch								Hill Gulch							
	$S < 4\%$				$S \geq 4\%$				$S < 4\%$				$S \geq 4\%$			
	T1	T2	T3	T4	T1	T2	T3	T4	T1	T2	T3	T4	T1	T2	T3	T4
n =	85	95	91	91	405	395	399	392	148	151	152	145	332	333	332	335
S	0.05	-0.02	0.10	0.09	**-0.17**	**0.31**	**-0.24**	**-0.15**	-0.06	-0.06	0.03	0.13	**-0.22**	**0.36**	**-0.30**	-0.08
ΔS	-0.07	0.15	-0.01	0.10	-0.03	0.05	0.04	-0.03	**-0.19**	0.10	0.01	-0.07	-0.06	-0.01	0.11	-0.06
A	**-0.39**	**-0.59**	-0.20	**-0.37**	**0.13**	**-0.69**	-0.02	**0.29**	**0.16**	-0.04	**-0.20**	-0.15	**0.37**	**-0.33**	0.03	**0.18**
w_{v}	0.01	0.02	-0.09	**-0.24**	**0.16**	**-0.10**	**0.18**	**0.15**	0.16	-0.01	0.00	-0.05	0.06	-0.04	**0.23**	-0.10
Δw_{v}	0.12	-0.10	0.00	-0.07	0.02	-0.06	-0.02	0.07	**0.22**	**-0.20**	0.01	**0.24**	0.02	0.05	-0.08	0.04
$\frac{S}{w_v}$	0.03	0.03	0.12	0.20	**-0.20**	**0.27**	**-0.24**	**-0.17**	-0.16	-0.09	-0.03	0.14	**-0.23**	**0.32**	**-0.34**	-0.04
$\Delta \frac{S}{w_v}$	-0.08	0.12	-0.04	0.07	-0.05	0.06	0.03	-0.01	**-0.22**	0.14	-0.05	-0.08	-0.05	0.00	**0.11**	-0.05
w_{c}	**-0.37**	**-0.59**	**-0.25**	**-0.34**	**0.25**	**-0.61**	0.02	**0.36**	**0.23**	-0.08	**-0.21**	-0.07	**0.52**	**-0.49**	0.09	**0.28**
C_{r}	0.19	**0.32**	0.14	-0.09	**-0.14**	**0.32**	0.07	**-0.21**	**-0.22**	**0.22**	**0.26**	-0.11	**-0.30**	**0.34**	0.05	**-0.27**
P	**-0.54**	**0.21**	-0.14	**-0.40**	**0.16**	**0.12**	**-0.13**	**-0.34**	-0.02	0.13	**0.27**	**0.26**	**0.23**	**0.22**	-0.06	**0.22**
MI_{30}	**-0.63**	**-0.24**	**-0.33**	**-0.29**	**0.17**	**-0.30**	-0.07	**0.26**	**0.19**	-0.11	-0.02	0.05	**0.28**	**-0.38**	0.05	**0.19**
BS_{m}	-0.14	**-0.37**	**-0.46**	-0.05	**-0.15**	0.04	**-0.36**	-0.04	0.05	0.08	0.08	**0.22**	**0.37**	**-0.25**	**0.11**	**0.26**
BS_{h}	**-0.29**	-0.03	0.18	-0.05	**0.16**	**-0.15**	**0.29**	**0.11**	-0.14	-0.07	-0.10	**-0.27**	**-0.43**	**0.23**	-0.08	**-0.33**
$BS_{\text{m+h}}$	**-0.36**	-0.12	0.10	-0.07	**0.15**	**-0.17**	**0.25**	**0.13**	-0.15	-0.06	-0.10	**-0.27**	**-0.42**	**0.21**	-0.07	**-0.33**

Table D.4: Correlation coefficients (r) between the independent geomorphic, hydraulic, precipitation, and burn severity metrics and net volume change , stratified by contributing area (A) $\geq$ 4 km^2 and A < 4 km^2. Independent variables include channel slope (S), ΔS, contributing area (A), valley width (w_{v}), change in valley width (Δw_{v}), $\frac{S}{w_v}$, $\Delta \frac{S}{w_v}$, channel width (w_{c}), confinement ratio (C_{r}), rainfall depth (P), maximum 30-min intensity (MI_{30}), and percent area burned at moderate severity (BS_{m}), high severity (BS_{h}) and moderate-to-high severity ($BS_{\mathrm{m+h}}$). Correlations in bold indicate $P \leq 0.05$.

Metrics	Skin Gulch								Hill Gulch							
	$A \geq$ 4 km^2				$A <$ 4 km^2				$A \geq$ 4 km^2				$A <$ 4 km^2			
	T1	T2	T3	T4	T1	T2	T3	T4	T1	T2	T3	T4	T1	T2	T3	T4
n =	94	94	94	87	396	396	396	396	81	81	81	80	403	403	403	403
S	-0.08	0.00	0.05	**0.23**	**-0.26**	**0.28**	**-0.25**	**-0.10**	-0.09	0.15	-0.15	0.10	**-0.22**	**0.32**	**-0.31**	-0.06
ΔS	-0.03	0.09	**-0.22**	-0.04	-0.04	-0.01	0.03	-0.03	0.00	-0.10	0.11	-0.10	-0.08	-0.01	0.10	-0.07
A	**-0.23**	**-0.31**	-0.09	**-0.54**	**0.53**	**-0.56**	0.05	**0.36**	-0.11	0.11	-0.10	**-0.29**	**0.56**	**-0.41**	**0.12**	**0.26**
w_{v}	0.08	-0.05	0.07	**-0.40**	**0.19**	-0.07	**0.11**	0.01	0.16	**-0.35**	-0.03	0.04	0.08	-0.01	**0.24**	**-0.12**
Δw_{v}	0.10	-0.15	-0.11	0.16	0.03	0.00	0.01	0.01	0.21	-0.08	0.07	0.15	0.05	-0.05	-0.07	**0.12**
$\frac{S}{w_v}$	-0.15	0.01	-0.05	**0.35**	**-0.28**	**0.26**	**-0.25**	**-0.14**	-0.14	**0.29**	-0.14	0.04	**-0.23**	**0.29**	**-0.34**	-0.02
$\Delta \frac{S}{w_v}$	-0.01	0.17	-0.13	-0.08	-0.07	0.03	0.01	-0.01	-0.12	-0.06	0.07	-0.10	-0.07	0.01	0.10	-0.07
w_{c}	**-0.27**	**-0.32**	-0.07	**-0.56**	**0.53**	**-0.55**	0.07	**0.37**	-0.08	0.11	-0.13	**-0.25**	**0.58**	**-0.48**	**0.14**	**0.29**
C_{r}	**0.34**	**0.21**	0.14	-0.10	**-0.22**	**0.32**	0.04	**-0.24**	0.14	**-0.31**	0.04	0.14	**-0.32**	**0.33**	0.07	**-0.28**
P	**-0.54**	**0.41**	**-0.32**	-0.05	**0.24**	**0.22**	**-0.11**	**-0.37**	-0.05	-0.12	0.01	0.17	**0.21**	**0.21**	-0.03	**0.24**
MI_{30}	**-0.63**	-0.10	**-0.24**	**-0.23**	**0.35**	**-0.12**	-0.06	**0.21**	0.00	0.04	-0.21	0.00	**0.28**	**-0.35**	0.09	**0.19**
BS_{m}	-0.07	-0.05	0.11	**-0.54**	**-0.15**	0.08	**-0.38**	0.00	**0.34**	-0.11	-0.21	**0.52**	**0.31**	**-0.18**	**0.13**	**0.26**
BS_{h}	**-0.50**	**-0.33**	**-0.27**	**0.36**	**0.19**	**-0.15**	**0.33**	0.05	-0.10	0.13	-0.11	**-0.29**	**-0.39**	**0.15**	**-0.12**	**-0.34**
$BS_{\mathrm{m+h}}$	**-0.54**	**-0.36**	**-0.28**	**0.31**	**0.20**	**-0.17**	**0.29**	0.06	-0.09	0.13	-0.12	**-0.27**	**-0.38**	**0.14**	**-0.10**	**-0.34**

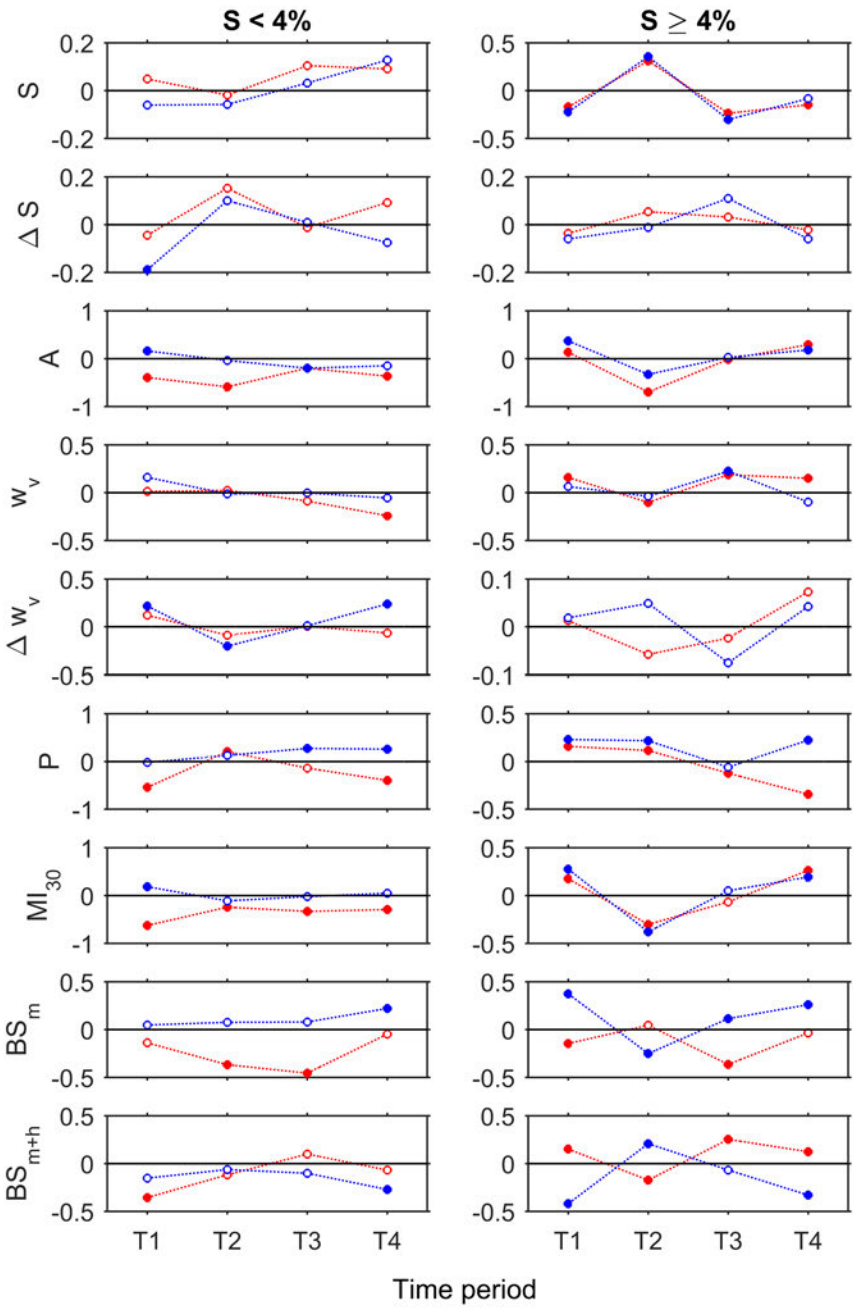

Figure D.5: Correlation coefficients for Skin Gulch (red dashed lines) and Hill Gulch (blue dashed lines) stratified by slope (< or $\geq$ 4%) for each time period between the independent metrics and net volume change. Time periods (T#) are for 201210–201307, 201307–201310, 201310–201409, and 201409–201506, respectively. Independent variables include channel slope (S), ΔS, contributing area (A), valley width (w_{v}), change in valley width (Δw_{v}), total rainfall (P), maximum 30-minute intensity (MI_{30}), and percent area burned at moderate severity (BS_{m}) and moderate-to-high severity ($BS_{\mathrm{m+h}}$). Filled circles indicate significant correlations, p-value ≤ 0.05.

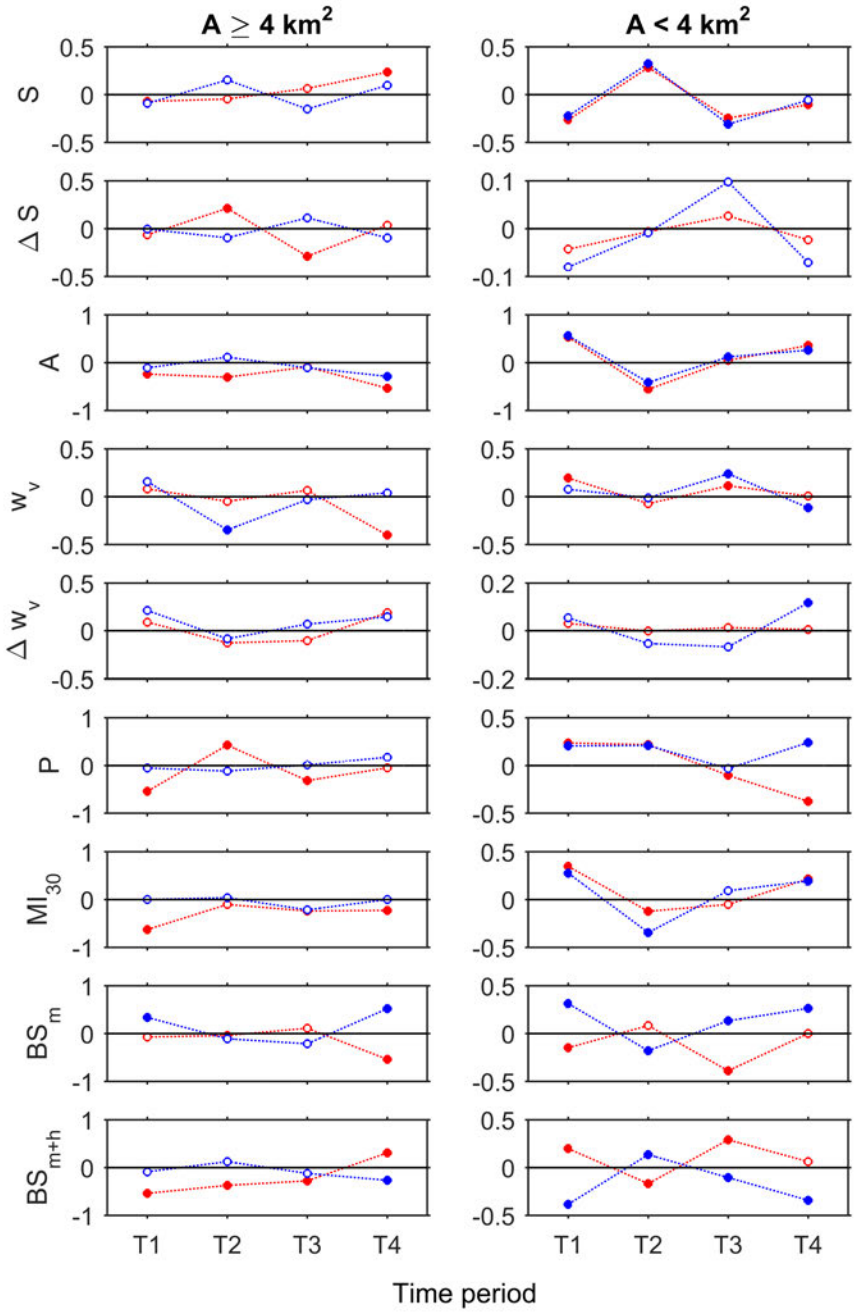

Figure D.6: Correlation coefficients for Skin Gulch (red dashed lines) and Hill Gulch (blue dashed lines) stratified by contributing area (A $\geq$ or $<$ 4 km^2) for each time period between the independent metrics and net volume change. Time periods (T#) are for 201210–201307, 201307–201310, 201310–201409, and 201409–201506, respectively. Independent variables include channel slope (S), ΔS, contributing area (A), valley width (w_{v}), change in valley width (Δw_{v}), total rainfall (P), maximum 30-minute intensity (MI_{30}), and percent area burned at moderate severity (BS_{m}) and moderate-to-high severity ($BS_{\mathrm{m+h}}$). Filled circles indicate significant correlations, p-value ≤ 0.05.

Table D.5: Correlation coefficients (r), p-values, and slopes for **Skin Gulch** for the dependent variable of **net volume change** to the independent geomorphic, hydraulic, precipitation, and burn severities metrics (n = 490). Independent variables include channel slope (S), ΔS, contributing area (A), valley width (w_{v}), change in valley width (Δw_{v}), $\frac{S}{w_v}$, $\Delta\ \frac{S}{w_v}$, channel width (w_{c}), confinement ratio (C_{r}), rainfall depth (P), maximum 30-min intensity (MI_{30}), moderate burn severity (BS_{m}), high burn severity (BS_{h}), and moderate-to-high burn severity ($BS_{\mathrm{m+h}}$).

Net change	201210–201307			201307–201310			201310–201409			201409–201506		
	r	p-value	Slope	r	p-value	Slope	r	p-value	Slope	r	p-value	Slope
S	-0.14	0.00	-54	0.35	0.00	541	-0.14	0.00	-43	-0.01	0.82	-2
ΔS	-0.03	0.50	-1796	0.03	0.47	7656	0.02	0.74	688	-0.02	0.65	-688
A	-0.03	0.55	0	-0.63	0.00	-38	-0.11	0.02	-1	-0.10	0.04	-1
w_{v}	0.13	0.00	0	-0.17	0.00	-2	0.07	0.12	0	-0.07	0.14	0
Δw_{v}	0.04	0.42	11	-0.06	0.18	-72	-0.01	0.83	-2	0.03	0.54	5
$\frac{S}{w_v}$	-0.17	0.00	-905	0.31	0.00	6681	-0.16	0.00	-689	-0.05	0.24	-168
$\Delta\ \frac{S}{w_v}$	-0.05	0.26	-34990	0.06	0.19	173297	0.01	0.86	4302	0.00	0.94	-1349
w_{c}	0.10	0.02	5	-0.62	0.00	-119	-0.08	0.09	-3	0.03	0.50	1
C_{r}	-0.10	0.02	0	0.35	0.00	3	0.09	0.04	0	-0.15	0.00	0
P	0.06	0.19	0	0.09	0.05	1	-0.12	0.01	0	-0.33	0.00	0
MI_{30}	0.00	0.92	0	-0.36	0.00	-4	-0.13	0.01	-1	0.07	0.11	0
BS_{m}	-0.14	0.00	-85	-0.01	0.79	-30	-0.35	0.00	-178	-0.04	0.42	-13
BS_{h}	0.11	0.02	17	-0.10	0.03	-63	0.27	0.00	34	0.08	0.07	7
$BS_{\mathrm{m+h}}$	0.09	0.04	18	-0.13	0.00	-102	0.22	0.00	35	0.09	0.05	10

Table D.6: Correlation coefficients (r), p-values, and slopes for **Hill Gulch** for the dependent variable of **net volume change** to the independent geomorphic, hydraulic, precipitation, and burn severities metrics (n = 484). Independent variables include channel slope (S), ΔS, contributing area (A), valley width (w_{v}), change in valley width (Δw_{v}), $\frac{S}{w_v}$, $\Delta\ \frac{S}{w_v}$, channel width (w_{c}), confinement ratio (C_{r}), rainfall depth (P), maximum 30-min intensity (MI_{30}), moderate burn severity (BS_{m}), high burn severity (BS_{h}), and moderate-to-high burn severity ($BS_{\mathrm{m+h}}$).

Net change	201210–201307			201307–201310			201310–201409			201409–201506		
	r	p-value	Slope	r	p-value	Slope	r	p-value	Slope	r	p-value	Slope
S	-0.25	0.00	-117	0.35	0.00	227	-0.26	0.00	-80	-0.02	0.67	-5
ΔS	-0.07	0.14	-4279	-0.01	0.83	-1003	0.10	0.04	4525	-0.07	0.15	-2386
A	0.28	0.00	4	-0.24	0.00	-5	-0.02	0.69	0	-0.04	0.38	0
w_{v}	0.17	0.00	1	-0.14	0.00	-1	0.15	0.00	0	-0.10	0.03	0
Δw_{v}	0.09	0.05	33	-0.06	0.23	-29	-0.04	0.35	-11	0.12	0.01	23
$\frac{S}{w_v}$	-0.25	0.00	-2181	0.32	0.00	3961	-0.29	0.00	-1706	0.01	0.85	39
$\Delta\ \frac{S}{w_v}$	-0.07	0.15	-72507	0.01	0.84	15303	0.09	0.05	70945	-0.06	0.21	-33991
w_{c}	0.40	0.00	20	-0.36	0.00	-25	0.02	0.64	1	0.05	0.25	1
C_{r}	-0.31	0.00	-1	0.33	0.00	1	0.08	0.09	0	-0.21	0.00	0
P	0.17	0.00	1	0.22	0.00	0	-0.02	0.68	0	0.21	0.00	0
MI_{30}	0.29	0.00	1	-0.33	0.00	-1	0.06	0.22	0	0.12	0.01	0
BS_{m}	0.29	0.00	218	-0.19	0.00	-201	0.12	0.01	59	0.23	0.00	87
BS_{h}	-0.37	0.00	-59	0.19	0.00	42	-0.10	0.03	-11	-0.29	0.00	-24
$BS_{\mathrm{m+h}}$	-0.37	0.00	-70	0.17	0.00	48	-0.09	0.05	-12	-0.29	0.00	-29

Table D.7: Correlation coefficients (r), p-values, and slopes for **Skin Gulch** for the dependent variable of **total erosion** to the independent geomorphic, hydraulic, precipitation, and burn severities metrics (n = 490). Independent variables include channel slope (S), ΔS, contributing area (A), valley width (w_{v}), change in valley width (Δw_{v}), $\frac{S}{w_v}$, $\Delta\ \frac{S}{w_v}$, channel width (w_{c}), confinement ratio (C_{r}), rainfall depth (P), maximum 30-min intensity (MI_{30}), moderate burn severity (BS_{m}), high burn severity (BS_{h}), and moderate-to-high burn severity ($BS_{\text{m+h}}$).

Net change	201210–201307			201307–201310			201310–201409			201409–201506		
	r	p-value	Slope	r	p-value	Slope	r	p-value	Slope	r	p-value	Slope
S	0.33	0.00	48	0.38	0.00	628	0.13	0.00	20	0.36	0.00	42
ΔS 3	0.06	0.23	1201	0.03	0.49	7920	0.07	0.14	1605	0.02	0.61	406
A	-0.56	0.00	-3	-0.71	0.00	-45	-0.27	0.00	-2	-0.44	0.00	-2
w_{v}	-0.27	0.00	0	-0.22	0.00	-2	-0.31	0.00	0	-0.62	0.00	0
Δw_{v} 3	0.06	0.17	7	-0.04	0.36	-52	0.09	0.06	10	0.14	0.00	12
$\frac{S}{w_v}$	0.31	0.00	616	0.34	0.00	7800	0.17	0.00	374	0.38	0.00	614
$\Delta\ FP$ 3	0.03	0.60	6138	0.06	0.19	182732	0.05	0.29	13823	0.01	0.77	2817
w_{c}	-0.57	0.00	-10	-0.68	0.00	-139	-0.33	0.00	-6	-0.45	0.00	-7
C_{r}	0.24	0.00	0	0.35	0.00	4	0.07	0.10	0	-0.06	0.21	0
P	-0.05	0.23	0	0.08	0.08	0	0.01	0.87	0	-0.02	0.59	0
MI_{30}	-0.42	0.00	0	-0.39	0.00	-5	-0.20	0.00	0	-0.32	0.00	-1
BS_{m}	-0.14	0.00	-34	-0.02	0.64	-57	-0.08	0.07	-21	0.08	0.10	14
BS_{h}	0.10	0.03	6	-0.09	0.04	-62	0.02	0.65	1	-0.07	0.13	-3
$BS_{\text{m+h}}$	0.07	0.10	5	-0.12	0.01	-102	0.00	0.99	0	-0.06	0.17	-4

Table D.8: Correlation coefficients (r), p-values, and slopes for **Hill Gulch** for the dependent variable of **total erosion** to the independent geomorphic, hydraulic, precipitation, and burn severities metrics (n = 484). Independent variables include channel slope (S), ΔS, contributing area (A), valley width (w_{v}), change in valley width (Δw_{v}), $\frac{S}{w_v}$, $\Delta\ \frac{S}{w_v}$, channel width (w_{c}), confinement ratio (C_{r}), rainfall depth (P), maximum 30-min intensity (MI_{30}), moderate burn severity (BS_{m}), high burn severity (BS_{h}), and moderate-to-high burn severity ($BS_{\mathrm{m+h}}$).

Net change	201210–201307			201307–201310			201310–201409			201409–201506		
	r	p-value	Slope	r	p-value	Slope	r	p-value	Slope	r	p-value	Slope
S	0.16	0.00	13	0.35	0.00	229	-0.05	0.28	-9	0.24	0.00	27
ΔS 3	0.12	0.01	1271	0.01	0.86	810	0.19	0.00	5312	0.05	0.30	782
A	-0.41	0.00	-1	-0.31	0.00	-6	-0.28	0.00	-2	-0.49	0.00	-2
w_{v}	-0.30	0.00	0	-0.17	0.00	-1	-0.06	0.19	0	-0.38	0.00	0
Δw_{v} 3	0.07	0.12	5	-0.04	0.40	-20	-0.04	0.45	-5	0.10	0.04	8
$\frac{S}{w_v}$	0.17	0.00	268	0.32	0.00	4023	-0.06	0.21	-201	0.27	0.00	548
$\Delta\ FP$ 3	0.11	0.02	20693	0.02	0.68	30751	0.17	0.00	75547	0.02	0.62	6074
w_{c}	-0.40	0.00	-4	-0.42	0.00	-29	-0.29	0.00	-6	-0.46	0.00	-5
C_{r}	0.11	0.01	0	0.35	0.00	1	0.18	0.00	0	0.10	0.02	0
P	-0.14	0.00	0	0.21	0.00	0	0.02	0.71	0	-0.09	0.05	0
MI_{30}	-0.26	0.00	0	-0.37	0.00	-1	-0.28	0.00	0	-0.24	0.00	0
BS_{m}	-0.18	0.00	-24	-0.20	0.00	-213	-0.14	0.00	-43	-0.09	0.04	-16
BS_{h}	0.27	0.00	8	0.20	0.00	47	0.20	0.00	13	0.16	0.00	6
$BS_{\mathrm{m+h}}$	0.28	0.00	10	0.19	0.00	53	0.21	0.00	16	0.17	0.00	8

Table D.9: Correlation coefficients (r), p-values, and slopes for **Skin Gulch** for the dependent variable of **total deposition** to the independent geomorphic, hydraulic, precipitation, and burn severities metrics (n = 490). Independent variables include channel slope (S), ΔS, contributing area (A), valley width (w_{v}), change in valley width (Δw_{v}), $\frac{S}{w_v}$, $\Delta\ \frac{S}{w_v}$, channel width (w_{c}), confinement ratio (C_{r}), rainfall depth (P), maximum 30-min intensity (MI_{30}), moderate burn severity (BS_{m}), high burn severity (BS_{h}), and moderate-to-high burn severity ($BS_{\mathrm{m+h}}$).

Net change	201210–201307			201307–201310			201310–201409			201409–201506		
	r	p-value	Slope	r	p-value	Slope	r	p-value	Slope	r	p-value	Slope
S	-0.28	0.00	-102	-0.30	0.00	-86	-0.23	0.00	-63	-0.21	0.00	-44
ΔS 3	-0.06	0.24	-2997	-0.01	0.89	-264	-0.02	0.60	-917	-0.04	0.43	-1095
A	0.19	0.00	3	0.65	0.00	7	0.04	0.40	0	0.14	0.00	1
w_{v}	0.25	0.00	1	0.36	0.00	1	0.26	0.00	0	0.28	0.00	0
Δw_{v} 3	0.02	0.75	4	-0.10	0.04	-20	-0.07	0.17	-12	-0.05	0.33	-7
$\frac{S}{w_v}$	-0.30	0.00	-1521	-0.28	0.00	-1118	-0.28	0.00	-1063	-0.27	0.00	-782
$\Delta\ FP$ 3	-0.07	0.17	-41128	-0.02	0.70	-9435	-0.02	0.66	-9521	-0.01	0.81	-4166
w_{c}	0.33	0.00	15	0.57	0.00	20	0.10	0.02	3	0.29	0.00	8
C_{r}	-0.20	0.00	0	-0.16	0.00	0	0.06	0.17	0	-0.13	0.01	0
P	0.08	0.06	0	0.03	0.49	0	-0.15	0.00	0	-0.34	0.00	0
MI_{30}	0.16	0.00	0	0.34	0.00	1	-0.03	0.57	0	0.26	0.00	1
BS_{m}	-0.09	0.05	-51	0.06	0.19	28	-0.36	0.00	-157	-0.08	0.07	-27
BS_{h}	0.08	0.09	11	-0.01	0.74	-2	0.30	0.00	33	0.13	0.01	11
$BS_{\mathrm{m+h}}$	0.07	0.14	12	0.00	1.00	0	0.26	0.00	35	0.13	0.00	14

Table D.10: Correlation coefficients (r), p-values, and slopes for **Hill Gulch** for the dependent variable of **total deposition** to the independent geomorphic, hydraulic, precipitation, and burn severities metrics (n = 484). Independent variables include channel slope (S), ΔS, contributing area (A), valley width (w_{v}), change in valley width (Δw_{v}), $\frac{S}{w_v}$, $\Delta\ \frac{S}{w_v}$, channel width (w_{c}), confinement ratio (C_{r}), rainfall depth (P), maximum 30-min intensity (MI_{30}), moderate burn severity (BS_{m}), high burn severity (BS_{h}), and moderate-to-high burn severity ($BS_{\text{m+h}}$).

Net change	201210–201307			201307–201310			201310–201409			201409–201506		
	r	p-value	Slope	r	p-value	Slope	r	p-value	Slope	r	p-value	Slope
S	-0.28	0.00	-130	-0.02	0.71	-2	-0.28	0.00	-71	-0.14	0.00	-31
ΔS 3	-0.09	0.05	-5550	-0.11	0.02	-1813	-0.02	0.66	-787	-0.09	0.05	-3168
A	0.35	0.00	5	0.36	0.00	1	0.18	0.00	1	0.19	0.00	1
w_{v}	0.23	0.00	1	0.17	0.00	0	0.23	0.00	0	0.08	0.10	0
Δw_{v} 3	0.08	0.10	28	-0.10	0.03	-9	-0.03	0.55	-6	0.08	0.08	15
$\frac{S}{w_v}$	-0.29	0.00	-2449	-0.03	0.52	-62	-0.31	0.00	-1505	-0.12	0.01	-509
$\Delta\ FP$ 3	-0.09	0.06	-93200	-0.06	0.23	-15448	-0.01	0.87	-4602	-0.07	0.12	-40065
w_{c}	0.47	0.00	23	0.34	0.00	4	0.23	0.00	6	0.28	0.00	7
C_{r}	-0.33	0.00	-1	-0.11	0.02	0	-0.03	0.44	0	-0.27	0.00	0
P	0.20	0.00	1	0.02	0.60	0	-0.04	0.44	0	0.26	0.00	0
MI_{30}	0.34	0.00	2	0.29	0.00	0	0.27	0.00	0	0.24	0.00	0
BS_{m}	0.33	0.00	242	0.07	0.14	12	0.25	0.00	102	0.28	0.00	103
BS_{h}	-0.42	0.00	-67	-0.12	0.01	-5	-0.27	0.00	-24	-0.38	0.00	-30
$BS_{\text{m+h}}$	-0.42	0.00	-80	-0.12	0.01	-6	-0.26	0.00	-28	-0.38	0.00	-36

Table D.11: Correlation coefficients (r), p-values, and slopes for **Skin Gulch** for the dependent variable of **net volume change** to the independent geomorphic, hydraulic, precipitation, and burn severities metrics, stratified by **channel slopes < 4%**. Independent variables include channel slope (S), ΔS, contributing area (A), valley width (w_{v}), change in valley width (Δw_{v}), $\frac{S}{w_v}$, $\Delta \frac{S}{w_v}$, channel width (w_{c}), confinement ratio (C_{r}), rainfall depth (P), maximum 30-min intensity (MI_{30}), moderate burn severity (BS_{m}), high burn severity (BS_{h}), and moderate-to-high burn severity ($BS_{\text{m+h}}$).

Net change	201210–201307			201307–201310			201310–201409			201409–201506		
	r	p-value	Slope	r	p-value	Slope	r	p-value	Slope	r	p-value	Slope
S	0.05	0.66	123	-0.02	0.86	-233	0.10	0.32	237	0.09	0.39	186
ΔS	-0.07	0.53	-5083	0.15	0.15	59010	-0.01	0.89	-637	0.10	0.36	4551
A	-0.39	0.00	-4	-0.59	0.00	-32	-0.20	0.06	-2	-0.37	0.00	-4
w_{v}	0.01	0.90	0	0.02	0.82	0	-0.09	0.42	0	-0.24	0.02	0
Δw_{v}	0.12	0.29	30	-0.10	0.36	-107	0.00	0.96	1	-0.07	0.54	-10
$\frac{S}{w_v}$	0.03	0.76	2097	0.03	0.81	7585	0.12	0.28	6666	0.20	0.06	9544
$\Delta \frac{S}{w_v}$	-0.08	0.45	-75995	0.12	0.25	573378	-0.04	0.69	-25800	0.07	0.50	38949
w_{c}	-0.37	0.00	-20	-0.59	0.00	-152	-0.25	0.02	-12	-0.34	0.00	-15
C_{r}	0.19	0.08	1	0.32	0.00	5	0.14	0.19	0	-0.09	0.42	0
P	-0.54	0.00	-2	0.21	0.04	2	-0.14	0.19	0	-0.40	0.00	-1
MI_{30}	-0.63	0.00	-1	-0.24	0.02	-5	-0.33	0.00	-2	-0.29	0.00	-3
BS_{m}	-0.14	0.21	-224	-0.37	0.00	-2792	-0.46	0.00	-592	-0.05	0.65	-50
BS_{h}	-0.29	0.01	-93	-0.03	0.77	-46	0.18	0.08	49	-0.05	0.64	-11
$BS_{\text{m+h}}$	-0.36	0.00	-128	-0.12	0.26	-204	0.10	0.35	31	-0.07	0.52	-17

Table D.12: Correlation coefficients (r), p-values, and slopes for **Skin Gulch** for the dependent variable of **net volume change** to the independent geomorphic, hydraulic, precipitation, and burn severities metrics, stratified by **channel slopes $\geq$ 4%**. Independent variables include channel slope (S), ΔS, contributing area (A), valley width (w_{v}), change in valley width (Δw_{v}), $\frac{S}{w_v}$, $\Delta \frac{S}{w_v}$, channel width (w_{c}), confinement ratio (C_{r}), rainfall depth (P), maximum 30-min intensity (MI_{30}), moderate burn severity (BS_{m}), high burn severity (BS_{h}), and moderate-to-high burn severity ($BS_{\text{m+h}}$).

Net change	201210–201307			201307–201310			201310–201409			201409–201506		
	r	p-value	Slope	r	p-value	Slope	r	p-value	Slope	r	p-value	Slope
S	-0.17	0.00	-68	0.31	0.00	453	-0.24	0.00	-75	-0.15	0.00	-31
ΔS	-0.03	0.63	-1395	0.05	0.38	8949	0.04	0.42	1896	-0.03	0.56	-867
A	0.13	0.01	3	-0.69	0.00	-66	-0.02	0.75	0	0.29	0.00	4
w_{v}	0.16	0.00	0	-0.10	0.05	-1	0.18	0.00	0	0.15	0.00	0
Δw_{v}	0.02	0.74	5	-0.06	0.27	-63	-0.02	0.68	-5	0.07	0.20	11
$\frac{S}{w_v}$	-0.20	0.00	-1018	0.27	0.00	5098	-0.24	0.00	-997	-0.17	0.00	-472
$\Delta \frac{S}{w_v}$	-0.05	0.36	-30239	0.06	0.23	148187	0.03	0.55	16426	-0.01	0.80	-4754
w_{c}	0.25	0.00	15	-0.61	0.00	-137	0.02	0.65	1	0.36	0.00	12
C_{r}	-0.14	0.00	0	0.32	0.00	3	0.07	0.18	0	-0.21	0.00	0
P	0.16	0.00	0	0.12	0.02	1	-0.13	0.01	0	-0.34	0.00	0
MI_{30}	0.17	0.00	0	-0.30	0.00	-3	-0.07	0.15	0	0.26	0.00	1
BS_{m}	-0.15	0.00	-81	0.04	0.39	87	-0.36	0.00	-160	-0.04	0.44	-11
BS_{h}	0.16	0.00	22	-0.15	0.00	-75	0.29	0.00	33	0.11	0.03	8
$BS_{\text{m+h}}$	0.15	0.00	27	-0.17	0.00	-110	0.25	0.00	35	0.13	0.01	12

Table D.13: Correlation coefficients (r), p-values, and slopes for **Hill Gulch** for the dependent variable of **net volume change** to the independent geomorphic, hydraulic, precipitation, and burn severities metrics, stratified by **channel slopes < 4%**. Independent variables include channel slope (S), ΔS, contributing area (A), valley width (w_{v}), change in valley width (Δw_{v}), $\frac{S}{w_v}$, $\Delta \frac{S}{w_v}$, channel width (w_{c}), confinement ratio (C_{r}), rainfall depth (P), maximum 30-min intensity (MI_{30}), moderate burn severity (BS_{m}), high burn severity (BS_{h}), and moderate-to-high burn severity ($BS_{\text{m+h}}$).

Net change	201210–201307			201307–201310			201310–201409			201409–201506		
	r	p-value	Slope	r	p-value	Slope	r	p-value	Slope	r	p-value	Slope
S	-0.06	0.47	-186	-0.06	0.48	-267	0.03	0.70	51	0.13	0.12	191
ΔS	-0.19	0.02	-19937	0.10	0.23	17197	0.01	0.91	587	-0.07	0.38	-4033
A	0.16	0.05	2	-0.04	0.64	-1	-0.20	0.01	-1	-0.15	0.08	-1
w_{v}	0.16	0.05	1	-0.01	0.88	0	0.00	0.97	0	-0.05	0.52	0
Δw_{v}	0.22	0.01	70	-0.20	0.01	-91	0.01	0.89	2	0.24	0.00	34
$\frac{S}{w_v}$	-0.16	0.05	-10592	-0.09	0.30	-8360	-0.03	0.71	-1034	0.14	0.10	4770
$\Delta \frac{S}{w_v}$	-0.22	0.01	-544461	0.14	0.09	560181	-0.05	0.58	-62758	-0.08	0.32	-97928
w_{c}	0.23	0.00	12	-0.08	0.30	-6	-0.21	0.01	-6	-0.07	0.40	-2
C_{r}	-0.22	0.01	-1	0.22	0.01	1	0.26	0.00	0	-0.11	0.18	0
P	-0.02	0.81	0	0.13	0.12	0	0.27	0.00	0	0.26	0.00	0
MI_{30}	0.19	0.02	1	-0.11	0.18	0	-0.02	0.79	0	0.05	0.56	0
BS_{m}	0.05	0.56	60	0.08	0.35	137	0.08	0.33	49	0.22	0.01	125
BS_{h}	-0.14	0.09	-32	-0.07	0.41	-22	-0.10	0.22	-11	-0.27	0.00	-30
$BS_{\text{m+h}}$	-0.15	0.07	-40	-0.06	0.45	-23	-0.10	0.22	-13	-0.27	0.00	-34

Table D.14: Correlation coefficients (r), p-values, and slopes for **Hill Gulch** for the dependent variable of **net volume change** to the independent geomorphic, hydraulic, precipitation, and burn severities metrics, stratified by **channel slopes $\geq$ 4%**. Independent variables include channel slope (S), ΔS, contributing area (A), valley width (w_{v}), change in valley width (Δw_{v}), $\frac{S}{w_v}$, $\Delta \frac{S}{w_v}$, channel width (w_{c}), confinement ratio (C_{r}), rainfall depth (P), maximum 30-min intensity (MI_{30}), moderate burn severity (BS_{m}), high burn severity (BS_{h}), and moderate-to-high burn severity ($BS_{\text{m+h}}$).

Net change	201210–201307			201307–201310			201310–201409			201409–201506		
	r	p-value	Slope	r	p-value	Slope	r	p-value	Slope	r	p-value	Slope
S	-0.22	0.00	-97	0.36	0.00	209	-0.30	0.00	-101	-0.08	0.13	-20
ΔS	-0.06	0.30	-3399	-0.01	0.84	-915	0.11	0.06	4877	-0.06	0.30	-1881
A	0.37	0.00	13	-0.33	0.00	-15	0.03	0.61	1	0.18	0.00	3
w_{v}	0.06	0.25	0	-0.04	0.50	0	0.23	0.00	1	-0.10	0.08	0
Δw_{v}	0.02	0.74	7	0.05	0.40	26	-0.08	0.19	-24	0.04	0.46	9
$\frac{S}{w_v}$	-0.23	0.00	-1758	0.32	0.00	3437	-0.34	0.00	-2082	-0.04	0.51	-157
$\Delta \frac{S}{w_v}$	-0.05	0.38	-43712	0.00	0.96	-3116	0.11	0.05	78398	-0.05	0.34	-26622
w_{c}	0.52	0.00	43	-0.49	0.00	-55	0.09	0.09	6	0.28	0.00	12
C_{r}	-0.30	0.00	-1	0.34	0.00	1	0.05	0.37	0	-0.27	0.00	0
P	0.23	0.00	1	0.22	0.00	0	-0.06	0.28	0	0.22	0.00	0
MI_{30}	0.28	0.00	1	-0.38	0.00	-1	0.05	0.36	0	0.19	0.00	0
BS_{m}	0.37	0.00	234	-0.25	0.00	-215	0.11	0.04	56	0.26	0.00	92
BS_{h}	-0.43	0.00	-60	0.23	0.00	45	-0.08	0.14	-9	-0.33	0.00	-26
$BS_{\text{m+h}}$	-0.42	0.00	-72	0.21	0.00	50	-0.07	0.22	-9	-0.33	0.00	-32

Table D.15: Correlation coefficients (r), p-values, and slopes for **Skin Gulch** for the dependent variable of **net volume change** to the independent geomorphic, hydraulic, precipitation, and burn severities metrics, stratified by **contributing area < 4 km^2**. Independent variables include channel slope (S), ΔS, contributing area (A), valley width (w_{v}), change in valley width (Δw_{v}), $\frac{S}{w_v}$, $\Delta\ \frac{S}{w_v}$, channel width (w_{c}), confinement ratio (C_{r}), rainfall depth (P), maximum 30-min intensity (MI_{30}), moderate burn severity (BS_{m}), high burn severity (BS_{h}), and moderate-to-high burn severity ($BS_{\mathrm{m+h}}$).

Net change	201210–201307			201307–201310			201310–201409			201409–201506		
	r	p-value	Slope	r	p-value	Slope	r	p-value	Slope	r	p-value	Slope
S	-0.26	0.00	-98	0.28	0.00	188	-0.25	0.00	-79	-0.10	0.04	-23
ΔS	-0.04	0.43	-2104	-0.01	0.84	-949	0.03	0.53	1371	-0.03	0.61	-778
A	0.53	0.00	22	-0.56	0.00	-42	0.05	0.32	2	0.36	0.00	9
w_{v}	0.19	0.00	0	-0.07	0.16	0	0.11	0.03	0	0.01	0.87	0
Δw_{v}	0.03	0.57	8	0.00	0.99	0	0.01	0.79	3	0.01	0.91	1
$\frac{S}{w_v}$	-0.28	0.00	-1356	0.26	0.00	2319	-0.25	0.00	-1066	-0.14	0.01	-410
$\Delta\ \frac{S}{w_v}$	-0.07	0.17	-41614	0.03	0.61	28982	0.01	0.87	4330	-0.01	0.88	-2891
w_{c}	0.53	0.00	39	-0.55	0.00	-74	0.07	0.18	4	0.37	0.00	16
C_{r}	-0.22	0.00	0	0.32	0.00	1	0.04	0.40	0	-0.24	0.00	0
P	0.24	0.00	1	0.22	0.00	0	-0.11	0.03	0	-0.37	0.00	0
MI_{30}	0.35	0.00	1	-0.12	0.01	-1	-0.06	0.27	0	0.21	0.00	1
BS_{m}	-0.15	0.00	-78	0.08	0.11	78	-0.38	0.00	-179	0.00	0.96	-1
BS_{h}	0.19	0.00	26	-0.15	0.00	-37	0.33	0.00	39	0.05	0.30	4
$BS_{\mathrm{m+h}}$	0.20	0.00	34	-0.17	0.00	-51	0.29	0.00	43	0.06	0.20	7

Table D.16: Correlation coefficients (r), p-values, and slopes for **Skin Gulch** for the dependent variable of **net volume change** to the independent geomorphic, hydraulic, precipitation, and burn severities metrics, stratified by **contributing area $\geq$ 4 km^2**. Independent variables include channel slope (S), ΔS, contributing area (A), valley width (w_{v}), change in valley width (Δw_{v}), $\frac{S}{w_v}$, $\Delta \frac{S}{w_v}$, channel width (w_{c}), confinement ratio (C_{r}), rainfall depth (P), maximum 30-min intensity (MI_{30}), moderate burn severity (BS_{m}), high burn severity (BS_{h}), and moderate-to-high burn severity ($BS_{\text{m+h}}$).

Net change	201210–201307			201307–201310			201310–201409			201409–201506		
	r	p-value	Slope	r	p-value	Slope	r	p-value	Slope	r	p-value	Slope
S	-0.08	0.42	-135	0.00	0.99	-9	0.05	0.63	53	0.23	0.03	194
ΔS	-0.03	0.78	-3436	0.09	0.37	63946	-0.22	0.03	-18389	-0.04	0.72	-2638
A	-0.23	0.02	-4	-0.31	0.00	-28	-0.09	0.41	-1	-0.54	0.00	-6
w_{v}	0.08	0.43	0	-0.05	0.62	-1	0.07	0.52	0	-0.40	0.00	-1
Δw_{v}	0.10	0.35	34	-0.15	0.14	-312	-0.11	0.31	-23	0.16	0.13	29
$\frac{S}{w_v}$	-0.15	0.15	-5559	0.01	0.89	3221	-0.05	0.62	-1273	0.35	0.00	6928
$\Delta \frac{S}{w_v}$	-0.01	0.90	-28375	0.17	0.10	2260512	-0.13	0.20	-203521	-0.08	0.47	-98601
w_{c}	-0.27	0.01	-24	-0.32	0.00	-173	-0.07	0.50	-4	-0.56	0.00	-35
C_{r}	0.34	0.00	5	0.21	0.04	17	0.14	0.18	1	-0.10	0.35	-1
P	-0.54	0.00	-2	0.41	0.00	10	-0.32	0.00	-1	-0.05	0.62	0
MI_{30}	-0.63	0.00	-1	-0.10	0.34	-10	-0.24	0.02	-2	-0.23	0.04	-3
BS_{m}	-0.07	0.52	-185	-0.05	0.65	-794	0.11	0.28	204	-0.54	0.00	-788
BS_{h}	-0.50	0.00	-171	-0.33	0.00	-676	-0.27	0.01	-61	0.36	0.00	64
$BS_{\text{m+h}}$	-0.54	0.00	-196	-0.36	0.00	-777	-0.28	0.01	-65	0.31	0.00	59

Table D.17: Correlation coefficients (r), p-values, and slopes for **Hill Gulch** for the dependent variable of **net volume change** to the independent geomorphic, hydraulic, precipitation, and burn severities metrics, stratified by **contributing area < 4 km^2**. Independent variables include channel slope (S), ΔS, contributing area (A), valley width (w_{v}), change in valley width (Δw_{v}), $\frac{S}{w_v}$, $\Delta\ \frac{S}{w_v}$, channel width (w_{c}), confinement ratio (C_{r}), rainfall depth (P), maximum 30-min intensity (MI_{30}), moderate burn severity (BS_{m}), high burn severity (BS_{h}), and moderate-to-high burn severity ($BS_{\mathrm{m+h}}$).

Net change	201210–201307			201307–201310			201310–201409			201409–201506		
	r	p-value	Slope	r	p-value	Slope	r	p-value	Slope	r	p-value	Slope
S	-0.22	0.00	-95	0.32	0.00	213	-0.31	0.00	-99	-0.06	0.26	-13
ΔS	-0.08	0.12	-4164	-0.01	0.87	-791	0.10	0.06	4329	-0.07	0.18	-2203
A	0.56	0.00	24	-0.41	0.00	-28	0.12	0.01	4	0.26	0.00	6
w_{v}	0.08	0.12	0	-0.01	0.81	0	0.24	0.00	1	-0.12	0.02	0
Δw_{v}	0.05	0.30	18	-0.05	0.31	-28	-0.07	0.20	-17	0.12	0.02	21
$\frac{S}{w_v}$	-0.23	0.00	-1791	0.29	0.00	3583	-0.34	0.00	-2058	-0.02	0.73	-73
$\Delta\ \frac{S}{w_v}$	-0.07	0.19	-61774	0.01	0.89	10294	0.10	0.06	68897	-0.07	0.21	-33011
w_{c}	0.58	0.00	48	-0.48	0.00	-62	0.14	0.01	9	0.29	0.00	13
C_{r}	-0.32	0.00	-1	0.33	0.00	1	0.07	0.15	0	-0.28	0.00	0
P	0.21	0.00	1	0.21	0.00	0	-0.03	0.51	0	0.24	0.00	0
MI_{30}	0.28	0.00	1	-0.35	0.00	-1	0.09	0.06	0	0.19	0.00	0
BS_{m}	0.31	0.00	197	-0.18	0.00	-176	0.13	0.01	64	0.26	0.00	90
BS_{h}	-0.39	0.00	-54	0.15	0.00	33	-0.12	0.02	-12	-0.34	0.00	-26
$BS_{\mathrm{m+h}}$	-0.38	0.00	-65	0.14	0.01	36	-0.10	0.04	-14	-0.34	0.00	-32

Table D.18: Correlation coefficients (r), p-values, and slopes for **Hill Gulch** for the dependent variable of **net volume change** to the independent geomorphic, hydraulic, precipitation, and burn severities metrics, stratified by **contributing area $\geq$ 4 km^2**. Independent variables include channel slope (S), ΔS, contributing area (A), valley width (w_{v}), change in valley width (Δw_{v}), $\frac{S}{w_v}$, $\Delta\ \frac{S}{w_v}$, channel width (w_{c}), confinement ratio (C_{r}), rainfall depth (P), maximum 30-min intensity (MI_{30}), moderate burn severity (BS_{m}), high burn severity (BS_{h}), and moderate-to-high burn severity ($BS_{\text{m+h}}$).

Net change	201210–201307			201307–201310			201310–201409			201409–201506		
	r	p-value	Slope	r	p-value	Slope	r	p-value	Slope	r	p-value	Slope
S	-0.09	0.42	-303	0.15	0.17	521	-0.15	0.18	-221	0.10	0.39	165
ΔS	0.00	0.97	-1103	-0.10	0.40	-23652	0.11	0.32	11061	-0.10	0.40	-9799
A	-0.11	0.34	-2	0.11	0.31	2	-0.10	0.35	-1	-0.29	0.01	-3
w_{v}	0.16	0.16	1	-0.35	0.00	-1	-0.03	0.78	0	0.04	0.72	0
Δw_{v}	0.21	0.06	85	-0.08	0.46	-33	0.07	0.53	13	0.15	0.19	28
$\frac{S}{w_v}$	-0.14	0.21	-12055	0.29	0.01	24442	-0.14	0.20	-5207	0.04	0.72	1673
$\Delta\ \frac{S}{w_v}$	-0.12	0.30	-789120	-0.06	0.61	-393538	0.07	0.53	198883	-0.10	0.39	-293251
w_{c}	-0.08	0.50	-9	0.11	0.33	13	-0.13	0.25	-7	-0.25	0.03	-14
C_{r}	0.14	0.22	2	-0.31	0.00	-3	0.04	0.72	0	0.14	0.21	1
P	-0.05	0.64	-2	-0.12	0.30	-4	0.01	0.91	0	0.17	0.13	1
MI_{30}	0.00	1.00	0	0.04	0.73	0	-0.21	0.06	-8	0.00	1.00	0
BS_{m}	0.34	0.00	4620	-0.11	0.34	-1433	-0.21	0.06	-1317	0.52	0.00	3362
BS_{h}	-0.10	0.36	-71	0.13	0.25	86	-0.11	0.34	-34	-0.29	0.01	-94
$BS_{\text{m+h}}$	-0.09	0.44	-61	0.13	0.27	85	-0.12	0.29	-38	-0.27	0.02	-88